

Determination of Residual Stress Profiles in A Friction Stir Welded Stringer-to-Skin
Lap Joint

A Thesis

Presented to

The Academic Faculty

By

Michael Bach

In Partial Fulfillment

of the Requirements for the Degree

Doctor of Philosophy in Mechanical Engineering

Carleton University

Ottawa, Ontario

©2012

Michael Bach



Library and Archives
Canada

Published Heritage
Branch

395 Wellington Street
Ottawa ON K1A 0N4
Canada

Bibliothèque et
Archives Canada

Direction du
Patrimoine de l'édition

395, rue Wellington
Ottawa ON K1A 0N4
Canada

Your file Votre référence

ISBN: 978-0-494-94207-9

Our file Notre référence

ISBN: 978-0-494-94207-9

NOTICE:

The author has granted a non-exclusive license allowing Library and Archives Canada to reproduce, publish, archive, preserve, conserve, communicate to the public by telecommunication or on the Internet, loan, distribute and sell theses worldwide, for commercial or non-commercial purposes, in microform, paper, electronic and/or any other formats.

The author retains copyright ownership and moral rights in this thesis. Neither the thesis nor substantial extracts from it may be printed or otherwise reproduced without the author's permission.

AVIS:

L'auteur a accordé une licence non exclusive permettant à la Bibliothèque et Archives Canada de reproduire, publier, archiver, sauvegarder, conserver, transmettre au public par télécommunication ou par l'Internet, prêter, distribuer et vendre des thèses partout dans le monde, à des fins commerciales ou autres, sur support microforme, papier, électronique et/ou autres formats.

L'auteur conserve la propriété du droit d'auteur et des droits moraux qui protègent cette thèse. Ni la thèse ni des extraits substantiels de celle-ci ne doivent être imprimés ou autrement reproduits sans son autorisation.

In compliance with the Canadian Privacy Act some supporting forms may have been removed from this thesis.

While these forms may be included in the document page count, their removal does not represent any loss of content from the thesis.

Conformément à la loi canadienne sur la protection de la vie privée, quelques formulaires secondaires ont été enlevés de cette thèse.

Bien que ces formulaires aient inclus dans la pagination, il n'y aura aucun contenu manquant.

Canada

ABSTRACT

Riveting has been for many years the conventional method of joining aluminum components such as aircraft stringer-to-skin panels in the lap joint configuration. Due to a demand for a more economical and improved joining method, friction stir welding has been proposed as an alternative welding process. Residual stresses left behind from the friction stir welding process caused the stringer-to-skin lap joint to twist after the clamps are removed. A post-welding process of hammer peening was able to remove the distortion in the plate. In this thesis, the crack compliance method is used to calculate the residual stresses in the friction stir welded lap joints in the through thickness, transverse, and longitudinal direction. A non-destructive residual stress measurement technique known as neutron diffraction was used on the lap joint in both as-welded and hammer peened conditions. The residual stress profiles in the through thickness, transverse and longitudinal directions were successfully measured and compared with the residual stress from the compliance method. It was determined that the compliance method was successful in calculating the residual stresses in the through thickness and transverse direction but was not able to calculate the residual stress in the longitudinal direction. Distortion in the plate was a result of a combination of non-uniform residual stress profile in the three principal directions. Fatigue testing was performed on the as-welded and hammer peened configuration and it was determined that the hammer peened condition outlived that of the as-welded condition under the same loading frequency. An examination of the failure locations in the friction stir welded lap joints concluded that the as-welded specimens failed at a location in the weld region with a combination of weld defects, lowest hardness value and highest tensile residual stresses.

ACKNOWLEDGEMENTS

I would like to firstly thank Professor Robert Bell and Professor Xin Wang of Carleton University for being my supervisor for the past 4 years. It has been a pleasure to have you both as my supervisors. Next I would like to thank Ali Merati, a senior research officer from the National Research Council of Canada and an adjunct professor at Carleton University, for being my supervisor at NRC. His invaluable guidance has tremendously influenced my graduate work and research experience. I would like to thank Michael Gharghouri and Ronald Rogge at the National Beam Center in Chalk River who were always positive and helping me with my neutrons diffraction experiments. I hope I will have the opportunity to come to Chalk River in the future to conduct more neutron experiments with them.

Last but not least, I would like to thank my family for their unconditional support they have given me through the years. Although they were not able to help me with my technical research, they were there to support and motivate me to push on and finish my thesis. I really appreciate all the support and encouragement they have given me. With that, I would like to dedicate this thesis to my grandparents because they made a big deal when I didn't dedicate my Masters thesis to them. Thank you all from the bottom of my heart.

TABLE OF CONTENTS

ABSTRACT	ii
ACKNOWLEDGEMENTS	iii
LIST OF TABLES	ix
LIST OF FIGURES	xi
TERMINOLOGY	xxii

CHAPTER

1.0 INTRODUCTION.....	1
1.1 Background.....	1
1.2 Objectives.....	8
1.3 Thesis Outline.....	9
2.0 LITERATURE REVIEW.....	10
2.1 Construction of Aircraft Components.....	10
2.2 Friction Stir Welding.....	14
2.2.1 Friction Stir Welding Process.....	14
2.2.2 Application of Friction Stir Welding.....	16
2.2.3 Friction Stir Weld Joint Configurations.....	18
2.2.4 Tool Geometries.....	20
2.2.5 Friction Stir Weld Zones.....	20
2.3 Residual Stresses.....	22
2.3.1 Residual Stresses in Welds.....	22
2.3.2 Residual Stress Relief Techniques.....	24
2.3.3 Residual Stress Measurement Techniques.....	26

2.4 Crack Compliance Method.....	29
2.4.1 Experimental Setup.....	30
2.4.2 Forward and Inverse Solutions.....	32
2.4.3 Finite Element Modeling.....	35
2.4.4 Error Analysis.....	38
2.5 Neutron Diffraction.....	44
2.5.1 Diffraction Theory.....	46
2.6 Fatigue Failure in Aircraft.....	51
2.6.1 Fatigue Life and Factors That Affect It.....	53
2.6.2 How to Measure Fatigue Life: S-N Curves.....	54
2.6.3 Design Against Fatigue.....	56
2.7 Summary of Current Literature Review.....	56
2.7.1 Current Friction Stir Welding Literatures.....	56
2.7.2 Crack Compliance Method Literatures.....	58
2.7.3 Neutron Diffraction Literatures.....	59
2.7.4 Other Residual Stress Measurement Techniques Literatures.....	60
2.7.5 Fatigue Performance Literatures.....	60
 3.0 TEST SPECIMEN.....	 62
3.1 Friction Stir Weld Specimens.....	62
3.1.1 Weld Configuration.....	64
3.1.2 Specimen Geometry.....	65
3.1.3 Material Properties.....	67
3.2 Friction Stir Weld Microstructure.....	69
3.2.1 FSW Weld Zones.....	69
3.3 Hardness Test.....	74

4.0 EXPERIMENTAL PROCEDURES.....	83
4.1 Crack Compliance Method.....	83
4.1.1 Validation Calculations.....	83
4.1.1.1 Prime Beam Bending Experiment.....	83
4.1.1.2 M.T. Milan AA2024-T3 FSW Butt Joint Experiment.....	88
4.1.1.3 NRC Butt Welded AA2024-T3 Experiment.....	93
4.1.2 Variation in Residual Stress (σ_x) of FSW Lap Joint in Through Thickness (y) Direction.....	111
4.1.2.1 As-welded and Hammer Peened Through Thickness Residual Stress (σ_x).....	111
4.1.3 Variation in Residual Stress (σ_z) in FSW Lap Joint in Transverse (x) Direction.....	114
4.1.3.1 As-welded Longitudinal Residual Stress (σ_z).....	114
4.1.4 Variation in Transverse Residual Stress (σ_x) in Longitudinal (z) Direction.....	119
4.1.4.1 As-welded Transverse Residual Stress (σ_x).....	119
4.2 Neutron Diffraction Experiments.....	124
4.2.1 Experiment Setup.....	124
4.2.2 First Set of Strain Measurements.....	128
4.2.2.1 Transverse Strain (ϵ_x) Measurements.....	129
4.2.2.2 Normal Strain (ϵ_y) Measurements.....	132
4.2.2.3 Longitudinal Strain (ϵ_z) Measurements.....	134
4.2.3 Neutron Diffraction to Determine Residual Stress in Longitudinal (z) Direction	136
4.3 Fatigue Testing.....	139

5.0 RESULTS AND DISCUSSION.....	142
5.1 Residual Stress Results Using Crack Compliance Method.....	142
5.1.1 Variation in Transverse Residual Stress (σ_x) Through The Thickness of the Weld (y-direction).....	142
5.1.2 Variation in Longitudinal Residual Stress (σ_z) Across the Weld (x-direction).....	157
5.1.3 Variation in Transverse Residual Stress (σ_x) Along the Weld Centerline in z-direction.....	169
5.2 Independent Verification Using Neutron Diffraction.....	175
5.2.1 Neutron Results of Residual Stress Component in Through Thickness (y) Direction.....	176
5.2.2 Neutron Results of Residual Stress Component in Transverse (x) Direction.....	180
5.2.3 Neutron Results of Residual Stress Component in Longitudinal (z) Direction.....	184
5.3 Comparison of the Residual Stress from the Crack Compliance Method and Neutron Diffraction.....	190
5.4 Validation of Using Crack Compliance Method on 3D and Asymmetric Test Specimens.....	199
5.5 Distortion in Friction Stir Welded Lap Joint.....	203
5.6 Results of Fatigue Performance.....	207
5.6.1 Fatigue Life of Friction Stir Welded Specimens.....	208
5.6.2 Examination of Fracture Surfaces Using Fractography.....	212
5.7 Examination of Failure Location in the FSW Stringer-to-skin Lap Joints....	219
6.0 CONCLUSIONS AND RECOMMENDATIONS.....	227
6.1 Conclusions.....	227

6.2 Contributions.....	231
6.3 Recommendations.....	232
6.4 Future Work.....	233
6.5 List of Presentations and Publications.....	235
REFERENCES.....	237
APPENDICES.....	247
A. MATLAB Algorithm Solve.m to calculate residual stress.....	247
B. MATLAB Algorithm to apply load based on Legendre polynomial.....	253

LIST OF TABLES

CHAPTER 2

Table 2.1: Summary of destructive methods of determining residual stresses.....	28
---	----

CHAPTER 3

Table 3.1: Material Properties of 20204-T3 and 7075-T6 aluminum alloys.....	68
Table 3.2: Elemental composition of aluminum alloys.....	68

CHAPTER 4

Table 4.1: Calculated residual stresses compared with Prime residual stress.....	88
Table 4.2: Comparison of maximum compressive and tensile stresses.....	93
Table 4.3: RSM values for strain fitting of gauge 13 using different number of polynomials.....	101
Table 4.4: Fatigue Test Specimen and loading parameters.....	141

CHAPTER 5

Table 5.1: RSM error for strain fitting of bottom gauge using different number of polynomials.....	145
Table 5.2: Calculated A_i values using different orders of polynomials.....	146
Table 5.3: RSM error for strain fitting of bottom gauge using different number of polynomials.....	149
Table 5.4: Calculated A_i values using different number of polynomials.....	150

Table 5.5: RMS error for strain fitting using gauge 3 position.....	159
Table 5.6: Calculated A_i values using different number of polynomials from gauge 3 position.....	160
Table 5.7: RMS error of fitted strains at gauge 1 position.....	170
Table 5.8: RMS error of fitted strains at gauge 2 position.....	172
Table 5.9: RMS error of fitted strains at gauge 3 position.....	173
Table 5.10: Comparison of transverse residual stress (σ_x) in as-welded and hammer peened specimens in through thickness (y) direction at weld centerline.....	177
Table 5.11: Comparison of longitudinal residual stress (σ_z) in as-welded and hammer peened specimens in transverse (x) direction.....	184
Table 5.12: Comparison of transverse residual stress (σ_x) in as-welded and hammer peened specimens in longitudinal (z) direction.....	189
Table 5.13: Comparison of transverse (σ_x) residual stresses from compliance method and neutron diffraction for as-welded specimen in through thickness (y) direction.....	196
Table 5.14: Comparison of transverse (σ_x) residual stresses from compliance method and neutron diffraction for hammer peened specimen in through thickness (y) direction.....	195
Table 5.15: Comparison of transverse (σ_x) residual stresses from compliance method and neutron diffraction for as-welded specimen in transverse (x) direction.....	197
Table 5.16: Comparison of transverse (σ_x) residual stresses from compliance method and neutron diffraction for as-welded specimen in longitudinal (z) direction.....	198
Table 5.17: Cycles to failure of FSW lap joints.....	209

LIST OF FIGURES

CHAPTER 1

Figure 1.1: Riveted stringer-to-skin construction in aircraft fuselages [web image, Ref. 85].....	1
Figure 1.2: Example of the FSW process [web image, Ref. 86].....	2
Figure 1.3: Schematic of typical residual stresses from FSW [Dalle (2001)].....	4
Figure 1.4: FSW plate before and after hammer peening [Merati (2009)].....	4
Figure 1.5: Components of the crack compliance method.....	6

CHAPTER 2

Figure 2.1: Semi-monocoque construction of aircraft fuselage [web image, Ref.87].....	10
Figure 2.2: Horizontal stringers fasten to skin panel [web image, Ref. 88].....	11
Figure 2.3: Stringers used in wing construction [web image, Ref. 89].....	12
Figure 2.4: Rivets positioned in place to attach panels together [web image, Ref. 90].....	13
Figure 2.5: a) Riveted stinger to skin panel [web image, Ref. 85] b) FSW stringer-to-skin panel [web image, Ref. 91].....	13
Figure 2.6: Friction stir welding process.....	14
Figure 2.7: Lockheed Martin's FSW Orion crew module [web image, Ref. 92].....	17
Figure 2.8: Joint configuration for friction stir welding a) butt joint, b) edge butt, c) T butt joint, d) lap joint e) multiple lap joint, f) T lap joint, g) fillet [web image, Ref. 93].....	18
Figure 2.9: a) Continuous weld b) Discontinuous weld [Merati (2009)].....	19
Figure 2.10: a) SP b) DPC outward hook c) DPC inward hook [Merati (2009)].....	19
Figure 2.11: Tool Tip Geometries [Elangovan (2008)].....	20
Figure 2.12: FSW Weld Zones: weld nugget, TMZ, HAZ, parent material [web image, Ref. 94].....	21

Figure 2.13: Superposition principle of slitting method [Cheng et al. (2007)].....	29
Figure 2.14: a) gauges placed on top and bottom face b) gauges placed on sides of plate next to slit line [Rankin et al.(2003)].....	30
Figure 2.15: Sample strain gauge measurement [Prime (1999)].....	32
Figure 2.16: Unknown stress distribution [Prime (1999)].....	33
Figure 2.17: Nuclear fission to separate neutrons [web image, Ref. 96].....	45
Figure 2.18: Scattering geometry for Bragg's Law [Gharghour (2009)].....	47
Figure 2.19: Nominal gauge volume [Gharghour (2009)].....	48
Figure 2.20: Effect of scattering angle (2θ) on nominal gauge volume (plan view) (a) $2\theta = 90^\circ$ (b) $2\theta < 90^\circ$ [Gharghour (2009)].....	49
Figure 2.21: Scattering geometry for lattice strain measurements [Gharghour (2009)]...50	
Figure 2.22: Forward Roof window of de Havilland Comet [web image, Ref. 97].....	51
Figure 2.23: Fatigue performance setup to determine fatigue life of a specimen [web image, Ref. 98].....	55
Figure 2.24: Typical S-N curve to determine fatigue life of a component [web image, Ref. 99].....	55

CHAPTER 3

Figure 3.1: FSW stringer-to-skin lap joint plate.....	63
Figure 3.2: As-welded and hammer peened test plates [Merati (2009)].....	63
Figure 3.3: Surface finishes of as-welded and hammer peened plates.....	64
Figure 3.4: Double pass weld configuration.....	65
Figure 3.5: Test specimen sections from whole plate.....	66
Figure 3.6: FSW Stringer-to-skin lap joint cross-sectional dimension.....	66
Figure 3.7: Cross section of FSW a) weld nugget, b) TMAZ, c) HAZ, d) onion ring pattern e) parent AA7075-T6, f) parent AA2024-T3.....	71
Figure 3.8: Central weld region showing the weld nugget.....	71
Figure 3.9: a) Parent 7075-T6 material, b) parent 2024-T3 material.....	72

Figure 3.10: Transition between weld nugget and TMAZ.....	72
Figure 3.11: Onion ring patterns created by mixing of two alloys, distinct bands of material reveal that the two alloys are not complete mixed with one another.....	73
Figure 3.12: Large voids found at edge of weld tool between weld nugget and TMAZ.....	73
Figure 3.13: a) Location of through thickness hardness profiles, b) location of transverse hardness profiles	74
Figure 3.14: Through thickness hardness profiles for as-welded specimen.....	76
Figure 3.15: Through thickness hardness profiles for hammer peened specimen.....	76
Figure 3.16: Hardness profiles of both specimens at location $x=-10$ mm.....	77
Figure 3.17: Hardness profiles of both specimens at location $x=0$ mm.....	77
Figure 3.18: Transverse hardness profiles of as-welded specimen.....	80
Figure 3.19: Transverse hardness profiles of hammer peened specimen.....	80
Figure 3.20: Transverse hardness profiles of both specimen in stringer section.....	81
Figure 3.21: Transverse hardness profiles of both specimens in skin section.....	82

CHAPTER 4

Figure 4.1: Strain gauge position for beam bending experiment [Prime (2009)].....	84
Figure 4.2: Measured bottom strain from beam bending experiment [Prime (2009)].....	84
Figure 4.3: Compliance matrix from top gauge of beam bending experiment.....	86
Figure 4.4: Compliance matrix from bottom gauge of beam bending experiment.....	86
Figure 4.5: Flow chart of crack compliance method and MATLAB algorithm.....	87
Figure 4.6: Transverse test piece for measuring longitudinal residual stresses [M.T. Milan (2007)].....	89
Figure 4.7: 2D FE model of FSW butt-welded plate.....	90
Figure 4.8: Compliance functions from bottom edge strain gauge.....	91

Figure 4.9: Comparison of Residual stress LEFM and crack compliance method.....	92
Figure 4.10: Advancing side residual stress profile [Dubuorg et al.(2007)].....	94
Figure 4.11: a) NRC FSW plate b) MB1 test piece to measure longitudinal stress on retreating side with c) stain gauge positioning.....	95
Figure 4.12: Slitting experiments strain measurement from gauges 4 and 13.....	96
Figure 4.13: 2D FEM model of FSW butt joint plate.....	98
Figure 4.14: Compliance functions for strain gauge location 4.....	98
Figure 4.15: Compliance functions for strain gauge location 13.....	99
Figure 4.16: Measured strain vs. fitted strain using 1 order polynomials.....	99
Figure 4.17: Measured strain vs. fitted strain using 5 order polynomials.....	100
Figure 4.18: Measured strain vs. fitted strain using 10 order polynomials.....	100
Figure 4.19: Variation in residual stress (σ_x) using different order of polynomials in fitting of strain.....	102
Figure 4.20: Variation in residual stress (σ_x) from gauge 13 using 9 order and 10 order polynomials.....	103
Figure 4.21: Comparison of residual stress from gauge 13 with previous neutron results [Dubuorg et al.(2007)].....	104
Figure 4.22: Variation in stress (σ_x) using different number of strain values from gauge 4.....	105
Figure 4.23: Variation in stress (σ_x) using 15,25, and 35 strain from gauge 4.....	105
Figure 4.24: Advancing side residual stress profile (σ_x) across weld.....	106
Figure 4.25: Final crack compliance method stress distribution plotted against neutron and thermal FEM model [Dubuorg (2007)].....	107
Figure 4.26: Variation in residual stress (σ_x) from gauge 7 and 12.....	109
Figure 4.27: Variation in residual stress (σ_x) from gauge 7 and 10.....	110
Figure 4.28: Variation in residual stress (σ_x) from gauges on the right and left side of weld centerline.....	110

Figure 4.29: Bottom gauge position for through thickness slitting experiment.....	111
Figure 4.30: Strain readings for as-welded and hammer peened through thickness slitting	112
Figure 4.31: 2D FEM model of FSW lap joint cross section.....	113
Figure 4.32: Bottom gauge compliance functions.....	114
Figure 4.33: Transverse test specimen gauge positions.....	115
Figure 4.34: Longitudinal strain (ϵ_z) measurements from gauge positions 1,2, and 3....	116
Figure 4.35: 2D FEM model of FSW lap joint	117
Figure 4.36: Gauge 1 compliance functions.....	118
Figure 4.37: Gauge 2 compliance functions.....	118
Figure 4.38: Gauge 3 compliance functions.....	119
Figure 4.39: Longitudinal test specimen gauge positions.....	120
Figure 4.40: Transverse strain (ϵ_x) measurements from as-welded test specimen.....	121
Figure 4.41: 2D FEM model of FSW lap joint	122
Figure 4.42: Gauge 1 compliance functions.....	122
Figure 4.43: Gauge 2 compliance functions.....	123
Figure 4.44: Gauge 3 compliance functions.....	123
Figure 4.45: FSW test specimen mounted onto the L3 spectrometer at NRU.....	126
Figure 4.46 Close up view of test specimen setup with detector	126
Figure 4.47: Strain mapping of as-welded plate.....	127
Figure 4.48: Strain mapping of hammer peened plate.....	127
Figure 4.49: Transverse strains (ϵ_x) in as-welded skin.....	130
Figure 4.50: Transverse strains (ϵ_x) in as-welded stringer.....	130
Figure 4.51: Transverse strains (ϵ_x) in hammer peened skin.....	131
Figure 4.52: Transverse strains (ϵ_x) in hammer peened stringer.....	131
Figure 4.53: Normal strains (ϵ_y) in as-welded skin.....	132
Figure 4.54: Normal strains (ϵ_y) in as-welded stringer.....	133

Figure 4.55: Normal strain (ϵ_y) in hammer peened skin.....	133
Figure 4.56: Normal strain (ϵ_y) in hammer peened stringer.....	134
Figure 4.57: Longitudinal strains (ϵ_z) in as-welded plate.....	135
Figure 4.58: Longitudinal strains (ϵ_z) in hammer peened plates.....	135
Figure 4.59: Position of longitudinal wall scan of as-welded plates.....	139
Figure 4.60: Transverse strains (ϵ_x) for as-welded and hammer peened plates.....	139
Figure 4.61: Normal strains (ϵ_y) for as-welded and hammer peened plates.....	138
Figure 4.62: Longitudinal strains (ϵ_z) for as-welded and hammer peened plates.....	138
Figure 4.63: Fatigue test setup.....	141

CHAPTER 5

Figure 5.1: Variation in transverse residual stress (σ_x) in the through thickness direction of plate.....	144
Figure 5.2: Fitted strain vs. measured strain values for as-welded test specimen.....	145
Figure 5.3: Total error of stress profile (σ_x) using Lp9 compared with using Lp10.....	146
Figure 5.4: Variation in transverse residual stress (σ_x) in the through thickness direction of as-welded test specimen.....	147
Figure 5.5: Fitted strain compared with measured strain values for hammer peened test specimen.....	150
Figure 5.6: Total error for stress using Lp9 compared with using Lp10 for hammer peened specime.....	151
Figure 5.7: Transverse residual stress profile (σ_x) in the through thickness direction of hammer peened test specimen.....	152
Figure 5.8: Comparison of the transverse stresses (σ_x) in through thickness direction of both specimens.....	153
Figure 5.9: Calculation of residual stress from measured strain and FE compliances...	154
Figure 5.10: Back-calculated strains from back substitution of stress into FE model....	155

Figure 5.11: Comparison of measured and back-calculated strains.....	156
Figure 5.12: Verification of stress by putting back into FE model to determine corresponding strain.....	157
Figure 5.13: Variation in longitudinal residual stresses (σ_z) calculated in transverse direction.....	158
Figure 5.14: Fitted strain vs. measured strain values from gauge 3 position.....	159
Figure 5.15: Residual stress profile (σ_z) calculated using 9 and 10 orders of polynomials with error bars.....	160
Figure 5.16: Variation in longitudinal residual stress (σ_z) across the weld of as- welded test specimen using gauge 3 alone.....	162
Figure 5.17: Back-calculated strain vs. original measured strain values in transverse direction.....	162
Figure 5.18: Variation in longitudinal residual stress (σ_z) across weld from gauge 1 position alone.....	163
Figure 5.19: Variation in longitudinal residual stress (σ_z) across the weld from gauge 2 position alone.....	164
Figure 5.20: Comparison of longitudinal residual stresses (σ_z) in transverse direction from gauges 1,2, and 3.....	164
Figure 5.21: Residual stresses using different combinations of gauges 1 and 3.....	166
Figure 5.22: Variation in longitudinal residual stress (σ_z) in transverse direction using a combination of gauges 1 and 3.....	167
Figure 5.23: Residual stresses using different combinations of gauges 2 and 3.....	167
Figure 5.24: Variation in longitudinal residual stresses (σ_z) in transverse direction using gauges 2 and 3.....	168
Figure 5.25: Variation in transverse residual stress (σ_x) along the weld centerline.....	170
Figure 5.26: Variation in transverse residual stress (σ_x) in longitudinal direction	

from gauge 1 position.....	171
Figure 5.27: Variation in transverse residual stress (σ_x) in longitudinal direction	
from gauge 2 position.....	173
Figure 5.28: Variation in transverse residual stress (σ_x) in longitudinal direction	
from gauge 3 position.....	174
Figure 5.29: Gauge 3 back-calculated strains.....	174
Figure 5.30: Transverse stress component (σ_x) in through thickness direction at	
weld centerline.....	177
Figure 5.31: Normal stress component (σ_y) in through thickness direction at weld	
centerline.....	178
Figure 5.32: Longitudinal stress component (σ_z) in through thickness direction.....	179
Figure 5.33: Longitudinal stress component(σ_z) on transverse plane of as-welded	
and hammer peened plate.....	181
Figure 5.34: Normal residual stress component (σ_y) in transverse direction for both	
specimens.....	182
Figure 5.35: Transverse residual stress component (σ_x) in transverse direction for	
both specimens.....	183
Figure 5.36: Transverse residual stress (σ_x) profile in the longitudinal direction for	
both specimens.....	185
Figure 5.37: Normal residual stress component (σ_y) in the longitudinal direction for	
both specimens.....	187
Figure 5.38: Longitudinal residual stress component (σ_z) in the longitudinal	
direction for both specimens.....	188
Figure 5.39: Triaxial residual stresses 6 mm to the right of the weld centerline of	
the as-welded plate in the transverse direction.....	189
Figure 5.40: Triaxial residual stress 6 mm to the right of welded centerline in	
peened plate in the transverse direction.....	190

Figure 5.41: Comparison of transverse residual stresses (σ_x) in the through thickness direction for as-welded plates using compliance method and neutron method.....	192
Figure 5.42: Comparison of transverse residual stresses (σ_x) in the through thickness direction for as-welded plates using compliance method and neutron methods at weld centerline with error bars.....	192
Figure 5.43: Comparison of transverse residual stresses (σ_x) in the through thickness direction for hammer peened plates using compliance method and neutron method.....	194
Figure 5.44: Comparison of transverse residual stresses (σ_x) in the through thickness direction for hammer peened plates using compliance method and neutron methods at weld centerline with error bars.....	194
Figure 5.45: Comparison of longitudinal residual stress (σ_z) in transverse direction from compliance and neutron methods.....	196
Figure 5.46: Comparison of transverse residual stress (σ_x) in longitudinal direction from compliance and neutron methods with error bars.....	198
Figure 5.47: 3D stringer modeled in 2D FE model in x-y plane.....	200
Figure 5.48: 3D stringer modeled in 2D FE model in x-z plane for transverse slitting experiment.....	201
Figure 5.49: 3D stringer modeled in 2D FE model in x-z plane for longitudinal slitting experiment.....	202
Figure 5.50: Angular rotation of FSW plate as-welded.....	204
Figure 5.51: Longitudinal weld shrinkage due to longitudinal residual stress in transverse (x) direction of weld.....	205
Figure 5.52: Transverse weld shrinkage due to transverse residual in longitudinal (y) direction of weld.....	206

Figure 5.53: Cycles to failure of as-welded and hammer peened test specimens compared with previous fatigue testing of FSW lap joint [Jung (2007)].....209

Figure 5.54: a) First visible crack in specimen, b) total separation of specimen.....210

Figure 5.55: Location of as-welded plate separation from fatigue testing.....210

Figure 5.56: Location of hammer peened plate separation from fatigue testing.....212

Figure 5.57: Fracture surface of first as-welded plate sample showing crack growth patterns.....213

Figure 5.58: Multiple crack nucleation sites originating from an edge crack at x790 magnification.....214

Figure 5.59: Transition between fatigue crack growth and fatigue overload at x300 magnification.....214

Figure 5.60: Fracture surface of a) slow fatigue region, b) overload region of first as-welded specimen at x800 magnification.....215

Figure 5.61: Fracture surface of a) slow fatigue region, b) overload region of second as-welded specimen at x800 magnification.....215

Figure 5.62: Fracture surface of first hammer peened specimen showing failure originating from edge of plate due to fretting at x25 magnification.....217

Figure 5.63: Magnification of crack growth emanating from dimple of the hydraulic grip at x490 magnification.....217

Figure 5.64: Fracture surface of a) typical fretting region b) overload region.....218

Figure 5.65: Fracture surface of second hammer peened specimen with no clear indication of crack growth pattern.....220

Figure 5.66: Highest transverse residual stress across the weld in the first as-welded test specimen.....220

Figure 5.67: Failure of first as-welded sample due to combination of high tensile residual stress and low hardness value to the left of weld centerline in

region between weld nugget and TMAZ.....	221
Figure 5.68: Highest transverse residual stress across the weld in the second as-welded test specimen.....	222
Figure 5.69: Failure of first as-welded sample due to combination of high tensile residual stress and low hardness value to the right of weld centerline in region between weld nugget and TMAZ.....	223

TERMINOLOGY

FSW	Friction stir welding
LEFM	Linear elastic fracture mechanics
CCM	Crack compliance method
AS	Advancing side
RS	Retreating side
D	Discontinuous
C	Continuous
SP	Single pass
DP	Double pass
TMAZ	Thermo-mechanical affected zone
HAZ	Heat affected zone
ND	Neutron diffraction
WEDM	Wire electric discharge machine
ε	Strain
$\varepsilon^{\text{meas}}$	Measured strain
ε^{fit}	Fitted strain
a_i	Slit Depth
y	Normalized by final slit depth
n	number of polynomials used
x_g	Distance from center of gauge to slitting line
P_i	Legendre polynomials
A_i	Unknown coefficients to be solved for
P_i	i^{th} order basis function
P_0	First order basis function
$\sigma_x(y)$	Stress normal to slit face

a_j	Final slit depth
FE	Finite element
C_{ij}	Element of compliance matrix
M	Number of slit depth
N	Number of terms in series expansion
a_k	Slit depth
$\Delta\varepsilon$	Change in strain
ε^c	Computed strains
$\varepsilon(a)$	Measured strain at a given slit depth
A	Vector representation of unknown coefficients
B	Vector representation of summation of compliance value and strain value
$[C]$	Compliance matrix
$[C]^T$	Transpose of compliance matrix
$[C]^{-1}$	Inverse of compliance matrix
A_j	Coefficient for j^{th} term in series expansion of stresses
$[B]$	Matrix that multiplies measured strains to determine $\{A\}$
$C_j(a_i)$	Calibrated coefficient at $a=a_i$ for P_j
e_i	Actual error in calculated stress at $x=a_i$
i	Index for number of slit depths, $i=1,m$
j	Index for terms in series expansion, $j=1,n$
$P_j(x_i)$	j^{th} term of series expansion evaluated at $x_i=a_i$
$s_{\text{model},i}$	Uncertainty in stress at $x=a_i$ due to model error
$s_{\cdot,i}$	Uncertainty in stress at $x=a_i$ from the strain measurement error
$s_{\text{total},i}$	Total uncertainty in stress at $x=a_i$
t	Thickness of specimen at cut location
$u_{\cdot,i}$	Uncertainty in strain measured when $a=a_i$
V	Matrix of covariances

x	Direction of slit
y	Direction normal to slit plane
ε_i	Measured strain when $a=a_i$
$\varepsilon_{f,i}$	Fitted strains for $a=a_i$
$\varepsilon_{r,i}$	Randomized strain
σ_i	Residual stress σ_y determined for $x=a_i$
$\bar{e}, \bar{s}, \bar{u}$	Root-mean-square average of vector entries
RMS	Root mean square average
ε_x	Transverse strain
ε_y	Normal strain
ε_z	Longitudinal strain
σ_x	Transverse stress
σ_y	Normal stress
σ_z	Longitudinal stress
ν	Poisson's ratio
E	Young's modulus of elasticity
γ_{yz}	Shear strain
τ_{yz}	Shear stress
G	Shear modulus
U	Uranium
Ta	Tantalum
Hg	Mercury
D ₂	Deuterated dichloromethane
D ₂ O	Heavy water
H ₂	Hydrogen
H ₂ O	Water
CH ₄	Methan

$\{hkl\}$	Miller indices
λ	Wavelength
2θ	Scattering angle
d	d-spacing
Q	Scattering vector
ε^{hkl}	Lattice strain
ϕ	Scattering angle
NRU	National Research Universal
L	Longitudinal
T	Transverse
N	Normal
Hz	Hertz
S	Cyclic Load
N	Cycles to failure
3D	Three-dimensional
2D	Two-dimensional
VPPA	Variable-polarity plasma-arc
NRC	National Research Council
°C	Degrees Celsius
N	Newtons
RPM	Rotations per minute
T3	Solution heat treated/cold worked
T6	Solution heat treated/artificially aged
GPa	Gigapascal
MPa	Megapascal
HV	Vickers hardness scale
ρ	Density

J/g-C	Specific heat capacity
W/m-K	Thermal conductivity
Al	Aluminum
Cr	Chromium
Cu	Copper
Fe	Iron
Mg	Magnesium
Mn	Manganese
Si	Silicon
Ti	Titanium
Zn	Zinc
HF	Hydrofluoric acid
ml	Milliliter
H ₂ S ₀ ₄	Sulfuric acid
Cr ₀ ₃	Chromium trioxide
μm	Micrometer
$\mu \epsilon$	Microstrain

Chapter 1

INTRODUCTION

1.1 Background

Aircraft structural members are typically fabricated from high strength 2xxx and 7xxx series aluminum alloys because of their high strength-to-weight ratio. These alloys are often considered very difficult to weld using conventional fusion welding techniques, therefore, riveting has been the primary method of joining these aerospace structural components, Staron et al. (2002), Root et al. (2003), and Sjeord (2006). Figure 1.1 shows a typical aircraft fuselage construction composing of stringers and frames riveted onto skin panels to help increase the fuselages structural rigidity. However, during recent years, due to the increasing demand for low cost, lighter and stronger aerospace structures, a new welding process has been developed as an alternative to riveted manufacturing of aluminum alloy components.

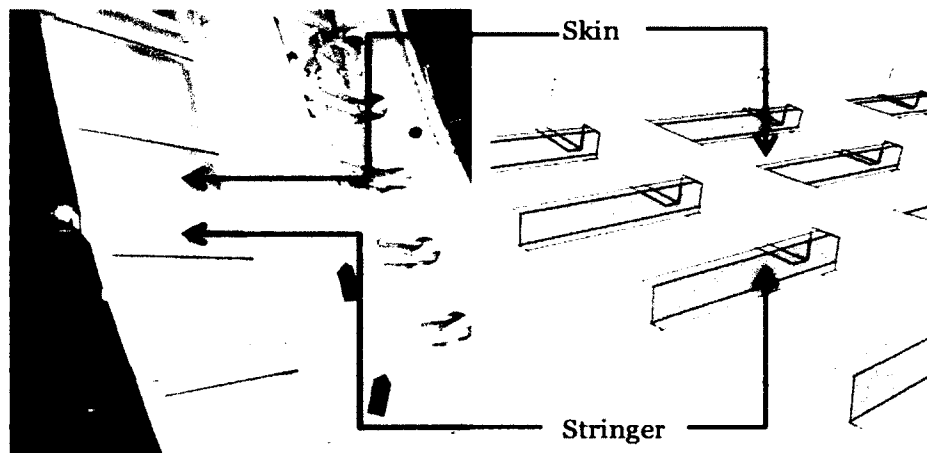


Figure 1.1: Riveted stringer-to-skin construction in aircraft fuselages [web image, Ref. 85]

In 1991, friction stir welding (FSW) was invented and patented at The Welding Institute in the UK. The process uses a combination of a rotating tool to produce frictional heat and a downward force to blend and mix the joining materials together as shown in Figure 1.2. FSW is a solid-state welding process, which means the metal does not melt during welding, this provides important metallurgical advantages over conventional fusion welding because it eliminates the possibility of solidification cracking during the cooling

of the weld. FSW has been successfully used to join different types of materials but its main contribution is the ability to weld different aluminum alloys together, which were considered un-weldable by other welding techniques such as arc welding.



Figure 1.2: Example of the FSW process [web image, Ref. 86]

The benefits of FSW aluminum alloys in aerospace structures include the ability to produce long lengths of welds without adding any welding consumables such as shielding gas or filler material, which can also increase the weight of the components, Sutton (2002). FSW is a desirable joining technique because not only does it reduce the weight of these structures, it has the potential to increase manufacturing efficiencies, reduce production time, and therefore reduce cost over the conventional riveting. On the basis of static strength, the FSW joints have been shown to be comparable with resistance spot welding and riveting. Erricsson et al. (2005) determined that the tensile strength of FSW joints was found to be 2.4 times that of a single row of riveted joints. These riveting techniques have been developed and used for decades so its process optimization has reached a plateau. FSW on the other hand is a relatively new method that can still be developed by improving welding parameters and efficiency through automation, which may be of economic value. Studies on the friction stir welding process by Peel et al. (2003), Wanchuck (2006), Prime (2006), Milan (2007), and Merati et al. (2009) have only been recently conducted in the last 10 to 15 years. The ability of FSW to join aluminum alloys makes it a likely technology to replace the riveting in the manufacturing of stringer-to-skin joints. However, to effectively apply the FSW process to these

structures, there are some issues that need to be addressed. One important issue relating to FSW, like other welding processes is the residual stresses that are left in the structures after the welding is completed. The presence of residual stresses in the welded structures affects its distortion behaviour and ability to sustain applied loads while maintaining structural integrity, Altenkirch et al. (2008). While compressive residual stresses can be in some cases beneficial, tensile residual stresses can cause stress corrosion cracking, distortion, fatigue cracking and premature failure.

Although the heat produced in FSW is lower compared to that of conventional welding methods, distortion and residual stresses are still present in FSW structures, Wanchuck (2006). Thermal residual stresses in the FSW process can be introduced from the frictional heat produced by the rotating tool. Distortion in welded structures may be the result of heating and cooling cycles during welding process, which causes non-uniform expansion and contraction of the welded and surrounding base material. The downward force exerted by the welding tool and the clamping force used to hold the component during welding can introduce mechanical residual stresses. It is believed that the very rigid clamping arrangements used in FSW exerts a much higher restraint on the deformation of the welded plates than the more compliant clamps used for fixing the parts during conventional welding processes. These restraints impede the contraction due to cooling of the weld nugget and heat affected zone in the longitudinal as well as in the transverse direction, introducing transverse and longitudinal residual stresses as shown in Figure 1.3, Dalle et al. (2001).

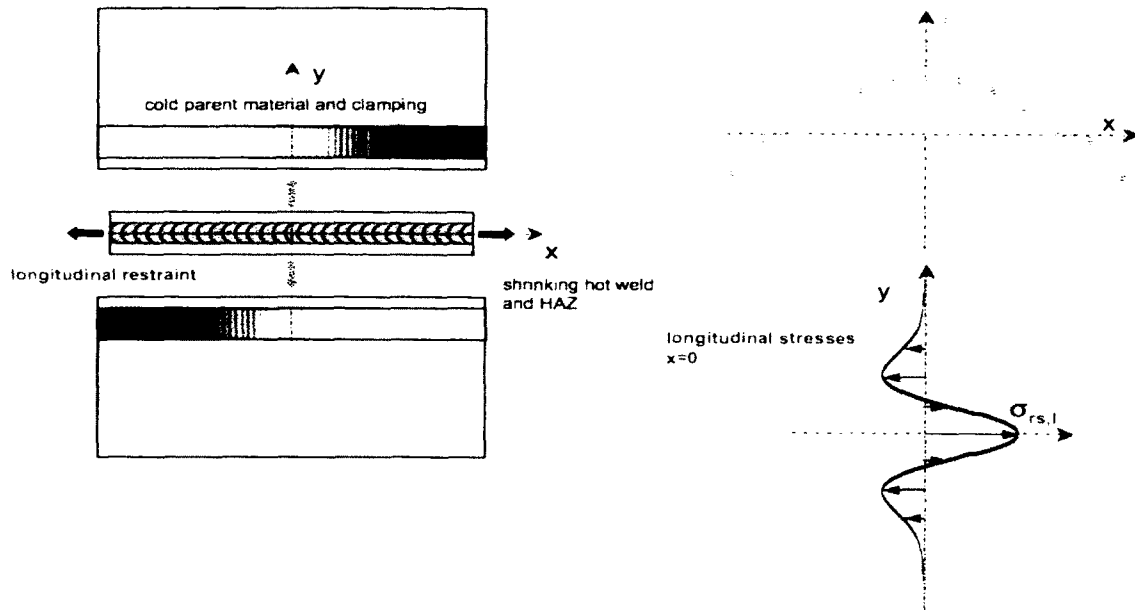


Figure 1.3: Schematic of typical residual stresses from FSW [Dalle (2001)]

An example of the effects of distortion in FSW is shown in Figure 1.4. The image on the left is that of an as-welded FSW AA 7075-T6 stringer to an AA 2024-T3 skin panel. There is a clear distortion in the 3.76 mm thick plate, which is due to the presence of residual stresses. The plate on the right has undergone a post-welding surface treatment process known as hammer peening which caused the distortion to be dramatically reduced, Merati (2009).



Figure 1.4: FSW plate before and after hammer peening [Merati (2009)]

No previous studies has examined the residual stresses in the weld zone of these FSW lap joints and how they relate to the distortion after welding, Deng et al. (2008). For this reason, prediction and control of welding deformation have become of critical importance in the performance and fatigue lives of these aerospace components. A detailed understanding of the residual stress distribution in the FSW plate may lead to the ability to modify and optimize welding parameters and procedures so that these stresses can be minimized and its design based on damage tolerance can further be improved. Also, reduced residual stress in the component during manufacturing process has economic benefits because the extra post-welding step will no longer be necessary.

To get a better understanding of the residual stresses in a manufactured component must be first determined. There are many non-destructive as well as destructive methods developed to measure residual stresses. Some non-destructive methods include neutron diffraction and x-ray diffraction while destructive methods include hole drilling, layer removal, contour method, as well as the slitting method. The slitting method is a powerful and relatively easy to implement technique employed to determine both near surface and through thickness residual stress profiles in any direction normal to the slit face. The method is based on the fact that when a slit, simulating crack growth, is incrementally introduced into a component, the residual stresses are relieved on the slit surface causing the part to deform. Such deformation can be measured by strain gauges attached to specific regions of the component. After strain measurements are taken, the residual stress profile that was originally in the plate can be evaluated. Residual stresses can either be calculated using a linear elastic fracture mechanics (LEFM) approach, using weight functions and stress intensity factors, Prime (1998) and Milan (2007) or a method known as the crack compliance method (CCM). The crack compliance method is a destructive technique, which uses a combination of slitting method, FEM analysis, and analytical solutions to determine the residual stress profile. The crack compliance method will be discussed in detail later in this thesis but a summary of the different components that make up the crack compliance method is shown in Figure 1.5 with the three main components in the highlighted boxes.

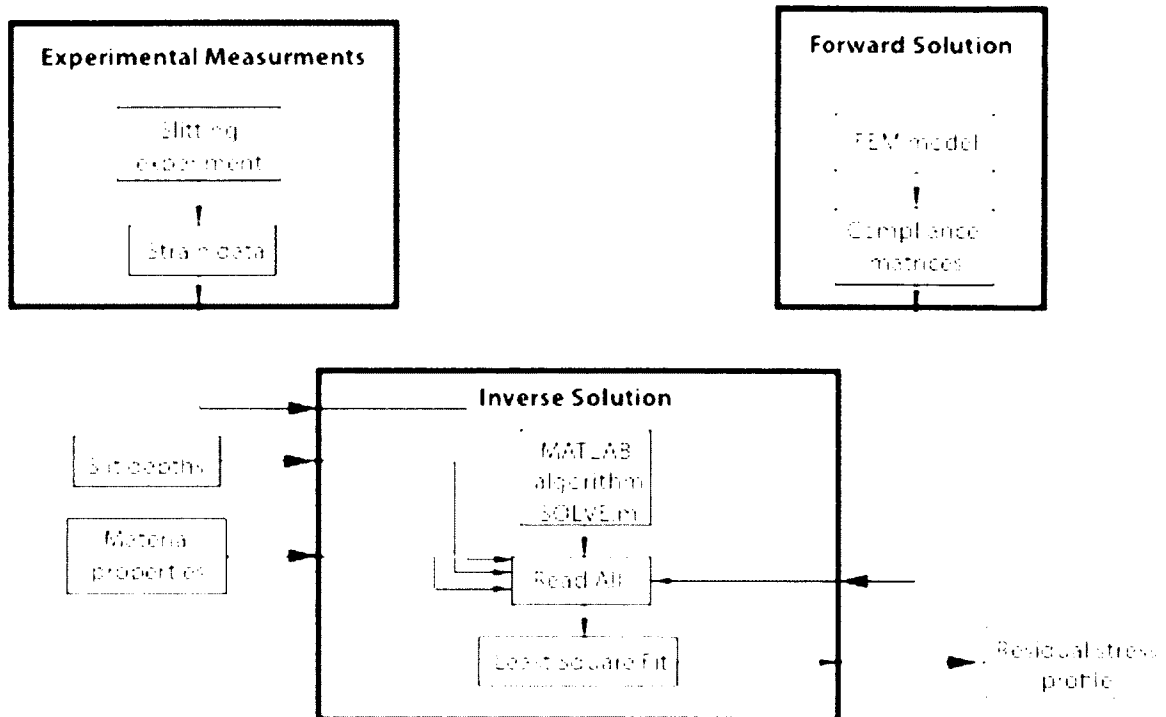


Figure 1.5: Components of the crack compliance method

In certain aerospace structures, riveted constructions are being gradually replaced, as new and improved joining technologies such as FSW are being developed as an alternative solution. FSW has seen increasingly successful applications in all industries from automotive, to aviation and even space exploration. The National Research Council Canada's Institute for Aerospace Research has undertaken a major initiative to develop and manufacture a large-scale aircraft structural element, e.g. a FSW fuselage panel composed of an aluminum stringer friction stir welded to an aluminum skin panel in a lap joint configuration, Dubourg et al. (2007). All of the FSW literature is limited to the past 10 to 15 years. Up to this date, FSW butt joints have been studied extensively by Nandan, (2008) and Deng et al. (2008) but very little research has been completed on this newly developed FSW double pass, stringer-to-skin lap joint. Little research has been conducted to understand these weld's mechanical properties including the residual stresses present in the panel and its effect on distortion or fatigue life.

The study of measuring residual stresses is very complex and still not yet understood completely. Researchers have been looking at different aspects of residual stresses in the hopes of understanding how they are created and how to mitigate related problems. The majority of literature on the crack compliance method as the residual stress determination technique investigates the stress evolution in one direction, Prime (1999). In many cases, knowing the residual stress evolution in only one direction is not sufficient. In the case of welded joints the residual stress field is neither homogenous in depth nor along the transverse direction of the joint. Thus, the knowledge of the two or even three-dimensional distribution of residual stress in the component is usually required for a proper understanding of the properties of the weld, Montay et al. (2009). No previous works have examined the measurement of residual stress in all three principal directions based on the crack compliance method. What makes residual stresses so important? These hard to detect/measure residual stresses can be a primary factor or secondary factors that when combined with design flaws and manufacturing defects can lead to catastrophic failure of aerospace structures. Therefore, it is crucial that these residual stresses be understood, especially for critical components of aircraft such as stringers welded to skin panels to increase its strength against cyclic bending and torsional loads. Catastrophic failures of aircraft structures due to buckling and fatigue solidifies the importance of knowledge of the residual stresses in these components right after manufacturing and also during its service life and how these residual stresses affect fatigue life of the component. All fatigue performance literature to date has been performed on simple FSW butt joints. Very few investigations has been carried out to study the effects of residual stresses of FSW lap joints on fatigue performance before and after hammer peening.

1.2 Objectives

The objectives of this thesis are:

- Develop a method of accurately predicting the residual stresses resulting from the FSW process in the stringer-to-skin lap joint as shown in Figure 1.1 based on the crack compliance method.
- Demonstrate the feasibility of the crack compliance method by using the method to recalculate the stresses in previous residual stress experiments taken from the literature.
- Testing of the FSW lap joints both in the as-welded and hammer peened test specimens to characterize the residual stresses in the longitudinal (z), transverse (x), and through-thickness (y) direction.
- To verify the results of the residual stresses calculated using the crack compliance method, an independent nondestructive residual stress measurement technique of neutron diffraction will be used to measure the same residual stresses in the stringer-to-skin lap joints.
- Results of both methods will be compared with one another to determine the validity of the compliance method and examine the merits of each method for residual stress determination.
- Qualitatively relate the effects of these residual stresses on the distortion present in the lap joint after the FSW process.
- Complete a fatigue performance test on these FSW lap joints in the as-welded and hammer peened configuration to examine the effects of residual stresses on fatigue lives.
- Measure the hardness values in the weld region of as-welded and hammer peened specimens in relation with residual stress and fatigue failure.
- Examine causes and location of failures in these FSW stringer-to-skin lap joints.

1.3 Thesis Outline

The thesis is divided into six chapters. The first chapter begins with the introduction, which gives some background information on the topic of friction stir welding and residual stresses. The objectives of the thesis are outlined in chapter one and will dictate the scope of the thesis. The second chapter consists of a comprehensive literature review on the topic of friction stir welding, residual stresses, residual stress measurement techniques: crack compliance method and neutron diffraction, and fatigue performance of FSW components. Chapter two also summarizes all current literature on the various topics of FSW and residual stress measurement techniques. Chapter three describes the test specimen and its geometry; weld configuration, and material properties. Hardness profiles of both weld configurations are examined in detail in chapter three. Chapter four contains the experimental procedures, which follow the procedures of the compliance method and neutron diffraction experiments that were carried out. Chapter four also looks at some fatigue testing of these friction stir welded plates. Chapter five is the results and discussion section where the results of the experiments are examined in detail. Chapter five links all the experimental procedures and answers the questions set out in the thesis objectives. Finally, chapter six is the conclusions gathered from the experimental procedures. The chapter also includes recommendations and possible future work. The appendices contain several MATLAB algorithms used in the compliance methods residual stress determination. The references used in this thesis are presented at the end of the thesis.

Chapter 2

LITERATURE REVIEW

2.1 Construction of Aircraft Components

The fuselage of an aircraft carries the payload, and is the main body to which all components are connected. The structural strength of the fuselage must be high enough to resist bending moments (caused by weight and lift from the wings and tail), torsional loads (caused by fin and rudder) and compressive cabin pressure caused by the climb and descent of the aircraft, Talwar et al. (2001) but at the same time, the structural weight must be kept to a minimum. The semi-monocoque fuselage construction in Figure 2.1 is virtually standard in all modern aircraft and consists of any combination of longerons, stringers, bulkheads, and frames to reinforce the skin and maintain the cross-sectional shape of the fuselage.

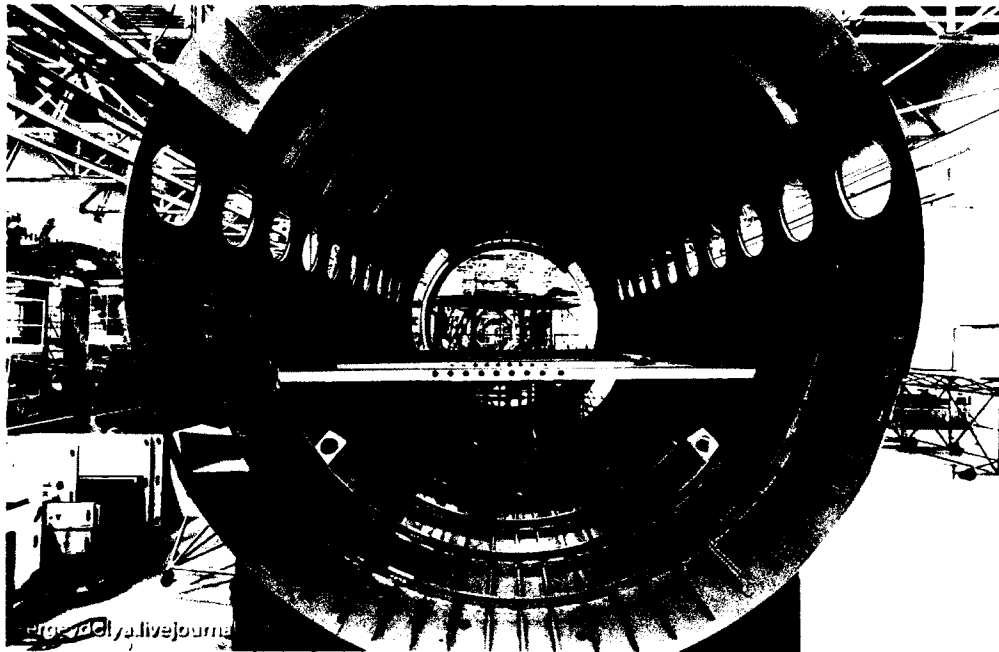


Figure 2.1: Semi-monocoque construction of aircraft fuselage [web image, Ref. 87]

The stressed skin of the fuselage is wrapped around the hoop-shaped skeletal frames, which gives the fuselage its cylindrical shape and support. Longerons connect the frames to one another and resist the majority of fuselages bending loads. The combination of

longerons and frames help improve the stability of the stringer in compression. Stringers shown in Figure 2.2 are longitudinal (lengthwise) members that are attached to the underside of the skin to give an increase in the stiffness of the skin under torsion, bending loads, and help resist buckling with minimal increase to the weight.

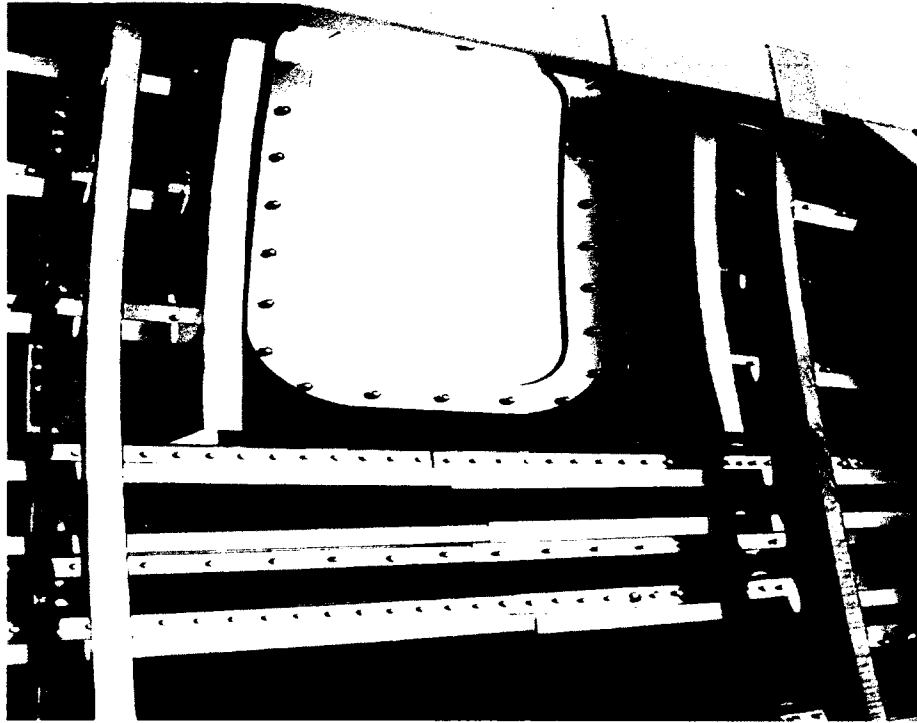


Figure 2.2: Horizontal stringers fasten to skin panel [web image, Ref. 88]

Stringers are not unique to the fuselage construction but can also be found in the wing construction as seen in Figure 2.3. In a typical wing assembly, the cross sectional shape of the wing, which gives the wing its profile, is determined by a series of ribs that run along the length of the wing. Stringers are attached perpendicular to these ribs and the skin of the wing is wrapped around these ribs.



Figure 2.3: Stringers used in wing construction [web image, Ref. 89]

Aluminum alloys are used in aircraft fuselage construction because of their combination of lightweight and high strength. Skin panels are typically made of 2xxx-series aluminum alloys and support such as frames and stringers are made of 6xxx-series and 7xxx-series aluminum alloys. It is a common design practice to use a higher yield strength alloy for the reinforcement component and a lower yield strength alloy for the skin so that if a growing crack is present in the skin, it will be arrested when it reaches the higher strength stringer as opposed to continuing to another panel of the fuselage. Riveting is the conventional method of attaching the frame and stringer to the aluminum skin panels. Rivets are used instead of welding because aerospace aluminum alloys are considered unweldable due to post-welding defects that occurs after they are fusion welded. As shown in Figure 2.4, thousands of individual rivets have to be used to attach sections of the skin panels to the frame. The addition of these rivets will increase the weight of the aircraft, which is undesirable in efficient aircraft design since the heavier the aircraft, the more fuel it will consume to produce the same amount of lift. The pieces of metals protruding out of the skin are put in place to temporarily secure the panel before riveting, which can be very time consuming. Also each rivet hole is a potential location for crack nucleation since they are local stress concentrators, Staron (2002).

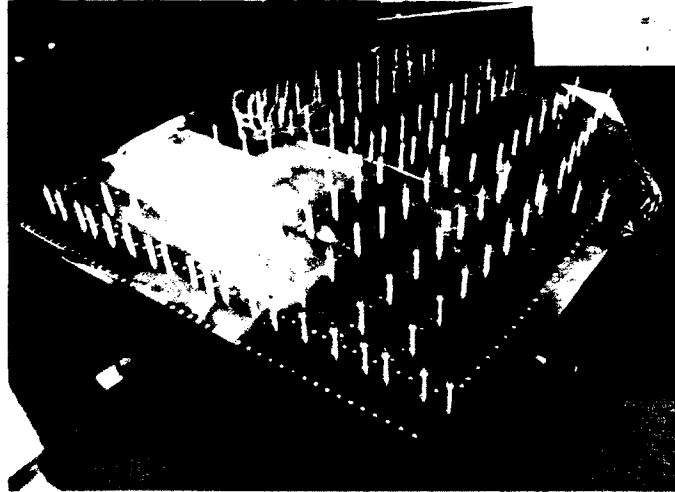


Figure 2.4: Rivets positioned in place to attach panels together [web image, Ref. 90]

In recent years, a new welding technique called friction stir welding has been developed that is able to weld different aluminum alloys to one another, Williams (2001), Staron (2002), and Root (2003). The key to this welding technique is that friction stir welding is a solid-state process, which means that solidification cracking; a problem exhibited in fusion welding is eliminated. Figure 2.5 illustrates the difference in riveted (a) and FSW (b) fuselage constructions. Notice how clean and smooth the FSW skin panel construction looks compared to the traditional riveted skin panel construction.

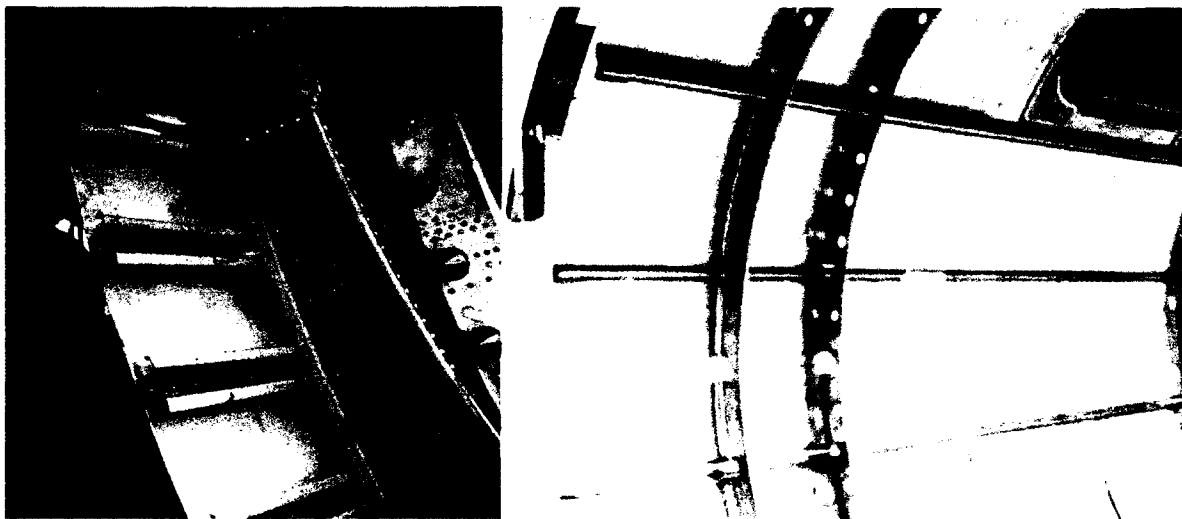


Figure 2.5: a) Riveted stinger to skin panel [web image, Ref. 85] b) FSW stringer-to-skin panel [web image, Ref.91]

2.2 Friction Stir Welding

2.2.1 Friction Stir Welding Process

Friction stir welding is a relatively new process developed at The Welding Institute in 1991. Friction stir welding is an innovative material joining process that enables the advantages of solid state joining for fabrication of continuous linear welds without bulk melting, Woo et al. (2007). The FSW process involves two key components; the first component is rotating a non-consumable tool on the substrate to produce frictional heat, and the second component is applying a downward pressure on the tool as it passes along the material being joined as shown in Figure 2.6. The rotating tool consists of a shoulder and pin made from a hard and wear-resistant material relative to the material being welded. This rotating tool is brought into contact with the work piece. Welding starts by plunging the rotating pin into the work piece so that the shoulder has contact with the top surface. Once a sufficient amount of frictional heat is produced in the work pieces, the tool begins to move along the weld.

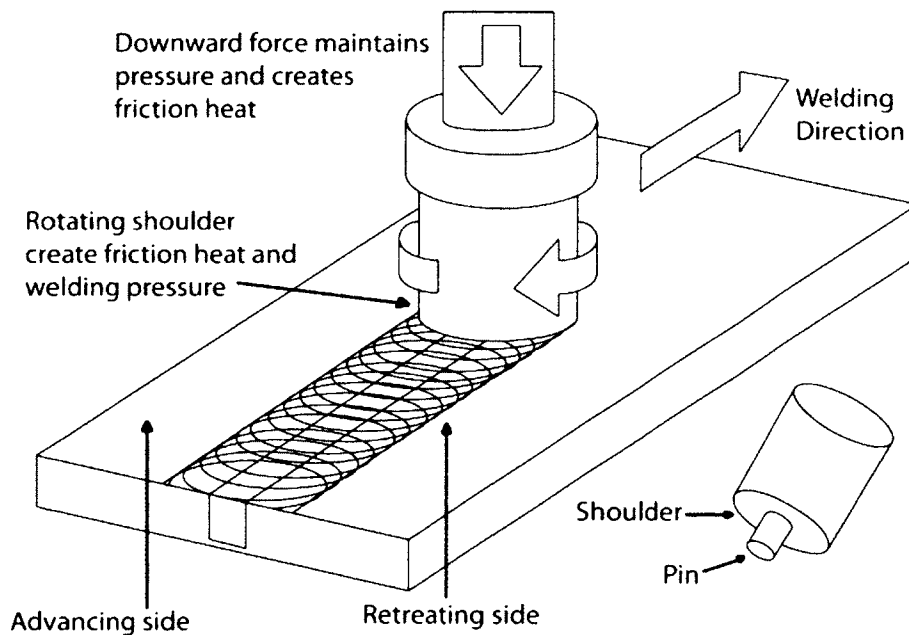


Figure 2.6: Friction stir welding process

Friction from the rotating pin heats and softens the material, which is then extruded around the tool before being forged by the downward pressure. The weld is produced by

the deformation of the material below the melting temperature, which is why the process is called a solid-state process. The material never reaches melting temperature; it just becomes soft enough to be mixed together. The simultaneous rotational and translational motion of the tool during the welding process creates a characteristic asymmetry between the two sides of the weld. The side where the tool rotation direction is the same with the direction of the translation of the welding tool is called the advancing side (AS) and the opposite side is called the retreating side (RS).

Fundamentally, FSW relies on extensive thermomechanical plastic deformation to develop the metallurgical bonding. The key factors contributing to a successful friction stir welding operation are the temperature and stress distributions during the process, particularly the temperature and stresses near the rotating tool where the material is stirred and metallurgical bond is formed.

Advantages of friction stir welding can be categorized into three benefits; metallurgical, environmental, and energy. In terms of metallurgical benefits, FSW has good repeatability, no loss of alloying elements, fine recrystallized microstructure, absence of solidification cracking, and the ability to weld all aluminum alloys. For the environmental benefits, FSW uses no shield gas, requires minimal surface cleaning prior to welding, eliminated grinding waste, no solvents required for degreasing, consumable materials savings, and has no harmful emissions. Finally, the energy benefits of FSW include: improved materials used, reduction in weight, less energy used compared with fusion welding techniques welding (2.5% of the energy needed for a laser weld), and decreased fuel consumption in lightweight aircraft, automotive and ship applications, Wanchuck et al. (2006).

However, friction stir welding does not come without limitations. One limitation of the FSW process is mechanical stability of the tool at operating temperatures. During FSW, the tool is responsible for not only heating the substrate material to forging temperatures, but also providing the mechanical action of forging. Therefore, the tool material must be capable of sustaining high forging loads and temperatures in contact with the deforming substrate material without either excessive wear or deformation. As a result, the bulk of the FSW applications have involved low forging temperature materials. Of these, the most important class of materials has been aluminum alloys. Another limitation of FSW is the type of geometries that can be welded. Since FSW requires more rigid clamping than conventional welding, special grips have to be used and therefore dictating the geometries that can be welded by FSW.

2.2.2 Applications of Friction Stir Welding

Friction stir welding has found application in many industries including aerospace, shipbuilding, automotive, and railway. The aerospace industry has greatly benefited from the invention of friction stir welding and is switching out riveted structures for FSW structures. An example of the successful implementation of friction stir welding in production is its use on the Delta II and Delta IV launch vehicles to join aluminum alloy panels in the inter-stage and tank sections. The space shuttle launch vehicles use FSW on their large external fuel tanks and other containers to reduce weight, which is crucial in spacecraft. Figure 2.7 shows the advance use of FSW in the construction of the Orion crew module by Lockheed Martin. Boeing uses FSW on the cargo barrier beam for the Boeing 747 large cargo freighter aircraft. FSW FAA approved wings and fuselage panels of the Eclipse 500 aircraft are currently being produced at Eclipse Aviation. Floor panels for the Airbus A400M military aircraft are also made using FSW technology. In the automotive industry, the drive to build more fuel-efficient vehicles has led to the increased use of aluminum in an effort to save weight, which also improves recyclability when the vehicles are scrapped.

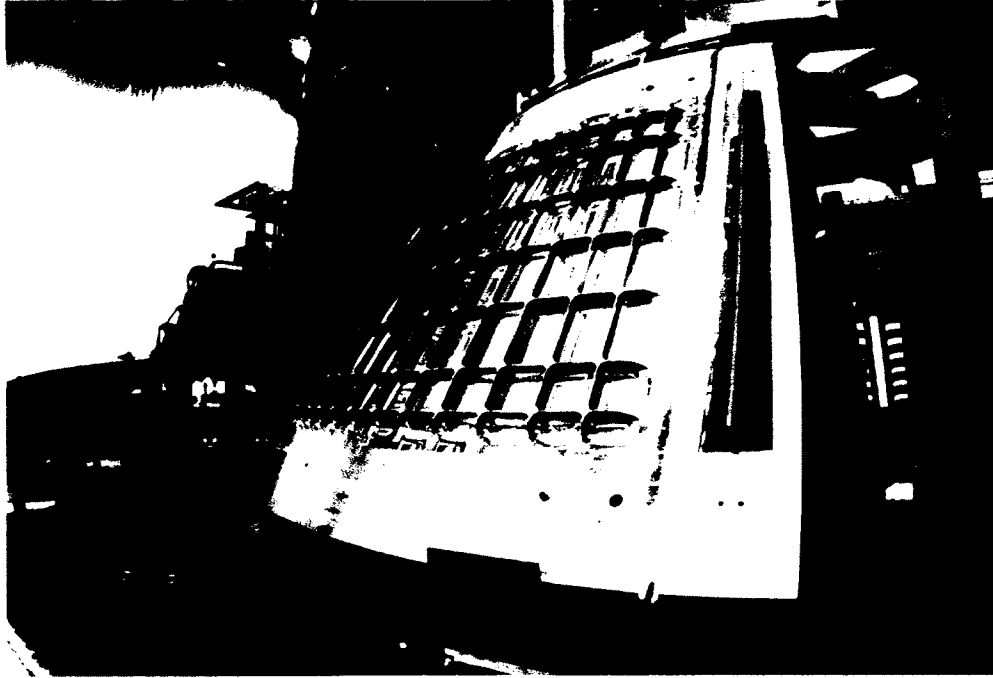


Figure 2.7: Lockheed Martin's FSW Orion crew module [web image, Ref. 92]

Aluminum wheels are FSW using different aluminum alloys. The center tunnel of the Ford GT is made from two aluminum extrusions friction stir welded to a bent aluminum sheet that houses the fuel tank. Aluminum engine cradles and suspensions struts for the stretch Lincoln Town Car were also friction stir welded. In Japan, FSW is applied to suspension struts at Showa Denka and for joining of aluminum sheets to galvanized steel brackets for the trunk of the Mazda MX-5. This demonstrates the success of FSW ability to join different materials to one another. Friction stir spot welding is successfully used for the hood and rear doors of the Mazda RX-8 and the trunk of the Toyota Prius. The railway sector uses FSW on their cargo decks and roofs for their carriages while ship builders and offshore rigs uses FSW in deck panels, fishing containers and helicopter landing platforms. In summary, FSW has found a promising future in all of the aforementioned industries as these industries look forward to new, improved, and economical methods of manufacturing their products.

2.2.3 Friction Stir Weld Joint Configurations

There are several joint configurations that can be accomplished through FSW. Figure 2.8 illustrates some common joint configurations. In the aerospace industry, butt joints and lap joints are the two most common configurations used to join similar or different sheets of metals to one another in fuselage and wing constructions. Butt joints (Figure 2.8a) are used to weld panels of metal to form larger structures, which are used in aircraft fuselages. Lap joints (Figure 2.8d) are used to join stringers and reinforcement plates to skin panels to help increase structural rigidity to the skin panels.

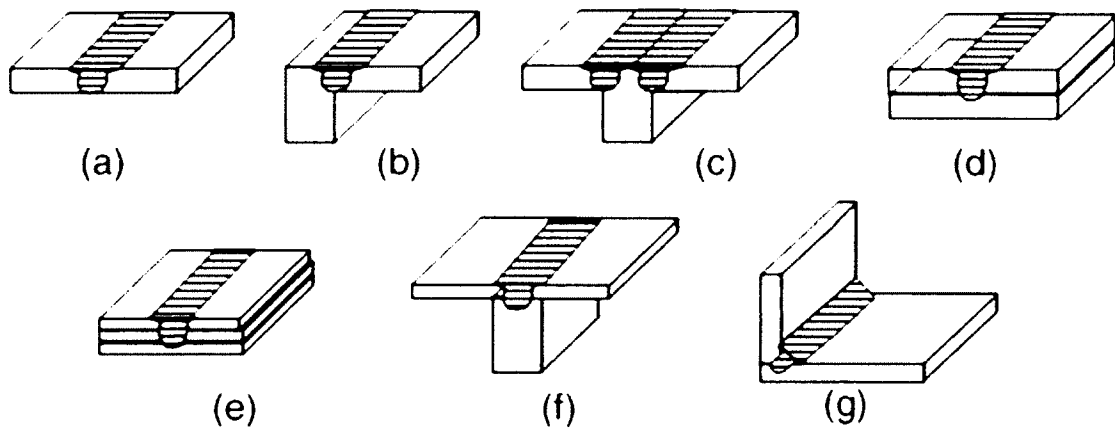


Figure 2.8: Joint configuration for friction stir welding a) butt joint, b) edge butt, c) T butt joint, d) lap joint, e) multiple lap joint, f) T lap joint, g) fillet [web image, Ref. 93]

FSW Terminologies: Continuous, Discontinuous, Single Pass, and Double Pass

There are several different welding configurations associated with FSW process. The first is continuous (C), which means that the weld plate does not contain the section where the tool enters or exits the material (exit hole) as shown in Figure 2.9a. Discontinuous (D) means that the weld plate contains the section where the tool exits the material and re-enters the material again as shown in Figure 2.9b.

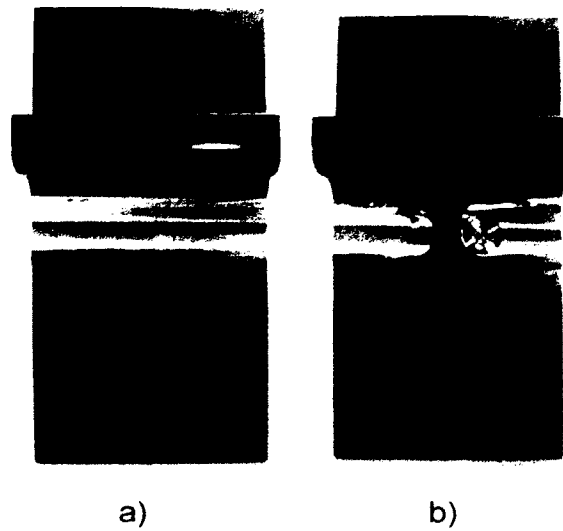


Figure 2.9: a) Continuous weld b) Discontinuous weld, [Merati (2009)]

A single pass (SP) in FSW as the name suggests involves completing a single pass of the welding tool. Figure 2.10a shows the welding tool traveling direction as well as rotation direction for a clockwise SP. Passing the welding tool twice creates a double pass (DP) where the second pass of the tool is offset from the first pass. The purpose of the second pass is to ensure proper mixture of the joining materials. Figure 2.10b shows a clockwise DPC with outward hook and Figure 2.10c shows the configuration of the clockwise DPC inward hook.

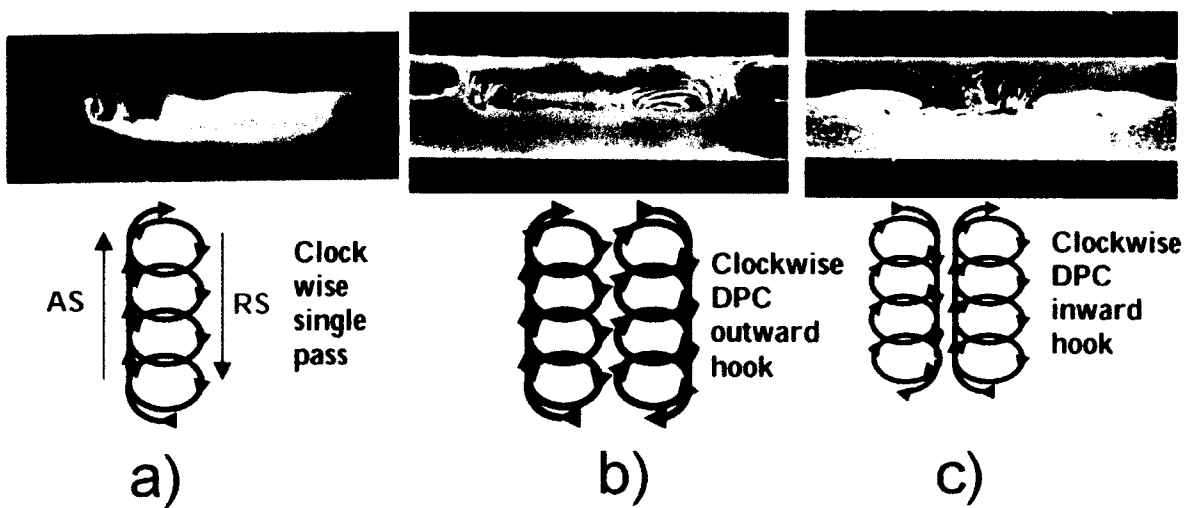


Figure 2.10: a) SP b) DPC outward hook c) DPC inward hook, [Merati (2009)]

2.2.4 Tool Geometries

Besides tool rotation and transverse speed, one important factor that determines a strong friction stir weld is the tool tip geometry, often left out when discussing FSW. Figure 2.11 shows several tool tip geometries that have been designed to produce different friction stir welds. Although the tool geometry is not discussed in this work, the author would like to mention that using different tool tips would have a great influence on resulting mechanical properties of the weld, James et al. (1999), Nunes et al. (2004), and Prime et al. (2006). Advanced tool design provides intensified material flow in the stirred zone and better weld quality.



Figure 2.11: Tool Tip Geometries [Elangovan (2008)]

2.2.5 Friction Stir Weld Zones

The following is a general description of the different friction stir weld zones present in most friction stir welded components. The size, shape and location of the weld zones may vary for different weld configurations, tool geometries, and materials used but in general, friction weld process produces three highly characterized zones: the weld nugget, thermomechanically affected zone (TMAZ), and heat affect zone (HAZ) as shown in Figure 2.12. The weld nugget or stir zone is a region of heavily plasticized material that roughly corresponds to the location of the pin during welding. The grains within the stir zone are roughly equiaxed and often an order of magnitude smaller than the grains of the parent material, Bussu et al. (2002).

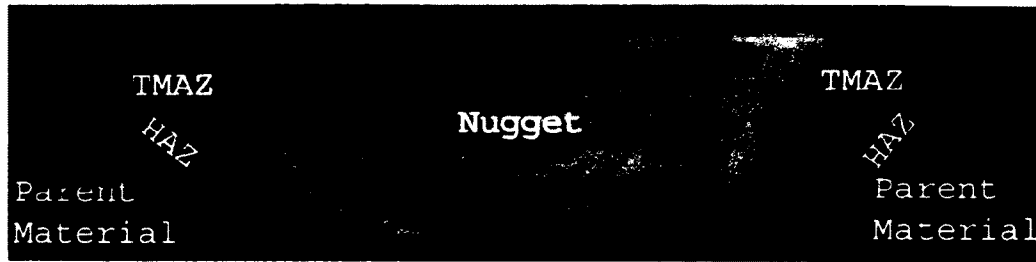


Figure 2.12: FSW Weld Zones: weld nugget, TMAZ, HAZ, parent material [web image, Ref. 94]

The mixing of the materials creates a unique feature of the stir zone, which are several concentric rings referred to as “onion rings”. High contrast in rings suggests different types of materials friction stir welded together. The edges of the onion rings is the flow zone which is the upper surface of the weld and consists of material that is dragged by the shoulder from the retreating side of the weld, around the head of the tool, and deposited on the advancing side of the weld. The second distinct zone is called the thermomechanically affected zone. This zone is located on either sides of the stir zone. In this region, the strain and temperatures are lower and the effect of the welding on the microstructure is correspondingly smaller. Unlike the stir zone, the microstructure is recognizably that of the parent material but has significantly deformed and rotated due to the plastically deformed material. The grains in this region has been plastically deformed but has not yet recrystallized like the weld nugget. There is a distinctive boundary between the TMAZ and the weld nugget that will be discussed in later chapters. The third zone is called the heat affected zone (HAZ), common to all welding processes. As the name suggests, this region is subjected to a thermal cycle but is not deformed during welding. The temperature is lower than those in the TMAZ but may still have a significant effect if the microstructure is thermally unstable. In age-hardened aluminum alloys, this region commonly exhibits the poorest mechanical properties even though no plastic deformation takes place. The unaffected material is that which is located remotely from the weld and although it may have experienced a thermal cycle from welding, it is not affected by the heat in terms of microstructure or mechanical properties, Wanchuck et al. (2006).

2.3 Residual Stresses

2.3.1 Residual Stresses in Welds

Residual stresses are internal, self-equilibrating stresses within a stationary solid body when no external forces are applied. Residual stresses are inherently introduced into materials through many thermal or thermomechanical processes such as welding, forming and heat treatment, Prime (2002). Although FSW offers various advantages for joining lightweight metals and alloys, significant residual stresses are inevitably introduced after welding is complete, Wang et al. (2000), Reynolds et al. (2006) and Woo et al. (2006). In the FSW process, the thermomechanically-deformed material is extruded underneath and around the tool as the tool moves along the weld line and subsequently forms a strong metallurgical joint. The causes of these residual stresses could be from external applied forces on the body used to extrude the material or heating gradients from the heating and cooling of material after the welding process, Hutchings (1992). Residual stresses can also occur when one region of the sample has been plastically deformed and other regions have been elastically deformed.

The clamps used to hold the components in place during the FSW process can introduce residual stresses after the welded component is released. The clamps apply a compressive force on the constrained component to prevent movement, which could leave tensile stresses in the component after the clamps are released. External forces may come from the downward force of the welding tool pushing along the component as it is being welded. The cooling of the FSW introduces a “thermal tensioning” effect on the welded metal, which may lead to residual stresses and distortion. Welding, in particular, because of the rapid thermal expansion and contraction created along a very localized area is a prime source of residual stress. A very high heat source is applied to a small area relative to the cooler surrounding area. The metal expands as it is brought to a softened state. As the metals cool down and solidifies along the joint, there is a resistance to its shrinkage by the already solidified base metal adjacent to the weld. This resistance creates a tensile strain in the longitudinal and transverse direction of the weld. Distortion is often the

result, and if the stress is excessive, buckling, stress corrosion cracking, and shortened fatigue lives are possible.

In ordinary welds, residual stresses develop in constrained assemblies during FSW due to expansion during heating and contraction during cooling as stated before. A feature unique to FSW is the additional stress caused by the rotational and translational components of the tool so that the welding parameters of FSW must affect the final state of stress. The stirring action of the tool is believed to relieve some of the stresses within the thermomechanically affected zone, Bussu (2007).

Tensile residual stresses are undesirable in any circumstances but especially in the areas around the weld zone because the weld zone is an area susceptible to cracks and defects. The presence of tensile residual stresses will further aid in the propagation of these cracks and can greatly reduce the fatigue life of these components. Stress corrosion cracking can occur if there is a combination of high tensile residual stress and corrosive environment present. There are, however, situations where compressive residual stresses are deliberately introduced into the component to prevent cracks from forming, Finnie (1996).

For mechanical components that operate in severe environments such as nuclear reactors for an extended time or in safety-critical structures such as an airplane, the presence of residual stresses has a profound influence on the integrity of these components. Slow growing cracks in radioactive environments can grow in the presence of residual tensile stresses near the surface, Prime et al. (2004) which are detrimental to fatigue life under cyclic loading. Residual stresses are not only important in crack initiation but also crack growth rates as well because they can change the path/growth of a crack as it grows below the surface. Since tensile stresses are balanced by a compressive stress below the surface, the growth of a crack is always substantially slowed when it reaches the zone of

compressive stress. Alternatively, if the crack grows into a region of high tensile stress, this might cause the crack to grow at a faster rate.

2.3.2 Residual Stress Relief Techniques

All welding process produces some residual stress, which could never be completely reduced to zero; therefore the following is a description of several methods commonly used to minimize these residual stresses. There are two major approaches to residual stress relief: thermal relief and mechanical relief. A major difference between the two is thermal treatment, which is in addition to relieving stress, will also affect the metallurgical changes in the metal. Post-weld heat treatment or annealing the component entails uniform heating of the weld, holding it at a temperature, and then a controlled cooling process. As the metal becomes hotter, it may become softer and weaker. Once a certain temperature is reached, there is a reduction in yield strength from the rated property of the material. The residual stress decreases to that of the lower yield strength, and is thereby relieved. The effect sometimes is visible by the straightening of a distorted component. It is important to note that certain welded components may be heat treated only if they are small enough to be treated. If a component is welded directly onto a larger assembly, then that component might not be able to be heat treated. In such a case the only option is mechanical stress relief.

Mechanical relief methods include laser, shot, and hammer peening. Shot peening is a cold working method that can reduce the residual stresses. Small round metal balls, or shots, are projected onto the surface of the weld. The shots impart small indentations into the surface, which induce compressive stress. The tensile residual stresses at the surface of the weld must “overcome” the compressive stress for a fatigue crack to initiate. If properly applied, the compression works to counteract the tensile stresses. Fatigue cracks have a low probability of developing in the shot peened area. Hammer peening is another mechanical method of stress relief. It uses the technique of a hand held gun with a rounded tip that oscillates at a very high speed. The rounded tip hits the surface of the

material causing the material to be in tension. The material just below the surface reacts by becoming compressive to pull the tensile material back together. This will leave the area under the surface of the material in compression. Another mechanical stress relief method is to plastically strain the material by pulling or stretching the component, which applies a tensile loading to relieve some of the residual stresses. This is a common practice in rolled and heat-treated metal plate to relieve some of the stresses in the plates after they are manufactured. An example of this mechanical method of stress relief is often used after quenching of rolled plates of alloys. The quenched aluminum alloys may have high strength but also have high levels of residual stresses, which cannot be thermally relieved while maintaining the alloys favorable mechanical properties. Therefore, the stresses are relieved by applying a uniform plastic strain, which for rolled plate involves uniaxially stretching in the rolling direction from 1.5% to 3% strain, Prime (2002).

Tensile stresses present inside FSW samples lead to poor mechanical properties. However, applying external tensioning during welding induced compressive stresses when the components are released, which have the benefit of inhibiting crack propagation, Nandan (2008). Tensile loading of welds during the welding process has been suggested as a means of significantly reducing the residual stresses, Altenkirch et al. (2007). This loading can be performed during or after welding where the entire component is mechanically loaded. The global mechanical tensioning of welds aims to reduce or minimize both the level of residual stresses and the amount of distortion in the plates. Staron et al. (2002) used strains measurements by neutron diffraction to determine the stress state in welds produced in 3.2 mm thick AA2024 sheet with and without mechanical tension during welding and found that the mechanically tensioned coupon had a reduced residual stress profile in the transverse direction.

In certain cases where the amount and direction of distortion due to friction stir welding is known, often in simple butt welded plates, the plates might be clamped and welded by an offset angle to compensate for weld shrinkage. When the plate is released and the residual stress distorts the plate, the preset angle will act to counter the effects of weld distortions.

2.3.3 Residual Stress Measurement Techniques

Residual stresses are more difficult to predict and detect than the in-service stresses on which they superimpose because these residual stresses remain hidden inside of the material. Because they satisfy equilibrium conditions, there is very little external evidence of their existence. For this reason, it is important to have a reliable and accurate method for the measurement of these stresses and to understand the level of information they can provide. There are several techniques developed to measure residual stresses, which are under two main categories of non-destructive and destructive.

Non-destructive (ND) techniques are based on methods, which do not physically alter the test pieces being examined. There are two common types of non-destructive techniques, which are neutron diffraction and x-ray scattering. Neutron diffraction is a method to examine the atomic structure of a material using a form of elastic scattering. Limitations of the neutron diffraction method include sensitivity to grain size and texturing effects. Crystalline structure anisotropy may render the measured residual strains to be ambiguous related to the actual macroscopic residual stress. Also, since diffraction can only occur in crystalline materials, neutron diffraction is currently unable to examine non-crystalline materials. Typical stress depth profiles obtained using neutron diffraction may take days to a week. The same stress profile using the compliance method could be accomplished in a day, Prime (1999). X-ray scattering technique is similar to that of neutron diffraction, which is used to study the crystallographic structure of materials. The method uses x-ray beams on the component, then looking at the scattering intensity of the beam hitting a component as a function of incident and scattering angles, polarization,

and wavelengths, Cheng et al. (1990). The method's principle is that the amount of diffraction of x-rays impinging on the atomic planes corresponds to the displacement of the planes affected by the residual stress in the material. Unfortunately, this x-ray technique is only able to detect surface residual stresses to a maximum depth of 1 mm. This method is not very desirable because the surface requires very careful cleaning and may require large and expensive testing facilities.

All destructive methods for residual stress measurement require measuring the deformation due to the release of residual stresses from slitting, which are then estimated by using an analysis based on linear elasticity. The methods involve removal of material either by hole drilling, in layers, contour, or by slitting to release the stresses that are in the material. The first method is called layer removal. This was the first method developed and assumed that the stresses vary only in the direction of thickness. This method can cause error as the material is removed from the test specimen due to error induced by machining. The second method is called hole drilling, which removes very little material. A specially made high speed drill makes it simple to produce a hole with little plastic deformation while the deformation near the hole is recorded. Hole-drilling techniques are only valid for measuring residual stresses near the surface (1 mm) where the hole is produced. This method uses strain gauges to detect the relation of residual stresses due to the production of the holes. The sectioning method uses an elaborate procedure to separate a part into sections, which are further divided into small pieces. The deformation due to each section is recorded and later used in a three-dimensional FE analysis to obtain the residual stresses. Table 2.1 shows the comparison between the methods described. It is also worth noting that while sectioning provides single stress measurements and hole drilling and slitting provides depth profiles, the contour method provides area maps of residual stresses.

Features	Layer removal	Hole-drilling	Sectioning	Slitting
Near surface	No ¹	Yes	No	Yes
Through Thickness	Yes	No	Yes	Yes
Experiment	Time consuming	Simple	Time consuming	Simple
Computation	Simple	Moderate	Complex	Moderate
In-field App.	No	Yes	No	No ²

Table 2.1: Summary of destructive methods of determining residual stresses, Prime (1999)

¹ Near surface measurements is possible only when combined with x-ray or neutron diffraction method

² Currently, there are no portable cutting machines that are available for the slitting method.

From Table 2.1, it can be seen that the slitting method is the ideal choice of destructive techniques for measuring residual stresses. It has the best application for near surface as well as through thickness stresses. Also the experimental and computational components are fairly straight forward and do not require big or expensive machinery.

It is important to note that residual stresses are categorized into two different types: macro and micro (intergranular) stresses. In microstresses, one grain with a particular crystallographic orientation might deform plastically under a given stress whereas other grains deform elastically. In general, both types are found in manufactured processes such as welding. This thesis looks at the macro stress levels and its effect on the component and does not examine the residual stress on the micro level since the current residual stress measurement techniques are limited to the determination of macro stresses only.

2.4 CRACK COMPLIANCE METHOD

The crack compliance method, which was coined by Cheng and Finnie (1985), was originally introduced by Vaidyanathan and Finnie (1971). It is a destructive residual stress evaluation technique based on the slitting method. The mechanical method of slitting to evaluate the residual stress distribution of a body is based on the simplified Bueckner's superposition principle. The principle shown in Figure 2.13 states that the residual stress profile in an undeformed body (A) is equal to the deformation of the body when a crack is introduced (B) and a stress applied to the crack face to return the body to its original shape (C).

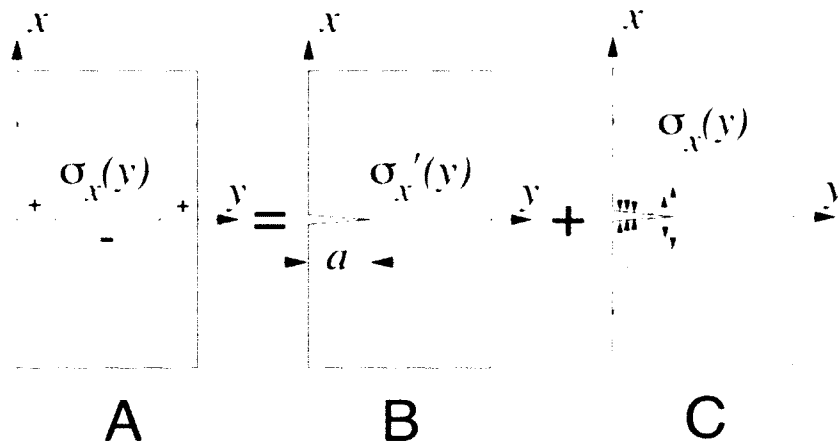


Figure 2.13: Superposition principle of slitting method [Cheng et al. (2007)]

Several assumptions are made in the compliance method. The first is that the material is linearly elastic and remains linearly elastic as the body is altered in the destructive testing process; hence the destructive testing does not introduce residual stresses. Only then can the principle of superposition be applicable through the destructive process. Other non-essential simplifying assumptions are that the material is isotropic and that the strains and stresses are calculated in the principal directions. The benefits of the crack compliance method includes the ability to measure through thickness profiles and is sensitive enough to detect low magnitudes of stresses, which are otherwise difficult to measure using other techniques such as layer removal, Prime (1999). The crack compliance method is

composed of three components. The first is the experimental measurements, the second is a forward solution and the third is an inverse analytical solution.

2.4.1 Experimental Setup

The first component of the crack compliance method is the experimental setup to measure strains in the test piece. Uniaxial strain gauges are placed on the test piece depending on the direction of the desired strains. The gauge grid pattern is oriented perpendicular to slitting axis to measure the strains normal to the slitting face. Typically, strain gauges are placed at the top of the test piece slightly offset from the slitting line and/or on the bottom of the test piece directly centered in the middle of the slitting line shown in Figure 2.14a.

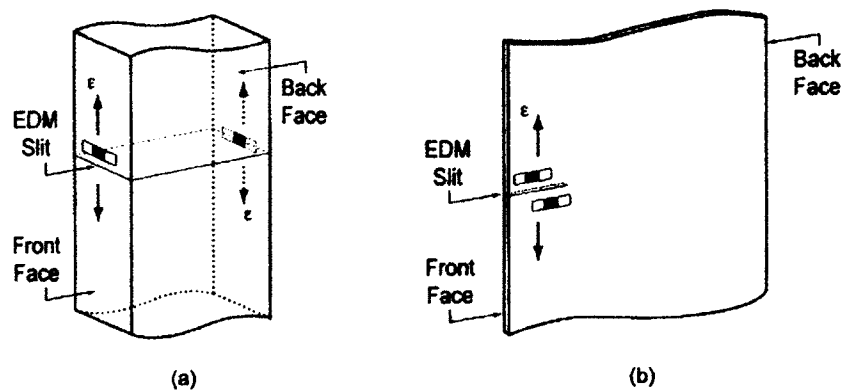


Figure 2.14 a) gauges placed on top and bottom face b) gauges placed on sides of plate next to slit line, [Rankin et al. (2003)]

When choosing a strain gauge, it is crucial to match the thermal expansion coefficient of the strain gauge with that of the surface on which the gauge will be installed. Also, the gauge length needs to be short enough to reduce the influence of strain gradients and increase the sensitivity of the measurement, Rankin et al. (2003). Top strain gauges are very good for taking sensitive strain readings at the beginning of the slit. Bottom gauges give good sensitivity when measuring strains at deeper slit depth. In this case, sensitivity refers to the level of data measurements for low residual stress levels. It is important to note that once the slitting depth is some distance past the strain gauge position, the strains

that are recorded will begin to level off to a single value, which means that the strain gauge is no longer able to detect any changes in deformation. The solution is to place multiple strain gauges distributed along the weld line. In cases where the test piece is too thin to place on the top edge or bottom edge, strain gauges can be placed on the sides of the piece running parallel to the slit line as shown in Figure 2.14b. Incremental slits are made using a wire electrical discharge machine (WEDM). Current discharges between two electrodes (the work piece and the wire) separated by a dielectric liquid and subjected to an electric voltage. As the wire move towards the work piece, a spark jumps the gap and locally melts and removes material while never actually contacting the work piece. WEDM has the advantage in that very little stresses are introduced to the work piece from the slitting, Prime (1999). Strain gauges are connected to a strain indicator and readings in microstrains are recorded for each strain gauge position and at each slit interval. To reduce the effects of the clamps on the strain measurement, the plane of cut should be located sufficiently away from the fixture. Figure 2.15 shows a typical strain data measured with respect to a normalized slit depth.

Two issues to keep in mind when performing strain measurements. Firstly, as the slit approaches the back face, the strain readings will become less stable. Eventually, the strain will reflect the specimen weight as well as the release stress, Prime (1999). Depending on how the test piece is supported, one might not be able to get a complete through thickness stress profile because strain measurements have to stop at some distance before the wire actually cuts through the test specimen. Another issue is wire breakage. EDM wires occasionally break, especially when using a thin wire. Moving the wire too fast across the slitting surface causes tension in the wire, which can cause the wire to snap. Another possible cause of wire breakage is due to the fact that the wire is moving into regions with high compressive stresses, causing the slit to close in on itself. This slit closure violates the crack compliance assumptions of linear elastic deformation and will give errors in the results. The slit will have to be re-opened by slitting to the position that caused the slit closure, Prime (1999). The presence of compressive residual

stress during measurement is not a problem as long as the slit faces do not come into contact.

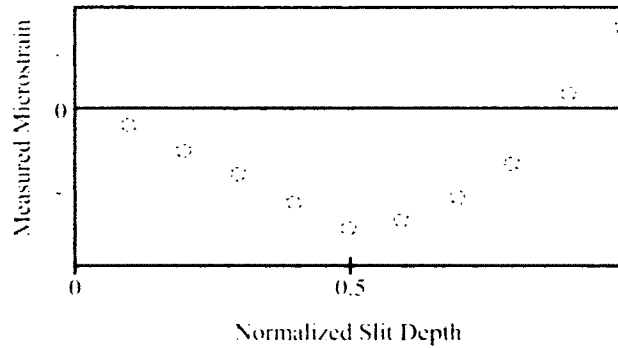


Figure 2.15: Sample strain gauge measurement [Prime (1999)]

2.4.2 Forward and Inverse Solutions

The forward solution of the crack compliance method answers the question “What are the strains or displacements that would be measured if one incrementally introduces a slit into a part with arbitrary known residual stress distribution?” Prime, (1999). The forward solution for determining the deformation due to the release of residual stress (B) is based on the rearrangement of the superposition principle shown in Figure 2.13. The original residual stress distribution in the body (A) can be evaluated by simulating a slit in a body and applying a stress with equal magnitude but opposite sign to that of the stress needed to bring the deformed body back to its original shape (-C).

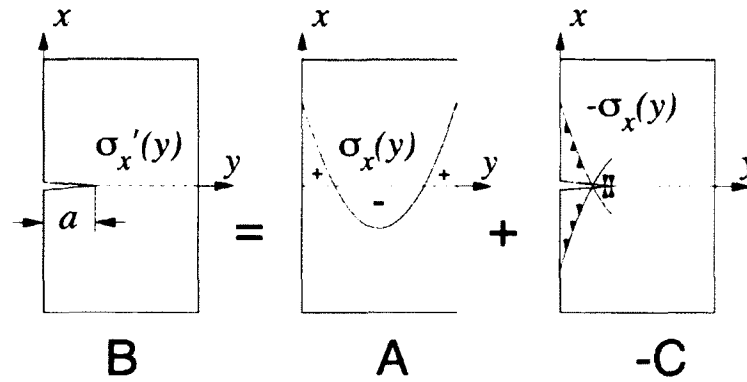


Figure 2.13: Superposition principle of slitting method [Cheng et al. (2007)]

The forward solution assumes that the unknown residual stress distribution as a function of through-thickness coordinates and can be written as a series expansion given by Eq.2.1 and illustrated in Figure 2.16.

$$\sigma_x(y) = \sum_{i=1}^n A_i P_i(y) = [P]\{A\} \quad (2.1)$$

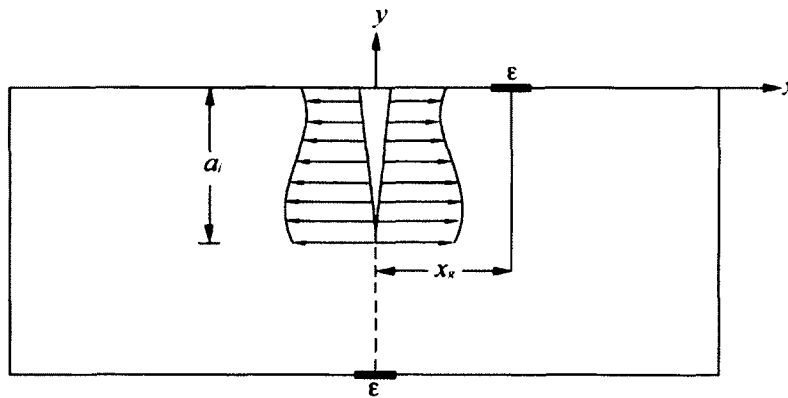


Figure 2.16: Unknown stress distribution [Prime (1999)]

Where A_i represents the unknown coefficients to be solved, y is generally normalized by the final slit depth. The P_i 's are represented by Legendre polynomials expanded over the length of the slit, where n is the number of order polynomials used. The general form of the Legendre polynomials are given as:

$$P_i(y) = \frac{\left(\frac{d}{dy}\right)^n \left[(y^2 - y)^n\right]}{n!} \text{ for } 0 \leq y \leq 1 \quad (2.2)$$

from which the first eight terms are

$$\begin{aligned} P_0 &= 1 \\ P_1 &= 2y - 1 \\ P_2 &= 6y^2 - 6y + 1 \\ P_3 &= 20y^3 - 30y^2 + 12y - 1 \\ P_4 &= 70y^4 - 140y^3 + 90y^2 - 20y + 1 \\ P_5 &= 252y^5 - 630y^4 + 560y^3 - 210y^2 + 30y - 1 \\ P_6 &= 924y^6 - 2772y^5 + 3150y^4 - 1680y^3 + 420y^2 - 42y + 1 \\ P_7 &= 3432y^7 - 12012y^6 + 16632y^5 - 11550y^4 + 4200y^3 - 756y^2 + 56y - 1 \end{aligned}$$

The 0th and 1st order polynomials are excluded because they do not satisfy force and moment equilibrium. This is proven by looking at a simple 2D body where the expression for residual normal stresses, σ that varies through the thickness must satisfy the following conditions given as

$$\begin{aligned} \int_0^1 \sigma(x) dx &= 0 \\ \int_0^1 \sigma(x)(2x - 1) dx &= 0 \end{aligned} \quad (2.3)$$

where, for simplicity, the distance x is normalized by the thickness. It is known that Legendre polynomials, $P_i(x)$ of orders $i \geq 2$ always satisfies Eq.2.3. Since $P_0(x) = 1$ and $P_1(x) = 2x - 1$ is guaranteed to hold when $\sigma(x)$ is replaced with $P_i(x)$ with $i \geq 2$. Therefore, a continuous residual normal stress is always expressible by a Legendre polynomial over the thickness as Eq.2.1. Typically orders ranging from 2nd order to 10th order are sufficient to use in the interpolation of the stress distributions.

To solve for the unknown coefficients, A_i , the strains that would be measured at the slit depth a_j , are calculated for each term in the series expansion. There are many methods of calculating these strains such as fracture mechanics solutions, the finite element method or other numerical techniques. In the crack compliance method approach, the finite element method will be used to determine these strains as a function of crack depth also known as compliances.

2.4.3 Finite Element Modeling

The purpose of a finite element (FE) model is to determine what are the strains that would be present in a test piece if an arbitrary load was to be applied to the slit face. The test piece is modeled in an FE software called ABAQUS CAE, Hibbit (2004). If the test piece is symmetrical, only half of the test piece needs to be modeled. Elements near the slitting edge are refined to give a more accurate calculation. Elements with size of half the EDM wire width are removed incrementally to simulate material removal. At each slit depth, a series of load distribution are applied to the slit face according to the orders of the Legendre polynomials. The strains are then recorded at the strain gauge positions for each slit depth and each Legendre polynomial load distribution. To measure the strain at a gauge position, displacement at the end nodes of the gauge length are subtracted and divided over the overall gauge length. The measured strains form the compliance matrix, C_{ij} . Once the compliance matrices are calculated, the next step is to use the compliances and measured strain to calculate the unknown coefficients, A_i .

Least Squares Fitting of Polynomials for Stress Estimation

For a linear elastic deformation the strain corresponding to the stress given by Eq.2.1 acting on the face of a cut of depth, a , becomes:

$$\varepsilon(a) = \sum_{i=0}^n A_i C_i(a) \quad (2.4)$$

where $C_i(a)$ is the compliance function for the i^{th} order function in Eq. 4. To determine the $n+1$ unknown coefficients in Eq.2.4, measurements of strains are made at $m > n+1$ depth of cuts. If there were no errors involved in the measurements and computations, and the order of variation of the unknown residual stress were equal or less than that given in Eq.2.1, identical results would be obtained for the coefficients A_i from strain measured at any $n+1$ depth of cut. In practice, however, some errors are always present, and different results will be obtained when strains for a different set of $n+1$ depths of cut are used. Denoting the strains computed by Eq.2.4 and those measured by ε' and ε respectively, the difference between them at the k^{th} depth a_k is given by:

$$\Delta\varepsilon(a_k) = \varepsilon'(a_k) - \varepsilon(a_k) = \sum_{i=0}^n A_i C_i(a_k) - \varepsilon(a_k) \quad (2.5)$$

Since the errors may be negative or positive, a summation of the squared of the error over all depths is taken, which from Eq.2.5 gives

$$\sum_{k=1}^m \Delta\varepsilon^2(a_k) = \sum_{k=1}^m \left[\sum_{i=0}^n A_i C_i(a_k) - \varepsilon(a_k) \right]^2 \quad (2.6)$$

The minimum of the total error is achieved only if the partial derivatives with respect to A_i for $i=0$ to n are equal to zero. That is, after changing the summation index of A from i to j , the equation becomes:

$$\begin{aligned} \frac{\partial}{\partial A_i} \sum_{k=1}^m \Delta\varepsilon^2(a_k) &= \frac{\partial}{\partial A_i} \sum_{k=1}^m \left[\sum_{j=0}^n A_j C_j(a_k) - \varepsilon(a_k) \right]^2 \\ &= \sum_{k=1}^m \left[\sum_{j=0}^n A_j C_j(a_k) - \varepsilon(a_k) \right] C_i(a_k) = 0 \end{aligned} \quad (2.7)$$

for $i=0, \dots, n$. In a matrix form, Eq.2.7 becomes:

$$[C]A = B \quad (2.8)$$

where the vectors

$$A = [A_0 \dots A_i \dots A_n]^T, B = \left[\sum_{k=1}^m C_{0k} \varepsilon_k \dots \sum_{k=1}^m C_{ik} \varepsilon_k \dots \sum_{k=1}^m C_{nk} \varepsilon_k \dots \right]^T \quad (2.9)$$

and the compliance matrix

$$[C] = \begin{bmatrix} \sum_{k=1}^m C_{0k} C_{0k} & \dots & \sum_{k=1}^m C_{0k} C_{jk} & \dots & \sum_{k=1}^m C_{0k} C_{nk} \\ \dots & \dots & \dots & \dots & \dots \\ \sum_{k=1}^m C_{ik} C_{0k} & \dots & \sum_{k=1}^m C_{ik} C_{jk} & \dots & \sum_{k=1}^m C_{ik} C_{nk} \\ \dots & \dots & \dots & \dots & \dots \\ \sum_{k=1}^m C_{nk} C_{0k} & \dots & \sum_{k=1}^m C_{nk} C_{jk} & \dots & \sum_{k=1}^m C_{nk} C_{nk} \end{bmatrix} \quad (2.10)$$

with $C_{ik} = C_i(a_k)$ and $\varepsilon_k = \varepsilon(a_k)$. The unknown coefficients A cannot be solved directly from the above equation because $m > n+1$. However, if the equation is multiplied both sides by the transpose array $[C]^T$, a system of $(n+1) \times (n+1)$ equations are obtained as

$$[C]^T [C] A = [C]^T \varepsilon \quad (2.11)$$

The least squares fit is used as a procedure for finding the best-fitting curve to a given set of points by minimizing the sum of the squares of the offsets (residuals) of the points from the curve. The sum of the squares of the offsets is used instead of the offset absolute value because this allows the residuals to be treated as a continuous differential quantity. The unknown coefficient, A_i , of the series expansion is calculated by finding a linear combination of the compliance functions that best fits the measured strains. The least squares fit is written in matrix form as

$$\{A\} = \left([C]^T [C] \right)^{-1} [C]^T \{ \varepsilon_{measured} \} \quad (2.12)$$

2.4.4 Error Analysis

The formulation for uncertainty analysis in series expanded inverse solutions for residual stresses will now be presented. Only with an accurate estimate of model error will the choice of optimal expansion order based on minimizing the stress uncertainty, Hill et al. (2002) give the actual optimal solution. Two main sources of error are considered in this work. These two sources are model error and strain error. In most practical cases, these two sources make the most significant contributions to stress uncertainty. Strain errors have been recognized as a main error source, and this assumption was confirmed by a more detailed study, Schajer et al. (1996). The calculation of stress uncertainty caused by random error is examined and provides a simple and accurate analytical formulation. Other significant errors are possible and should be minimized through careful experimental procedure. Many other likely errors source can be grouped together as geometry errors. They include errors in assumed slit depth, gauge location and orientation. These errors can be efficiently eliminated by measuring such geometric quantities before and after the experiment and then calculating the compliances for the actual geometry. Another major assumption is that the method used to introduce the slit does not produce any stress itself. Careful machining can generally limit such errors.

Plasticity

Other likely error sources include violations of the assumptions used to calculate the stresses in the slitting method. For example, plasticity during stress relaxation violates the elasticity assumption. Such plasticity can be a major source of errors, Beghini et al. (1995). Local plasticity ahead of the slit tip and the finite width of the slit may produce non-linear effects. In other words, the strain measured during the cutting process on the slit face could be not only the response to the released stresses on the slit faces but also caused by localized plastic yielding immediately ahead of the slit tip. Plastic zones in the weld may cause crack retardation or acceleration depending if the crack grows into a soft-hard or hard-soft transition, Cheng et al. (1990) and Cheng et al. (1991). In fusion welding where the temperatures are higher, the residual stresses may be higher than the

yield stress of the material but no work on FSW has shown that the residuals stresses were higher than the yield stress so plasticity should not be an issue when the stresses are released by the slitting method, Prime (2010).

Propagated Uncertainty

Before looking at random strain errors, the general error propagation formulation for series expanded stress is shown. The derivation typically follows the notion and terminology of Bevington and Robinson (1992). The uncertainty in the calculated stress at each depth is determined from a first order expansion of the propagated uncertainty in the fit coefficients

$$s_i^2 = u_{A_1}^2 \left(\frac{\partial \sigma_i}{\partial A_1} \right)^2 + u_{A_2}^2 \left(\frac{\partial \sigma_i}{\partial A_2} \right)^2 + \dots + 2u_{A_1 A_2}^2 \left(\frac{\partial \sigma_i}{\partial A_1} \right) \left(\frac{\partial \sigma_i}{\partial A_2} \right) + \dots \quad (2.13)$$

where generally, u_h is used for the uncertainty in parameter h but in this case, s is used for uncertainty in stress. The covariant terms, $u^2 A_k A_l$ with $k \neq l$, make important contributions to the uncertainties in parameters determined by least-squared fitting so they cannot be taken as zero here as they are in other situations. From Eq.2.1

$$\frac{\partial \sigma}{\partial A_j} = P_j(x_i) \quad (2.14)$$

Substituting Eq.2.14 into Eq.2.13, using symmetry in the covariant terms, and writing in matrix form gives

$$\{s_i^2\} = \text{diag}([P][V][P]^T) \quad (2.15)$$

where V is the matrix of covariance $u^2 A_k A_l$ and diag indicated forming a vector from the matrix elements on the diagonal. Individual values of s_i are obtained by taking the square root of every element.

Random Errors in Strain Data

For the major source of experimental uncertainty, the measured strains, the matrix of the covariance of the A_i is calculated considering the uncertainty in the measured strains

$$V_{kl} = u_{A_k A_l}^2 = \sum_{i=1}^m \left[u_{\varepsilon,i}^2 \frac{\partial A_k}{\partial \varepsilon_i} \frac{\partial A_l}{\partial \varepsilon_i} \right] \quad (2.16)$$

where $u_{\varepsilon,i}$ is the uncertainty in the strain measured when $a=a_i$. From differentiating Eq.2.16, one gets

$$\frac{\partial A_k}{\partial \varepsilon_i} = B_{ki} \quad (2.17)$$

Substituting into Eq.2.16 and writing in matrix form gives

$$[V] = [B][DIAG\{u_{\varepsilon}^2\}][B]^T \quad (2.18)$$

where *DIAG* indicates a diagonal matrix whose diagonal elements are the elements of the vector. Eq.2.18 can now be substituted back into Eq.2.15 to get the vector of stress uncertainties

$$\{S_{\varepsilon,i}^2\} = \text{diag}\left([P][B][DIAG\{u_{\varepsilon}^2\}][B]^T [P]^T\right) \quad (2.19)$$

where the addition subscript ε on s indicates that the source of this stress uncertainty is the uncertainty in the measured strains. To avoid confusion with the uncertainty in the strains themselves, $u_{\varepsilon,i}$ this uncertainty in stress will be reference as “measured” uncertainty.

Estimating Uncertainty in Individual Strains

An estimate of the standard deviation of the strain misfits, unbiased by the number of degrees of freedom in the series expansion, is given by

$$\bar{u}_\varepsilon = \sqrt{\frac{1}{m-n} \sum_{i=1}^m (\varepsilon_i - \varepsilon_{f,i})^2} \quad (2.20)$$

where the overbar indicates a root-mean-square (rms) average over all measured strains. To be consistent with this average, the uncertainty of an individual value can be taken as

$$u_{\varepsilon,i} = \sqrt{\frac{m}{m-n}} |\varepsilon_i - \varepsilon_{f,i}| \quad (2.21)$$

Model Error and Uncertainty

In the general case when actual stresses cannot be perfectly fit by the chosen series expansion, a conventional analysis of all the propagated uncertainty fails to adequately estimate total uncertainty, Schajer et al. (1996). The propagated uncertainty analysis implicitly assumes that the model, the series expansion, can match the actual stress. When it cannot match, the uncertainty is underestimated. This type of error is called model error. For too low an expansion order, one that does not adequately fit the data, the model uncertainty should represent that increasing the expansion order will better capture the stress profile. For expansion order in the neighborhood of some optimal fit, the model uncertainty should reproduce the observations that the fit can be relatively stable in this region.

First, it must be assumed that the chosen basis function spans the space of physically possible stress profiles. Such a series could in principle reproduce the actual stresses. One can argue that the series truncation results in the error. Therefore, the expansion order, n , is seen as a parameter in the inherent uncertainty. Similar to Eq.2.16, the stress uncertainty from uncertainty in n is given as

$$s_{\text{mod } \varepsilon, i}^2 = u_n^2 \left(\frac{\partial \sigma_i}{\partial n} \right)^2 \quad (2.22)$$

where there are no covariant terms since n is a single parameter. Because n has to be an integer, analytical evaluation of this expression is not possible. A finite difference could be used since n is not experimentally measured, and it is hard to estimate its uncertainty. At each depth where stress is calculated, x_i , a standard deviation of the stresses calculated from different order expansions is taken

$$s^2_{\text{mod } el, i}(n) = \frac{1}{N-1} \sum_{k=a}^b (\sigma_i(n=k) - \sigma_i)^2 \quad (2.23)$$

where the average stress at $x=a_i$, σ_i , is averaged over the expansion orders from $a \leq n \leq b$ but not averaged over other depths. N is the number of the stress solutions on the sum, $b-a+1$. The calculations are repeated at each cut depth.

Total Uncertainty

The total uncertainty is obtained by pointwise combining the individual uncertainty in quadrature since they are assumed to be independent from which an average uncertainty can be calculated using an RMS average over the cut depths. The total uncertainty of the calculated stress is given as

$$s_{\text{total}, i} = \sqrt{s^2_{\epsilon, i} + s^2_{\text{mod } el, i}} \quad (2.24)$$

A crucial aspect of error analysis is to identify the sources of errors that are associated with the crack compliance method. Sources of errors can come from the measurements of strains, the FE model as well as the analysis.

Errors in measurements can be categorized as either continuously varying or randomly distributed errors. Continuous varying errors are the changes in temperature during strain measurements or misalignment of the strain gauge. Randomly distributed errors are caused by errors in strain readings and in the measurement of the slit depths. For an example, when the slit is made using a wire EDM, the depth of cut is estimated from the

readings of the wire position, which can be off by 0.0024 mm. These offsets can accumulate as the slitting depth increase giving an error in the actual slit depth, Qian et al. (2004). Misalignment errors can be reduced by taking care in placing strain gauges so that the grid pattern is perpendicular to the slit line.

The errors associated with the analysis come from the difference between the computed compliance functions and the actual response to the release of the residual stresses. Errors also come from the difference between the stress distribution of the evaluated and the approximated stress distribution used in the estimation. Also, stress components that are not normal to the face of the slit will affect the strain measurements and when the computation is carried out based on the normal stresses, there will be some errors involved, Qian et al. (2004).

Normal Stress and Shear Stress

The literature covered in this review only reports crack compliance measurements of the strains normal to the face of the slit from the release of normal stresses. However, the slit will also release two shear stress components, τ_{yz} and τ_{xy} . Such shear strain, if present at the slit location, could affect the strains measured after extending the slit and, hence, the determination of the stress normal to the slit face. There are several reasons why this is usually not a practical concern for the compliance method measurements. The shear stress in the plane of the surface of the part, τ_{yz} , is measured by other methods such as hole drilling. There is little discussion of this shear stress in the crack compliance method, but two simple arguments can explain why it has little effect on the compliance measurements. First, by geometrical consideration, this shear stress component will have only a small effect on the normal strain measurements by the surface strain gauge. At a material point, normal strains are only affected by normal stress at the material point. For the surface strain gauge, this relation is

$$\varepsilon_y = (\sigma_y - \nu\sigma_z) / E \quad (2.25)$$

The local shear stress only affects the shear strain

$$\gamma_{yz} = \tau_{yz} / G \quad (2.26)$$

Releasing shear stresses at the slit location has only a small effect on normal stresses at a typical strain gauge location. Because the hole drilling methods used a strain gauge rosette and measures at least one normal strain at an angle to the y and z-axes, the shear stress does have a direct effect on the strain measurement. Second, by the free surface condition, τ_{yz} must be zero on the edges of this part. These stresses are not likely to build to a significant value unless the part is large in the z-direction at the location of the slit. The x-y component of shear stress is more often discussed in the crack compliance method literature. However, it also has little effect on measurements. By the free surface condition, this shear stress must be zero on the top face where the slit is initiated. For this same reason, it was assumed to be negligible for near surface measurements using CCM. Cheng and Finnie (1992) showed that this component of residual shear stress has no effect on the y-strains measured on the back face directly opposite the slit. This is the location most commonly used in the literature for through-thickness measurements.

2.5 Neutron Diffraction

Neutron diffraction is a non-destructive technique used to calculate residual stresses by measuring the lattice strains of a crystalline material. The deep penetration capabilities of neutrons into most industrial alloys, metallic materials, and ceramics, make neutron diffractions a unique and powerful tool for the investigation of their structure and properties. Neutrons are capable of non-destructively mapping strains and stress at depth, often in full-scaled industrial components, Holden et al. (1995).

Neutrons are subatomic particles with no net electric charge (neutral), which are found in almost all atoms. Neutrons are usually bonded via strong nuclear force in the atomic nuclei, which consist of protons and neutrons. To obtain a neutron source, individual neutrons must be liberated from their atomic bonds. Nuclear reactors are sites to facilitate

separation of these nuclear bonds. There are two methods of separation of neutrons. The first is fission and the second is spallation. In nuclear fission (Figure 2.17), a fast moving neutron is collided with a uranium nucleus. The collision will separate the uranium nucleus into fast moving liberated neutron particles as well as fragments of the uranium. Another method is neutron separation called spallation, involves taking a fast moving proton and colliding it with a heavy nucleus such as U, Ta, or Hg. The collision will cause neutrons to be released.

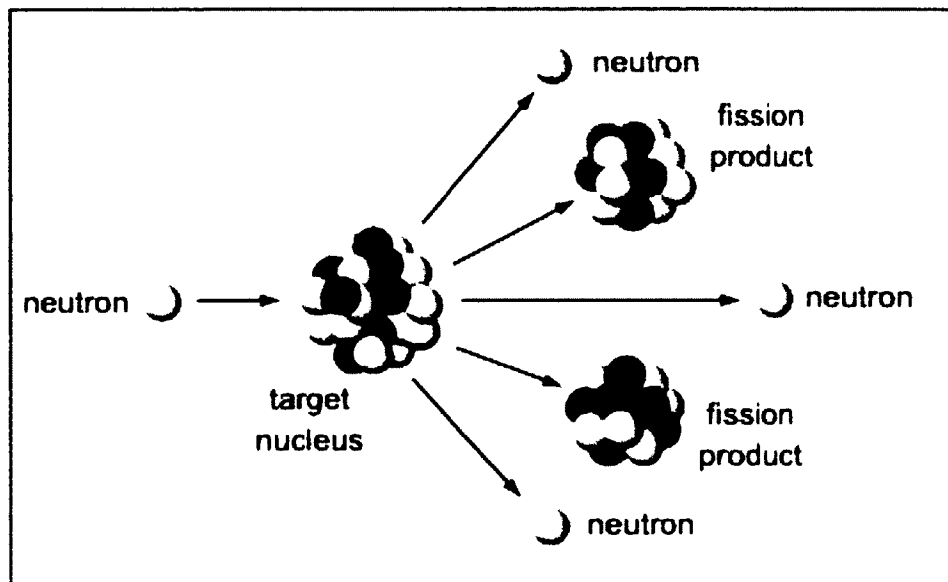


Figure 2.17: Nuclear fission to separate neutrons [web image, Ref. 96]

Once the neutrons are separated from their bonds, they are still traveling at very high speeds. They need to be slowed down before they can be harnessed for diffraction testing. Moderators are used to slow down fast moving neutrons. Every time a neutron hits a moderator, it loses energy and slows down. Deuterium (liquid D_2 , D_2O) or Hydrogen (liquid H_2 , H_2O , CH_4) nuclei are used as moderators because its mass is similar to that of the neutrons. The slowed down neutrons have one more step before they are sent to the specimen. Choppers or velocity selectors are used to define the neutron's initial energy; only the neutrons travelling at the correct velocity can pass through the blades of the turbines and hit the desired test specimen.

2.5.1 Diffraction Theory

Neutron diffraction is a volume-averaged measurement of interplanar spacing (d-spacing) in a crystalline material based on Bragg's law. Firstly, the structure of all crystals can be described in terms of lattice, the group of atoms (basis) attached to every lattice point. Repeat of basis in space forms crystal structures. The planes are identified and labeled using Miller indices. Miller indices $\{hkl\}$ are three lattice points used to identify orientation of a set of parallel planes of atoms within a crystal structure, Woo et al. (2009). Liberated neutrons of a certain wavelength, λ , are directed onto a specimen. Passing through the specimen, these neutrons are scattered and produce a pattern or spectrum of reflections. These reflections are called diffraction peaks. Each Diffraction peak has its own scattering angle and intensity that are characterized by the phases present in the material. Each reflection corresponds to a specific family of lattice planes $\{hkl\}$ of a particular phase. The spectrum is collected by scanning a single detector across a range of scattering angles. A digitized diffraction pattern is obtained, plotted as numerical intensity versus scattering angle, 2θ . The mean scattering angle, $2\theta^{hkl}$, is determined by fitting the diffraction curve and getting the diffraction peak. The scattering angle, $2\theta^{hkl}$, of the reflection (peak) corresponding to the family of planes $\{hkl\}$ is given by Bragg's Law, where d^{hkl} is the spacing of the $\{hkl\}$ lattice planes.

$$\lambda = 2d^{hkl} \sin \theta^{hkl} \quad (2.27)$$

For a selected wavelength, Eq.2.27 shows that the d -spacing can be calculated from the measured mean scattering angle. Figure 2.18 shows the scattering geometry for Bragg's Law. The incident and scattered beams make an angle θ^{hkl} with the scattering planes $\{hkl\}$. The scattering vector, Q , which is normal to the scattering planes, is the bisector of the incident and scattered beams. The measured d -spacing, d^{hkl} , is therefore measured parallel to Q and refers to the perpendicular distance between pairs of nearest planes.

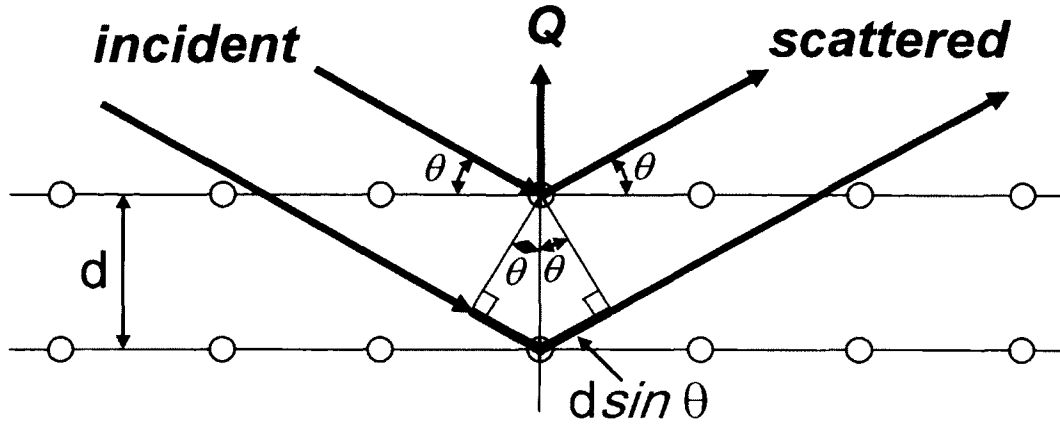


Figure 2.18: Scattering geometry for Bragg's Law [Gharghour (2009)]

Measurement of the change in d-spacing will reveal information on the residual stresses that are in the crystalline structure. Tensile stress will cause d-spacing to pull apart while compressive stresses will push the d-spacing closer together, Woo et al. (2009). A stress-free reference specimen will have a plane spacing d_0^{hkl} , corresponding to a scattering angle $2\theta_0^{hkl}$. Measuring the distance between two given planes will give information on the strains that are present in a specimen under load, or with residual stresses, the lattice spacing will be d^{hkl} ($\neq d_0^{hkl}$), with a corresponding scattering angle $2\theta^{hkl}$. According to Bragg's law, a change, Δd in the lattice spacing by internal strains will result in a shift of a Bragg peak $\Delta\theta$ that can be measured. The strain in the direction normal to the reflecting lattice plane is calculated by

$$\varepsilon^{hkl} = \frac{d^{hkl} - d_0^{hkl}}{d_0^{hkl}} \quad (2.28)$$

combining Eq.2.27 and Eq.2.28, the lattice strain can be calculated as

$$\varepsilon^{hkl} = \frac{\sin \theta_0^{hkl}}{\sin \theta^{hkl}} - 1 \quad (2.29)$$

Note that what is actually measured is 2θ , which is referred to as ϕ by convention at Chalk River (i.e. $\phi = 2\theta$). In this case, Eq.2.29 can be expressed as

$$\varepsilon^{hkl} = \frac{\sin(\phi_0^{hkl} / 2)}{\sin(\phi^{hkl} / 2)} - 1 \quad (2.30)$$

Eq.2.29 and Eq.2.30 show that only normal lattice strains can be measured by this technique. This is not generally a limitation, because normal strains can usually be measured in sufficient directions to allow the strain tensor to be completely specified.

Geometry for strain measurement

In a strain measurement experiment, monochromatic (single-wavelength) neutrons provided by a nuclear reactor (NRU) are directed onto the specimen. The incident and diffracted neutron beams are shaped by slits cut in neutron-absorbing cadmium masks. The volume defined by the intersection of these rectangular cross-section beams is called the instrumental gauge volume as shown in Figure 2.19. The shape of the gauge volume is dependent on the scattering angle shown in Figure 2.20. Only the gauge volume defined by the intersection of the incident and scattered beams is sampled by the detector. The size of the sample volume is dependent on diffraction angle and beam slit, Gharghouri (2009).

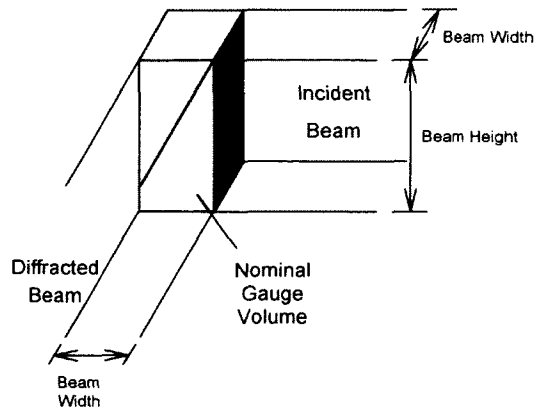


Figure 2.19: Nominal gauge volume defined by the intersection of rectangular cross-section incident and diffracted neutron beams ($2\theta = 90^\circ$). The height of the parallelepiped is defined using a height limiter on the scattered slit, [Gharghouri (2009)]

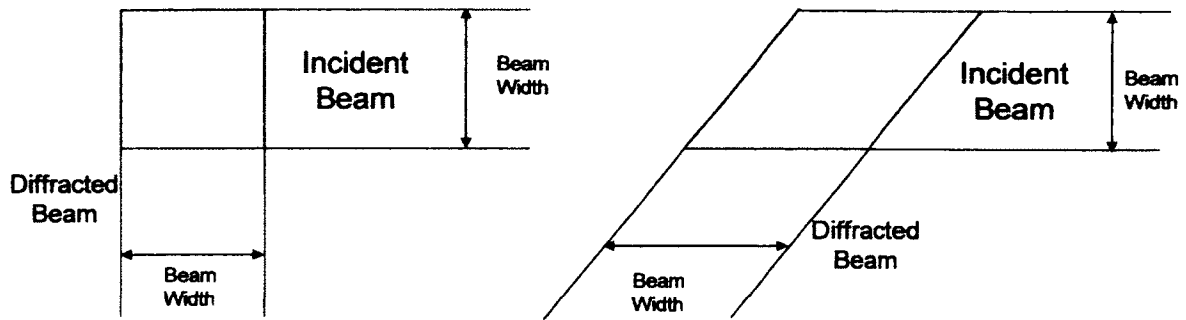


Figure 2.20: Effect of scattering angle (2θ) on nominal gauge volume (plan view)

(a) $2\theta = 90^\circ$ (b) $2\theta < 90^\circ$ [Gharghouri (2009)]

In Figure 2.21, a polycrystalline specimen is represented in two dimensions as a rectangle, which is subdivided into equally sized grains (smaller rectangles). The unit cell, considered to be tetragonal, is represented by a rectangle, the long edge having Miller indices (001), and the short edge having Miller indices (100). The orientation of the unit cell in each grain is represented by a coloured rectangle, each colour representing a particular orientation of the unit cell with respect to the specimen edges.

The detector is positioned at a scattering angle corresponding to the (001) planes. Since the (001) planes must be normal to Q for Bragg's Law to be satisfied, only those grains having the (001) planes normal to Q scatter neutrons into the detector. Thus, in the present case, only the grains having the unit cell represented by the red orientation contribute to the signal acquired by the detector. In addition, only the grains in the sampling volume contribute to the measurement. In order to measure strain parallel to a given sample direction, it is necessary to orient the specimen such that the desired measurement direction is parallel to Q. As an example, the setup in Figure 2.21 results in strain being measured parallel to the short dimension of the polycrystal. The strain parallel to the long dimension of the polycrystal can be measured simply by rotating the polycrystal about an axis normal to the page to make the long dimension parallel to Q. In this case, only the grains having the unit cell represented by the gray orientation (which would now have the (001) planes normal to Q) would contribute to the signal acquired by the detector. The location of the sampling volume is fixed in the laboratory frame of

reference. Consequently, residual stress fields can be mapped by simply translating the specimen relative to the fixed sampling volume to interrogate locations of interest within the specimen.

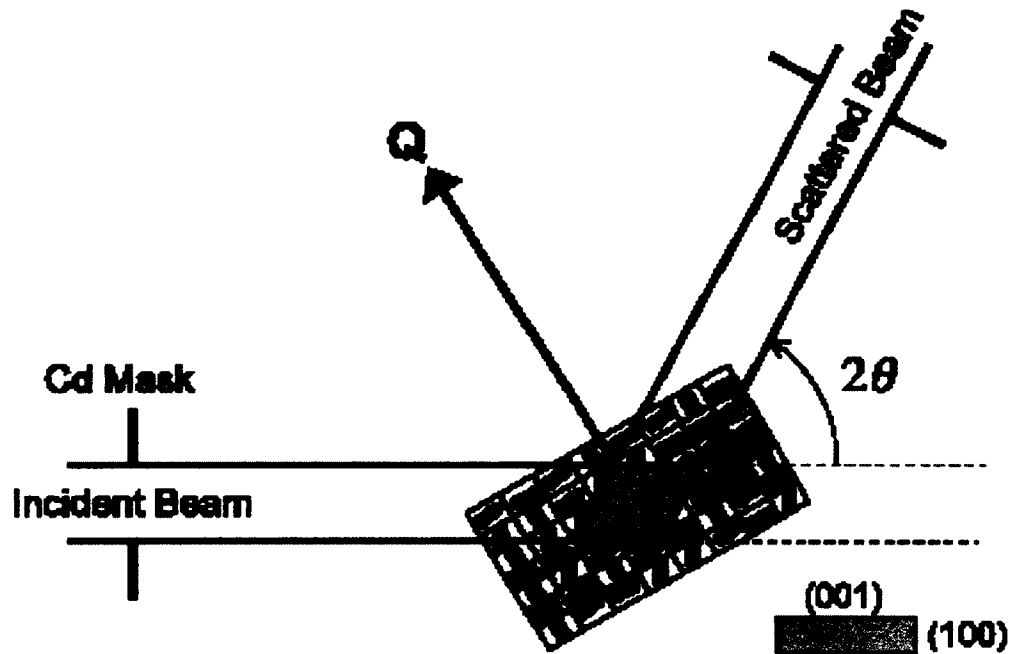


Figure 2.21: Scattering geometry for lattice strain measurements. [Gharghouri (2009)]

Determining stress from measured lattice strains

Lattice plane spacing is relatively insensitive to plastic deformation, such that lattice strains reflect only the elastic component of the strain tensor. Fortunately, this is precisely the component needed to calculate the associated stresses. In a typical experiment, the lattice strains are measured in at least three orthogonal directions, for example the longitudinal (L), transverse (T), and normal (N) directions in a rolled plate. The three corresponding normal residual stress components, σ_x , where $x = (L, T, \text{ or } N)$, can then be calculated from the three measured strain components using the Generalized Hooke's Law:

$$\sigma_x = \frac{E}{1+\nu} \left[\varepsilon_x + \frac{\nu}{1-2\nu} (\varepsilon_L + \varepsilon_T + \varepsilon_N) \right], \text{ for } x = [L, T, N] \quad (2.31)$$

where E is Young's modulus and ν is Poisson's ratio. Eq.2.31 assumes isotropic elasticity. If the directions of the three principal stresses are known, then it is sufficient to measure the residual strains along these directions to completely specify the strain and stress tensors. Normal stresses can be calculated from three normal strains measured in orthogonal directions, Gharghouri (2009).

2.6 Fatigue Failure in Aircraft

Of the many failures due to fatigue, the following is a summary of three examples of fatigue related failures in aerospace structures. The de Havilland Comet crashes of 1954 is a famous example of fatigue failure when two de Havilland passenger jets broke up in mid-air and crashed within a few months of one another. As a result of the accidents, systematic testing was conducted on a fuselage immersed and pressurized in a water tank. The investigation concluded that the accident was due to failure of the pressure cabin at the forward window shown in Figure 2.22.

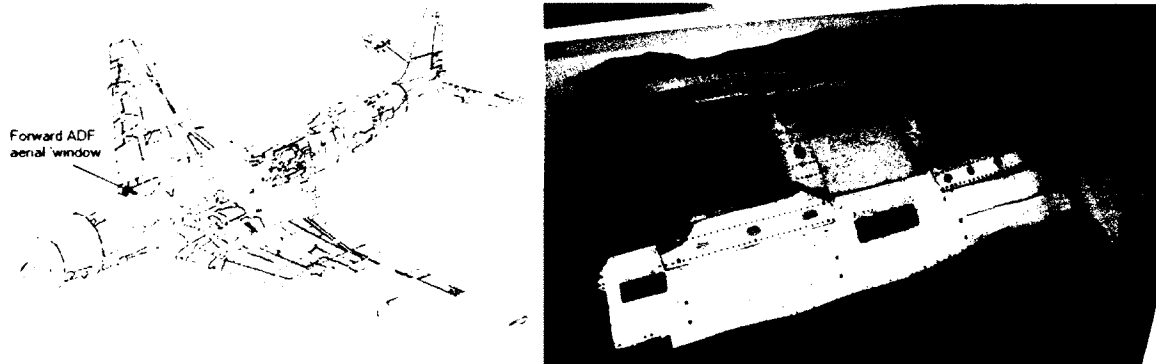


Figure 2.22: Forward Roof window of de Havilland Comet [web image, Ref. 97]

The failure was a result of metal fatigue caused by the repeated pressurization and depressurization of the aircraft cabin. Another fact was that the supports around the windows were rivets, not welded, as the original specifications had called for. The problem was increased by the punch rivet construction technique. The nature of the rivet holes caused cracks, which may have caused the start of fatigue cracks around the rivet.

In addition, the skin of the airframe was also too thin, and the crack from manufacturing stresses (residual stresses) was present as well.

The Los Angeles Airways Flight 417 was a helicopter crash in 1968. The accident, according to the National Transportation Safety Board, was caused by fatigue failure. One of the five main rotor blades separated at the spindle, which attached the blade to the rotor head. The cracks originated in an area of substandard hardness and inadequate shot peening. The cracks initiated due to possible detrimental effects of residual tensile stress from the plating of the rotor blades.

A more recent incident involving fatigue failure happened in 2005 on Chalk's Ocean Airways Flight 101. All 20 passengers and crew on board died in the crash, which was attributed to metal fatigue on the starboard wing resulting in separation of the wing from the fuselage. A more detailed investigation shows that there was a fatigue failure in the right wing initiated by a crack in a span-wise stringer close to the wing root. The crack was missed during previous scheduled inspection because a sealant used to repair another section of the wing was applied over the damaged lower stringer. This stringer was an important, load-bearing structural member of the wing. The cracks under the sealant grew on the underside of the wing until the wing was so weakened it was unable to support the flight loads, and the wing separated. This accident shows that residual stresses in stringers can lead to catastrophic fatigue failures in aircraft components. In this case, it was the stringers in the wing of an aircraft subjected to high levels of cyclic loading.

A structure should be designed and produced in such a way that undesirable fatigue failures do not occur. To design against fatigue, one must first know how the factors that affect fatigue and how to measure the fatigue of a component due to those factors.

Fatigue is a failure mechanism that is described by progressive and localized structural damage that occurs when a material is subjected to cyclic loading. The nominal maximum stress values are less than the ultimate tensile stress limit and may be below the yield stress limit of the material. Fatigue occurs when a material is subjected to a repeat or cyclic loading and unloading. If the loads are above a certain threshold, microscopic cracks will begin to form. If the material continues to be loaded and unloaded, eventually a crack will grow on a macroscopic scale. Once the crack reaches a critical size, the structure will fracture and fail.

2.6.1 Fatigue Life and Factors That Affect It

Fatigue life, N_f , is defined as the number of stress cycles a material can sustain before failure. Fatigue life scatter tends to increase for longer fatigue lives. The greater the applied stress range, the shorter the fatigue life of the material. The damage caused in fatigue is cumulative so the material is not able to recover when it is unloaded. Fatigue life is usually split into crack initiation period and a crack growth period. The initial period is supposed to include some microcrack growth, but the fatigue cracks are still too small to be visible. This period includes cyclic slip, crack nucleation, and micro crack growth. In the second period, the crack is growing until complete failure. This period is where the macrocracks grow. Fatigue life is influence by a variety of factors, such as geometry, temperature, surface finish, microstructure, the presence of oxidizing or inert chemicals, material type, size and distribution of internal defects, grain size, environment and, residual stresses. Notches and variations in cross section through a part can lead to stress concentrations where fatigue cracks initiate. Surface roughness can cause microscopic stress concentrations that lower the fatigue strength. In terms of material type, fatigue life, as well as the behaviour during cyclic loading, varies widely for different material. Environmental conditions can cause erosion or corrosion, which all affect fatigue life. Corrosion fatigue is a problem encountered in many aggressive environments. Temperature can cause fatigue because extreme high or low temperatures can decrease fatigue strength. Finally, residual stresses can affect fatigue life; welding, cutting, casting and their manufacturing process involving heat or deformation can

produce high levels of tensile residual stresses, which decrease the fatigue strength. Residual stress can affect the material on a microscopic level introducing microscopic cracks which with the addition of cyclic loading experienced by these aircraft structures cause cracks to grow. As stated in previous sections of this chapter, mechanical stress relief in the form of shot peening or hammer peening can be used to introduce compressive stresses on the surface of the materials to increase its fatigue life. Shot peening will introduce plastic deformation in the surface layer of the material. As a result, residual compressive stresses are left in a thin surface layer. It is important to note that residual stresses do not affect cyclic shear stresses, which causes microcrack forming. The residual compressive stresses reduce or prevent crack opening of the microcracks only.

2.6.2 How to Measure Fatigue Life: S-N Curves

High cycle fatigue typically requires more than 10^4 cycles to failure where stress is low and deformation is primarily elastic. In high cycle fatigue situations, material performance is commonly characterized by an S-N curve, which focuses on the normalized stress required to cause a fatigue failure in some number of cycles. Figure 2.23 is a test specimen attached to a load-controlled servo-hydraulic test rig. The specimen undergoes sinusoidal stress, which counts the number of cycles the material can withstand before failure. The frequency of the loads can range from 10 to 50 Hz. This test is known as coupon testing.

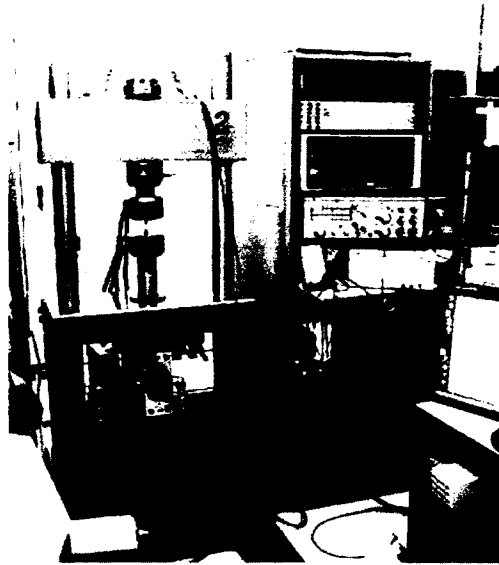


Figure 2.23 Fatigue performance setup to determine fatigue life of a specimen [web image, Ref. 98]

This test results in data presented as a plot of stress, S , against the number of cycles to failure, N , which is known as an S-N curve (Figure 2.24). A log scale is almost always used for N . The data is obtained by cyclically loading smooth or notched specimens until failure. The usual procedure is to test the first specimen at a high peak stress where failure is experienced in a fairly short number of cycles. The test stress is decreased for each succeeding specimen until one or two specimens do not fail in the specified number of cycles, which is usually at 10^7 cycles. The highest stress at which a runout (non-failure) occurs is taken as the fatigue threshold, Ericsson et al. (2005).

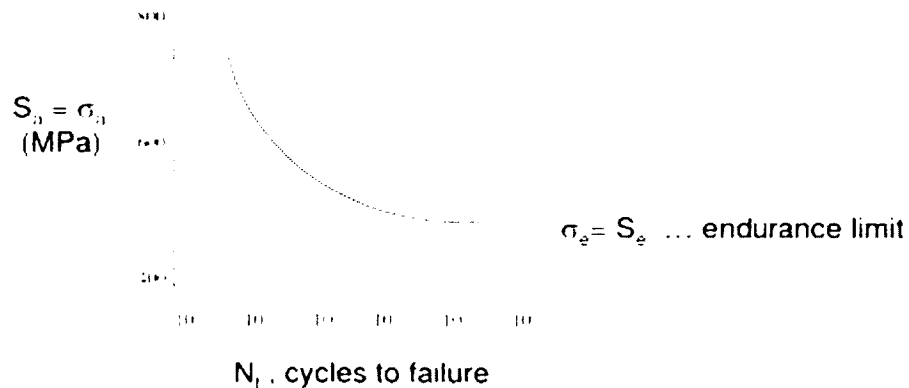


Figure 2.24 Typical S-N curves to determine fatigue life of a component [web image, Ref. 99]

Fractographic Observations

After specimens are loaded to failure, the fracture surface is examined to help determine where the fatigue fractures started, and in which direction it grows. Under certain loading conditions, fractography pictures can reveal striations, which could be correlated with individual load cycles. The surface of the fracture can give information on what kind of failure occurred, Bussu (2002). The scanning electron microscope (SEM) is a powerful tool used to examine the fracture surface using electrons as oppose to light to generate the image.

2.6.3 Design Against Fatigue

Designing a component to be reliable and be able to sustain fatigue failure requires thorough knowledge and extensive experimentation of the component on a mechanical as well as materials base. There are three principal approaches to life assurance for these components that vary in degrees of sophistication. The first approach is to design the component to keep service stresses below threshold of fatigue limit otherwise called infinite lifetime concept. The second design approach is fairly conservative, which is to design for a fixed life after which the components are to be replaced with a new component. This concept is called safe life design practice. Finally the third approach is to have a component inspected for cracks and replace the part once a crack exceeds a specified length. This approach usually uses the technologies of nondestructive testing and requires an accurate prediction of the rate of crack-growth between inspections (S-N curves). This is often referred to as damage tolerant design.

2.7 Summary of Current Literature Review

2.7.1 Current Friction Stir Welding Literatures

The following is a literature survey on the process and properties of FSW by several authors. Each paper examines a specific issue related to FSW such as weld parameters, joint configuration, modeling, mechanical properties, residual stress, and residual stress

measurement techniques used to measure residual stresses in these various FSW components. Reynolds et al. (2003) wrote a paper on the structure; properties and residual stresses of 304L stainless steel and aluminum friction stir welds. The stainless steel plates were welded in the butt joint configuration. Neutron diffraction was used to determine the residual stress in the transverse and longitudinal directions focused on the flaws in friction stir welds. In particular, they looked at 2xxx and 7xxx series aluminum alloys and concluded that insufficient mixing of material by the rotating pin caused voids in the welds.

Leonard (2003) studied the effect of tensioning and sectioning on residual stresses in aluminum AA7749 FSW. A number of authors examined residual stresses in FSW butt joints. All concluded that the FSW tool produces a signature “M” shaped longitudinal stress profile in the transverse direction configurations (Deng (2008), Wanchuck (2006), Dalle et al. (2001), Ali (2006), and Staron (2002)).

There are a few papers written on numerical analysis of the friction stir welding process and the resulting residual stresses. The first is the thermomechanical modeling. There have been considerable efforts in modeling FSW to optimize the thermomechanical conditions. Rajesh et al. (2007) used a commercially available FE software called ANSYS, to perform 3-D FSW simulations for studying thermal impact, and the evolution of longitudinal, and transverse stresses in the weld by considering mechanical effects of the tool. A FE-based 3D thermal model of the FSW process has been present by Uyyuru (2005), Khandkar et al. (2006), Rajesh et al. (2007), and Goldak et al. (2009) independently used a thermoelasto-plastic FE model to numerically determine the residual stresses in friction stir and constrained welds.

There have been numerous attempts to characterize the microstructure of FSW of aluminum alloys such as 2024, 7075, 7050, 6061, and 1550, Ali (2006). The

microstructure of FSW 2024-T3 aluminum butt-welds has been studied Sutton et al. (2002). He examined the different weld zones and the corresponding residual stresses that were determined in these zones. Peel and Steuwer (2006) wrote a paper on the microstructure, mechanical properties, and residual stresses as a function of welding speed in AA5083 FSW plates. The weld was beaded onto a single sheet of aluminum alloy, Sjoerd et al. (2006). Both studies suggest that residual stresses are affected by the different microstructures of the weld. Depending on plate thickness and tool rotation speed, the size of these zones. The changes in the microstructure and mechanical properties via severe thermo-mechanical deformation have been studied extensively for FSW aluminum alloys, Hatamleh (2007).

2.7.2 Crack Compliance Method Literatures

The destructive method of mapping residual stress known as the contour method is recently a popular area of study. Zhang and Ganguly (2004) applied the contour method to map cross sectional residual stresses in variable-polarity plasma-arc (VPPA).

Prime is a big advocate of the contour method and has written many papers on its use to map residual stresses in various metals (Prime et al. (2004), Prime et al. (2006), Prime (2004)). Unfortunately, the contour method works best on thick materials where varying strains released on the surface of the slit can be mapped properly. Problems arise when trying to apply the contour method to thin plates because the released stresses do not provide distinctive contours for mapping. Although the contour method is described in this thesis, the method itself was not used and the crack compliance was deemed the better option for residual stress determination.

The following is a list of all the literature on the compliance method to date. Although W. Cheng and I. Finnie did not invent the slitting method, they are the two individuals that have influenced the development of the crack compliance method. They wrote a book on

the various applications of the slitting method; one being to determine residual stresses, Finnie (1996). W. Cheng and I. Finnie (1991) wrote a paper on the study of residual stresses near the surface of a component using the crack compliance method. Similarly, Tochilin and Nowell (1998) also wrote a paper on near surface stresses using the crack compliance method. Nervi et al. (2006) estimated the residual stresses in an un-welded thick block of 7050-T7451. Wang and Ke (2003) studied the effects of residual stress relief of a 7050 aluminum alloy by the crack compliance method. In the paper residual stresses were determined for plates before and after heat treatment and determined the residual stress in only one direction (transverse).

Prime has to date the most published works on the crack compliance method. He wrote several papers on the crack compliance method used to measure residual stress in different components. Prime and Hill (2003) studied the effect of residual stress and inhomogeneity in 7xxx series aluminum plates. Prime et al. (1997) looked at residual stresses in bi-material laser clad using the crack compliance method. Prime wrote several papers on the experimental procedures for crack compliance measurement of residual stress, which is used by many practitioners of this method. Prime (2002). Prime (2010) examines plasticity effects in incremental slitting measurements of residual stress, something that is not very easy to find in literature due to the complex nature of the effects and little known knowledge on the methods of determining such effects. Prime and Hill (2006) wrote a paper on uncertainty analysis, model error, and order selection for series-expanded, residual stress inverse solutions to help calculate the errors involved when dealing with the compliance method.

2.7.3 Neutron Diffraction Literatures

Several authors employed neutron diffraction and x-ray diffraction on the estimation of residual stresses in FSW. Woo et al. (2009) studied the time-dependent residual stresses generated by severe thermomechanical deformation using neutron diffraction. Woo and Ungar (2009) also used neutrons to measure dislocation density and subgrain size in a

friction stir welded 6061-T6 aluminum alloy. Holden et al. (1995) used neutron diffraction to measure residual stresses in steel as well as determination of diffraction elastic constants. Dubourg et al. (2007) used neutron diffraction to determine longitudinal residual stresses in 2.3 mm thick AA2024-T3 butt-welded plates in the transverse direction. Sutton et al. (2006) reported asymmetric residual stress distributions in the transverse and longitudinal direction of 2024-T3 Al alloy friction stir welded butt plates measured using neutron diffraction techniques.

2.7.4 Other Residual Stress Measurement Techniques Literatures

Several authors have attempted to determine residual stresses using different techniques that are not yet mentioned. Fett (1996) chose to use fracture mechanics weight functions to determine residual stress in components. Different weight functions have to be used depending on the complexity of the geometry. There are weight functions already available for simple and common geometries. Milan et al. (2007) examined residual stress in butt-welded AA 2024-T3 joints with the help of weight functions for a simple plate with a rectangular geometry. The residual stresses were determined in the transverse and longitudinal directions. Montay and Sicot (2009) developed a new method of residual stress determination in two directions simultaneously with electronic speckle pattern interferometry. The method is based on stress relaxation in a groove that is machined incrementally. Strains are measured both in the depth and length directions to infer the residual stresses in the component.

2.7.5 Fatigue Performance Literatures

Several authors have reported the effects of residual stresses on the fatigue crack propagation. Buus and Irving (2002) investigated the role of residual stress and HAZ on fatigue crack propagation in FSW 2024-T3 aluminum joints. Their studies showed that crack growth rate depended on orientation and distance from the butt-welded joint. Weld residual stresses were relieved and the rate of crack propagation was reduced. Root et al.

(2003) studied the effects of residual stress on fatigue crack growth in friction stir welds of 7050-T7451. Dalle et al. (2006) looked at the effects of weld imperfections and residual stresses on the fatigue crack propagation in FSW butt joints. Ericson (2005) and Mustafa et al. (2006) independently investigated the effects of tool rotation and pin diameter on fatigue properties of FSW joints. Only one journal was found on the study of buckling failure of FSW aluminum panels made from 2024-T3 plates by Sjoerd (2006).

Chapter 3

TEST SPECIMEN

3.1 Friction Stir Weld Specimens

All of the experiments in this thesis were conducted on the fuselage panel composed of an aluminum stringer friction stir welded to an aluminum skin panel in a lap joint configuration. The friction stir welded test specimens (Figure 3.1) consisted of a 191 mm x 500 mm x 1.55 mm AA 7075-T6 stringer friction stir welded to an AA 2024-T3 skin panel measuring 191 mm x 500 mm x 2.21 mm using a MTS I-STIR machine at the National Research Council Canada's Institute for Aerospace Research in Montreal (NRC-IAR Montreal) with a tool shoulder diameter of 15.49 mm. Although it was never specified, the forging force of a typical FSW operation was around 8500 N, Woo et al. (2009) and the temperatures in the weld have been measured in the literature to reach 500°C, Woo et al. (2007). Two sets of FSW plates were manufactured, each set of FSW plates included two samples. One set of FSW plates is called as-welded and the other set is referred to as hammer peened. As stated before, the plate on the left in Figure 3.2 is that of the as-welded configuration and the plate on the right is that of the hammer peened configuration. Hammer peening is a cold work process, which uses a tool with a small rounded tip that impacts the surface of the material causing plastic deformation. The tensioning from the plastic deformation at the surface imparts compressive stresses right below the surface of the material. The residual stresses present in the hammer peened specimen will be examined in the next chapter but a visible difference between the two plates was that the hammer peened plate appears to have less distortion to the point where the plate was able to lay flat on a surface. Figure 3.3 compared the surface finishes of the two samples. On the left, a ripple pattern was apparent from the rotation of the weld tool moving along the material similar to that of a cake batter when an electric mixer is put into the batter. The combination of rotation and translation of the electric mixer produced ripples in the batter as the ingredients are mixed together. In the FSW plates, it's the rotating weld tool that softens and mixes the two metals together to form a solid bond when the material cools down. On the right is the surface finish of the weld

after hammer peening which shows the tool hits the surface of the metal with a small rounded tip and smoothes out the ripples from the weld.



Figure 3.1: FSW stringer-to-skin lap joint plate

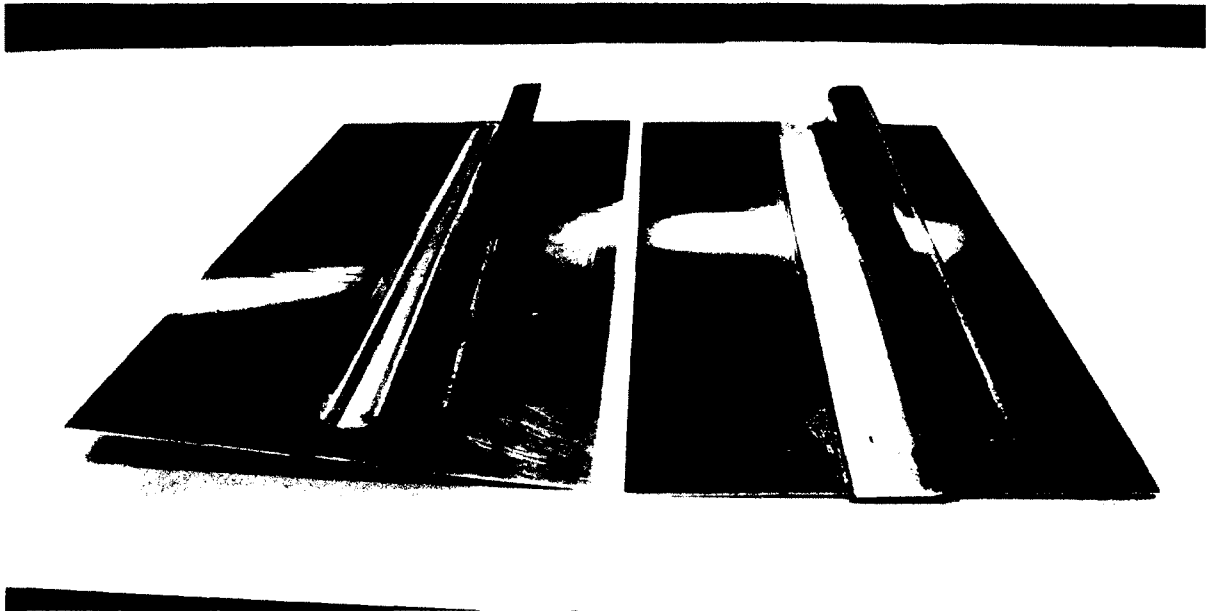


Figure 3.2: As-welded and hammer peened test plates [Merati (2009)]

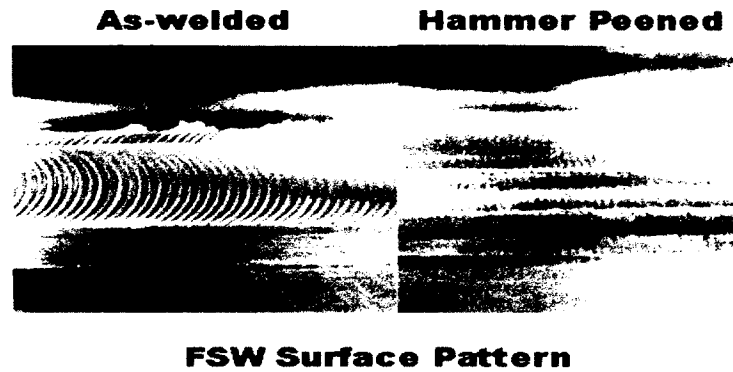


Figure 3.3: Surface finishes of as-welded and hammer peened plates

3.1.1 Weld Configuration

The weld configuration that is being studied in this thesis is a double pass weld with inward hook. Figure 3.4 is a close-up view of a section of the double pass. The purpose of using a double pass weld is to go back along the first pass and mix the material a second time for better material cohesion and remove any voids formed by the first pass. Previous literature had stated that the stresses present on the advancing side of the tool is slightly higher than that on the retreating side due to the faster relative speed of the rotating tool on the advancing side, Ericsson (2005). By making a second pass that overlaps the first pass's advancing side, the stresses may be reduced or altered. The area where the tool pin is removed from the weld is called the exit hole. The term hole is misleading because the pin produces a circular indent that does not go through the entire material. Jung (2007) examined the fatigues lives of single pass and double pass welds and determined that the double pass welds outperformed that of the single pass. From pervious literature, it was determined that the double pass inward hook had the best mechanical performance of the three types of weld and that is where this work continues to examine the optimal weld configuration chosen by the National Research Council, Merati et al. (2009). In a single pass weld, the weld centerline would be exactly at a distance that divides the weld in two equal sections. This thesis deals with the double pass geometry so there are two weld

centrelines. To avoid confusion, in this work the weld centreline will be determined by taking the overall length of the two weld passes and dividing it by two.

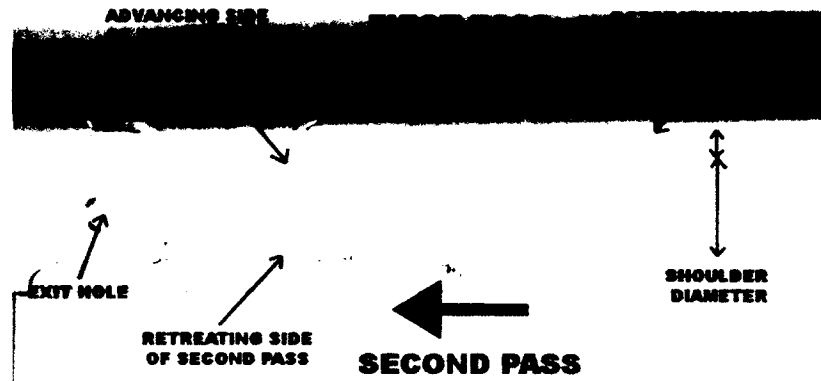


Figure 3.4: Double pass weld configuration

3.1.2 Specimen Geometry

Both sets of welded plates (as-welded and hammer peened) were sectioned into smaller test specimens for the various slitting, metallographic and fatigue experiments as shown in Figure 3.5. The specimen cross-sectional dimension of the FSW lap joint is shown in Figure 3.6. It is important to note that in a real FSW component, there is always an entry hole where the tool is initially plunged into the metal plate and an exit hole where the tool is removed from the surface of the material. For the experiments in this work, the two holes were ignored and sectioning of the test specimens were made to exclude these two end pieces that contained these two holes. The purpose of excluding them is to study the residual stresses in a continuous section of the FSW without the effects of the hole influence. Thus the goal of this study was to measure the residual stresses in the FSW plate before and after hammer peening and including the hole would introduce one more variable that is not necessary for the scope of this project. Also, some basic assumptions were made for testing of the as-welded and hammer peened plates. Since friction stir welding offers ease of handling, precise external process control and high level of repeatability thus creating very homogenous welds, Deng (2008) and Dewald (2006), it is

assumed that the weld residual stress in each specimen is similar. Therefore, measuring the residual stress in two specimens, one with and one without hammer peening, will demonstrate the effect of the hammer peening on the welded plate.

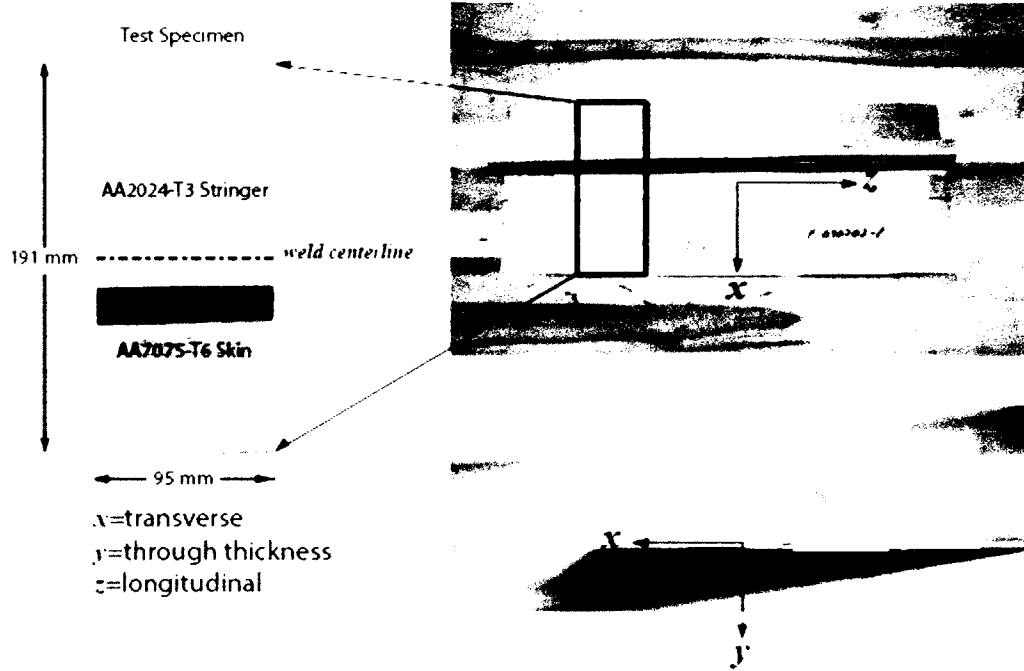


Figure 3.5: Test specimen sections from whole plate

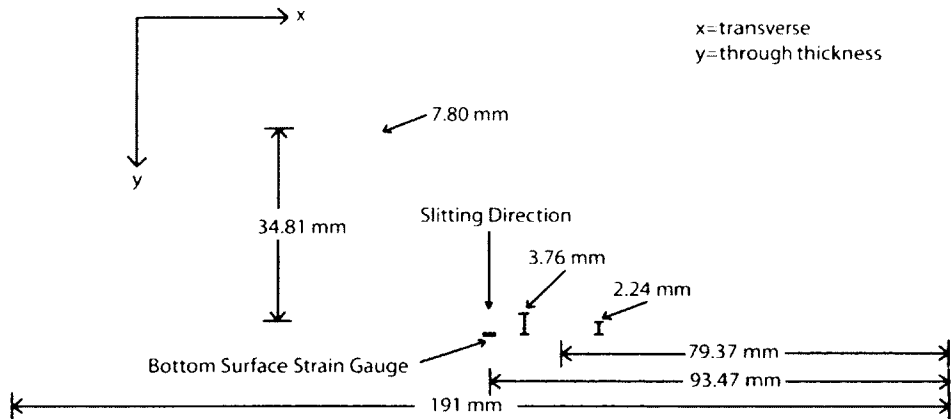


Figure 3.6: FSW Stringer-to-skin lap joint cross-sectional dimension

3.1.3 Material Properties

Aluminum and its alloys are considered one of the most practical of metals for a number of reasons. It is low cost, lightweight, non-sparking, electrically conductive, thermally conductive, and chemically resistant. It is popular in the construction, marine and aircraft industries. The two materials used in this thesis is AA 2024-T3 and AA 7075-T6. The skin panel composed of a rolled sheet of AA 2024-T3 aluminum alloy. The 2xxx series contain high content of copper, which has excellent damage tolerant characteristics, Zhang et al. (2004). The 2xxx series also exhibits high mechanical properties; increase yield strength, which is very desirable in the aerospace industry, Prime et al. (2002). 7xxx series have high zinc content. These 7xxx series alloys are the highest strength of alloys and are used in airframe structures. The stringer is made up of a rolled sheet of AA 7075-T6, which has been bent to form an “S” shape. The letter T behind the alloy represents families of heat treatable alloys. T3 represents alloys that are solutions heat-treated and then cold worked. The T6 represents alloys that are solutions heat-treated and then artificially aged. AA 7075-T6 alloys are artificially aged which is also known as precipitate hardening. Solution heat treatment of AA 2024-T3 involves heating the alloy to a specific temperature for a specific amount of time, then rapidly quenched. The super saturated solution will cause the copper content to solid solution with the aluminum, allowing the crystal structure to form compounds containing higher concentrations of copper. These copper rich compounds migrate to the metallic grain boundaries and interfere with movement between slip planes as load is applied to the alloy. Hence, the result is a hardening effect similar to cold working. Precipitate heat treatment of AA 7075-T6 is also known as artificial aging process. The treatment involves taking an alloy that is solution heat treated and forcing the material to age by holding it at a prescribed temperature for a considerable period of time. During the aging period, some of the alloy compounds precipitate out of solution and end up at the grain boundaries to increase material strength. Artificial aging also helps improve resistance to intergranular corrosion. The stringers are typically made out of higher strength aluminum than the skin panel so that in cases where cracks are growing in the skin panel, they will reach the stringer and stop because of the increase in strength of the stringer. The material

properties of the two aluminum alloys are given in Table 3.1 and their chemical compositions are given in Table 3.2.

Mechanical Properties	AA 2024-T3	AA 7075-T6
Young's Modulus (GPa)	72	71.7
Poisson's Ratio	0.33	0.33
Yield Strength (MPa)	345	503
Ultimate Tensile Strength (MPa)	483	572
Hardness (Vickers)	137	175
Physical Property (g/cc)		
Density	2.78	2.81
Thermal Properties		
Thermal Conductivity (W/m-K)	121	130
Specific Heat Capacity (J/g-C)	0.88	0.96
Melting Point (C)	638	635

Table 3.1: Material Properties of AA 2024-T3 and AA 7075-T6 aluminum alloys

Component (Wt.%)	AA 2024-T3	AA 7075-T6
Al	90.7-94.7	87.1-91.4
Cr	Max 0.1	0.18-0.28
Cu	3.8-4.9	1.2-2
Fe	Max 0.5	Max 0.5
Mg	1.2-1.8	2.1-2.9
Mn	0.3-0.9	Max 0.3
Si	Max 0.5	Max 0.4
Ti	Max 0.15	Max 0.2
Zn	Max 0.25	5.1-6.1

Table 3.2: Elemental composition of aluminum alloys

3.2 Friction Stir Weld Microstructure

3.2.1 FSW Weld Zones

The following section details the examination of the microstructures of the different weld zones in the FSW lap joint. The microstructure of the weld zones were investigated using standard metallurgical preparation and imaging methods such as digital and optical microscopes. The samples were sectioned in the x-y plane, mounted and polished to remove any residual damage from the cutting process. For optical microscopy, it was sufficient to finish the polishing process with a short chemical polish before etching in solutions of 4 ml HF, 4 ml H₂SO₄, 2 g CrO₃ in 90 ml water. The microstructure of the weld zone for the double pass FSW is shown in Figure 3.7.

The center of the weld consists of the weld nugget shown in Figure 3.8, which measures approximately 15 mm wide. The heavily worked microstructure of the base material has been completely replaced by equiaxed grains around 10-13 μm in diameter that have little substructures, typical of a recrystallized microstructure, and similar to that found previously in 5xxx, 6xxx and 7 xxx series aluminum stir welds.

The area surrounding the weld nugget is called the thermomechanical-affected zone (TMAZ). It is worth noting that the microstructure in the TMAZ showed an elongated grain structure caused by severe plastic deformation that takes place during welding. The grain size in TMAZ is approximately 200 to 400 μm, slightly bigger than that of the parent material.

The heat affected zone or HAZ lies just beyond the TMAZ and is an area that is unaffected by the mechanical effects of the welding tool. The grain structure in the HAZ and parent plate is similar, with a size in the order of 150 to 200 μm, Ali (2006). As the name suggests, the HAZ is only affected by the heat generated from the welding process.

At the edge of the welding tool's pin, an abrupt transition occurs from the highly refined, equiaxed, grains comprising the nugget to the deformed based metal grains. At a location corresponding to approximately the tool shoulder radius on the advancing side, a relatively coarse, recrystallized grains structure is observed. At 4.5 mm from the edge of the shoulder, the microstructure appears to be identical to the original elongated grain structure present in the rolled AA 2024-T3 base metal, Sutton et al. (2002).

Figure 3.9a shows the microstructure of the parent AA 7075-T6 material and Figure 3.9b shows the microstructure of the parent AA 2024-T3 material. The AA 2024-T3 has larger and longer grains than the AA 7075-T6. Typical grain size of the AA 2024-T3 measures approximately 120 μm compared to the 5 μm of the AA 7075-T6.

Figure 3.10 is the transition between the weld nugget and the TMAZ. The image shows a difference in grains size between the fine grains of the weld nugget and the larger, elongated grains of the TMAZ.

Figure 3.11 shows a common pattern found in friction stir weld microstructures which is the elliptical "onion ring" pattern produced by the rotation of the tool as it mixes the two materials together. The difference in contrast between the onion rings has been attributed to the incremental advancement of the tool per revolution, Lee et al. (2005).

Figure 3.12 shows a typical large void found at the edge of the weld nugget and TMAZ on both the advancing and retreating sides of the weld nugget. The length of the void measures 200-250 μm in length. The formation of these voids is from the inadequate mixing of the material as the tool passes along the weld line.



Figure 3.7: Cross section of FSW a) weld nugget, b) TMAZ, c) HAZ, d) onion ring pattern, e) parent AA 7075-T6, f) parent AA 2024-T3



Figure 3.8: Central weld region showing the weld nugget

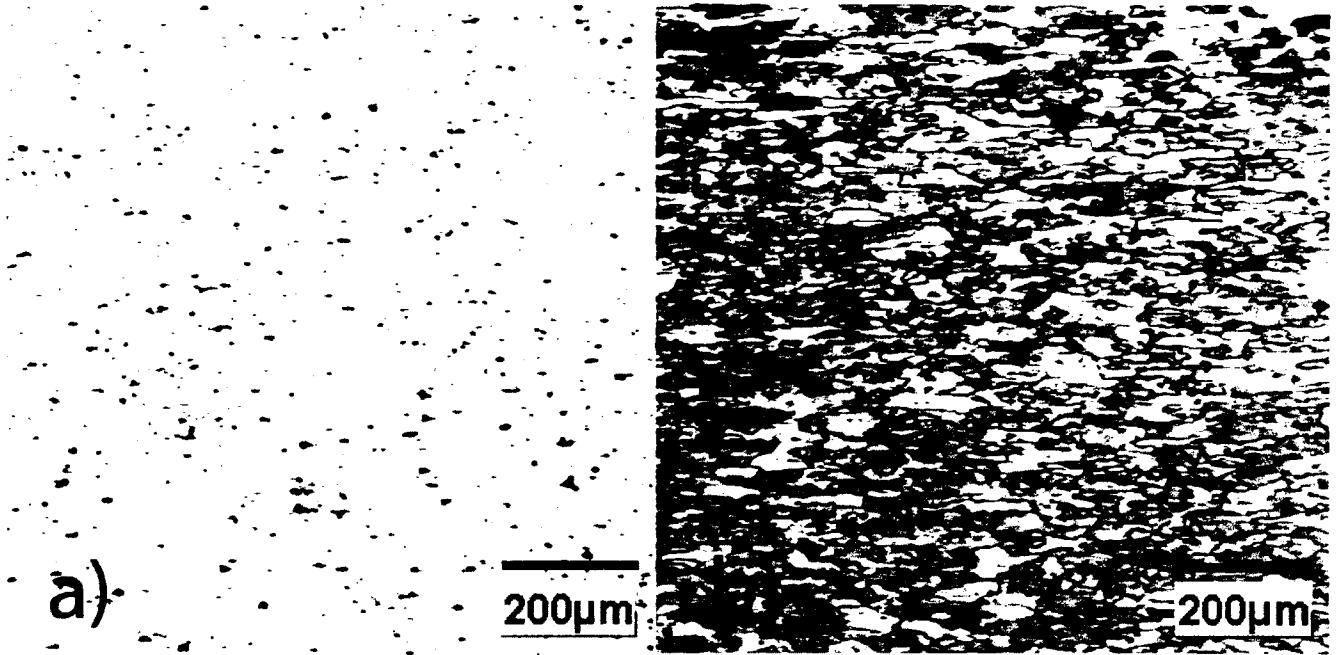


Figure 3.9: a) parent 7075-T6 material, b) parent 2024-T3 material



Figure 3.10: Transition between weld nugget and TMAZ

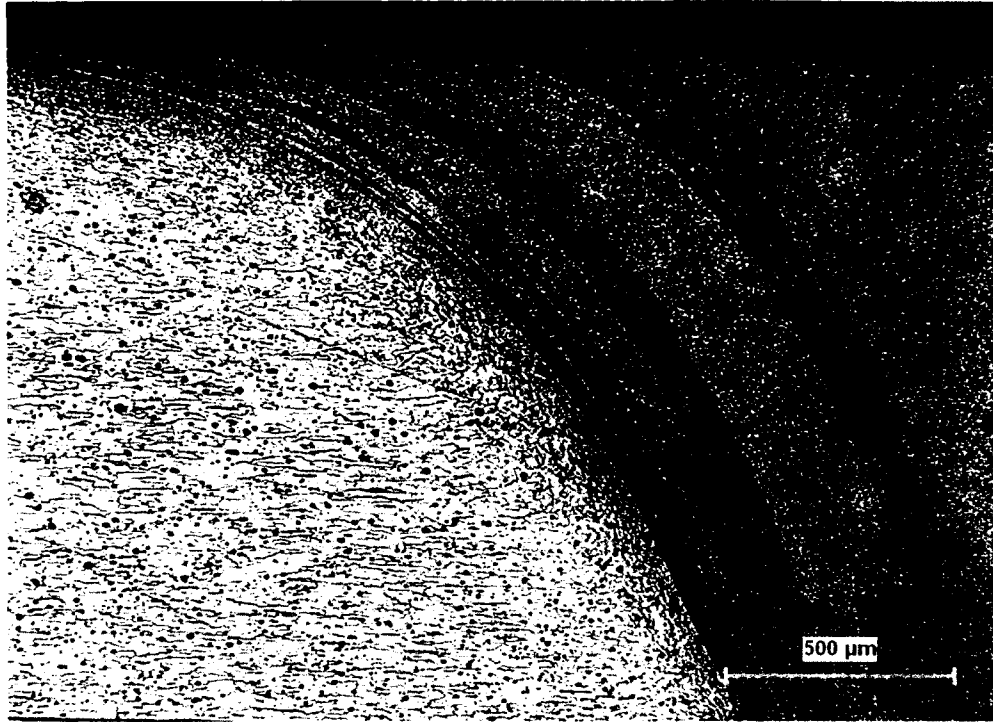


Figure 3.11: Onion ring patterns created by mixing of two alloys, distinct bands of material reveal that the two alloys are not completely mixed with one another

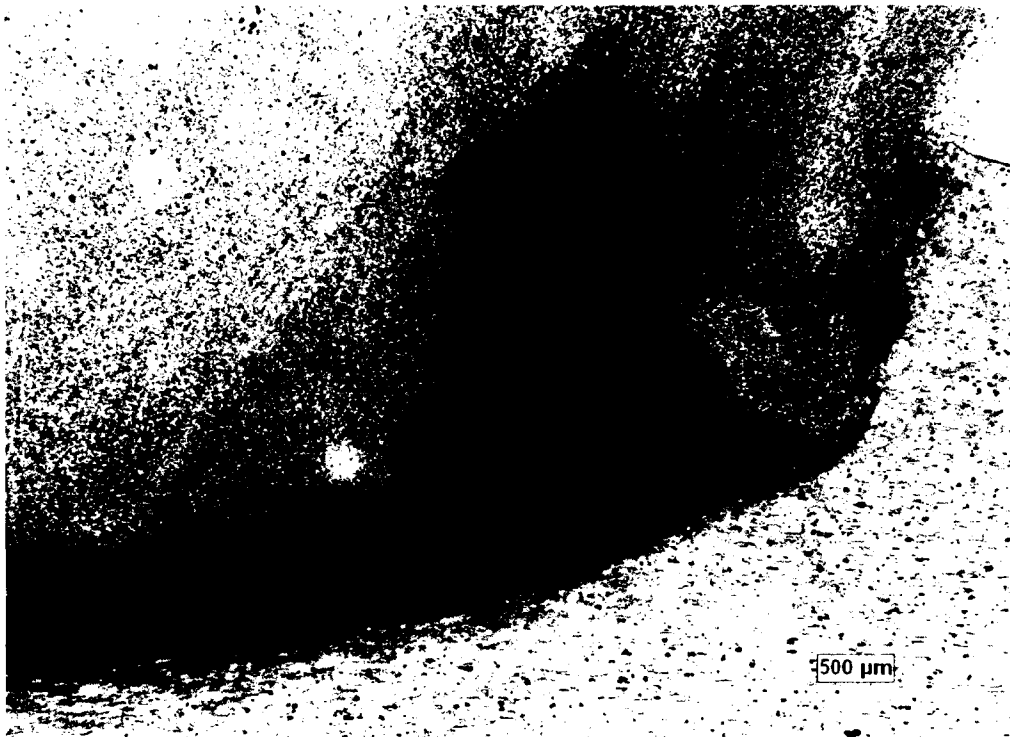


Figure 3.12: Large voids found at edge of weld tool between weld nugget and TMAZ

3.3 Hardness Test

Hammer peening techniques, like laser and shot peening, have been reported to increase the hardness of the peened surface and enhance mechanical properties in FSW but no investigations in the literature assessed the hammer peening effects on the hardness of various regions of the double pass FSW lap joints. Material hardness tests were performed on both sets of test specimens using a Clark CV-800AT Vickers harness tester with 1g force for 10 seconds for each measurement. The hardness profile was taken in the through thickness direction at five locations starting at the weld centerline as shown in Figure 3.13a and in the transverse (x) direction at two depths as shown in Figure 3.13b. The hardness scale used in this experiment is the Vickers scale (HV) where the values are determined by producing pyramid-shaped indents in the material and measuring the diagonal length of the pyramids to determine the hardness of the material.

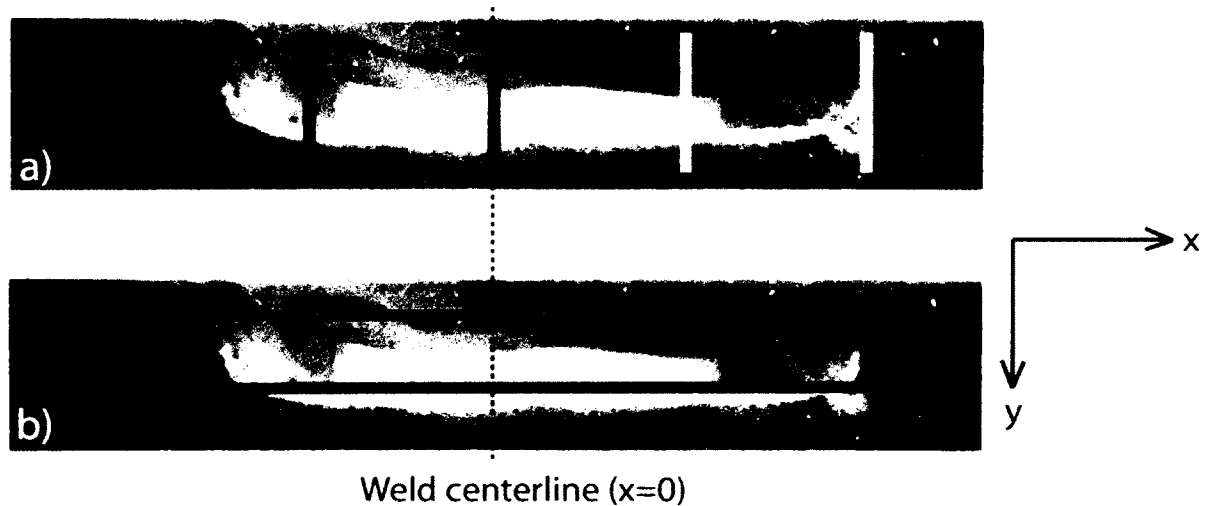


Figure 3.13 a) location of through thickness hardness profiles at various distances from weld centerline, b) location of transverse (x-direction) hardness profiles in stringer (red) and skin (green) sections

The hardness value of the AA 2024-T3 parent material is approximately 135 HV and the hardness of the AA 7075-T6 parent material is 175 HV. Both these values were confirmed to be correct by taking hardness values of the parent materials at several locations on the FSW lap joints. Figure 3.14 is the through thickness hardness profile measured at 5 locations from the weld centerline at an interval of 5 mm each for the as-

welded configuration. The first four points represents the hardness measured in the stringer material and the remaining 6 depths are taken in the skin section. From Figure 3.14, all but one location ($x=-10$ mm) showed values of hardness that was similar to the parent skin material. The explanation as to why the location of $x=-10$ mm has high values of hardness is because this region in the stringer section was not welded and therefore has the same magnitude of hardness as the stringer.

Figure 3.15 is the through thickness hardness profile of the hammer peened specimen. The hammer peening appeared to have increased the hardness values at the top of the specimen. Hardness values at the bottom of the specimen were similar to the as-welded specimen at the same location, which suggests that the hammer peening was not able to penetrate through the entire thickness of the plate and only affected the top 1-1.5 mm of the plate. The hardness values in the stringer increased because the peening essentially work hardened the surface of the material causing more dislocations to form. The more dislocations are present, the harder the material becomes.

The effects of the areas in which the hammer peening has affected the FSW plate is shown in Figure 3.16 which plots the hardness profiles of both as-welded and hammer peened specimen at the location of $x=-10$ mm. At this location both specimens show the same hardness values because in the hammer peened specimen, the hammer does not touch this region.

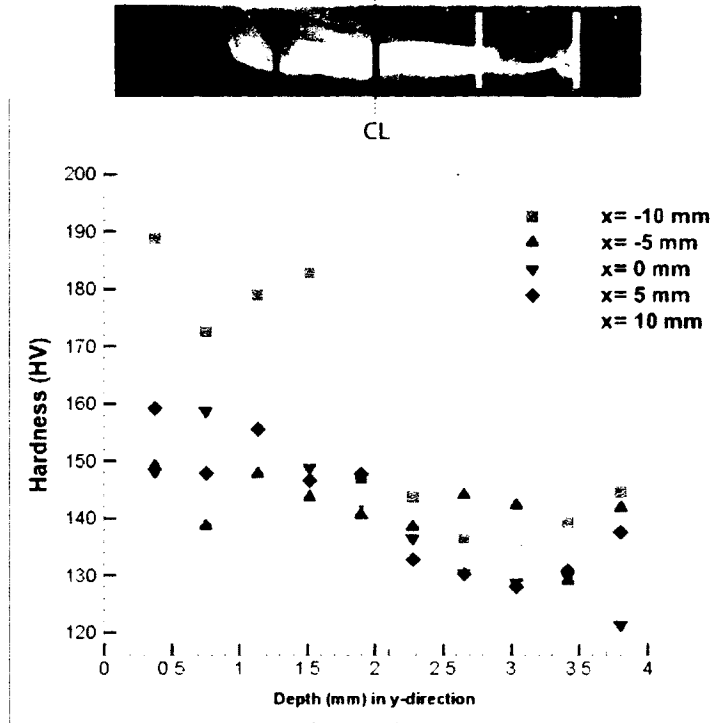


Figure 3.14: Through thickness hardness profiles for as-welded specimen

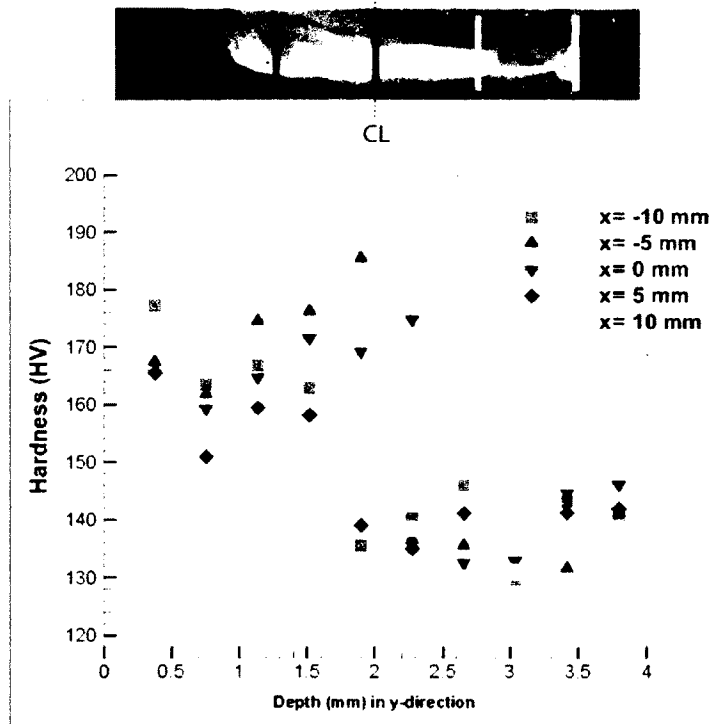


Figure 3.15: Through thickness hardness profiles for hammer peened specimen

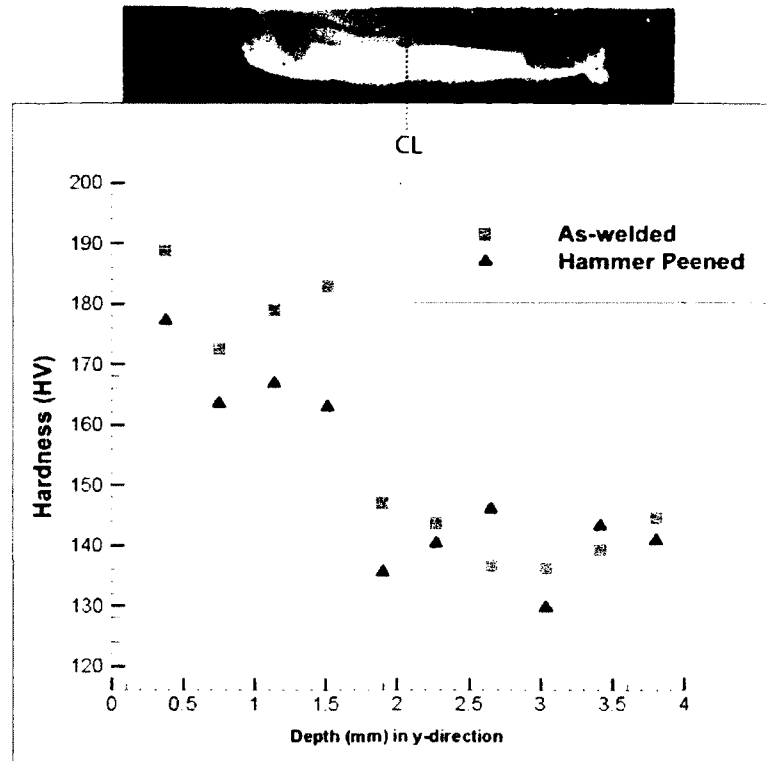


Figure 3.16: Hardness profiles of both specimens at location $x = -10$ mm

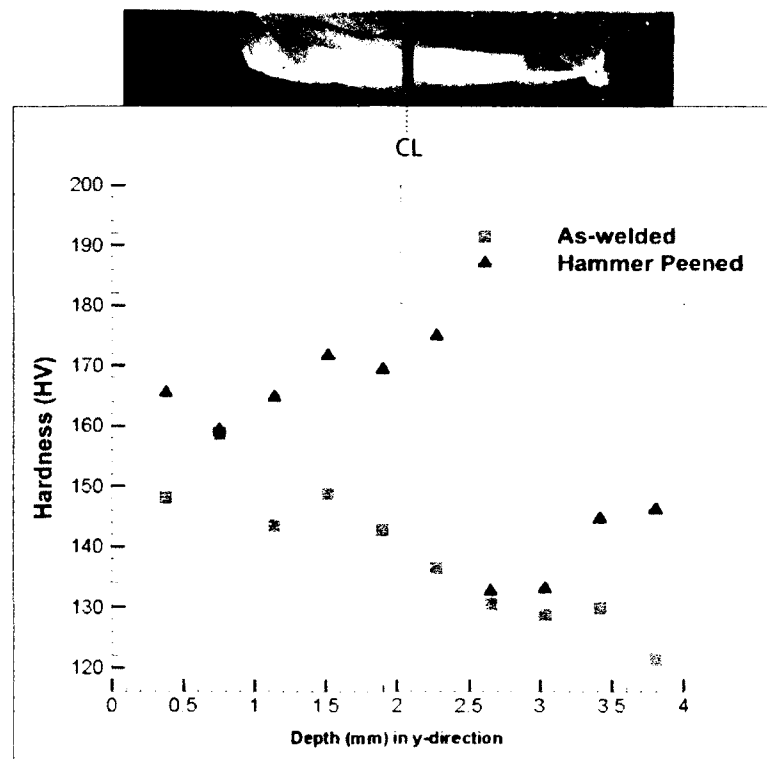


Figure 3.17: Hardness profiles of both specimens at location $x = 0$ mm

Figure 3.17 shows the hardness profile plots at $x=0$ mm where the difference in hardness between the two specimens can be seen more clearly. In the stringer section, the hammer peening appears to have increased the hardness of the material. The hardness values of both specimens in the bottom of the weld are similar to one another since this region is untouched by the weld tool and the tool does not completely penetrate the thickness of the two plates.

The next hardness profile that was measured was in the transverse direction (x -direction) for the two specimens. Figure 3.18 is the transverse hardness profile measured in the as-welded specimen. In the stringer section, the hardness at the edge of the weld zone is similar to that of the parent AA 7075-T6 material and was 175 HV. The hardness drops to 140 HV at the edge of the weld tool and then increases to 143 HV in the middle of the weld. In the skin section, the hardness was much lower due to the softer AA 2024-T3 material. The softest region corresponds to the weld nugget, Hatamleh (2007) and the lowest hardness in the skin section was 116 HV. In both stringer and skin sections, the hardness drops in the vicinity of the welding and is relatively symmetrical about the weld centerline. The aluminum alloy sheets, which were cold rolled, tend to increase the mechanical properties of the produced sheets by increasing the dislocation density. As the grains undergo recrystallization in the weld nugget due to extreme plastic deformation, the strain-induced dislocations will be annihilated, resulting in a decrease in the mechanical properties of the weld. The softening of the material can also be due to the coarsening and dissolution of the strengthening precipitates during the thermal cycles of FSW. The hardness outside the weld zone is similar to the AA 2024-T3 parent material but there is some fluctuation in hardness values due to partial recrystallization, Ali (2002).

The hardness profiles show a softened region at the top portion of the weld was relatively wider than the one on the bottom. This could be due to the specimen heating characteristics during welding. For example, the top region generally exhibits higher temperature compared to the bottom region due to the heating from the tool shoulder, whilst the bottom surface is in contact with the backing plate, which acts as a heat sink, Hatamleh (2007). The lower heat input at the bottom can significantly reduce the extent of metallurgical transformations such as re-precipitation and coarsening of precipitation that takes place during welding. Therefore, the local strength of individual regions across the weld zone is improved. This is seen where the hardness levels at the weld nugget is represented. The average values on the top regions were lower than their values on the bottom regions.

Figure 3.19 is the transverse (x-direction) hardness profile of the hammer peened specimen at the two depths. In the stringer section, the hardness profile was uniform and had an average value of 165 HV. The hammer peening appears to have flattened out and increase the magnitude of the hardness profile in the stringer section. The increase in the hardness in the stringer section is explained by the work hardening effects caused by the extreme plastic deformation of the peening process, any softening of the material from the weld tool is hardened again by the peening process. In the skin section, the hardness profile reflected that of the skin's hardness which was approximately 130 HV. The hardness decreased to the lowest value of 123 HV at the weld centerline. The highest recorded hardness value in the skin section is at the HAZ located approximately 10 mm from weld centerline. The higher hardness values in the region can be explained by the increase in hardness of the stringer due to the bending of the AA 7075-T6 plate to form the s-shape stringer. Work hardening of the stringer is similar to the effects of bending a metal paper clip to straighten it out. The drop in hardness in the weld region suggests the mixing of the AA 2024-T3 up into the AA 7075-T6 plate. When looking at the transverse (x-direction) hardness profile in the skin section, away from the weld region, the values reflect that of the parent AA 2024-T3 material. Again, the profile across the skins is symmetrical.

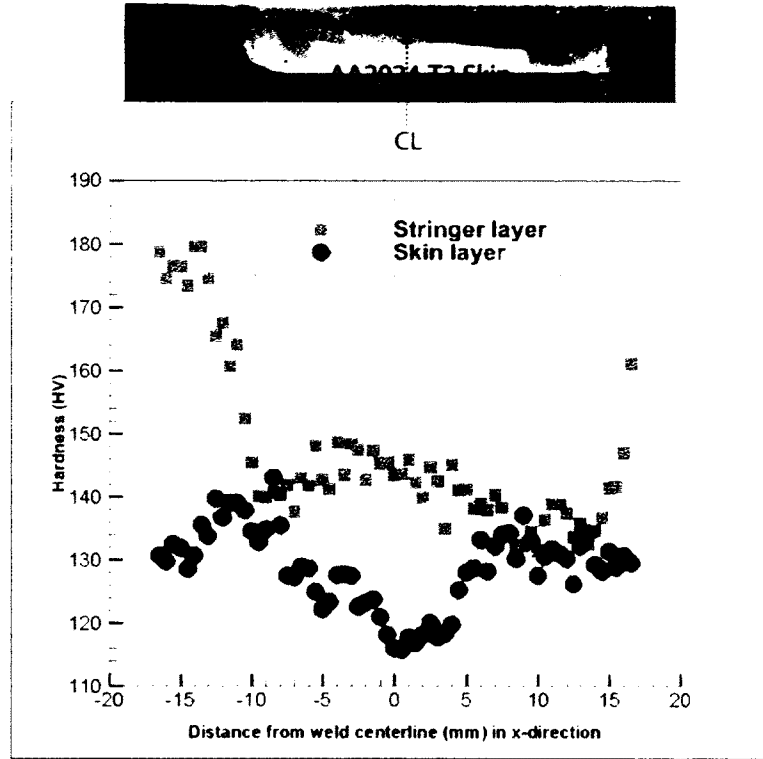


Figure 3.18: Transverse (x-direction) hardness profiles of as-welded specimen

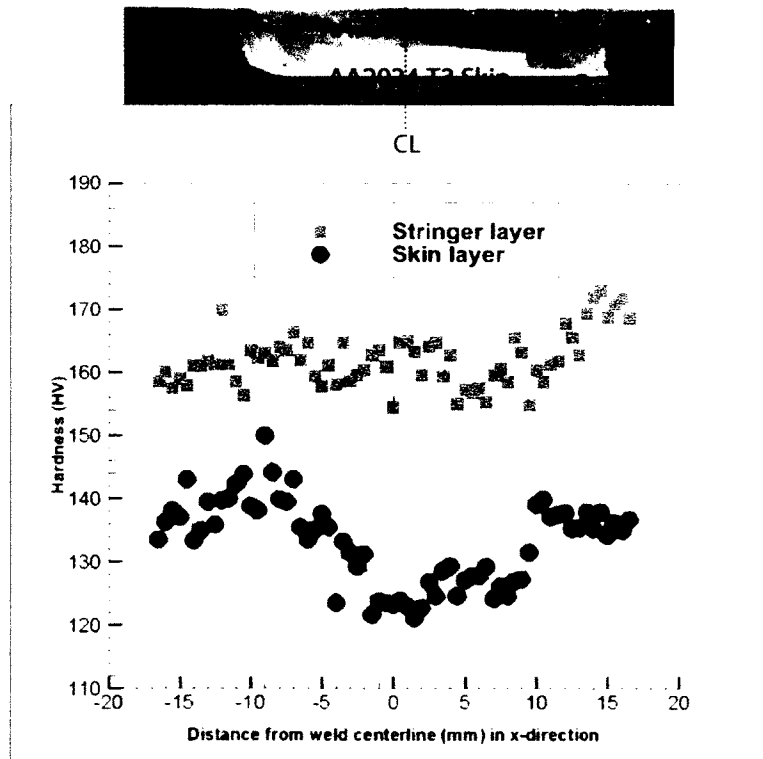


Figure 3.19: Transverse (x-direction) hardness profiles of hammer peened specimen

A comparison of the two transverse (x-direction) hardness profiles in the stringer section of both material (Figure 3.20) illustrates the change in hardness before and after hammer peening. Peening the surface caused the material to become work hardened which is reflected in the increase in hardness of the material to almost the same values as the unwelded parent material. Figure 3.21 shows the hardness profiles in the skin section for both specimens. Since the effects of the hammer peening was not able to penetrate the entire surface of the lap joint, the hardness values in the skin section were almost identical to one another.

The hardness profile measured in the as-welded and hammer peened specimens will be examined in relations to the residual stresses and fatigue failure location of the FSW lap joints in the following chapter in order to determine if there is any correlation between the residual stresses, hardness values of the specimen and where the specimens are most likely to fail at.

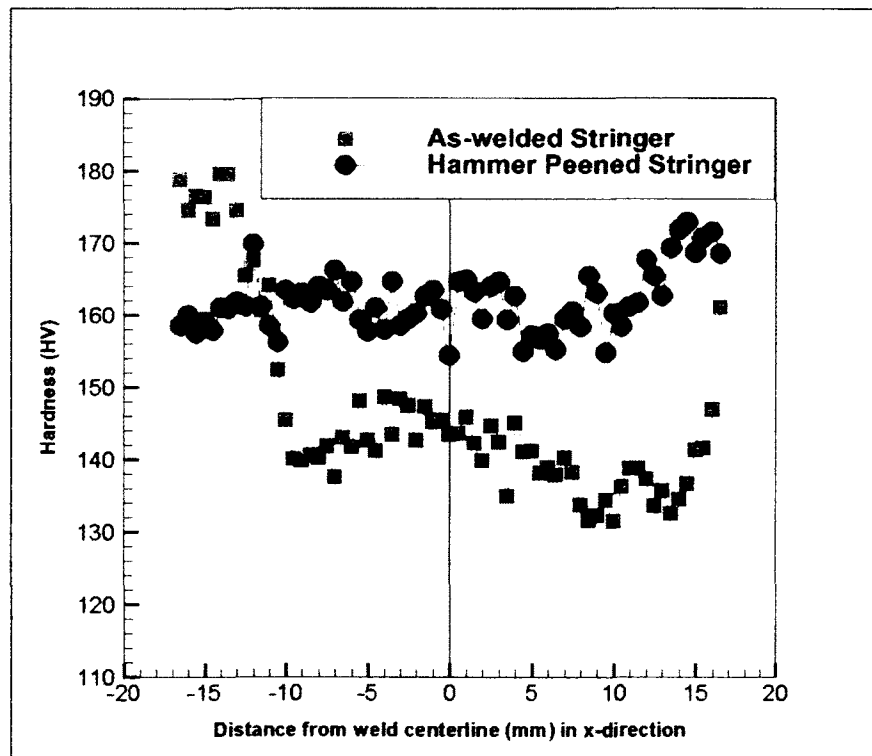


Figure 3.20: Transverse (x-direction) hardness profiles of both specimen in stringer section

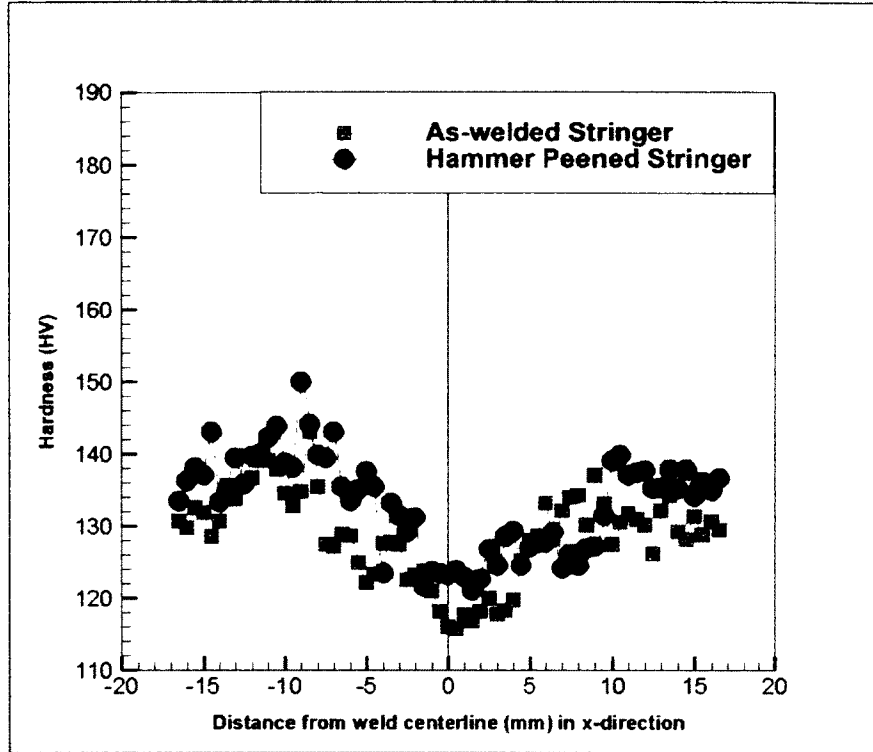


Figure 3.21: Transverse (x-direction) hardness profiles of both specimens in skin section

Chapter 4

EXPERIMENTAL PROCEDURES

4.1 Crack Compliance Method

4.1.1 Validation Calculations

Before applying the theories of the crack compliance method to determine the residual stress profile of the FSW lap joints, the procedures of the crack compliance method had to be first verified. Using the compliance theory of Chapter 2, three different validation calculations were performed.

4.1.1.1 Prime Beam Bending Experiment

The purpose of the first validation calculation was to determine if the crack compliance method could be used to reproduce the residual stress profile from a previous residual stress experiment. Reproduction of the residual stress profile using the compliance method will demonstrate that the finite element model and MATLAB algorithm used in the crack compliance method is correct. The validation was based on a sample file provided by Prime at the Los Alamos National Laboratories in New Mexico, Prime (2004). In this experiment, a stainless steel beam with a cross section of 30 mm x 10 mm was bent in a 4-point bending fixture. Prime used the crack compliance method to evaluate the residual stress profile through the thickness of the beam. Strain gauges with gauge lengths of 1.57 mm were placed on the top and bottom surfaces of the beam as shown in Figure 4.1. A wire EDM with a width of 0.27 mm was used to produce the incremental slits while the strains at every 0.813 mm slit intervals were recorded for a total of 28 strain readings. Figure 4.2 shows the measured bottom strain data from this experiment.

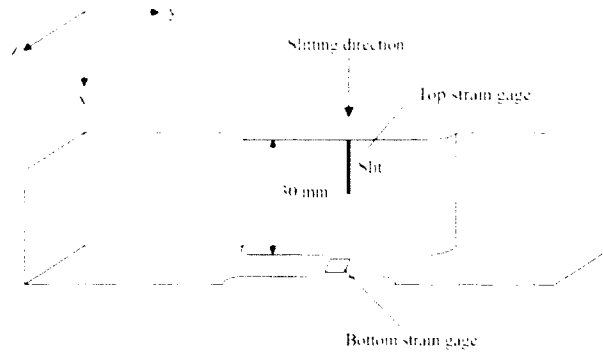


Figure 4.1: Strain gauge position for beam bending experiment [Prime (2009)]

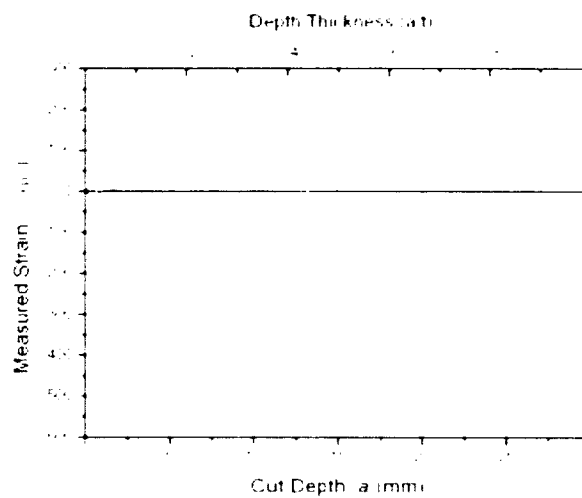


Figure 4.2: Measured bottom strain from beam bending experiment [Prime (2009)]

Finite Element Modeling

To reproduce the residual stress profile from the experiment, a 2D FE model of the beam was required. Half of the beam was modeled using a numerical software called ABAQUS CAE with dimensions and parameters identical to the model in Prime's experiment. Each step consisted of an element removal of 0.813 mm to simulate a slit increment. The end nodes of the gauge length were selected and assigned to a set called GNODE. A user-defined load distribution was applied to the slit face at every slitting interval based on various orders of Legendre polynomials and an input file was created. A total of 28 input files were created to correspond with the 28 strain measurements obtained. To run the FE model, ABAQUS COMMAND was used, 10 simulations were

carried out for each input file (one simulation for each load) for a total of 280 simulations. Each simulation required the selection of an input file and a user-defined load distribution. The simulation output to the results into an output database file. To get the strain measurements, a report file was created to display the displacement of the set GNODE. From the report files, individual values of the compliance matrix was calculated by subtracting the left node displacement with the right node displacement and then dividing by the total gauge length (1.57 mm) at each slit depth. The top and bottom compliance functions are shown in Figures 4.3 and 4.4 respectively, where $Lp1$ represents the compliances for the load based on the second order Legendre polynomial, $Lp2$ represents the compliances for the load based on the third order, etc.

Once the compliances were calculated, Figure 4.5 shows the flow chart of the parameters that are inputs of the MATLAB algorithm and are used to inversely solve for the residual stress. Both the measured strain data and calculated compliance matrices are input into the algorithm. The algorithm allows for the selection of number of compliance functions used to fit the measured strains and produce the resulting stress. Also, the number of gauges used in the least squares fit can be specified. For example, if two gauges are used in the experiment, then the number of cuts to be used from each gauge needs to be defined. If one gauge is specified then all strain data and compliances will be taken from that one strain gauge position. In this experiment, two strain gauges were used (top and bottom gauges). This meant that for a total slit increment of 30, the first 5 slits had the

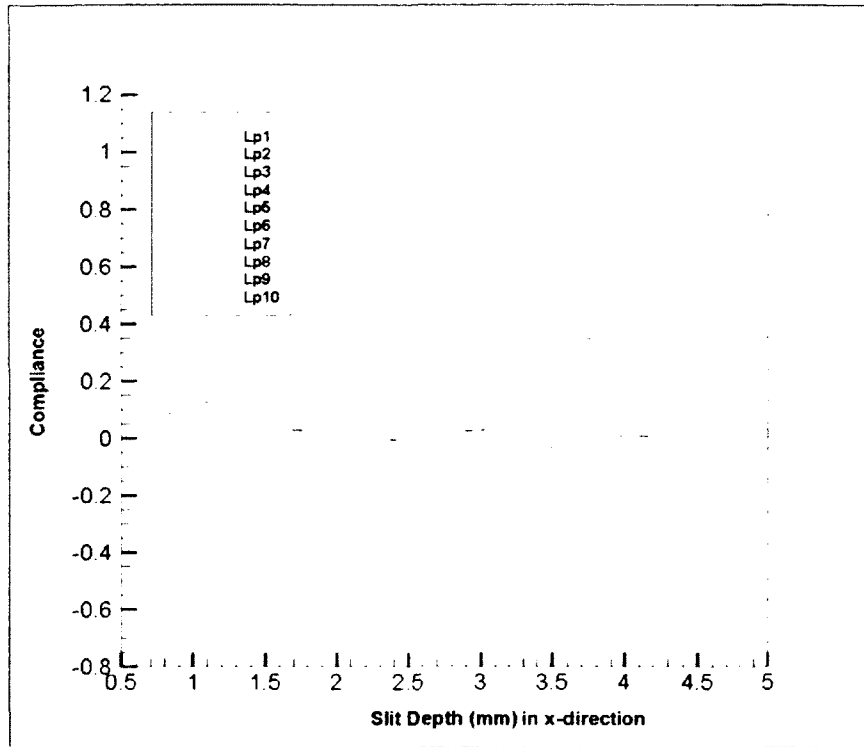


Figure 4.3: Compliance matrix from top gauge of beam bending experiment

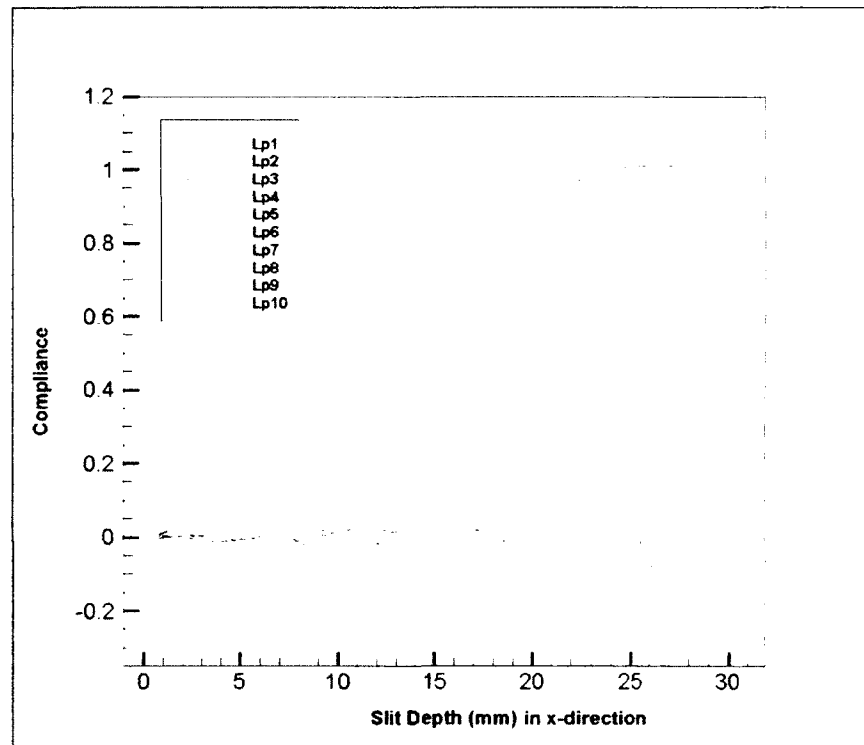


Figure 4.4: Compliance matrix from bottom gauge of beam bending experiment

corresponding compliances and strain data taken from the top gauge position while the remaining 25 slits had the compliances and strain data taken from the bottom strain gauge position. The reason for selecting the first 5 strain readings to be taken from the top gauge position is that the top gauge is able to record more sensitive strain readings for slits near the top surface. Another reason for choosing only the first 5 slit increments is because the strain readings from the top gauge began to level off after the 7th reading. Once all parameters are set in the algorithm, the residual stresses (σ_y) are calculated based on the compliance equations in Chapter 2. All calculations in MATLAB are performed using double precision.

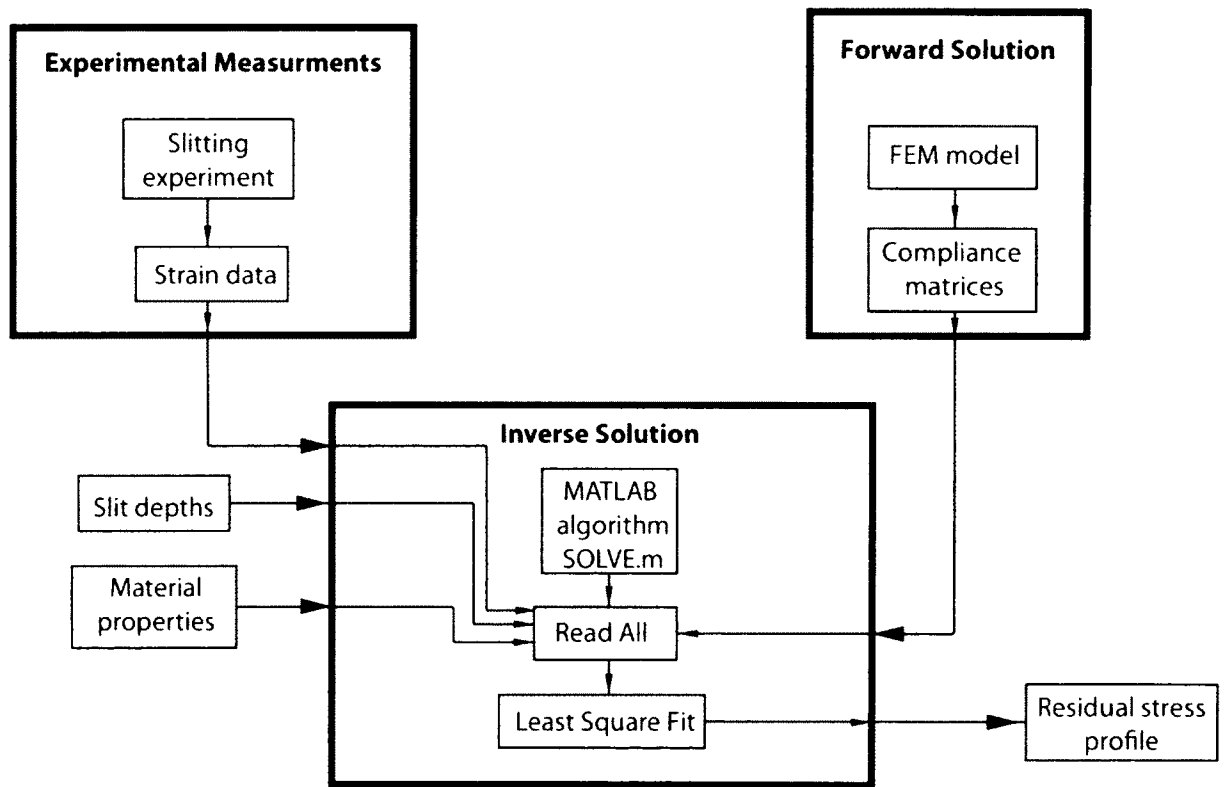


Figure 4.5: Flow chart of crack compliance method and MATLAB algorithm

Results

Using the calculated compliance matrices, the variation in residual stress (σ_y) was determined. The results of the two calculated stresses are summarized in Table 4.1 with three decimal places since the stress result provided by Prime used three decimal places. The results of the residual stress in this experiment are almost identical to the established results with a maximum difference of 0.01 %. The reproduction of the residual stress profile for the beam bending experiment was successful which demonstrate that the FEM model and MATLAB algorithm used in the crack compliance method was verified to be correct.

Slit Depth (mm)	Stress from Prime [14] (MPa)	Stress of CCM (MPa)
0.81	-114.087	-114.099
1.63	-88.031	-88.029
2.44	-69.511	-69.507
3.25	-54.976	-54.973
4.06	-40.319	-40.318

Table 4.1: Calculated residual stresses compared with Prime residual stress

4.1.1.2 M.T. Milan AA 2024-T3 FSW Butt Joint Experiment

The purpose of the second validation calculation was to compare the results of residual stresses calculated from the compliance method with a different analytical method. Milan et. al. (2007) determined the residual stress profile for an AA 2024-T3 FSW butt joint in both the x-direction (longitudinal), and y-direction (transverse) using a linear elastic fracture mechanics (LEFM) approach based on stress intensity factors and weight functions. The verification calculation was performed on the transverse test piece to

determine the variation in longitudinal (σ_x) residual stress across the weld because that particular longitudinal strain data was provided by the author of the paper. The 60 x 120 x 3.2 mm plate was FSW by EMBRAER but the welding parameters were not disclosed. The slitting was performed perpendicular to the weld centerline and a single strain gauge was attached to the bottom edge of the plate so that it would align with the slit as shown in Figure 4.6. Slitting was performed in 0.5 mm increments and the strains at the bottom gauge position were recorded. The strain data was combined with the geometry dependent influence function to calculate the residual stress intensity factor at every slit depth. The variation in residual stress (σ_x) was inversely calculated based on the residual stress intensity factors and weight function for this particular rectangular geometry.

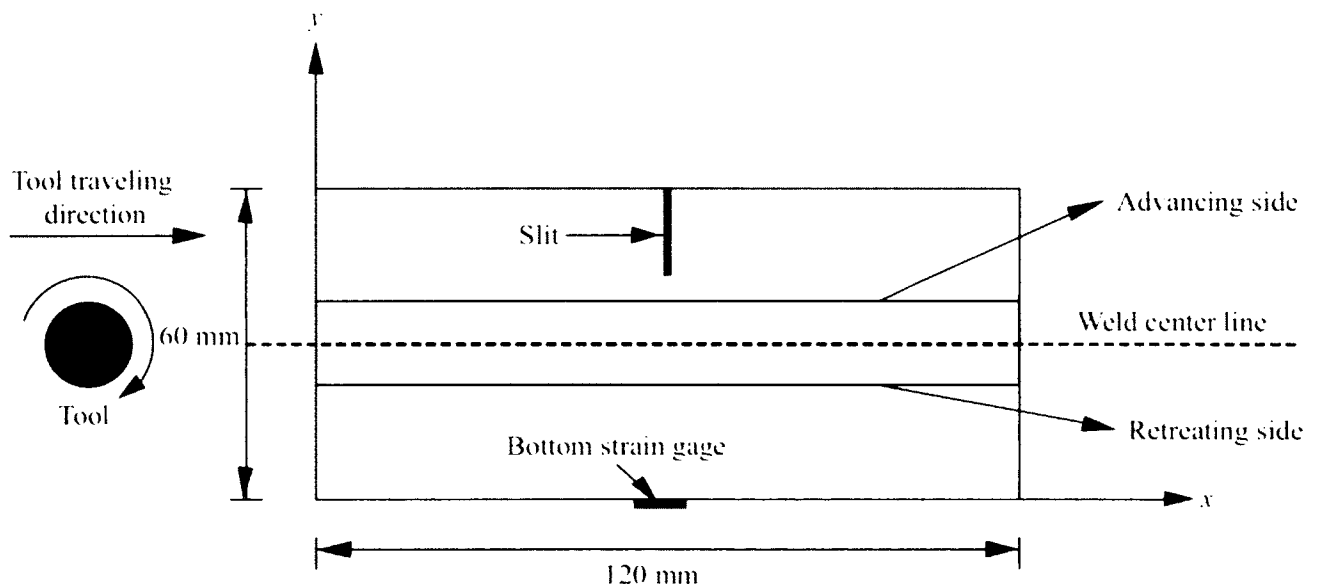


Figure 4.6: Transverse test piece for measuring longitudinal residual stresses (σ_x) [M.T. Milan (2007)]

Finite Element Modeling

To obtain the compliance functions for the bottom edge gauge, a 2D FE model of the plate had to be developed. Only half the aluminum plate was modeled in ABAQUS CAE using quadrilateral, plane-strain elements as shown in Figure 4.7. Elements of size 0.50 x 0.20 mm were removed to simulate material removal due to slitting. Load distributions based on Legendre polynomials were applied to the crack face at each slit depth and displacements in the x-direction were recorded. The AA 2024-T3 plate had a Young's modulus of 70 GPa and Poisson's ratio of 0.3. Figure 4.8 shows the calculated compliance functions for the bottom edge gauge.

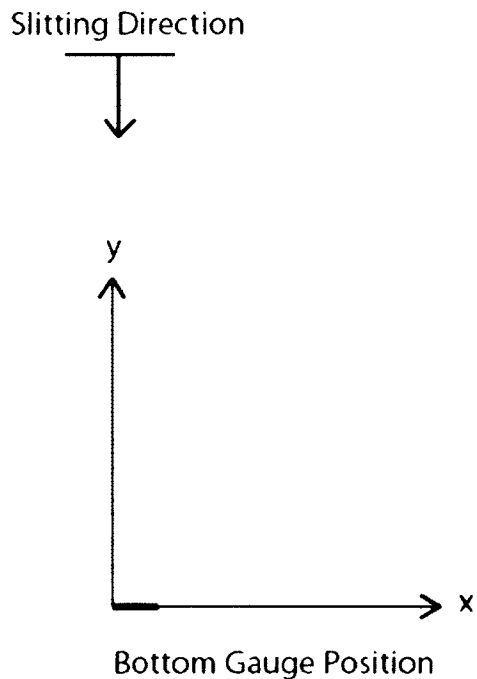


Figure 4.7: 2D FE model of FSW butt-welded plate

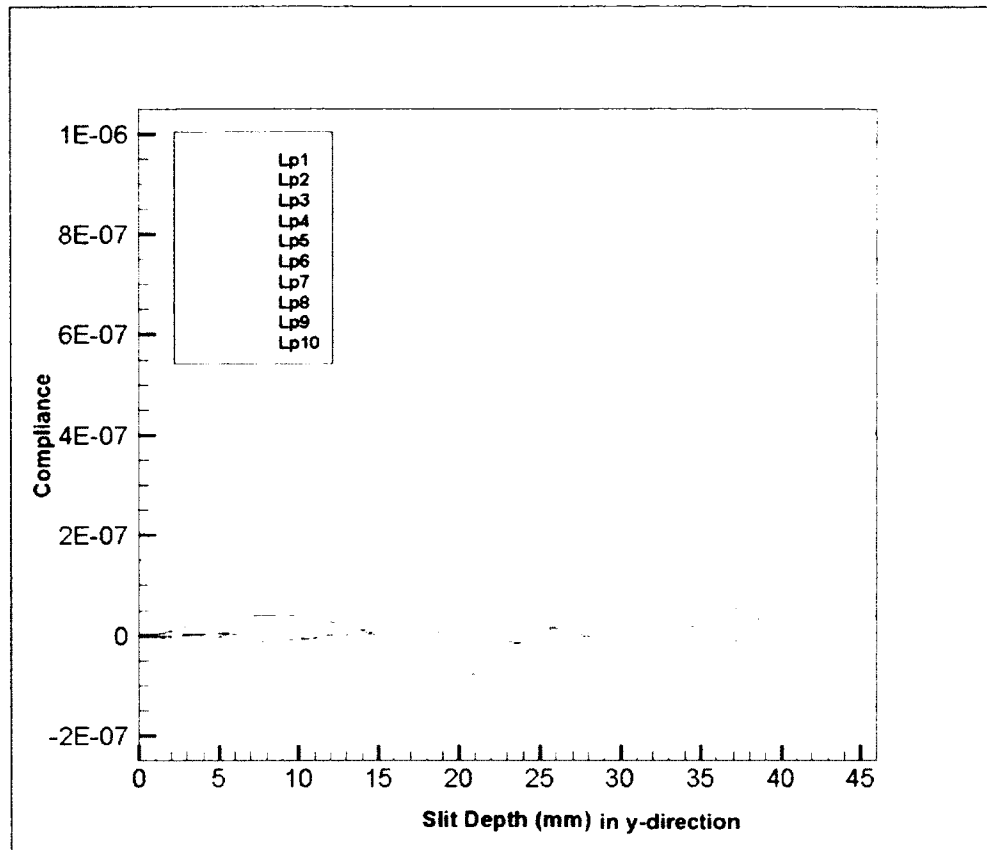


Figure 4.8: Compliance functions from bottom edge strain gauge

Results

The compliance matrix, strain data, and slit depths were all inputs of the MATLAB algorithm, SOLVE2.m that was used to determine the variation in residual stress (σ_x). The stress results were plotted against the stresses determined by the LEFM approach and compared in Figure 4.9. The stress profiles agree very close with one another. The maximum tensile stress using the compliance method was 200 MPa, located on the advancing side of the weld. The maximum compressive stress from the compliance method was approximately -120 MPa located 5 to 10 mm from the edge of the plate. Table 4.2 shows the comparison of maximum compressive and tensile stress for both methods. The residual stress profile calculated from the compliance method has a smooth distribution because of the least squares fitting technique used to interpolate the polynomials. The crack compliance results show that the advancing side has a higher

tensile stress than the retreating side, which agrees with previously published papers, Altenkirch et al. (2008) and Dalle et al. (2001). The weld zone contains mainly tensile stresses while the parent material further away contains mostly compressive stresses. Typically, for FSW aluminum alloys, the residual stress profile at the weld has been found to have an “M” shape profile with the maximum tensile stress occurring just beyond the edge of the weld tool shoulder and the compressive balance stress far from the weld line. In this experiment, the crack compliance method had been able to generate a residual stress profile with the same characteristic “M” shape profile for the FSW butt joint configuration.

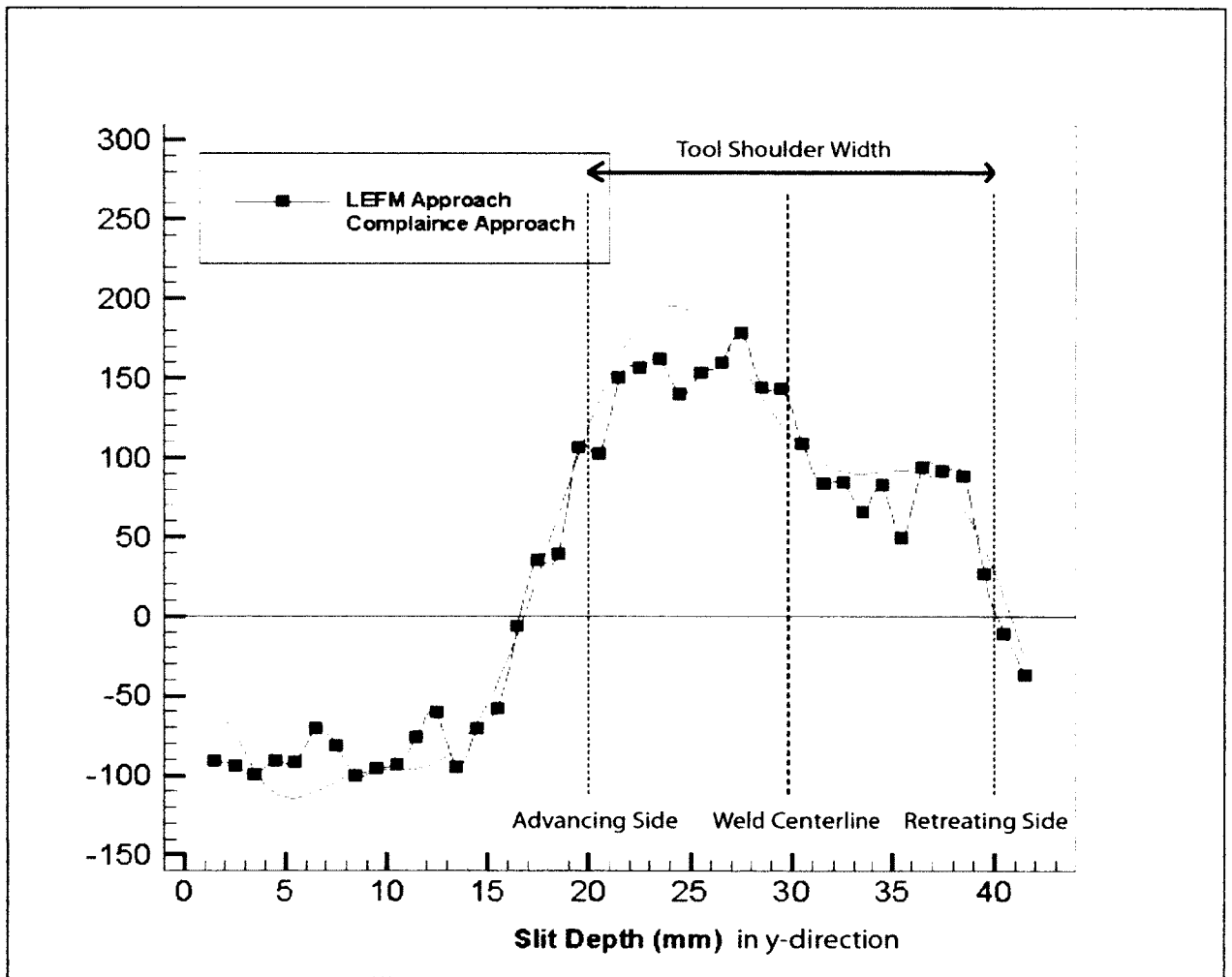


Figure 4.9: Comparison of Residual stress from LEFM and crack compliance method

The stress profile is slightly asymmetric in the transverse direction reflecting the somewhat asymmetric nature of the FSW process. It is important to note that there is a large variance in stress at the top of surface of the plate due to insensitivity and cumulative errors from strain gauge readings taken from the back surface. To get a more accurate result, multiple strain gauges could have been used. One strain gauge placed at the top to improve sensitivity in strain reading close to the top surface where the bottom strain gauge might not be able to detect properly. The crack compliance stress profile is very similar to that from the LEFM technique and therefore the compliance method is proven successfully verified.

	LEFM (M.T. Milan)	CCM	Percent Difference (%)
Maximum Compressive Stress (MPa)	-100	-120	20
Maximum Tensile Stress (MPa)	220	200	9.1

Table 4.2: Comparison of maximum compressive and tensile stresses

4.1.1.3 NRC Butt Welded AA 2024-T3 Experiment

The purpose of the third preliminary verification experiment was to perform all aspects of the crack compliance method (experimental slitting, FEM model, and analytical calculations) on a panel of FSW AA 2024-T3 aluminum alloy welded in the butt joint configuration to determine the residual stress profile across the weld zone. Dubuorg et. al. (2007) has determined the residual stress profile for this aluminum plate. In the paper, a finite element model using the LS-DYNA software was created to predict the thermal cycles and induced stresses that were present during the FSW process. The residual stresses were then determined by using a combination of the temperature distribution from a thermal FE model and a mechanical FE model. The results of the residual stress (σ_x) from the FE model was compared with a non-destructive evaluation technique using neutron diffraction on the advancing side of the weld and shown in Figure 4.10.

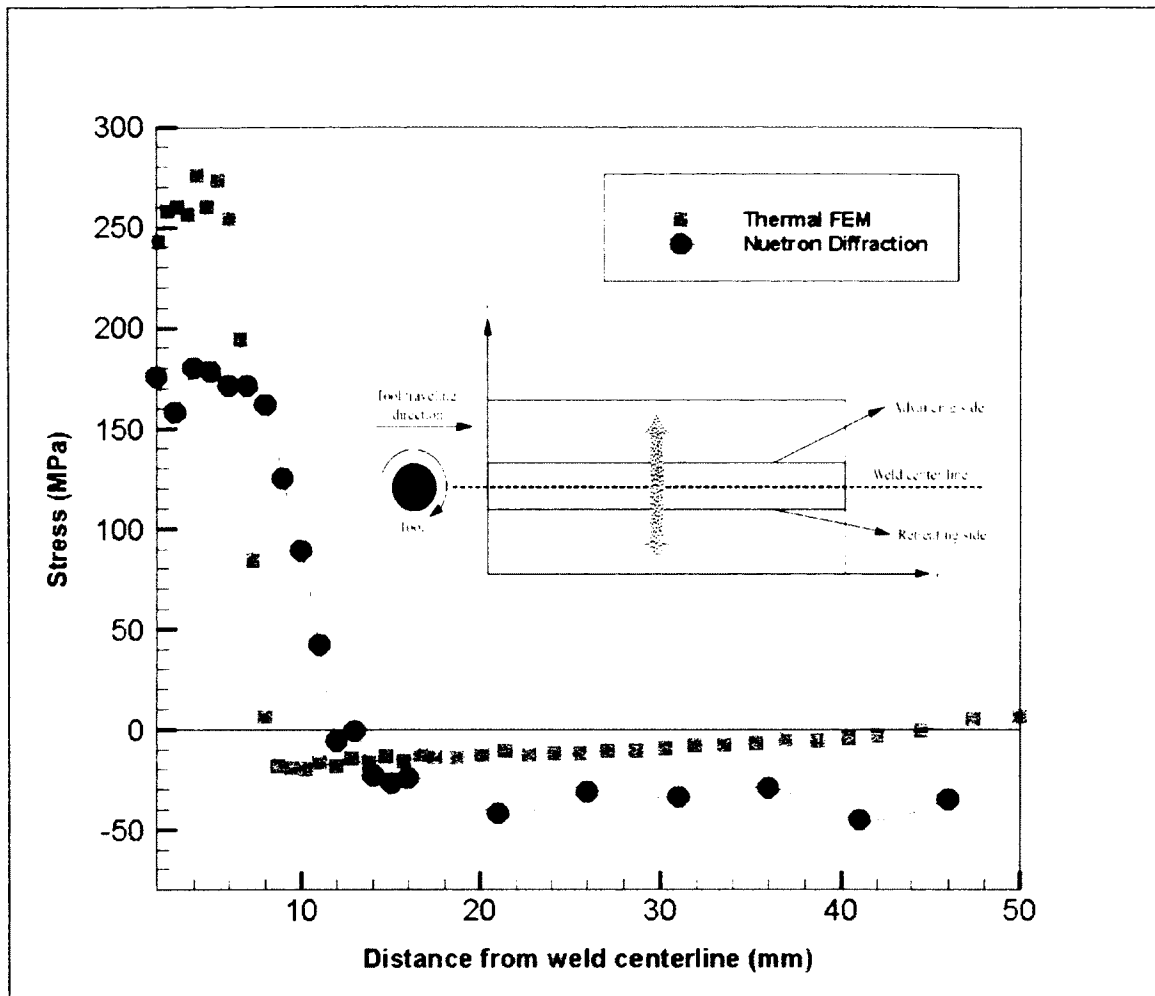


Figure 4.10: Advancing side residual stress profile (σ_x) [Dubuorg et al. (2007)]

The variation in residual stress (σ_x) across the weld was determined using the crack compliance method and compared with the thermal FE model and neutron diffraction results.

Experimental Procedure

The slitting experiment was performed on the same piece of aluminum that had been tested by neutron diffraction as shown in Figure 4.11a). The plate was cut into a smaller test coupon with dimensions of 60 x 120 x 3.4 mm (Figure 4.11b). Several general purpose, uniaxial strain gauges were placed along the slitting line. Three single gauges

with a gauge length of 3.18 mm were placed at the top followed by a strip gauge with 10, 1.53 mm gauges on the retreating side of the weld. Another three strain gauges were placed on the advancing side of the weld as shown in Figure 4.11c). A strip gauge was placed on the left hand side of the slit line and was aligned with the strip gauge on the right. Slitting was performed using an EDM wire cutter at the National Research Council. Strains were recorded for each strain gauges every 1 mm interval for a total of 90 intervals. A total of 20 strain gauges were used in this experiment. For simplicity, only strain readings from gauges 4 and 13 were plotted in Figure 4.12. It is important to note that the strains gauges on the right and left side of the slitting line had similar magnitudes of strains at every slit depth.

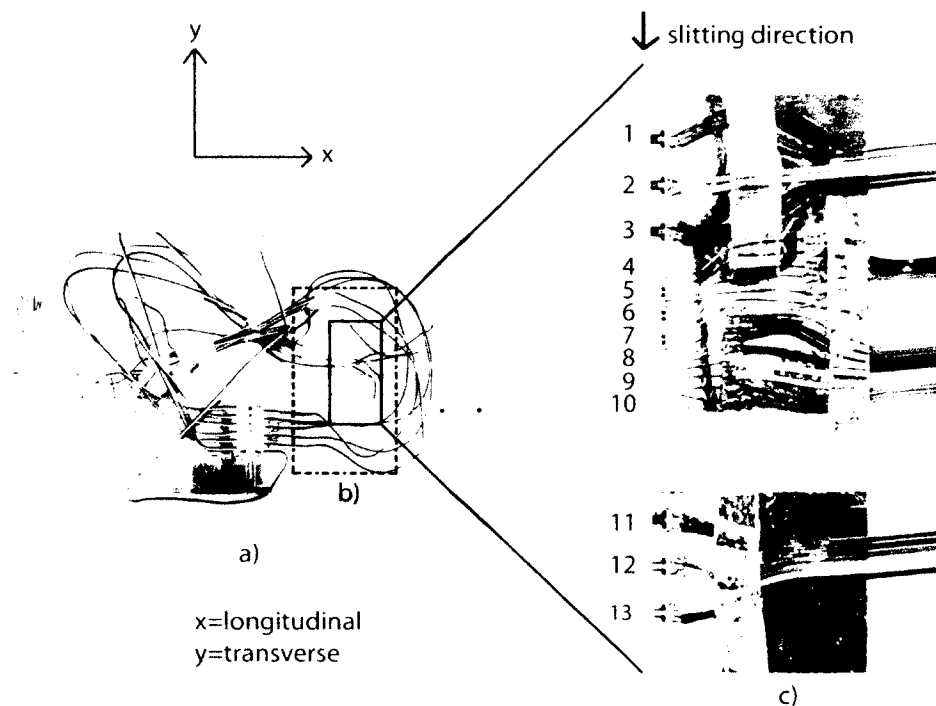


Figure 4.11: a) NRC FSW plate b) MBI test piece to measure variation in longitudinal stress (x-direction) across weld (y-direction) on retreating side with c) strain gauge positioning

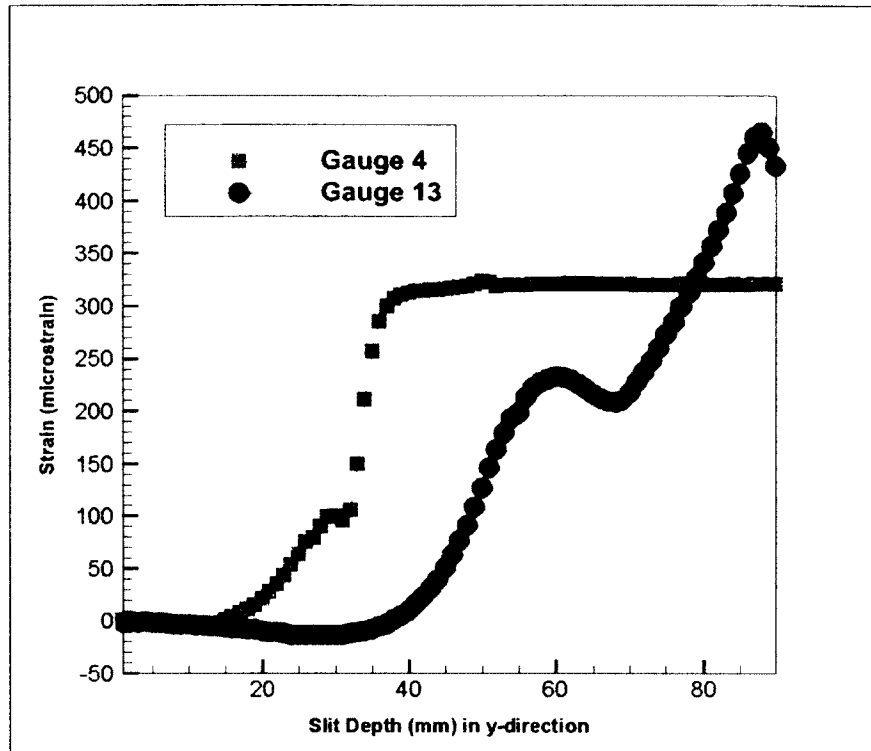


Figure 4.12: Slitting experiments strain measurement from gauges 4 and 13

Finite Element Modeling

It was possible to realistically simulate the slitting procedure by sequentially removing elements in the finite element model. The FSW plate was modeled as a two dimensional, linearly elastic model using ABAQUS CAE. Only half of the plate was modeled due to symmetry in the plate geometry. 13,000, 8 node quadrilateral elements were used in the model. The mesh was refined in the vicinity of the slit and the strain gauges as shown in Figure 4.13. Elements of dimension 1 x 0.18 mm were removed to simulate the material removal by wire EDM. The FE model simulates a square-bottomed slit while in the actual wire EDM, the slit has a semicircular bottom. However, the difference in these two geometries is negligible when dealing with long narrow slits, Prime (2002). Each slit was divided into a single step in the simulation where each step was further divided into 10 iterations. The iterations represented the various load distributions having the basis function of the Legendre polynomials. For every step and iteration, the displacement at the gauge's end nodes was recorded. There was a total of 13 compliance matrices

generated for this experiment based on the 13 different strain gauge positions. Figure 4.14 is the compliance functions plotted for strain gauge location 4 and Figure 4.15 is the compliance functions plotted for strain gauge location 13.

Results

The selection process for the number of polynomials used to fit the measured strain to produce the most accurate residual stress profile will be discussed. It is important to note that the measured strain is defined as the strains measured from slitting experiments using the strain gauges while the fitted strains are calculated using the compliance functions and measured strain values via the least squared fit technique. Figure 4.15 shows a set of 10 compliance functions that was calculated for a single gauge position. Conventionally, all 10 compliance functions are used to fit the measured strain data. Using different number of compliance functions will give different corresponding fitted strains. For example, Figure 4.16 shows the plot of the measured strains from EDM cutting at gauge position 13 as well as the fitted strain using only one order polynomial (2nd order). The 2nd order compliance function was not able to match the measured strain accurately. Figure 4.17 shows the plot of measured strain from gauge position 13 and the fitted strain using 5 orders of polynomials (2nd order to 6th order), the fitted strain agrees better with the measured strain values. When the number of polynomials used in the fit is increased to 10, the fitted strain is able to match the measured strain almost identically as shown in Figure 4.18. In conclusion, increasing the number of polynomials used will increase the accuracy of the fitted strain when compared with the original measured strain values. A quantitative proof of this observation is explained in the following section with the help of the root mean square error.

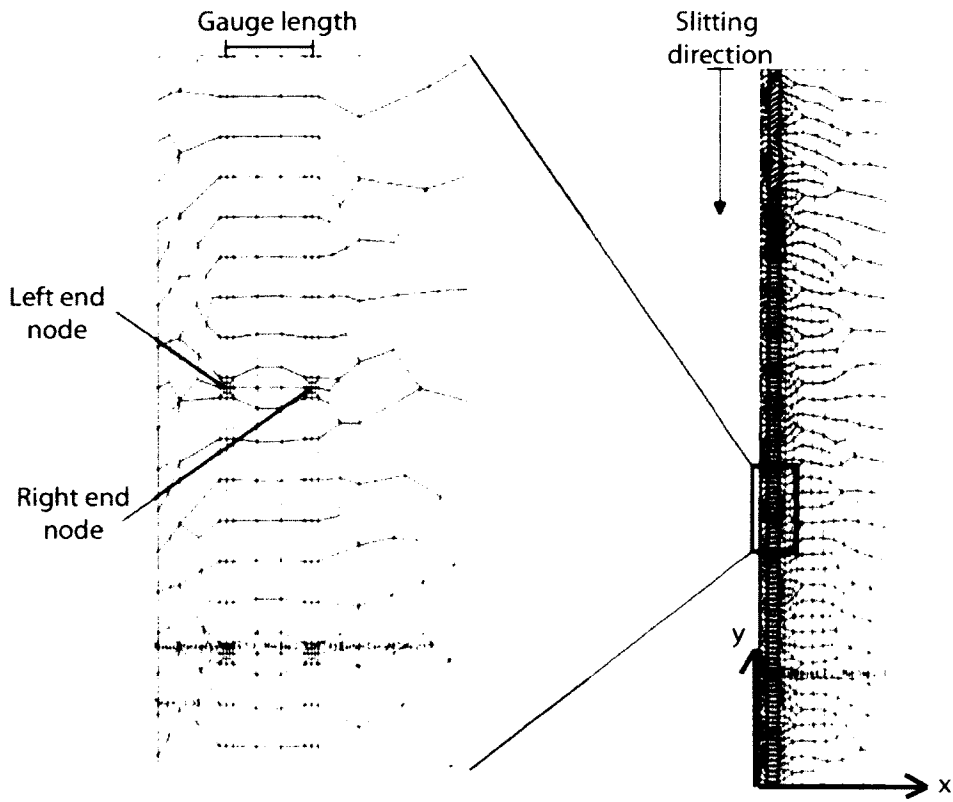


Figure 4.13: 2D FEM model of FSW butt joint plate

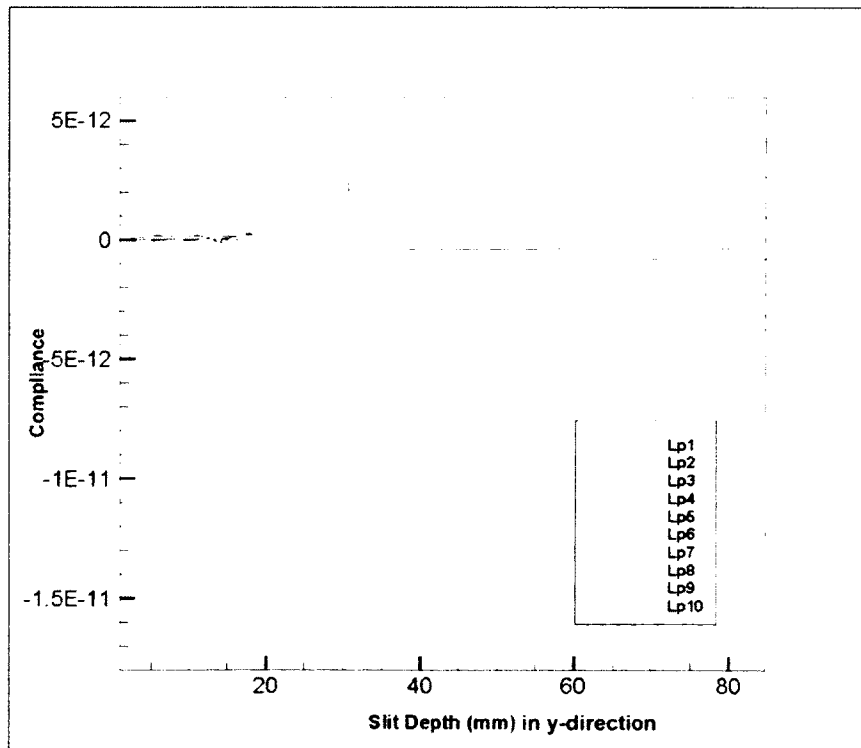


Figure 4.14: Compliance functions for strain gauge location 4

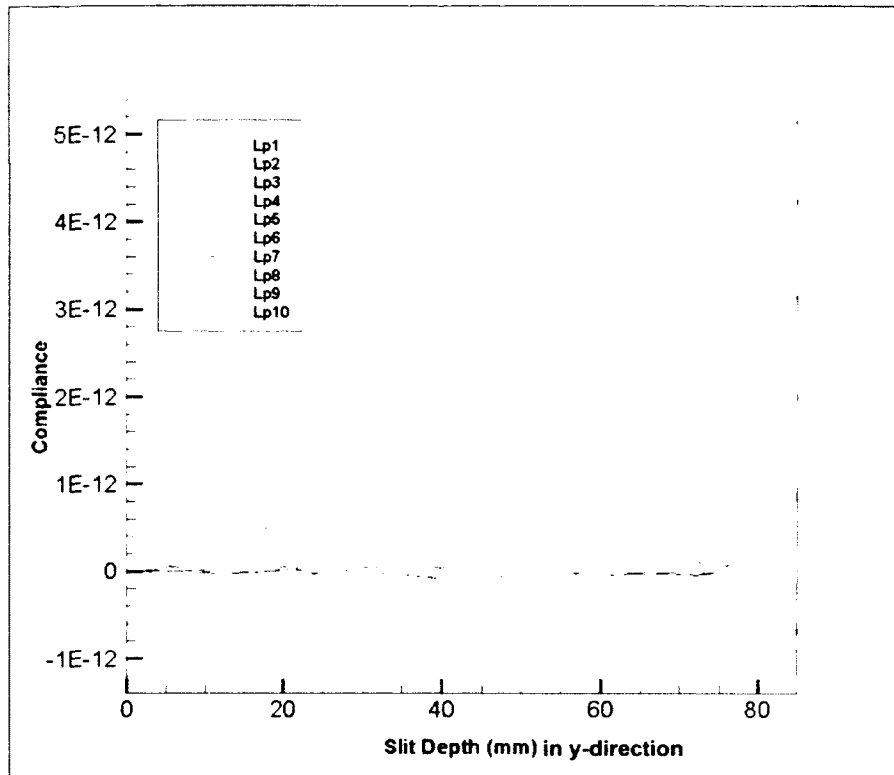


Figure 4.15: Compliance functions for strain gauge location 13

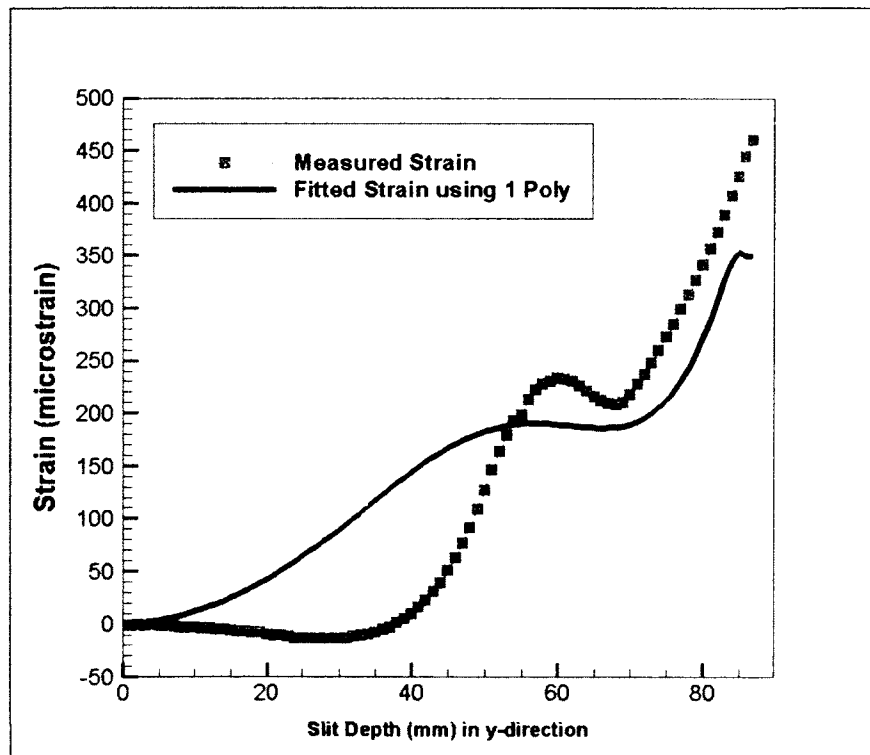


Figure 4.16: Measured strain vs. fitted strain using 1 order polynomials

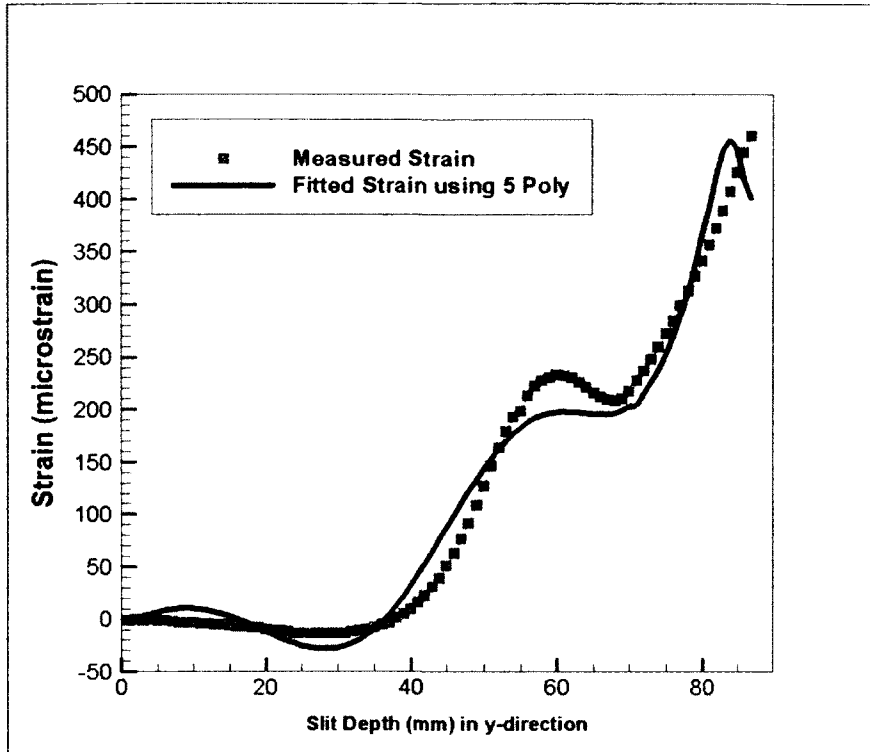


Figure 4.17: Measured strain vs. fitted strain using 5 order polynomials

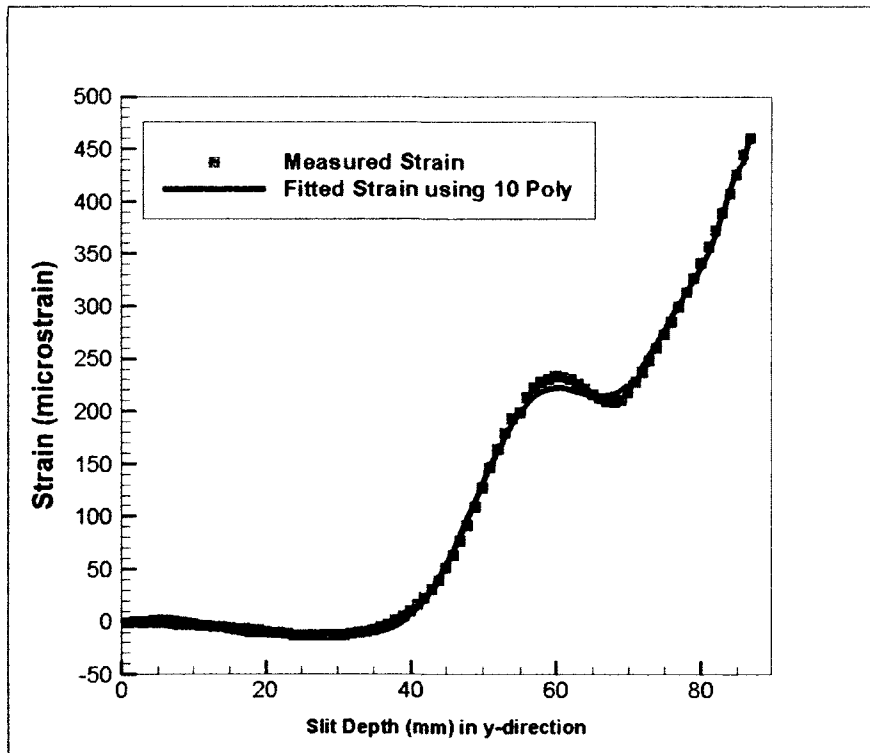


Figure 4.18: Measured strain vs. fitted strain using 10 order polynomials

In terms of the root mean square errors described in section 2.6, increasing the order of polynomials for strain fitting reduced the RMS error. However, the RMS levels off to a single value when the order of polynomials used was around the 9th and 10th order. The trends using various numbers of orders of polynomials are shown in Table 4.3. Using one polynomial to fit the strain will give a RMS error of approximately 72 microstrains between the two strain curves. Increasing the order to 10 reduced the RMS to approximately 5.10 microstrains. Therefore, the method of selecting the order of polynomials was chosen such that the RMS error was minimized. Conventionally, 10 orders of polynomials are sufficient to reproduce the residual stress profile in any given experiment, Prime (2006) and increasing the order of polynomials from 10 to 14 did not reduce the RMS error so it was not necessary to use higher order above 10.

Order of polynomials	Root mean square error
1	72.24
2	45.84
3	34.97
4	23.09
5	22.99
6	13.56
7	7.35
8	6.31
9	5.07
10	5.10

Table 4.3: RMS values for strain fitting of gauge 13 using different number of polynomials

From the various fitted strains from Figures 4.16 to 4.18, the variation in residual stress (σ_x) were calculated and plotted in Figure 4.19. It can be seen that using the fitted strain based on one order polynomial, a residual stress profile was produced that looked like a

curved line, this result is not every accurate and does not represent the actual stress profile very well. The residual stress profile changes as the fitted strain using more polynomials are used. For this experiment, all 10 orders of polynomials are used to fit the strain and calculate the residual stress profile. Figure 4.20 shows the residual stress profile (σ_x) calculated from using 9 orders vs. 10 orders; the two residual stress profiles are almost identical.

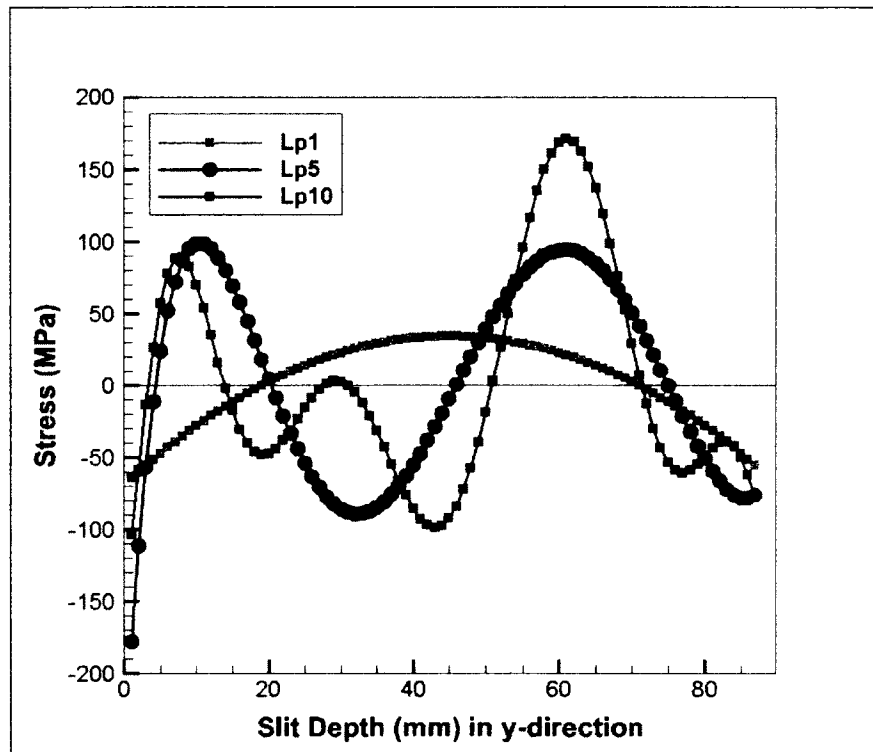


Figure 4.19: Variation in residual stress (σ_x) using different order of polynomials in fitting of strain

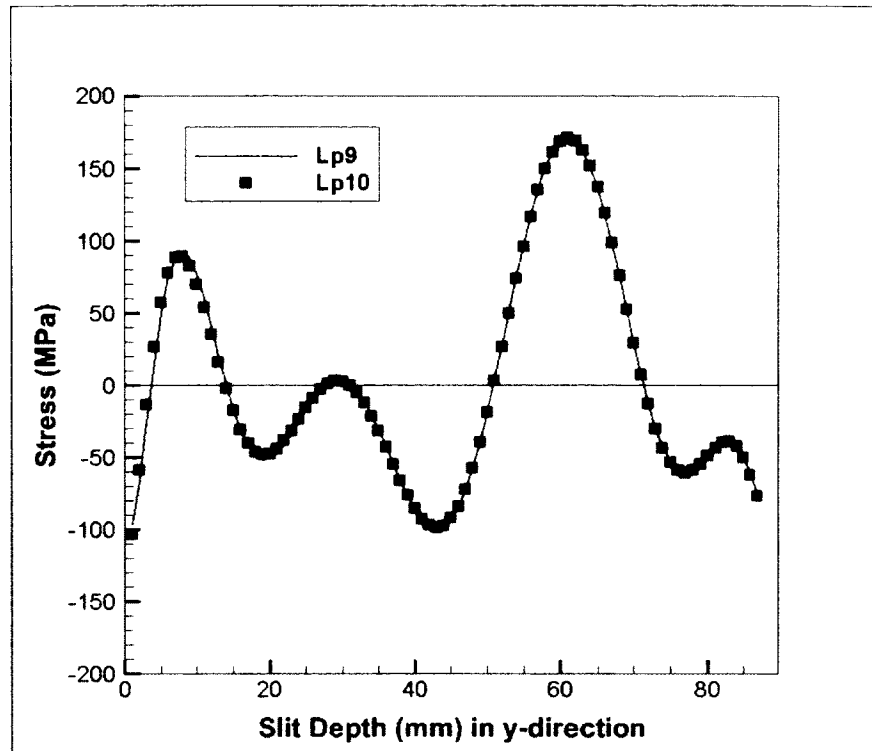


Figure 4.20: Variation in residual stress (σ_x) from gauge 13 using 9 order and 10 order polynomials

The residual stress profile from the crack compliance method is plotted and compared with the stress from earlier neutron testing and thermal FEM modeling and is shown in Figure 4.21. Near the weld centerline, the results of the crack compliance method agree well with the neutron diffraction results, with a maximum tensile stress of 178 MPa at the weld centerline, further away from the weld centerline the residual stress profile produce two peak stresses at $x= 30$ mm and 15 mm from the edge of the plate. The advancing side of the weld shows that the stresses are very low and level off further away from the weld zone since the welding tool does not affect this area (un-welded). It is assumed that the same position on the opposite side of the weld should exhibit the same low magnitudes of residual stress, which is not the case as shown from the stress profile calculated by the crack compliance method. An explanation for this is that strains were measured from gauge 13, which is located on the advancing side of the weld. Strains measured far away from this gauge, i.e. at $x= 15$ mm would not be accurate since it is too far from the gauge to accurately measured the strains. As the slit moves closer to the strain gauge 13, the strains values increase and also the accuracy of the measured strain increase, that is why the residual stress values agrees well with the neutron method near the gauge 13 location.

To obtain a more accurate residual stress distribution far from the weld centerline, a second gauge located at position 4 (20 mm from the edge) can be used to increase sensitivity of strains measured near the edge of the plate. The following is a parametric study of using two strain gauges and varying the contribution of each gauge to study the effects on the resulting residual stress profile. Firstly, if only one strain gauge (gauge 13) was used, the variation in stress (σ_x) would be that shown in Figure 4.21. Figure 4.22 shows the change in residual stress when different number of strains from gauge 4 is used at the surface and then switches to gauge 13 for the bottom section. Figure 4.23 is a plot of the stress distribution (σ_x) for the first 40 mm with various numbers of strains taken from gauge 4. Figure 4.23 show that the beginning of the stress profile (σ_x) converges when 20-25 strains were taken from the gauge 4. When 30 and 35 strains were taken, the stress profile diverges again. It was determined that using 20 strain measurements from gauge 4 and then switching to the rest of the strain measurement from gauge 13 for the 87 slit depths results in the best residual stress profile. Increasing strains measurement from gauge 4 will give error in the results since after 30 slits increments; the strains from gauge 4 levels off and is no longer able to detect any changes in strains past this depth.

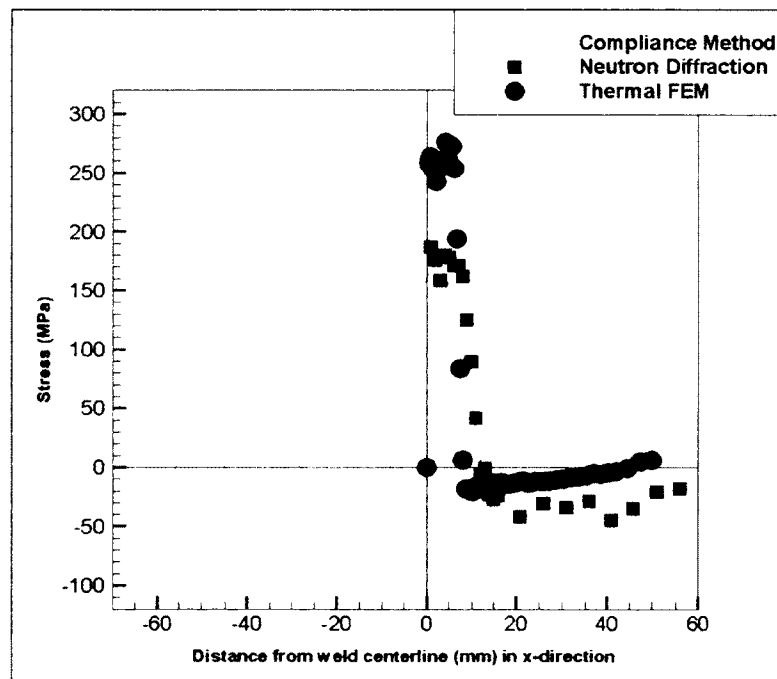


Figure 4.21: Comparison of residual stress from gauge 13 with previous neutron results [Dubuorg et al. (2007)]

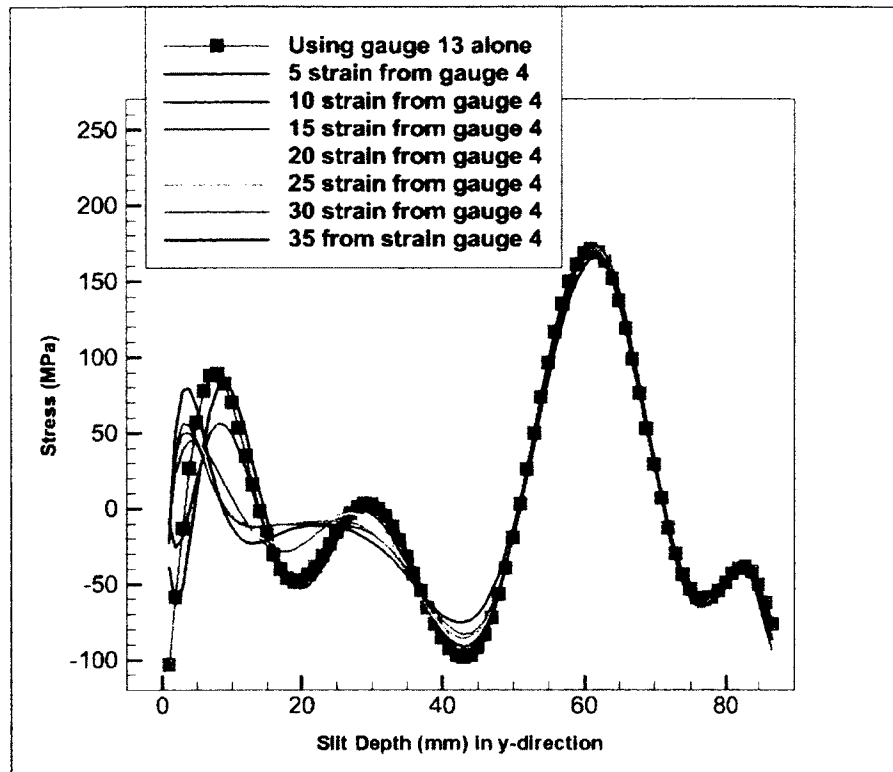


Figure 4.22: Variation in stress (σ_x) using different number of strain values from gauge 4

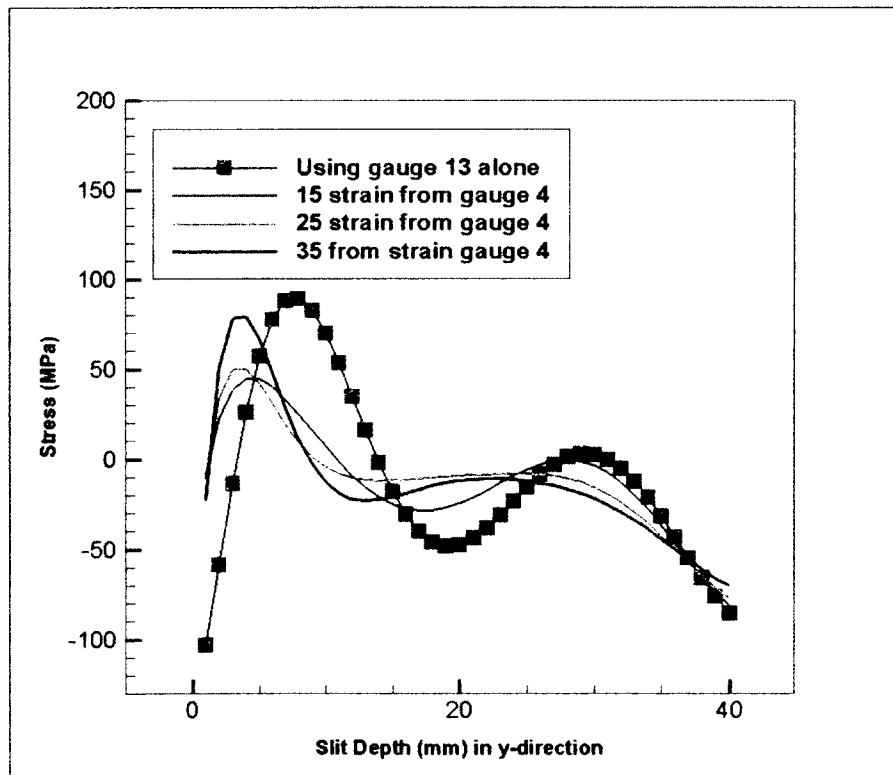


Figure 4.23: Variation in stress (σ_x) using 15, 25 and 35 strains from gauge 4

Figure 4.24 illustrates the change in stress distribution (σ_x) when using a combination of gauges 4 and 13 compared to just using strains from gauge 13. The second gauge closer to the top surface helps smooth out the stress distribution and increase sensitivity to strains recorded near the top surface. Therefore, it is concluded that using two gauges will help increase accuracy of the residual stress profile. The final residual stress profile using a combination of gauges 4 and 13 and by 10 orders of polynomials are plotted with the thermal FEM and neutron diffraction results in Figure 4.25.

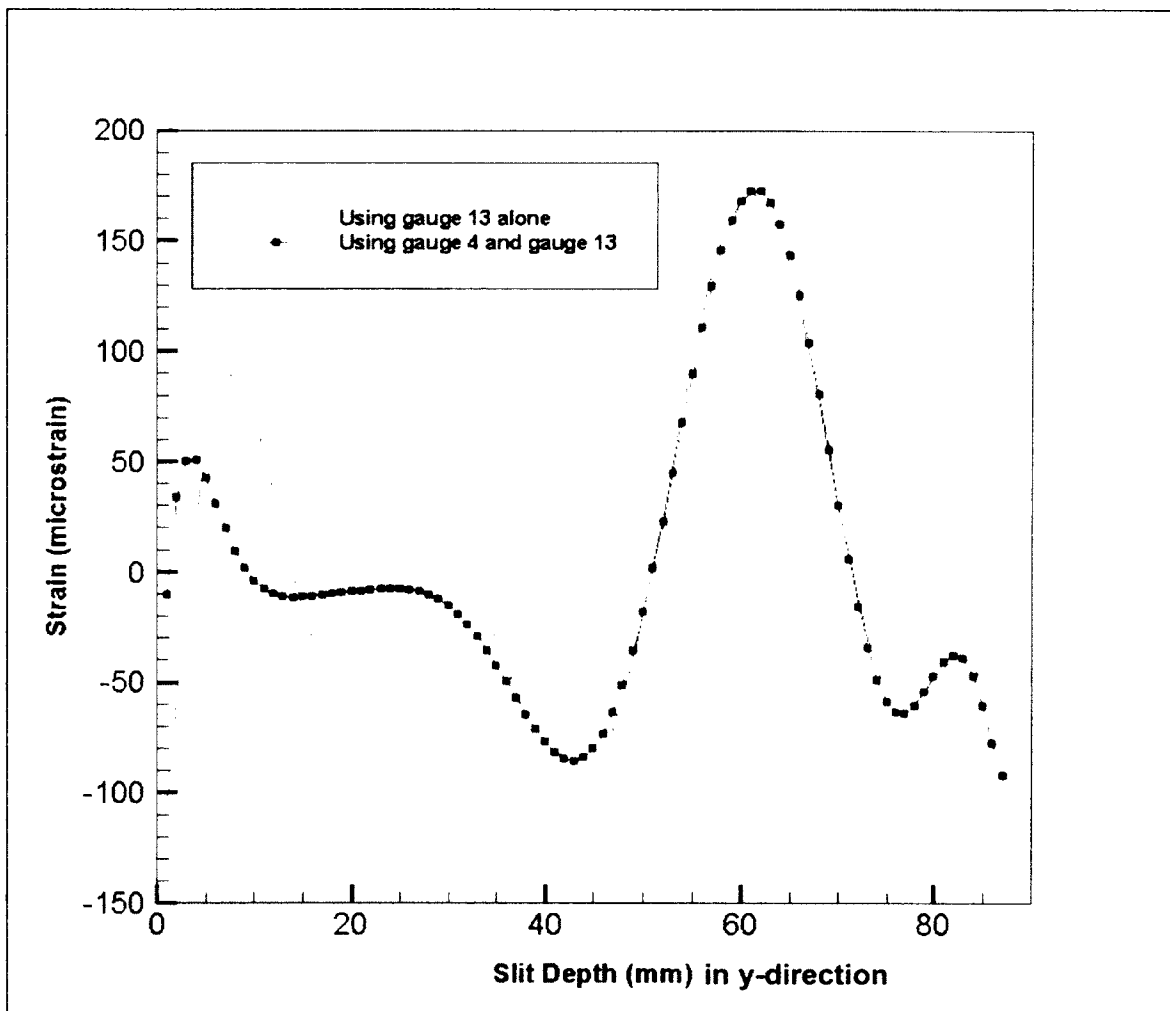


Figure 4.24: Advancing side residual stress profile (σ_x) across weld

To date, there has not been a standard developed to decide the precise number of strain gauges to use and how many strain values from each gauge is used in the residual stress calculations if more than one strain gauge is used. There are however several procedures that can be implemented to ensure an increase in accuracy of calculated residual stress.

From taking the RMS error of the measured and fitted strain, it was determined that using 10 orders of polynomials produced the lowest value of error between fitted and measured strain values. Once, it was decided that using 10 orders of polynomials resulted in the most accurate residual stress profile; the next decision is to decide how many strain gauges will be used in the experiment. From Prime's beam bending experiment in section 4.1.1.1, Prime states that for through thickness stress measurements, using two gauges (one on top surface and one on bottom surface) will improve accuracy of strain measurements at the surface of the specimen. The number of strain values taken from the top strain gauges is decided on a case-by-case basis but a rule of thumb is to take the first 5-15 strain values from the top strain gauge and then switching back to the bottom strain gauge position.

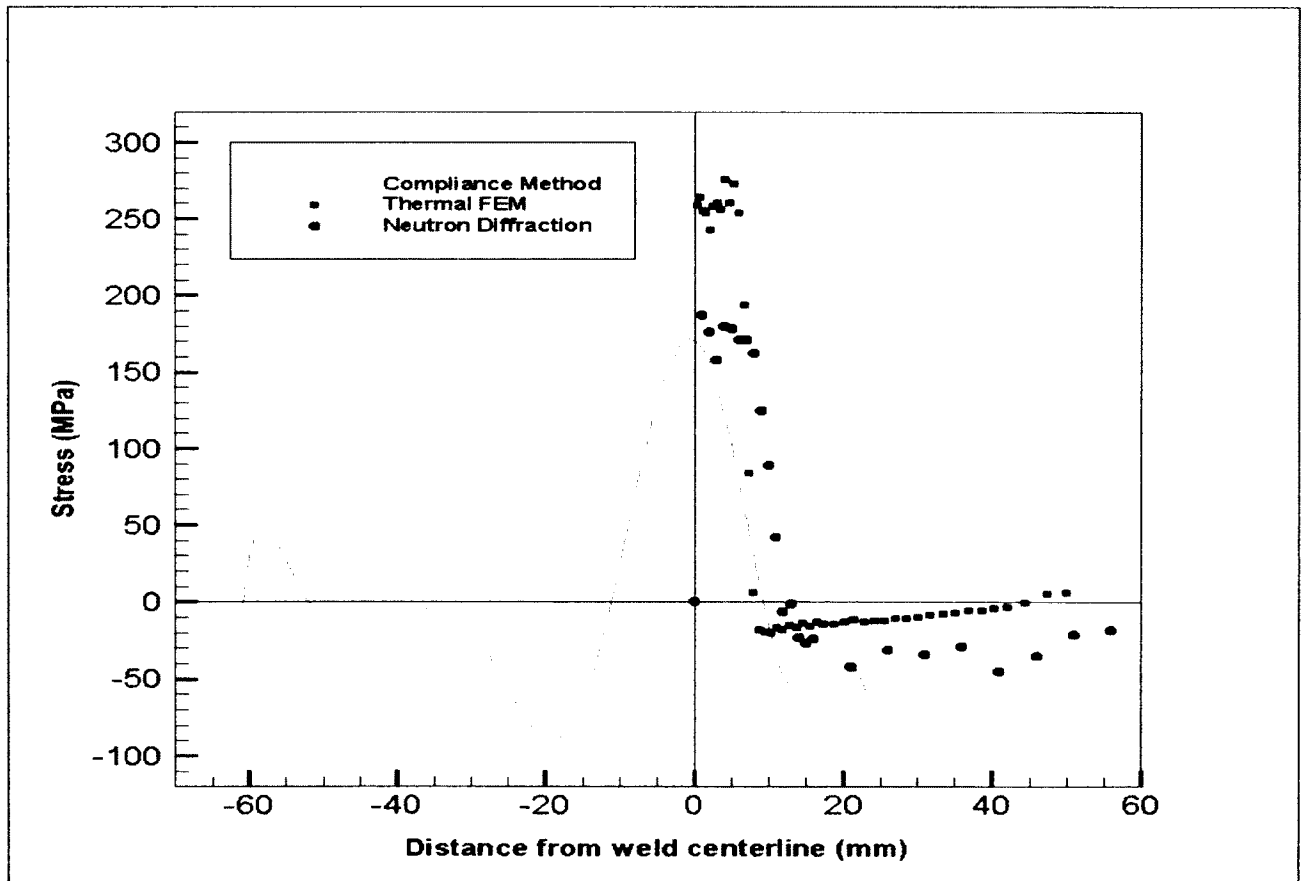


Figure 4.25: Final crack compliance method stress distribution plotted against neutron and thermal FEM model [Dubuorg et al. (2007)]

Sensitivity of Strain Gauge Measurement

The following section examines the issue regarding the sensitivity of the different strain gauge measurement with respect to its location on the test specimen. If two strain gauges are close to one another (1-2mm) apart the strain readings from both gauges will be different, yet they might result in the same residual stress profile. If two gauges are placed too far apart from one another, the residual stress results will not be the same. It is possible to use a combination of strain gauges to measure the residual stress through a thick component. As stated before, gauges placed on the top surface will have good sensitivity to strains release near the top surface. Strains on the bottom face will have a higher sensitivity to strains released near the bottom surface. It is possible to use a combination of the two strain gauges to measure the residual stress. If more points are taken from the top gauge than the bottom gauge, then the stress profile will reflect that by being more biased to the top strain gauges.

Similarly, if more points are taken from the bottom gauge then the residual stress profile will be more influenced by the bottom strains. Having said that, if all the strain measurements were taken from the top and a residual stress profile is produced, it will not be the same as the stress profile taken from all strains from a bottom face strain gauge. This means that although there is only one residual stress profile present in a given test specimen, placing strain gauges at various distance from the slitting line will affect its sensitivity to strain measurement and therefore variance in the calculated residual stress profile.

An example is shown to demonstrate the sensitivity of strains measured from different strain gauges on a test specimen. Figure 4.26 shows a comparison between residual stress results using 40 strain measurements from gauge 7 and 40 strain measurements from gauge 12 (gauge positions are shown in Figure 4.11). At $y = 1$ mm from the edge of the plate, using gauge 7 produced a stress of 10 MPa while using the values of strain reading

from gauge 12 at the same location gave a stress of 200 MPa. The distance between gauge 7 and gauge 12 is 30 mm apart.

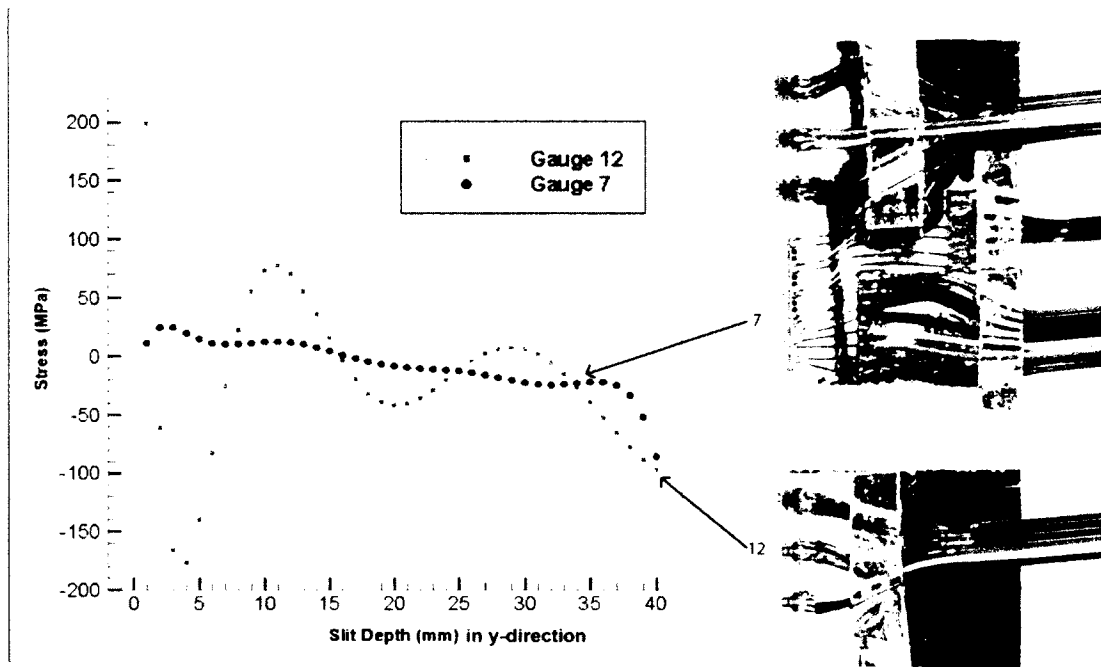


Figure 4.26: Variation in residual stress (σ_x) from gauge 7 and 12

Figure 4.27 shows the variation in residual stress (σ_x) from gauges 7 and 10, which are close to one another at 1 mm apart. It can be seen that using strain measurements from any one of the three strain gauges have a similar effect on the residual stress profile. Comparing gauge 7 and 10, at $y = 2$ mm, the stress values are different but the magnitudes of stress are closer to one another than when comparing gauges 7 and 12. Figure 4.28 shows the residual stress profile from two strain gauges placed at equal distance on either side of the weld centerline. Both strain gauges give similar residual stress distribution, which suggests that the strain is released symmetrically about the slit line at every slit depth.

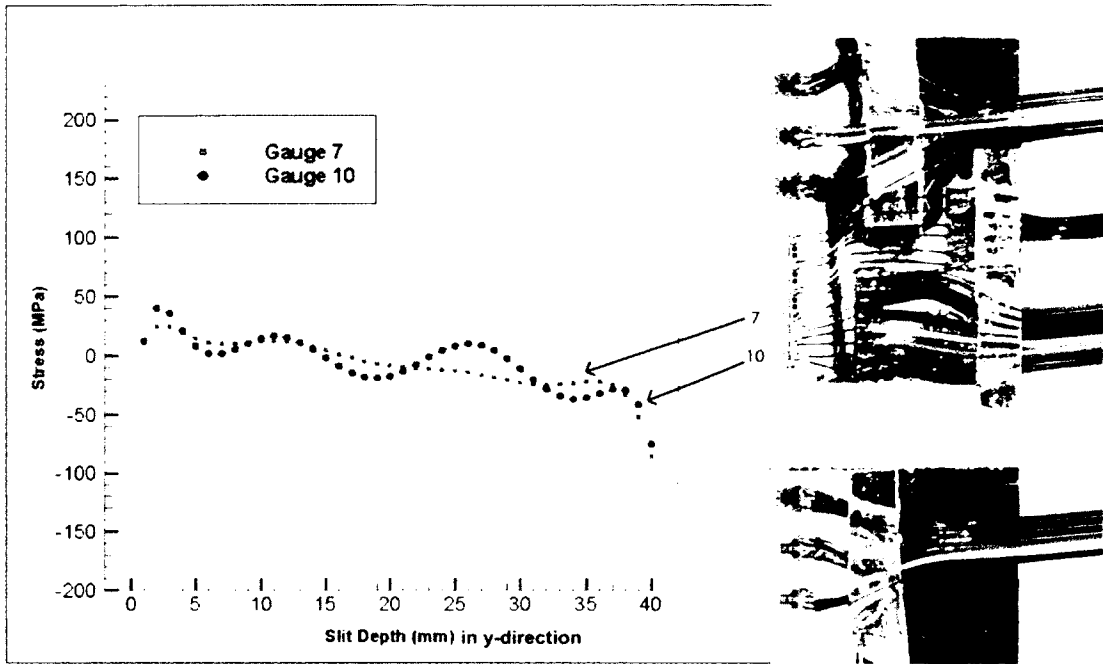


Figure 4.27: Variation in residual stress (σ_x) from gauge 7 and 10

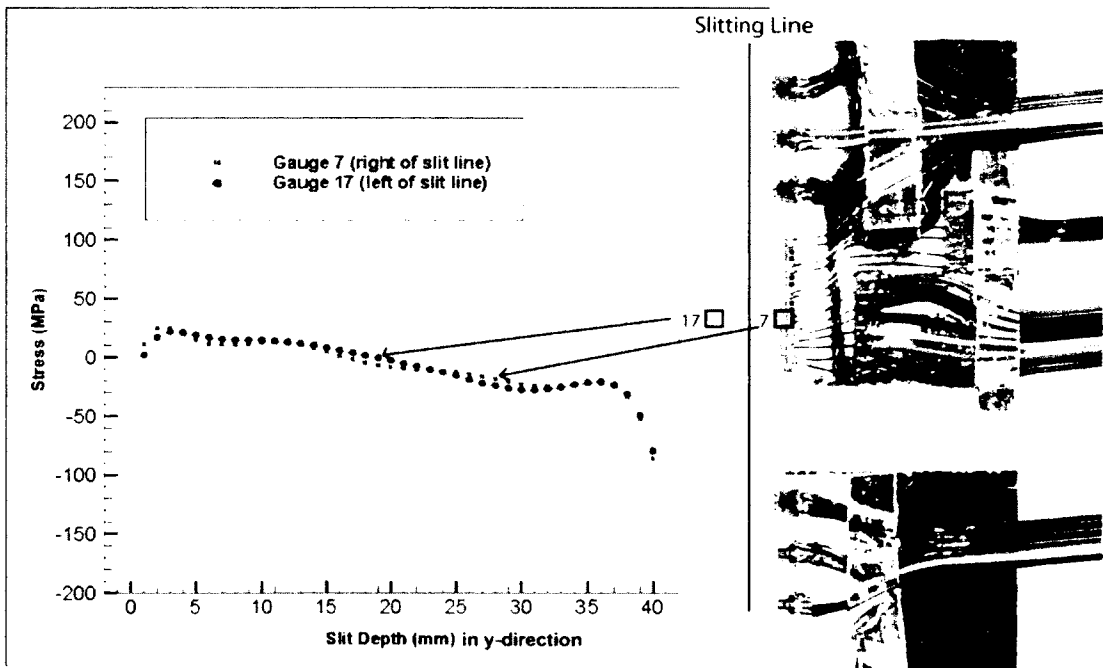


Figure 4.28: Variation in residual stress (σ_x) from gauges on right and left side of weld centerline

4.1.2 Variation in Residual Stress (σ_x) of FSW Lap Joint in Through Thickness (y) Direction

4.1.2.1 As-welded and Hammer Peened Through Thickness Residual Stress (σ_x)

Experimental Setup

The first set of residual stress measurements were carried out to determine the residual stress in the x-direction as a function of the plate thickness (y). Two test specimens were used in the experiment. The first specimen was cut from the as-welded, double pass FSW panel with a dimension of 191 x 95.5 x 3.76 mm and the second specimen was cut from the hammer peened, double pass FSW panel with the dimension of 191 x 95.5 x 3.76 mm. Figure 4.29 shows a cross sectional view of the stringer-to-skin lap joint.

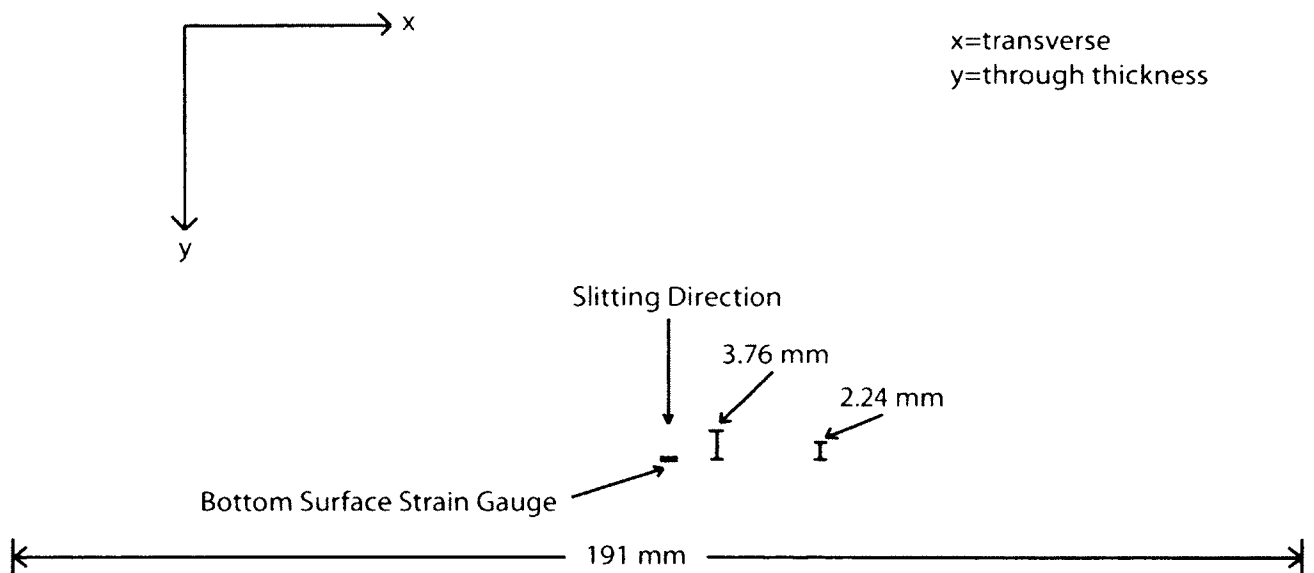


Figure 4.29: Bottom gauge position for through thickness slitting experiment

For both test specimens, a single uniaxial strain gauge with a gauge length of 3.18 mm was placed on the bottom surface of the plate directly centered below the slitting line as shown in Figure 4.29. A wire EDM was used to produce 0.125 mm deep slits and strain

readings (microstrains) were taken at the bottom gauge position for each slit depth. Figure 4.30 shows the strain measurements in the x-direction from the as-welded and hammer peened test specimen as a function of the plate's thickness.

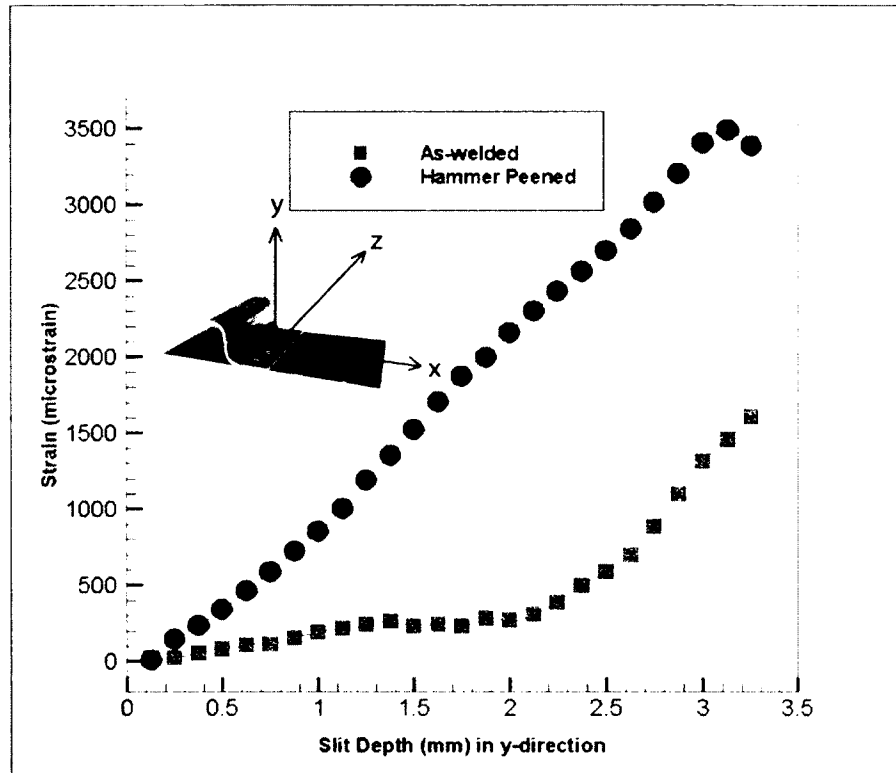


Figure 4.29: Strain readings for as-welded and hammer peened through thickness slitting

Finite Element Model

The entire cross section of the FSW lap joint was modeled as a 2D FE model in ABAQUS CAE as shown in Figure 4.31. Plane strain, 8-node, quadrilateral elements were used in the FE model. The aluminum plate's material properties were set to $E = 72$ GPa and $\mu = 0.33$. The Young's modulus of the two aluminum alloys were very close to one another and their Poisson's ratio was identical so a single E and μ value was used for the model. The bottom surface of the plate was constrained to prevent rigid body motion. For each slit increment, 0.125 mm elements were removed incrementally to simulate material removal by wire EDM. Various pressure loads were applied to the slit face of

the model based on the various orders of Legendre polynomial. Strains were recorded at nodes, which represent the ends of the bottom gauge length. From the FEM model, the compliance functions were calculated for the slitting experiment in the through thickness direction. Figure 4.32 is the compliance functions of orders 2 to 11 for the bottom strain gauge position. Since the as-welded and hammer peened had the same cross sectional geometry and since the slitting was performed at the exact same position for both tests, only one compliance matrix was needed to calculate both the residual stresses in the as-welded and hammer peened plate. The only variable that changed was the different strains measured in the as-welded and hammer peened test specimens.

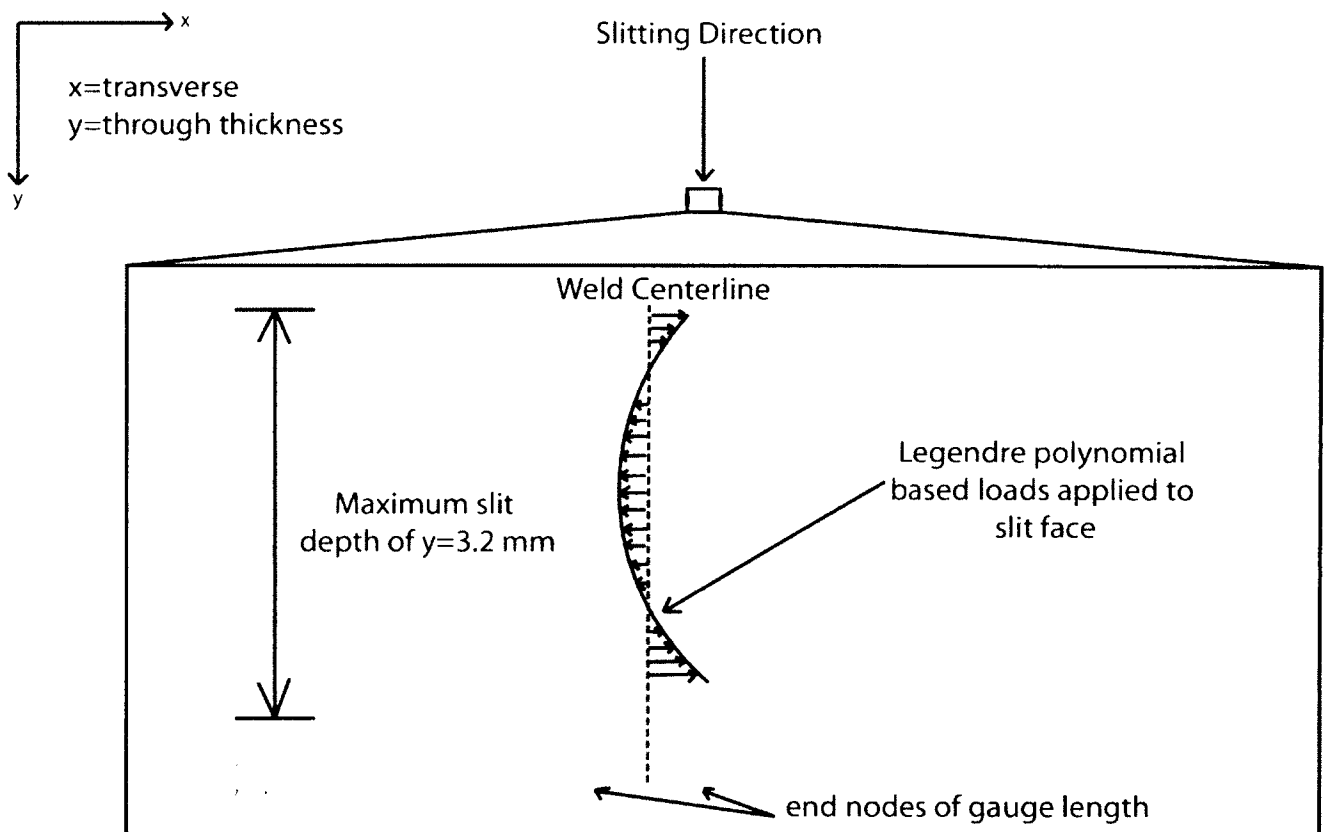


Figure 4.31: 2D FEM model of FSW lap joint cross section

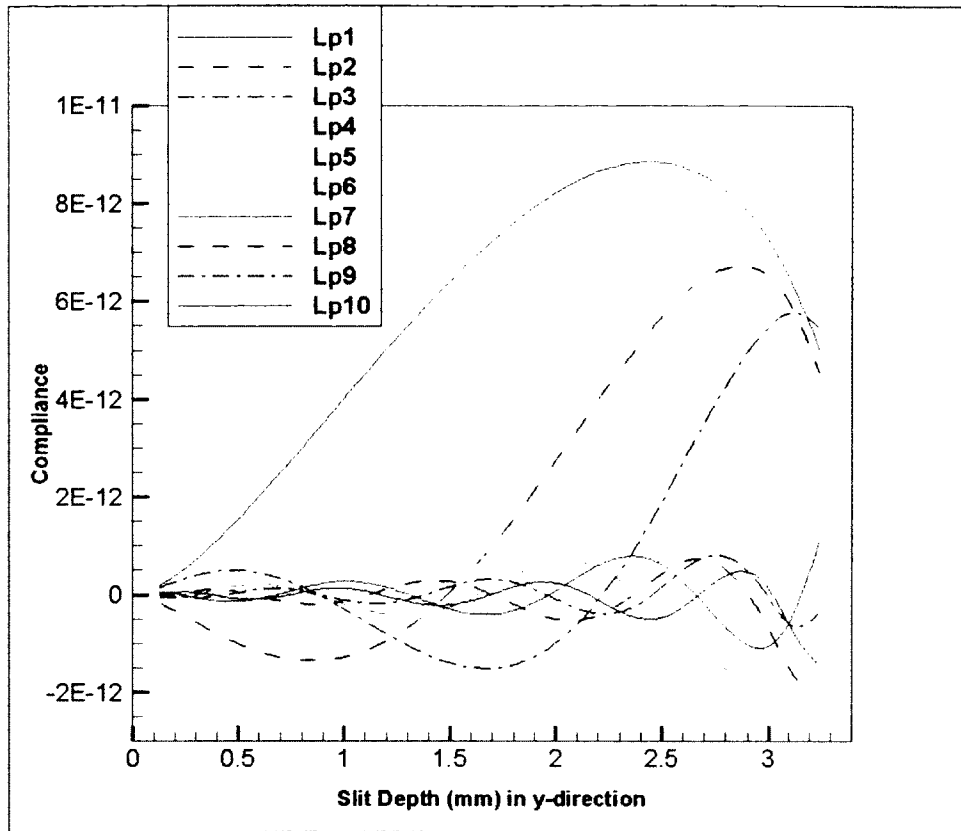


Figure 4.32: Bottom gauge compliance functions

The residual stress variation in x-direction through the thickness of the weld obtained from these strain measurements and calculated compliances will be presented in later section 5.1.1.

4.1.3 Variation in Residual Stress (σ_z) in FSW Lap Joint in Transverse (x) Direction

4.1.3.1 As-welded Longitudinal Residual Stress (σ_z)

Experimental Setup

The second slitting experiment measured the strains in the z-direction on the transverse plane. One as-welded test specimen was used in this experiment. The dimension of the plate was 98.5 x 75.2 x 3.76 mm as shown in Figure 4.33. Four strain gauges were placed on the bottom edge of the test specimen because this surface was smooth and easier to apply the strain gauge close to the slit line. The strain gauges shown in Figure 4.33 are

placed so that the gauge length was perpendicular to the slitting line and parallel to the z-direction. It is important to note here that although four gauges were placed on the test specimen, gauge 4 was damaged during setup and therefore was omitted from the strain measurements. Strain measurements at gauge positions 1, 2, and 3 are plotted in Figure 4.34.

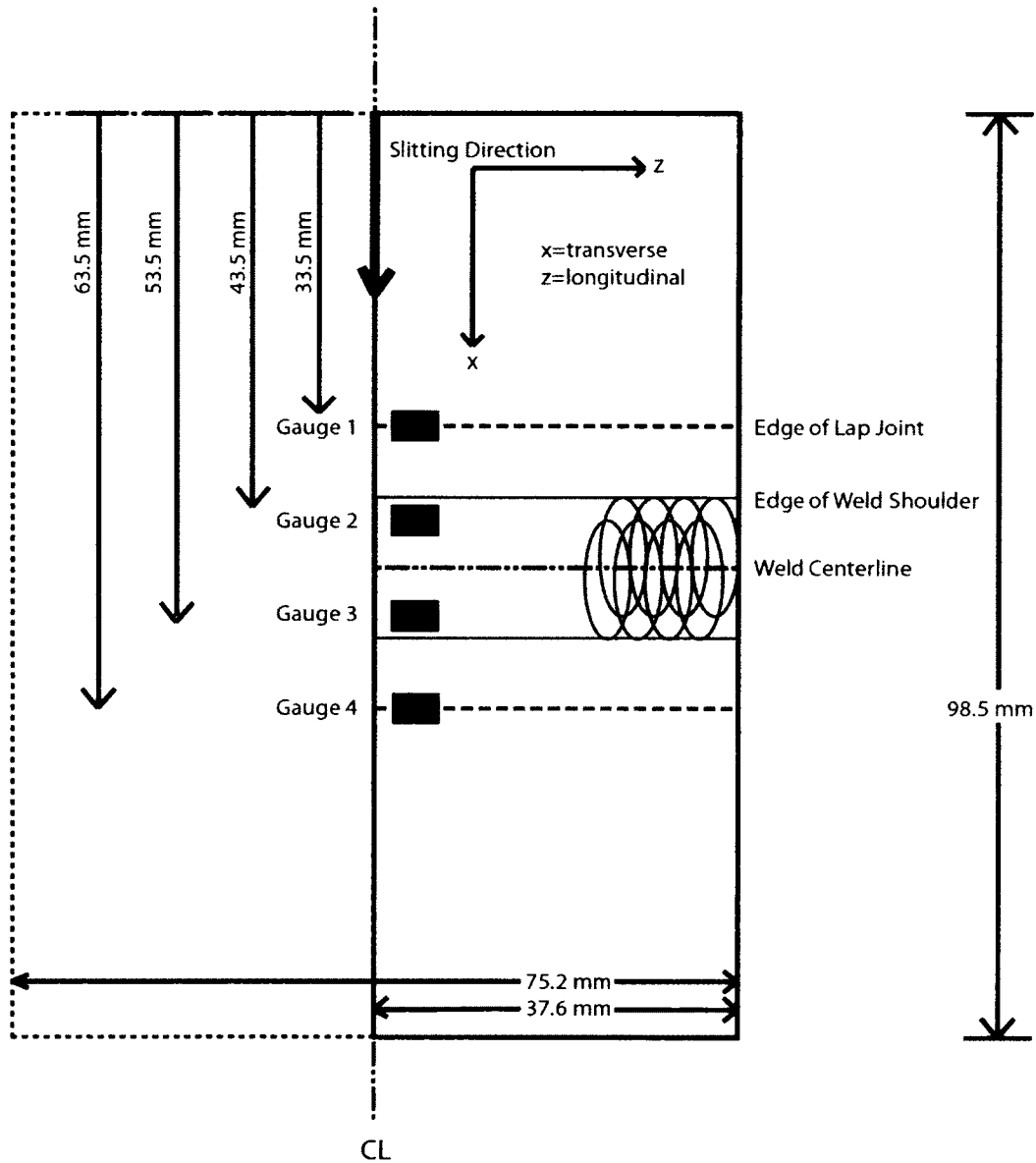


Figure 4.33: Transverse test specimen gauge positions

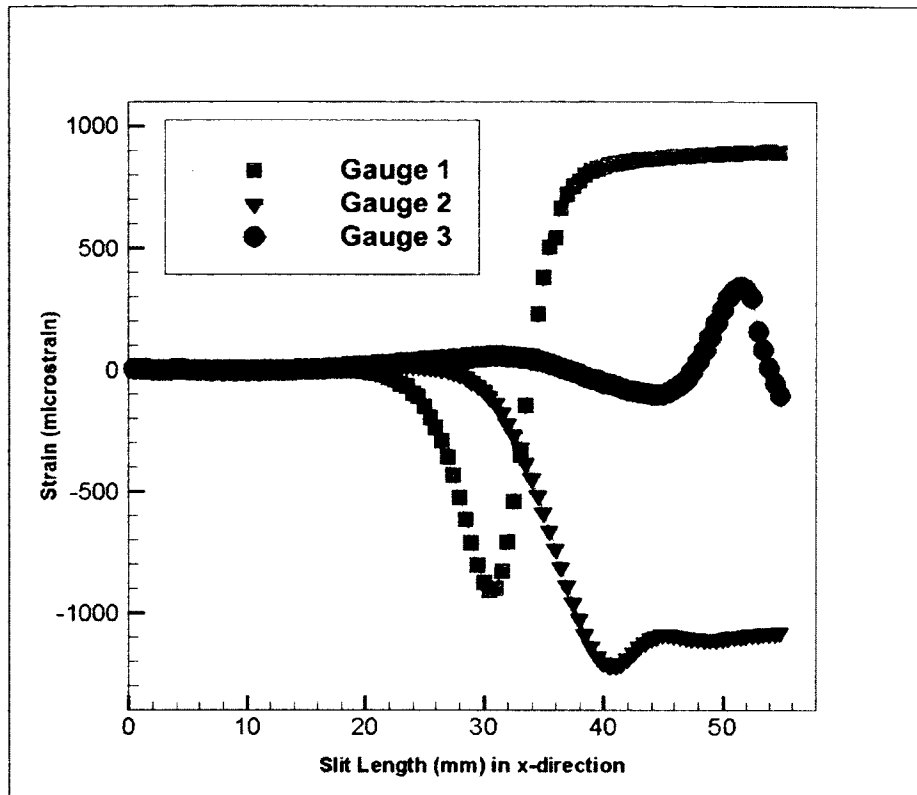


Figure 4.34: Longitudinal strain (ϵ_z) measurements from gauge positions 1,2 and 3

Finite Element Model

For the 2D FEM modeling, only half of the plate was modeled due to symmetry of the plate about the slitting line. Plane stress, 8-node quadrilateral elements were used in the meshing of the model. Although the plate thickness varies in the y-direction, for the FEM model, it was assumed that the plate had a uniform thickness in the y-direction. This simplification was made in order to apply the crack compliance method to measure the residual stress profile in the transverse direction. Figure 4.35 shows a close-up view of the FEM model where the strain gauge was located. The area surrounding the end nodes had an increase in the number of element as well as the area near the slitting line. Slits were made using an EDM wire cutter at every 0.5 mm increments to a final slit depth of 60 mm. Similar to the through thickness compliance calculations, various loads based on the 10 orders of Legendre polynomials were applied at each slit interval and the strains at the three strain locations were recorded.

The compliance functions for gauges 1, 2, and 3 are plotted in Figures 4.36, 4.37, and 4.38 respectively. Figure 4.36 shows that for gauge position 1, after 35 mm of slitting, the gauge is no longer able to detect any changes in strains and therefore all slitting measurements after the 35 mm depth results in no change of strain. Similarly for the second gauge location, the strains readings level off at around 45 mm.

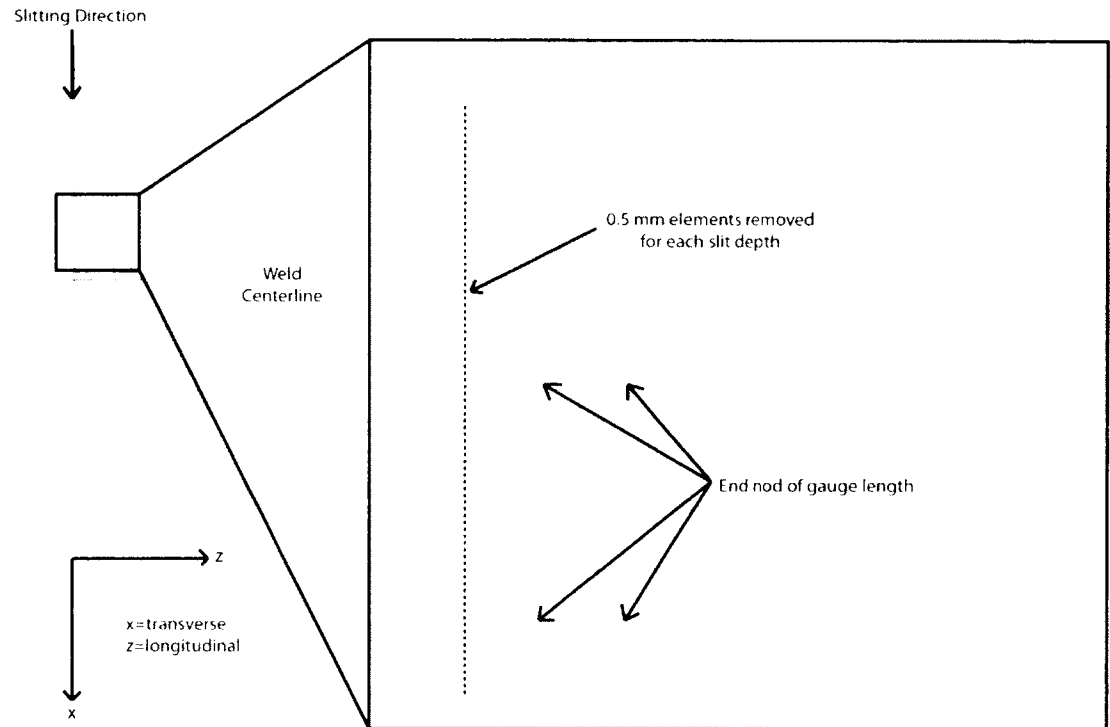


Figure 4.35: 2D FEM model of FSW lap joint

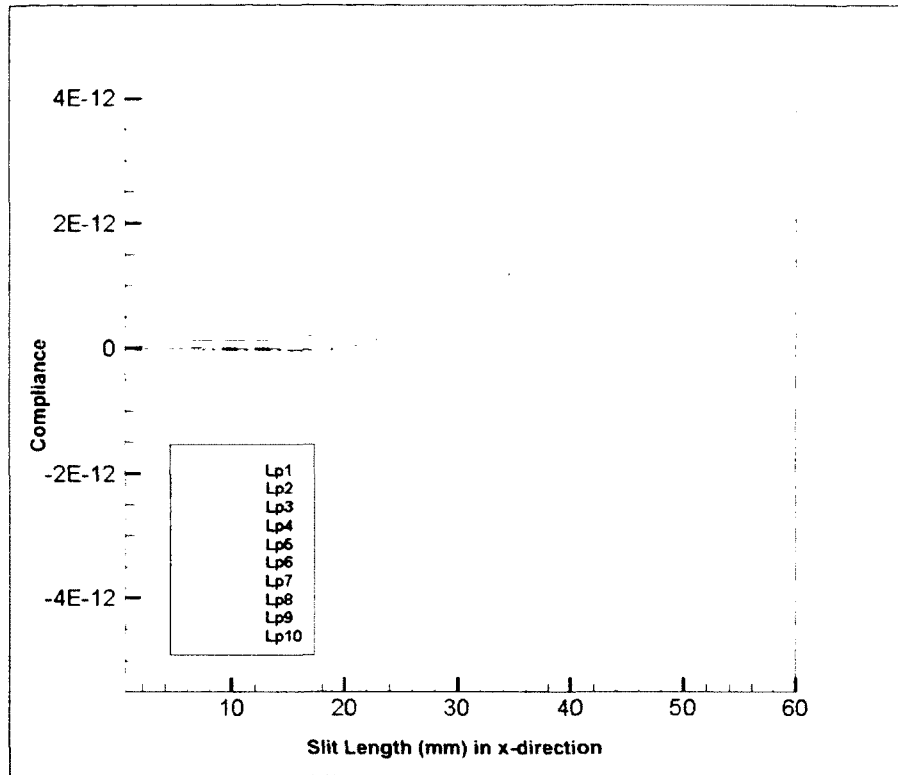


Figure 4.36: Gauge 1 compliance functions

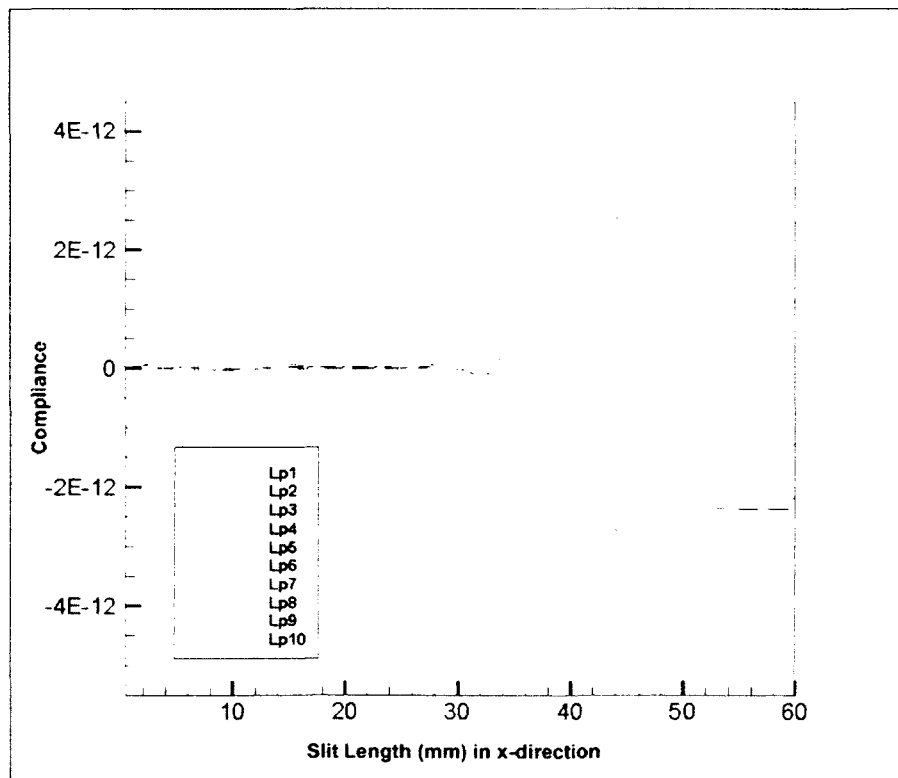


Figure 4.37: Gauge 2 compliance functions

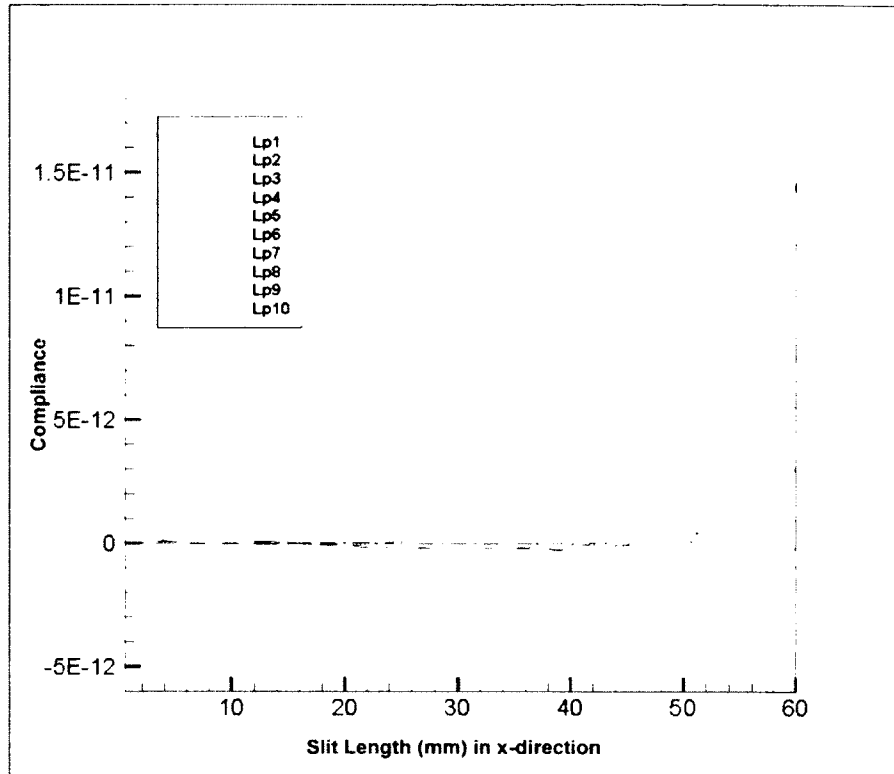


Figure 4.38: Gauge 3 compliance functions

The residual stress variation in z-direction across the weld obtained from these strain measurements and calculated compliances will be presented in later section 5.1.2.

4.1.4 Variation in Transverse Residual Stress (σ_x) in Longitudinal (z) Direction

4.1.4.1 As-welded Transverse Residual Stress (σ_x)

Experimental Setup

The third and final slitting direction was carried out in the longitudinal (z) direction. An as-welded test specimen was used with a dimension of 192.2 x 93.5 x 3.76 mm and is shown in Figure 4.39. Three uniaxial strain gauges with a gauge length of 3.18 mm were placed along the back face of the plate right next to the slitting line. Slits were made at every 0.5 mm interval for a total depth of 50 mm. The strains at the three gauge positions are plotted in Figure 4.40. The first gauge produced usable strains up to the 15 mm depth,

the second gauge produced strains up to 34 mm and the third, 48 mm. These depths correspond to where the slitting passes the positions of the strain gauges and therefore unable to detect any further changes in strains.

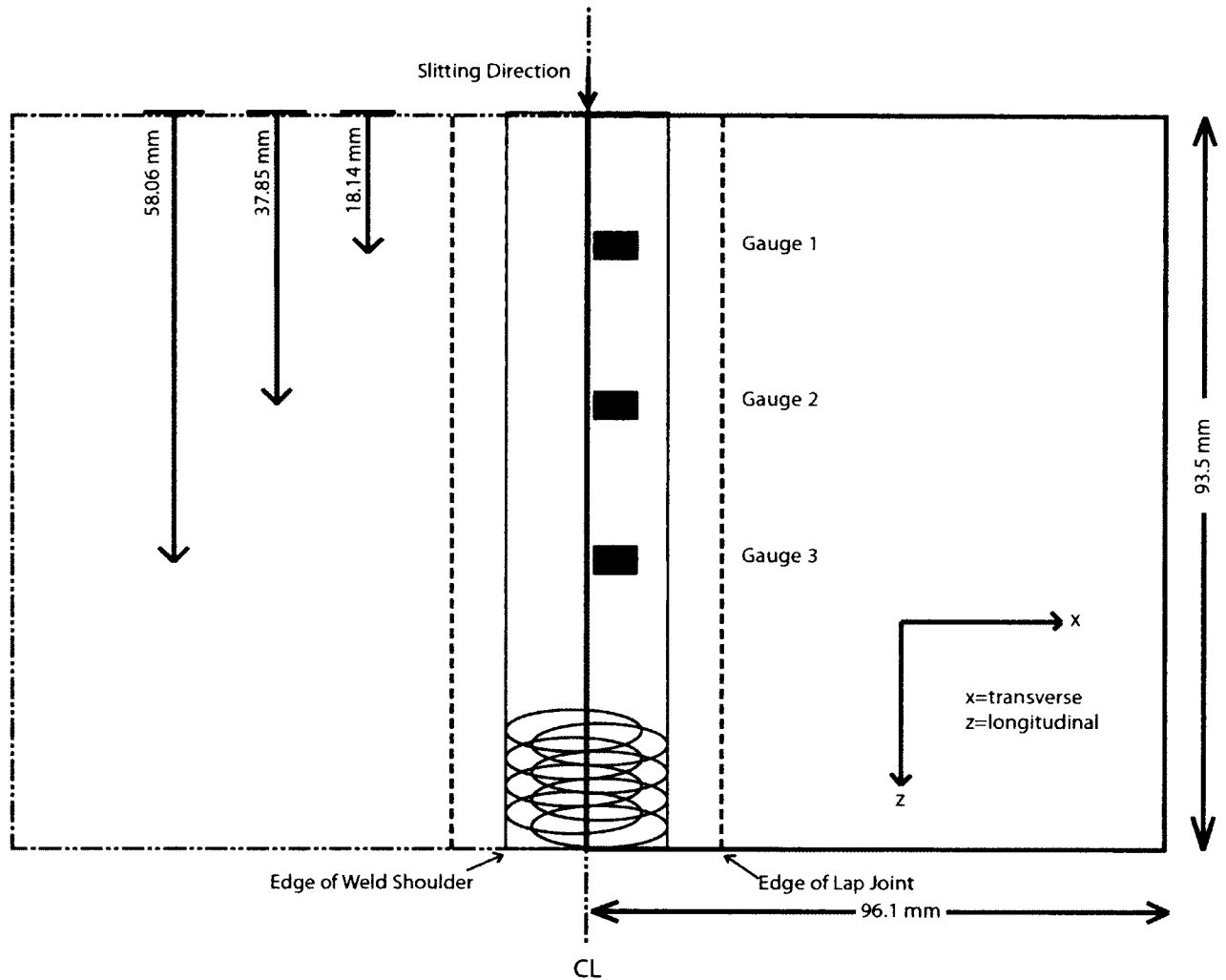


Figure 4.39: Longitudinal test specimen gauge positions

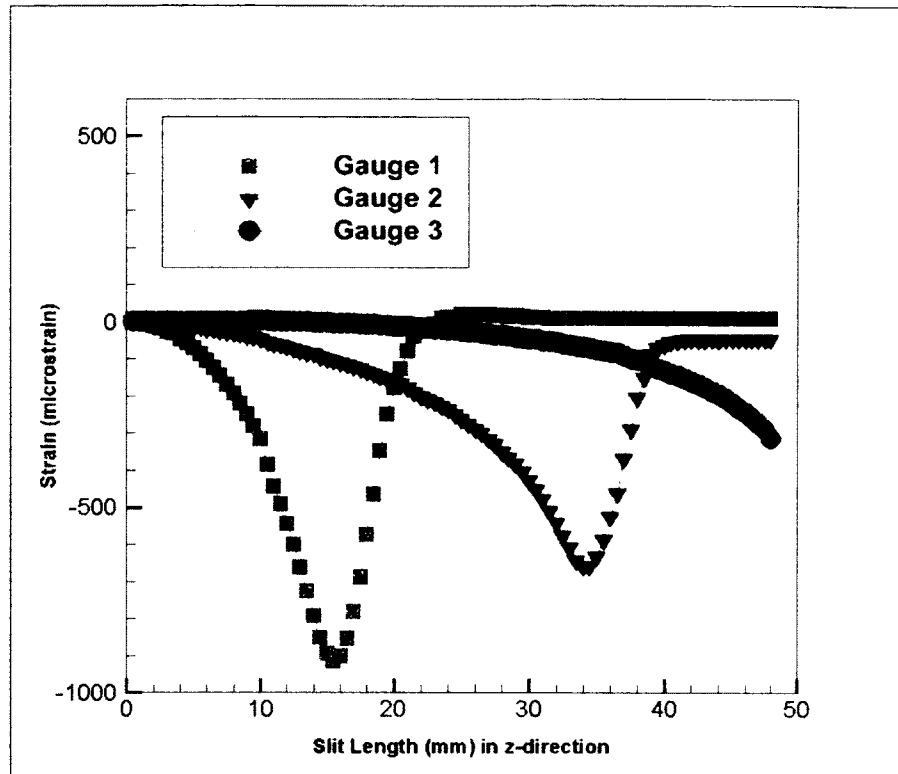


Figure 4.40: Transverse strain (ϵ_x) measurements for as-welded test specimen

Finite Element Modeling

The 3D test specimen was modeled as a simplified 2D FE plate as shown in Figure 4.41. The FE model of the plate this experiment is similar to that of the transverse stress experiment. The thickness of the plate is assumed to be uniform in the z-direction. 8-node, quadrilateral, plane stress elements were used.

The compliance functions for the three strain gauge positions are plotted in Figures 4.42, 4.43, and 4.44. For the first strain gauge position, the compliance functions level off after the first 18 mm slit depth, which corresponds with the measured strain values for the first strain gauge. This means that using only strain gauge 1 values, the residual stress measurements are only valid up to the 15-18 mm depth. The second strain gauge compliance functions level off after the 34 mm depth so the residual stress profile using only strain gauge 2 is valid up to the 30-34 mm depth.

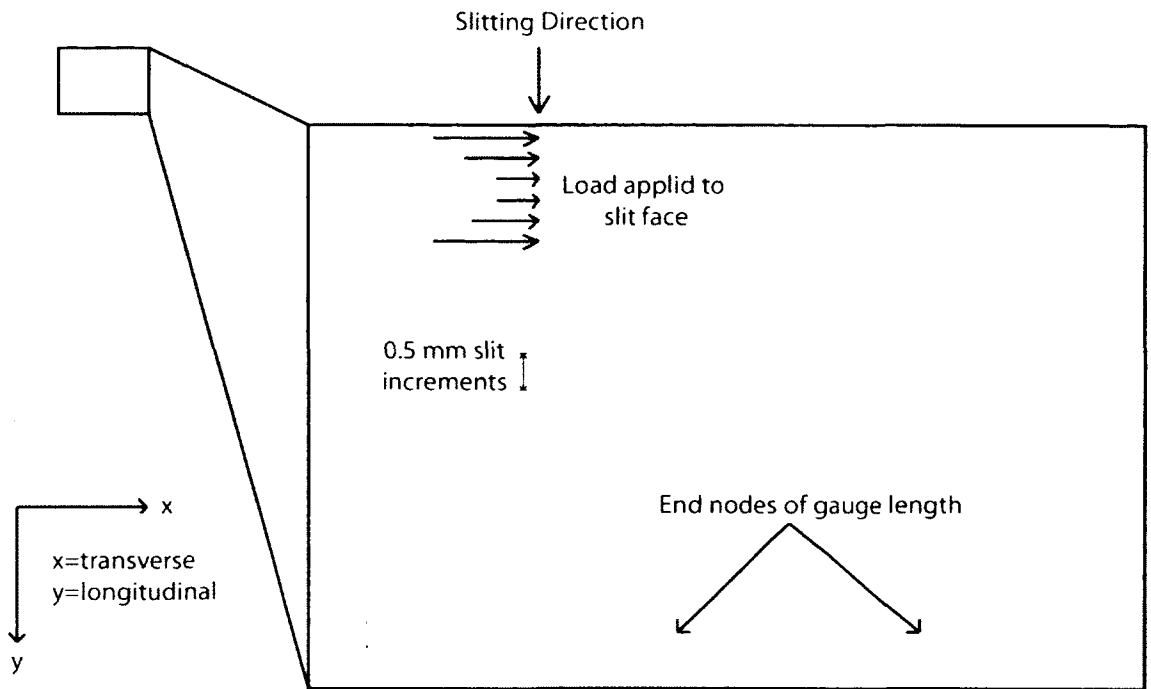


Figure 4.41: 2D FEM model of FSW lap joint

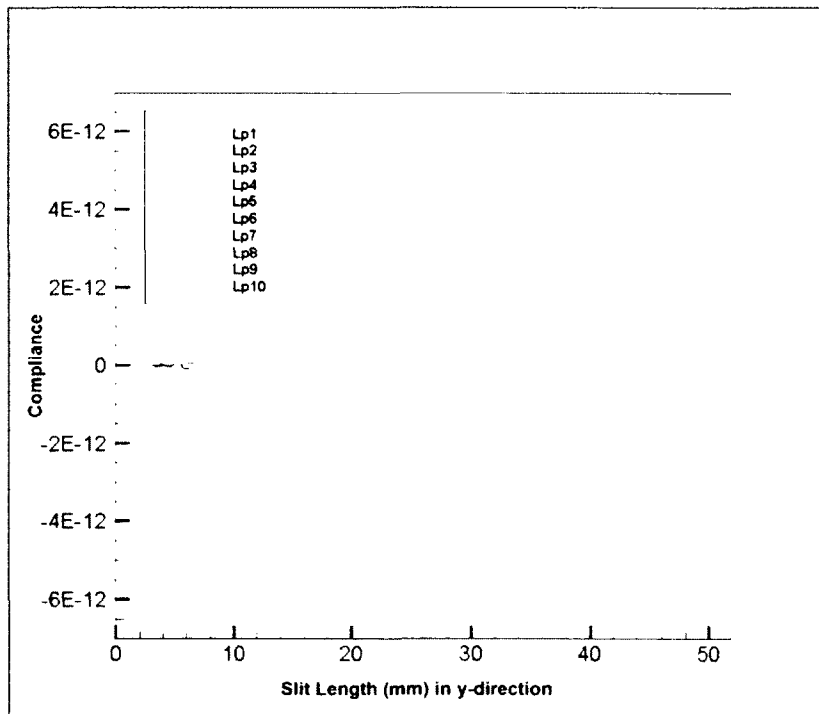


Figure 4.42: Gauge I compliance functions

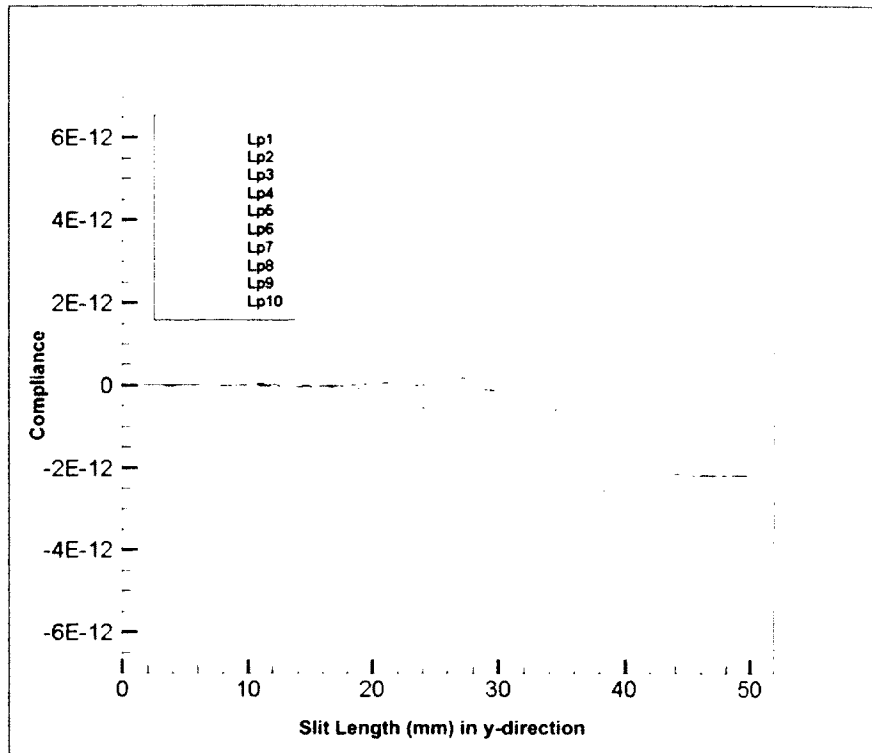


Figure 4.43: Gauge 2 compliance functions

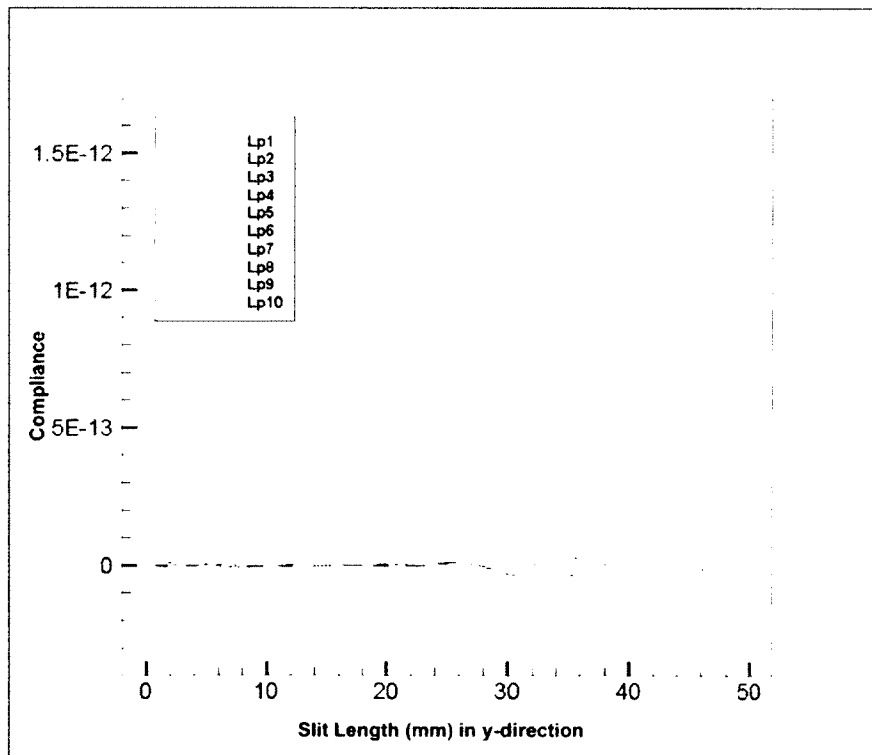


Figure 4.44: Gauge 3 compliance functions

The residual stress variation in x-direction along the weld obtained from these strain measurements and calculated compliances will be presented in later section 5.1.3.

4.2 Neutron Diffraction Experiments

Several destructive as well as non-destructive methods were described in Chapter 2. The crack compliance method was chosen as the best over all method of measuring the residual stresses in these FSW stringer-to-skin lap joints. However, without an independent verification method, it would be difficult to determine the validity of the residual stresses calculated using the crack compliance method. Therefore, an alternative method of residual stress determination was considered.

Neutron diffraction was chosen as a non-destructive method of determining the internal distribution of strains by means of intersecting incident and diffracted neutron beams to form a small sampling volume that was fixed in space. The corresponding residual stresses were then calculated in the three principal directions and compared with the results of the compliance method. Neutron diffraction has proven to be a highly reliable method of non-destructively examining test specimens and has the ability to map strains and therefore stresses in all principal directions at a single point.

4.2.1 Experiment Setup

All neutron diffraction experiments were carried out at the National Research Council's Canadian Neutron Beam Centre in Chalk River on an L3 spectrometer. Two test specimens were used in the experiments. The first specimen was an as-welded plate measuring 191 x 95 x 3.76 mm, and the second specimen was the hammer peened plate with identical dimensions. After careful alignment and calibration, the two specimens were mounted onto the L3 spectrometer. Figure 4.45 shows a FSW test specimen mounted to the spectrometer. Figure 4.46 is a close-up view of the experimental setup, which shows the scattering and diffraction beam slits. Using neutron scattering, wall

scans were completed on both specimens to determine the physical edge of the plates. Although the surface of the plates may appear flat, in reality, they might not be and so if strains are arbitrarily measured from a surface that is assumed to be flat, accumulated error can occur as the gauge volume is moved deeper into the plate. All strain positions were measured with respect to the positions of the wall scans. Strain measurements for both test specimens were taken at the mid section of the plates in the x-y plane and are shown in Figure 4.47 and Figure 4.48. The weld centerline was taken to be zero position, five points were chosen to the right side of the weld centerline, towards the stringer and eight points were chosen to the left of the weld centerline. Since the gauge volume produced by the intersection of the incident and scattering beam was 0.5 mm, strains were measured at six depths of $y = 0.325, 0.97, 1.625, 2.275, 2.925,$ and 3.575 mm from the top surface. Near the weld centreline, the strains were measured 2 mm apart and increased to 4 mm away from the weld centerline where residual stress variations might not be as predominant. A total of 75 positions were measured for each FSW specimen.

The locations on the strain map in Figure 4.47 and 4.48 are where the lattice strains in the x, y, and z directions were measured. Using a slit with a neutron-absorbing cadmium mask, the dimensions of the match-like gauge volume were defined to be 0.5 mm x 0.5 mm x 20 mm with the long axis pointing in the z-direction. An Si monochromatic neutron beam with wavelength, $\lambda = 1.72$ Å, and diffraction from {311} lattice planes were used for the analysis as it is most representative of the elastic response of the bulk material (AA 2024-T3). According to Bragg's law, the corresponding scattering angle (2θ) was determined to be 83° .

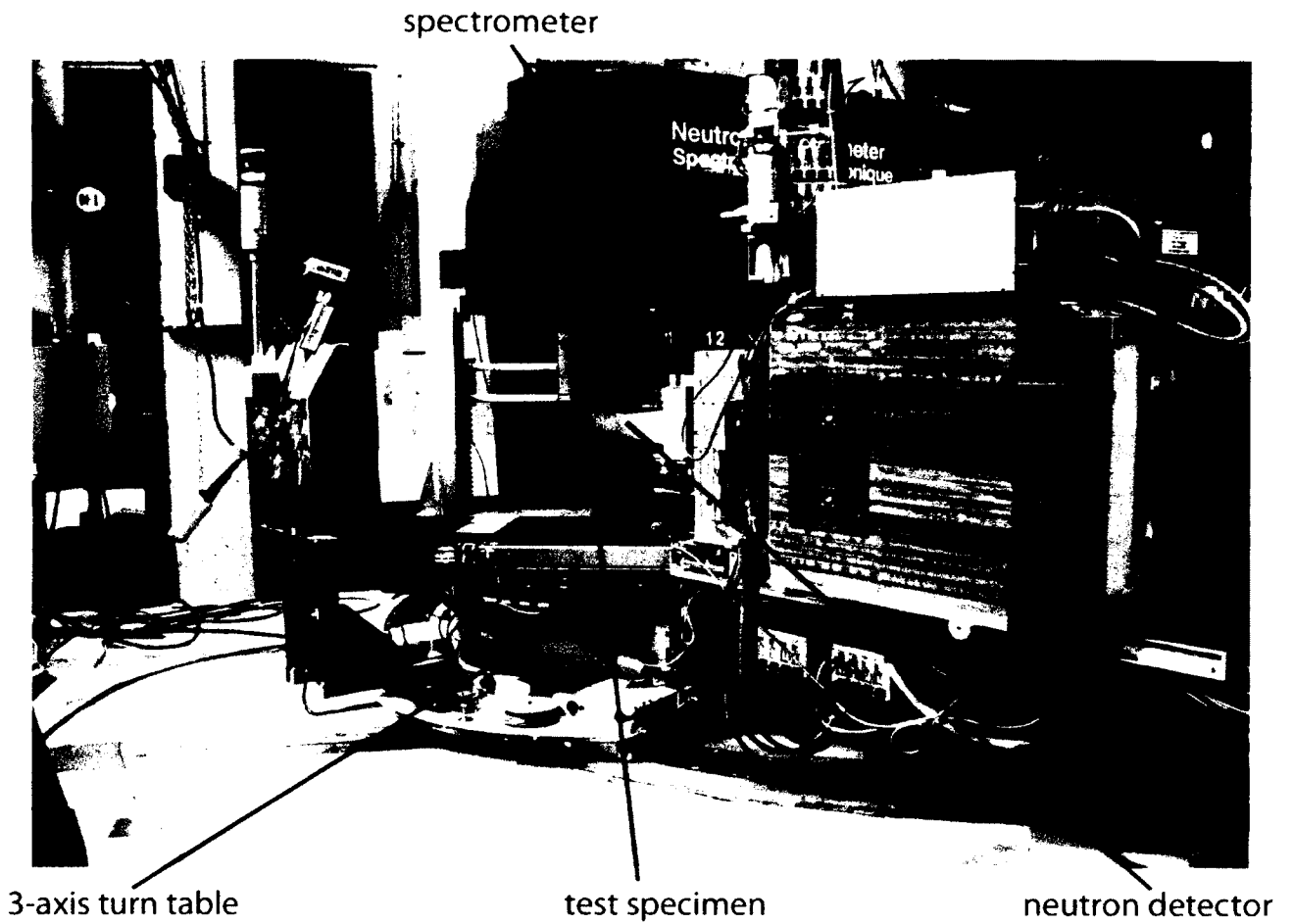


Figure 4.45: FSW test specimen mounted onto the L3 spectrometer at NRU

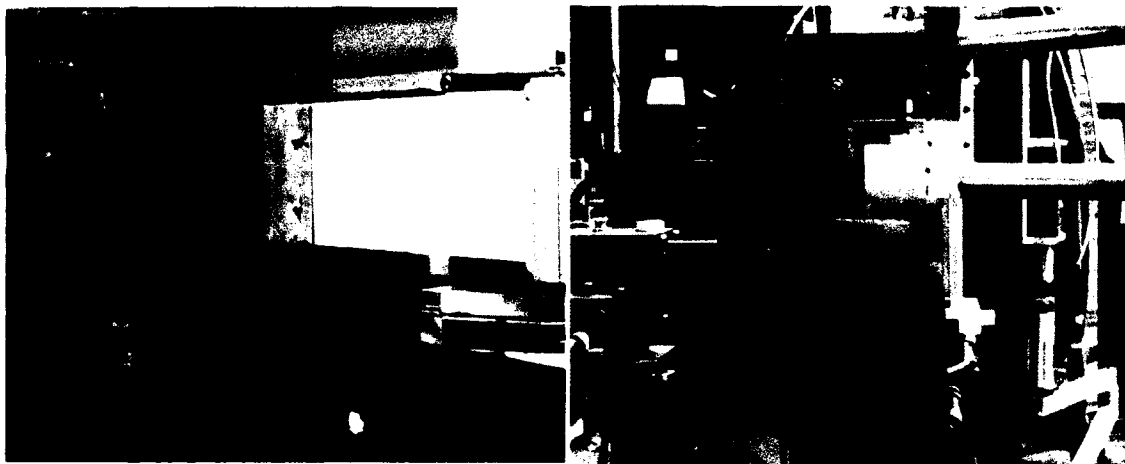


Figure 4.46: Close up view of test specimen setup with detector

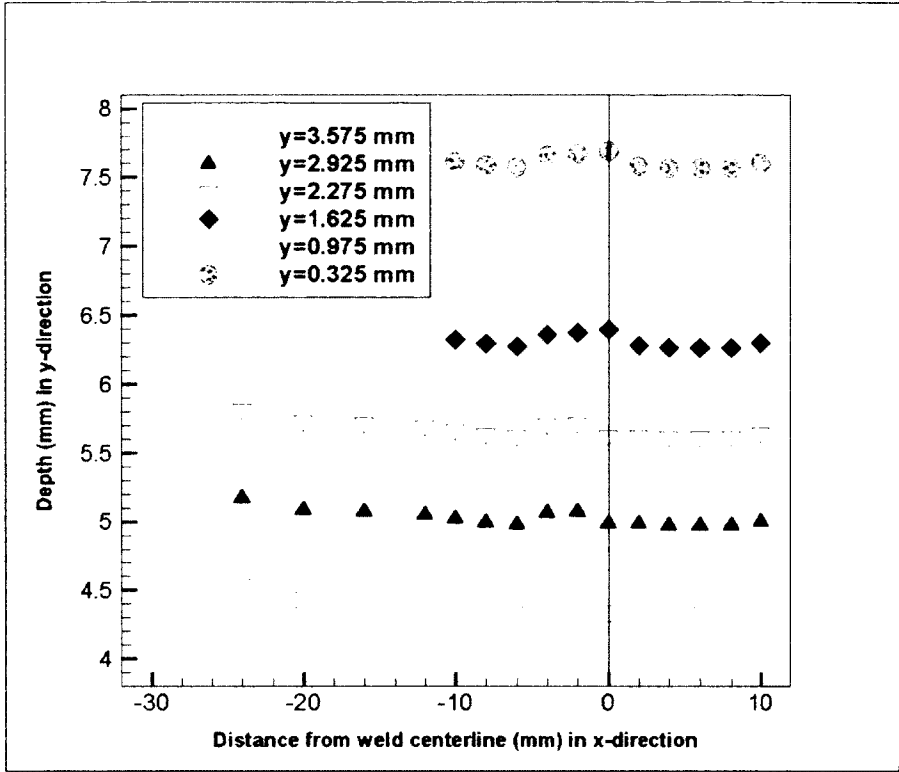


Figure 4.47: Strain mapping of as-welded plate

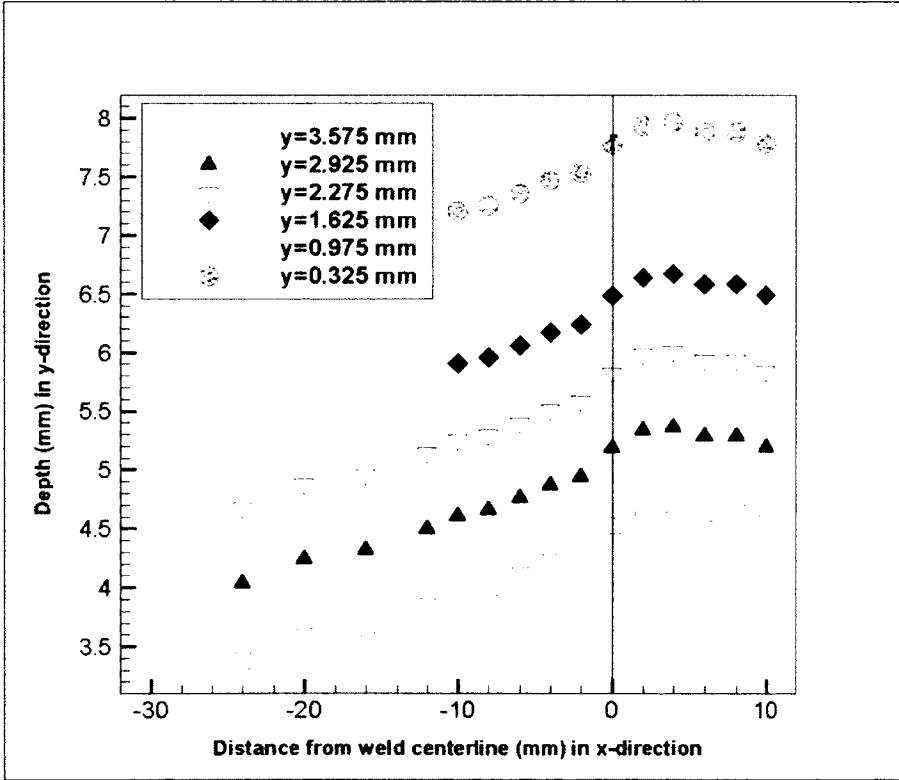


Figure 4.48: Strain mapping of hammer peened plate

Reference Sampling of Unstrained Material

Since lattice strain is determined by measuring the difference between the *d-spacing* of a strained material and the initial atomic spacing of an unstrained material, d_o , reference samples were required to obtain the d_o values for both the stringer and skin material. Rectangular comb-shaped samples with dimensions of 1.55 mm x 3 mm x 24 mm for the stringer and 2.21 mm x 3 mm x 24 mm for the skin panel were cut from a different test specimen at a location where the plate was assumed to have no residual stress. The corresponding d_o values were used when calculating strains in the skin and stringer.

4.2.2 First Set of Strain Measurements

The strain measurement directions were selected by orientating the plates such that the bisector lay parallel to the direction of interest. To measure the transverse strains (ϵ_x), the bisector of the incident and diffraction beams were positioned parallel to the transverse direction. Strain measurements in the normal direction (ϵ_y) were completed by rotating the incident and diffraction beam by 90°. The test specimen had to be taken off the frame and re-oriented to measure the strains in the longitudinal direction (ϵ_z). Consequently, a different gauge volume was used with dimensions of 1 x 1 x 1 mm.

The crystal-lattice strain was purely elastic, reflecting the stresses in crystalline structure, and was not directly sensitive to plastic strain. Note that the three directions are assumed as the three principal directions of the measured strain tensor in the given plate, Woo et al. (2006).

4.2.2.1 Transverse Strain (ϵ_x) Measurements

The first set of strains, ϵ_x , were measured in the transverse direction. Scan time for each point range from 30 minutes to an hour. Figure 4.49 and 4.50 show the transverse strains plotted in the skin and stringer material respectively. Figure 4.49 show that at all three depths, the strains have similar trends. Near the weld centerline, the strain readings are all negative but become less negative as the position moves towards the top surface. Away from the weld centerline, the strains become increasingly positive, which suggest tension is present. The maximum strain (1000 μm) was recorded at around 12 mm from the left of the weld centerline. Figure 4.50 continues the transverse strain (ϵ_x) measurements in the stringer section of the plate for the different positions in the y-direction.

For the hammer peened plate, the transverse strains, ϵ_x , in the skin and stringer are plotted in Figure 4.51 and Figure 4.52 respectively. Transverse strains (ϵ_x) away from the weld centerline for both as-welded and hammer peened plates are similar to one another. The sudden spike in strains at weld centerline of hammer-peened plate suggests that this is an effect of hammer peening around the weld zone. Effects of hammer peening penetration depths can be explained as follows; at a depth, $y = 3.575$ mm, the transverse strains are similar in magnitude of the as-welded plate. Similarity in strain measurement in both specimens suggest that hammer peening only affects the area around the top surface of the plate. However, when looking at the strains in the hammer peened plate at $y = 2.925$ mm and 2.275 mm depth, there is a sudden spike in strain at the weld centerline, which measured 1200 microstrains.

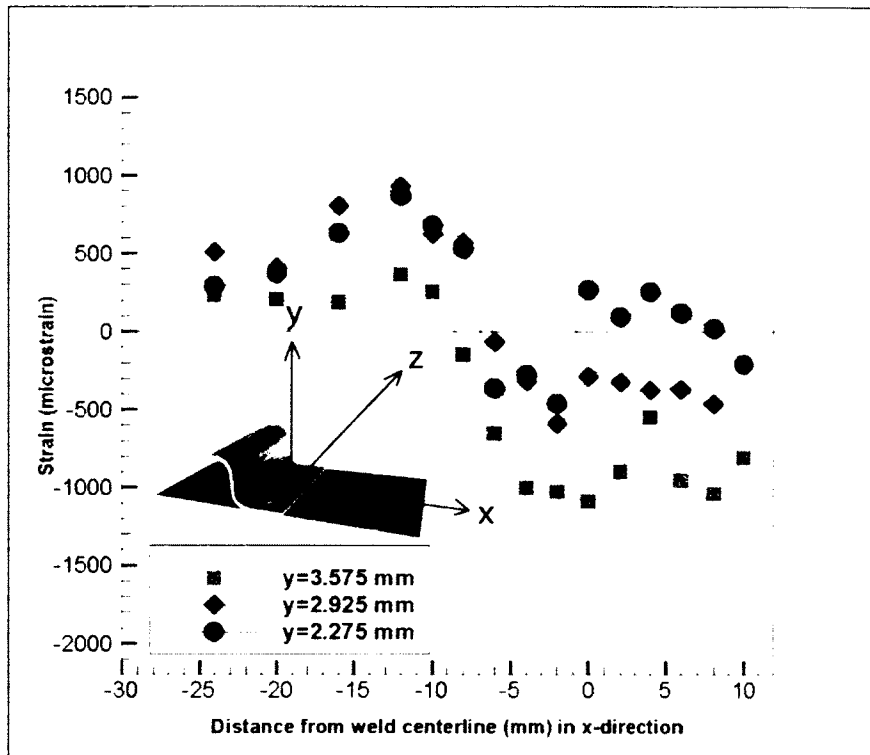


Figure 4.49: Transverse strains (ϵ_x) in as-welded skin

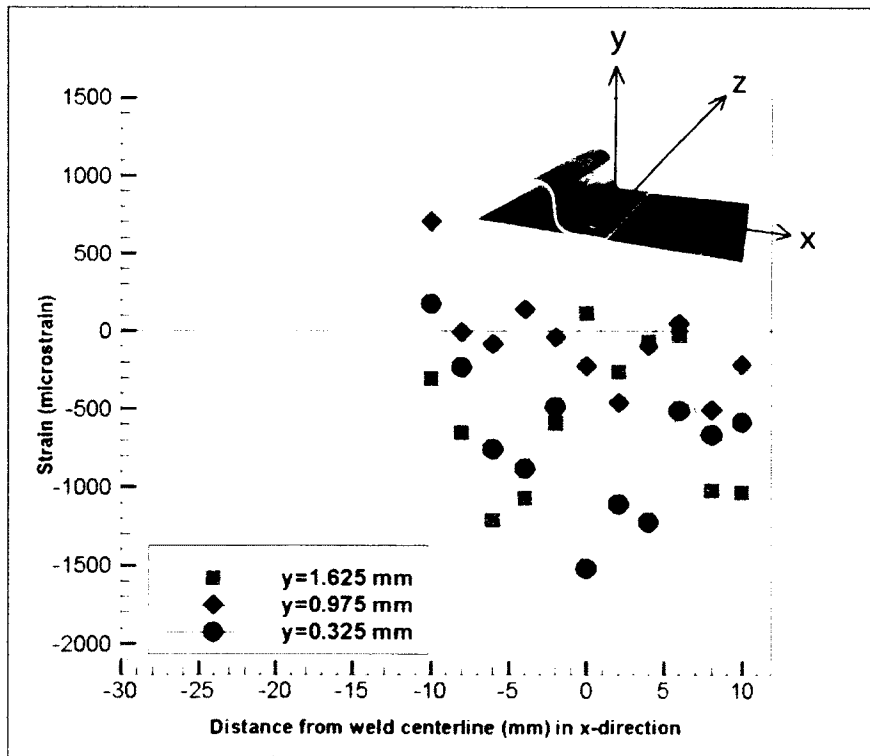


Figure 4.50: Transverse strains (ϵ_x) in as-welded stringer

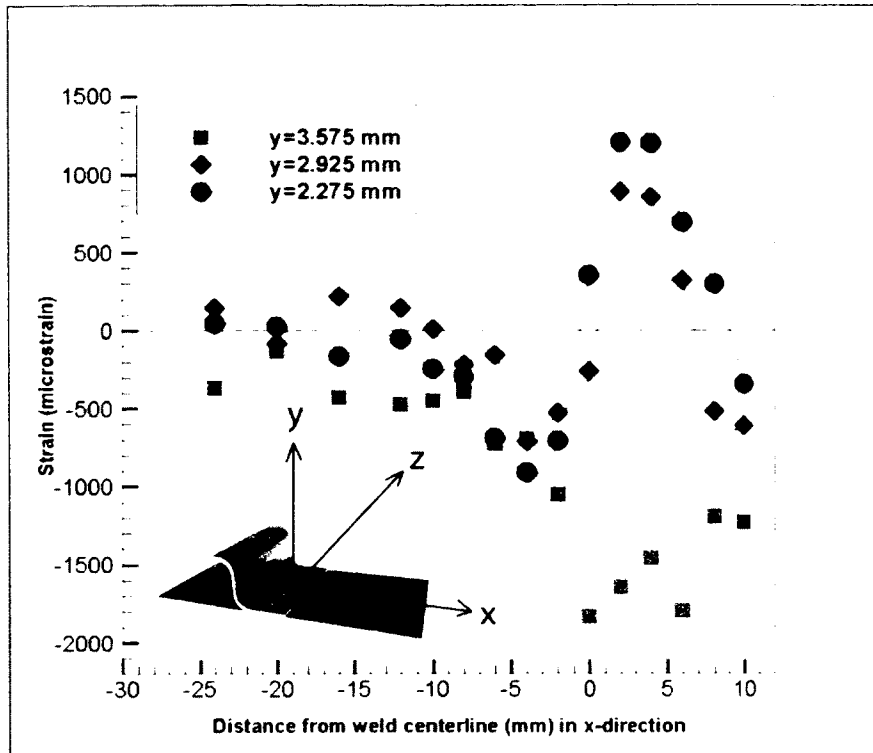


Figure 4.51: Transverse strains (ϵ_x) in hammer peened skin

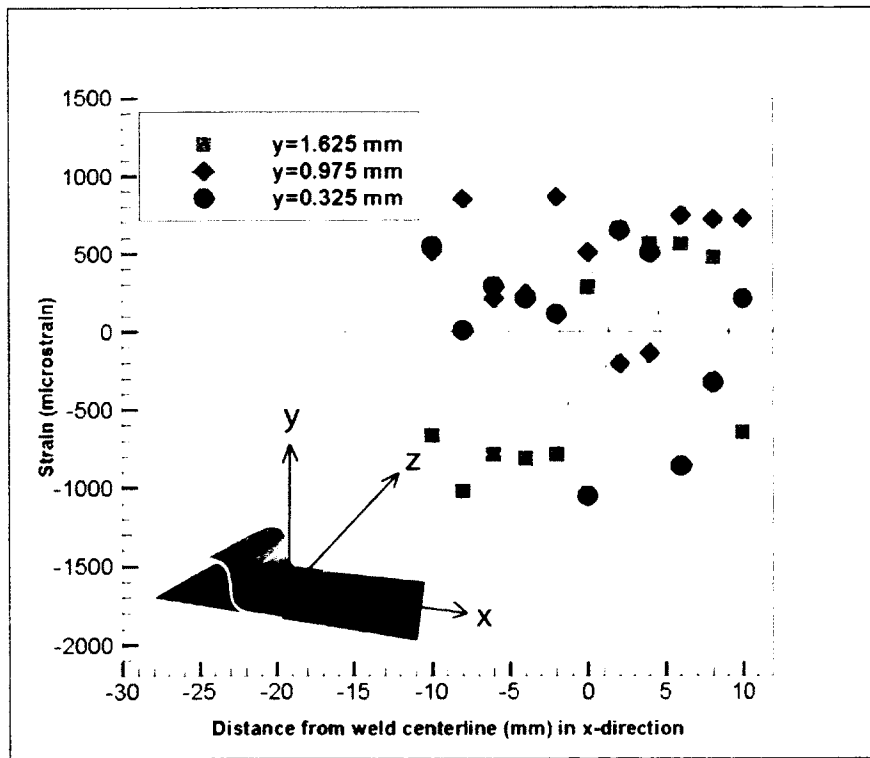


Figure 4.52: Transverse strains (ϵ_x) in hammer peened stringer

4.2.2.2 Normal Strain (ϵ_y) Measurements

Figure 4.53 and 4.54 show the plots for the normal strain (ϵ_y) in the as-welded skin and stringer material respectively. Figure 4.55 and 4.56 show the plots for the normal strains (ϵ_y) in the hammer peened skin and stringer respectively. The magnitudes and trends of the normal strain in the as-welded plate are similar to that in the transverse direction. In Figure 4.52, the normal strains in the skin of the hammer peened plate are fairly uniform with strain ranging from 500 to -500 microstrains. There is a gradual increase in strain readings towards the top surface of the plate. The maximum value of normal strains are recorded at a depth of $y = 0.325$ mm which is 3000 microstrains. Strains recorded in the normal direction for the hammer peened plate has the highest values recorded for all three directions.

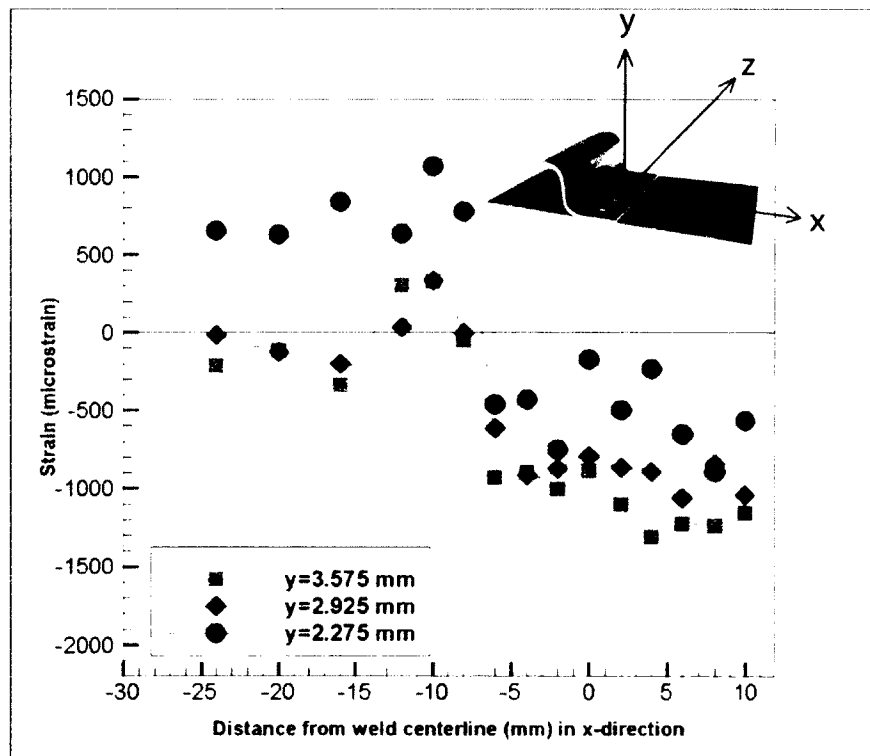


Figure 4.53: Normal strain (ϵ_y) in as-welded skin

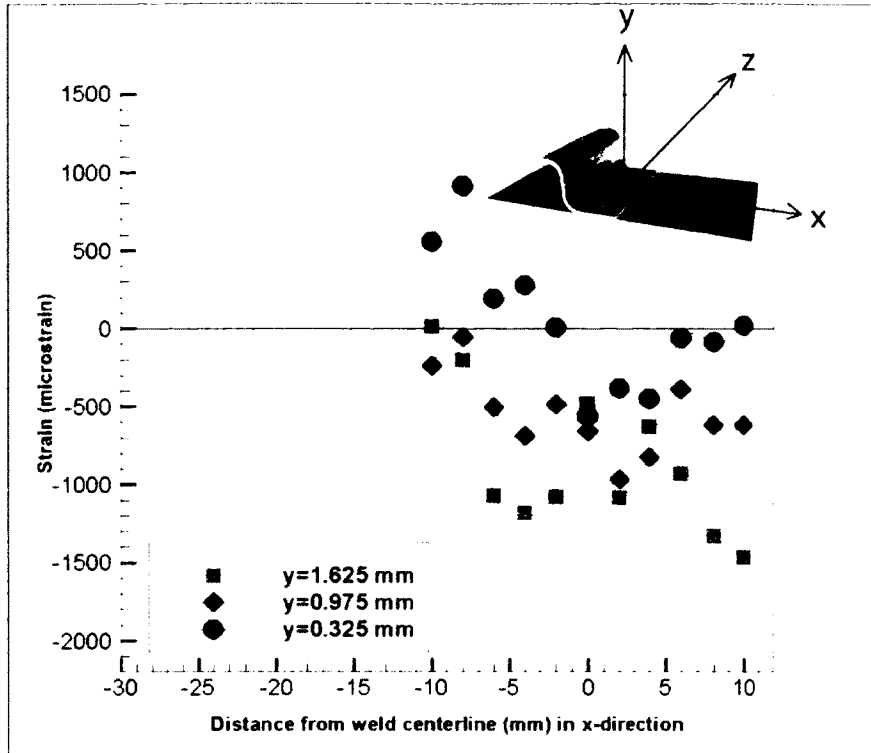


Figure 4.54: Normal strain (ϵ_y) in as-welded stringer

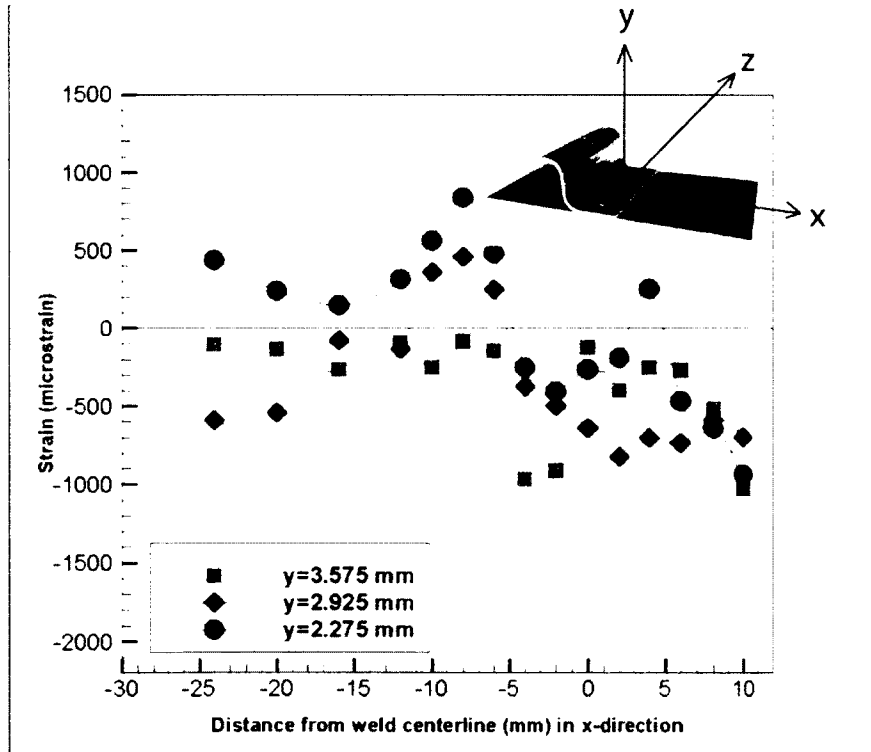


Figure 4.55: Normal strain (ϵ_y) in hammer peened skin

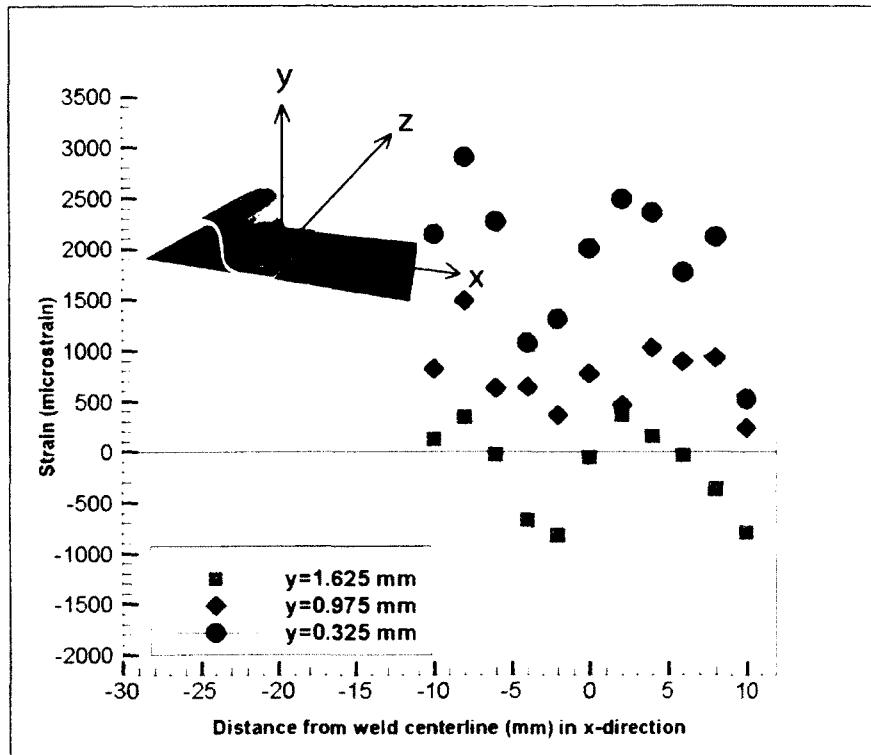


Figure 4:56: Normal strain (ϵ_y) in hammer peened stringer

4.2.2.3 Longitudinal Strain (ϵ_z) Measurements

The third measurement of strains (ϵ_z) was in the longitudinal direction. Referring to the strain map in Figure 4.47, not all points were considered when measuring strain in the longitudinal direction. Due to the limited beam time available, complete longitudinal strains were measured at only two out of the six depths ($y = 0.925$ mm and 2.925 mm), and at three positions with respect to the weld centerline ($x = 0$ mm, $x=2$ mm and $x=-2$ mm). It was determined that measuring the longitudinal strains (ϵ_z) at these points would give a complete residual stress profile in the through thickness and transverse direction. Figure 4.57 and 4.58 are the longitudinal strain (ϵ_z) measurements in the as-welded and hammer peened plates respectively. Strain values and trends in the as-welded plate are similar to one another. In the hammer peened plate, the strain values in the skin are higher than in the stringer.

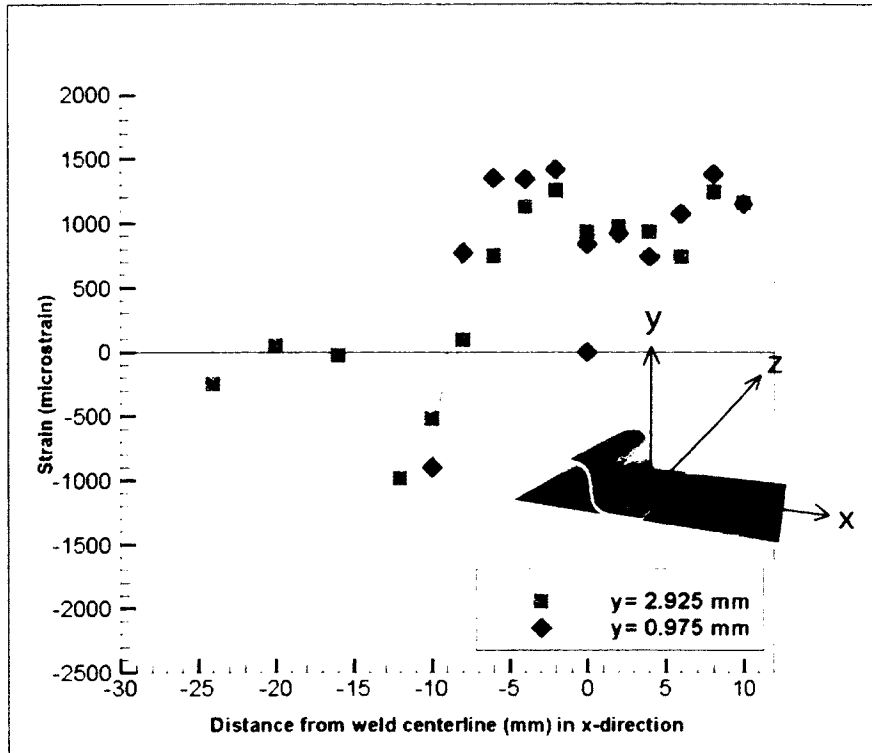


Figure 4.57: Longitudinal strain (ϵ_z) in as-welded plate

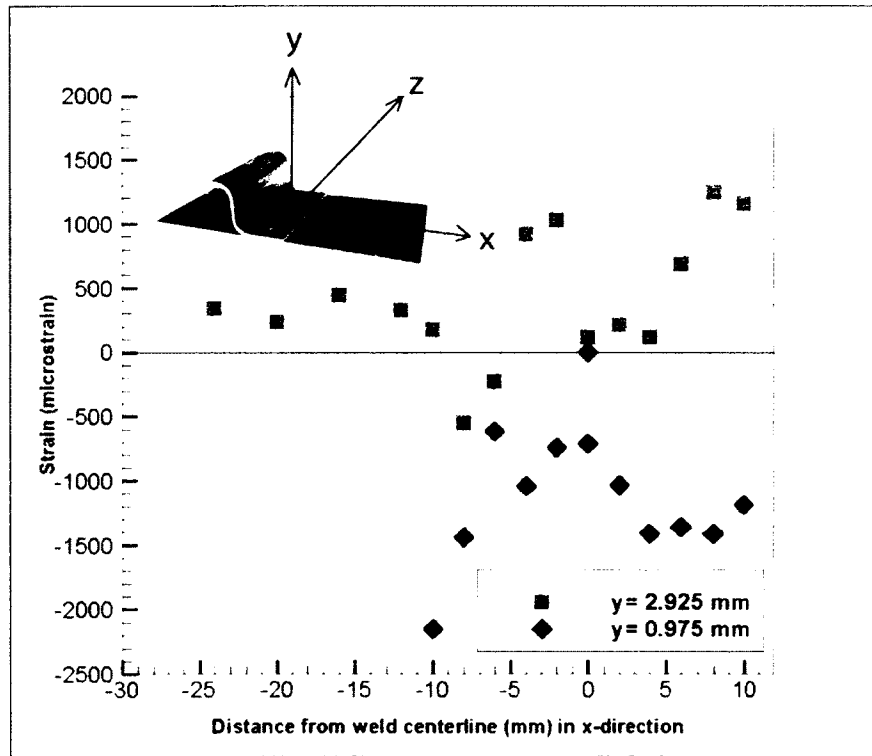


Figure 4.58: Longitudinal strain (ϵ_z) in hammer peened plate

4.2.3 Neutron Diffraction to Determine Residual Stress in Longitudinal (z) Direction

The first neutron experiment was able to determine the variation in residual stress in the through thickness (y-direction) and transverse (x) directions. There was no testing completed along the weld line in the longitudinal (z) direction. The purpose of the second neutron experiment was to determine the variation in residual stress (σ_x) in the longitudinal direction to give a complete three dimensional residual stress profile of the FSW stringer-to-skin lap joints.

Experimental Setup

Neutron diffraction was carried out on the same two test specimens used in the first set of experiment containing one as-welded and one hammer peened plate. Several points were selected along the weld line as shown in Figure 4.59. The points were taken at $z = 5$ to 90 mm in 10.625 mm increments and located in the middle of the plate. Wall scans were completed for both samples and the various strain points were recorded with respect to the test specimen's edge, which was determined from the wall scans. The lattice strains were reordered in all three principal directions. Figure 4.60 shows the transverse strain component (ϵ_x) in the longitudinal direction for both as-welded and hammer peened plates. Figure 4.60 shows the normal strain (ϵ_y) component in the longitudinal direction for both specimens. Finally, Figure 4.62 is the longitudinal strain (ϵ_z) in the longitudinal direction for both specimens.

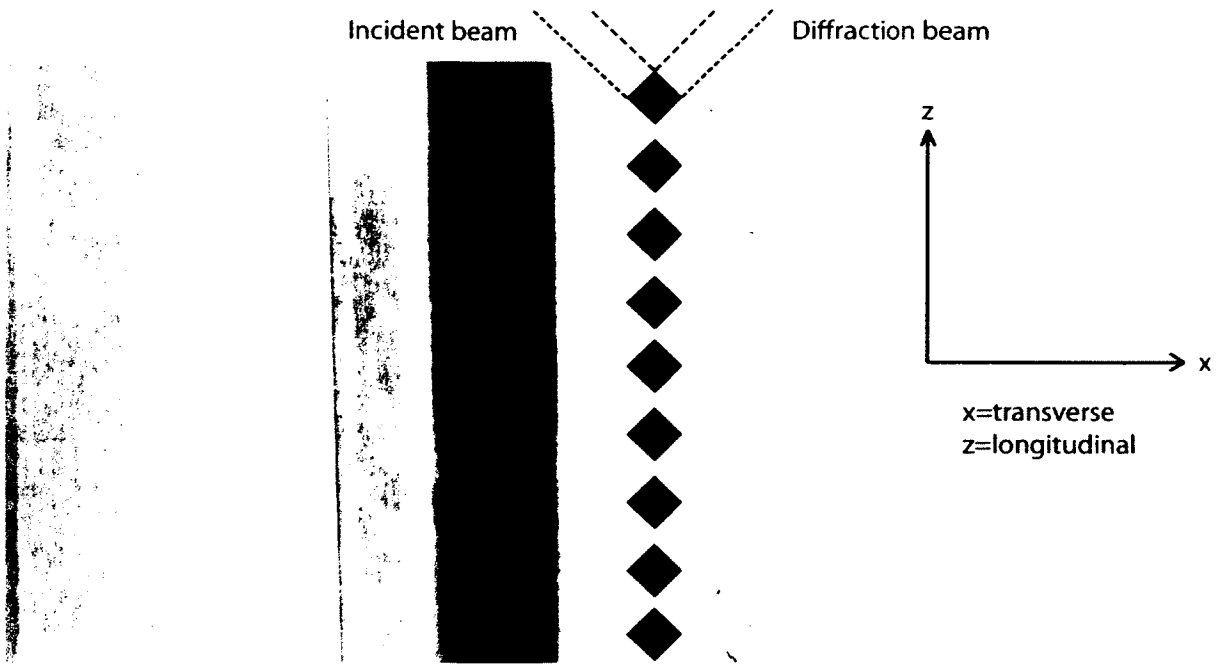


Figure 4.59: Position of longitudinal wall scan of as-welded plate

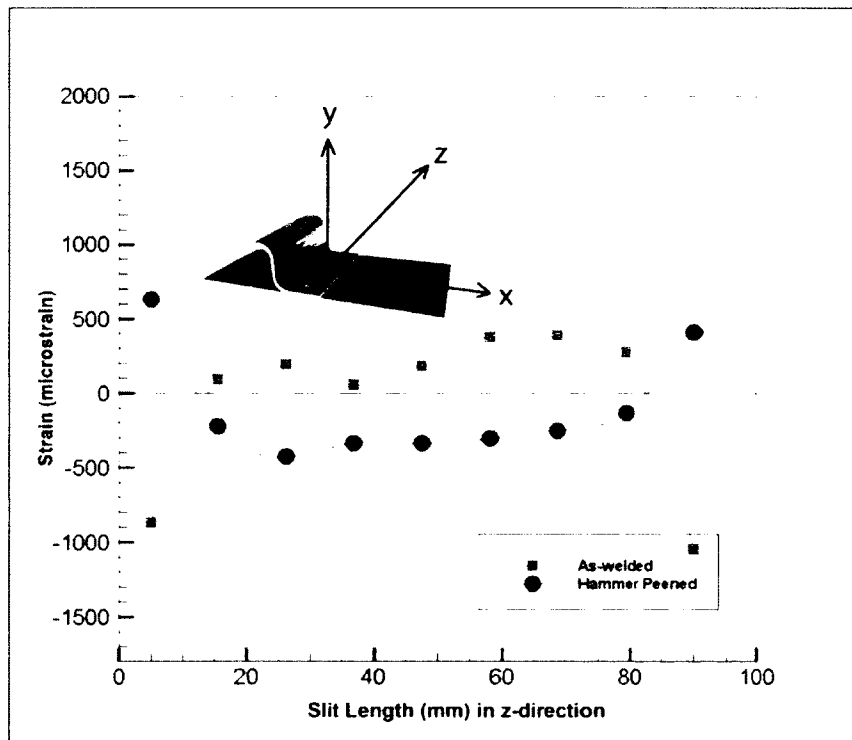


Figure 4.60: Transverse strains (ϵ_x) for as-welded and hammer peened plates

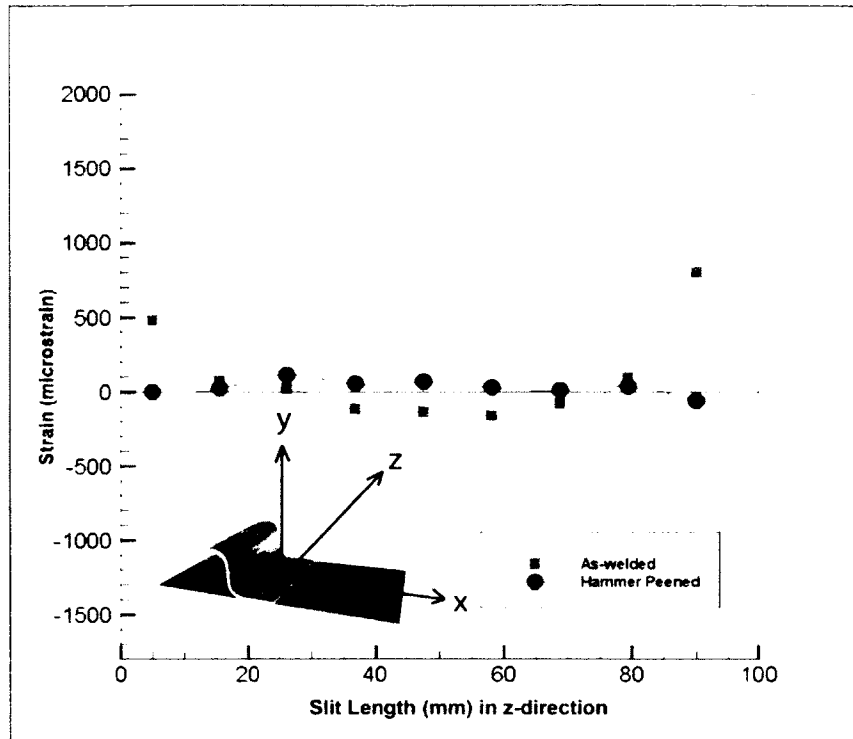


Figure 4.61: Normal strains (ϵ_y) for as-welded and hammer peened plates

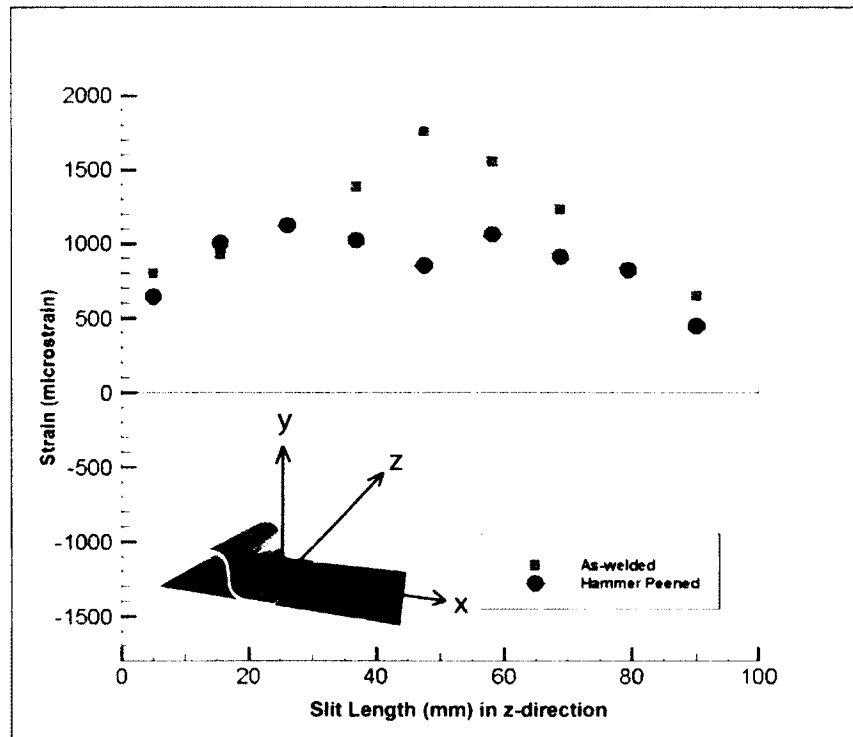


Figure 4.62: Longitudinal strains (ϵ_z) for as-welded and hammer peened plates

Once lattice strains were measured in all three principal directions, the three corresponding stresses were determined using a generalized Hooke's law equation, Eq.2.31.

$$\sigma_{\alpha} = \frac{E}{1+\nu} \left[\varepsilon_{\alpha} + \frac{\nu}{1-2\nu} (\varepsilon_x + \varepsilon_y + \varepsilon_z) \right], \alpha = (x, y, z) \quad (2.31)$$

In general, the diffractometric elastic constants have to be used for values of E and ν that depend on the indices $\{hkl\}$ of the reflection used for the strain measurements. However, the crystallographic anisotropy of the elastic constants is small for aluminum alloys and therefore the macroscopic values were used in stress calculations ($E = 72$ GPa and $\nu = 0.33$), Staron (2002).

The results of the residual stress calculated using the strain from neutron diffraction will be presented in section 5.2.

4.3 Fatigue Testing

Fatigue testing was performed on the as-welded and hammer peened test specimens to study the fatigue lives of these two welding configuration under cyclic loading, which simulates aircraft operation conditions. The purpose of the testing was to determine what effects post welding process of hammer peening had on the fatigue lives of these FSW stringer lap joints. Another purpose of the testing was to determine where the cracks nucleated from and grew; therefore, fractography was carried out on the specimens after the specimens failed.

Experimental Setup

Two sets of test specimens were used in the fatigue tests. The first specimen consisted of two as-welded stringer-to-skin lap joints cut side by side from the test plate. The dimensions of these specimens were 191 x 95 x 3.76 mm. The second set of specimens consisted of two hammer peened lap joints with identical dimensions as the as-welded specimens. The stringer was cut off to allow for optimal gripping of the test specimen in the experimental setup. It was assumed that the removal of the stringer will not affect the fatigue performance of the weld area. Fatigue testing was done on an MTS hydraulic machine with 4 inch grips. Typical fatigue life graphs require testing of several samples at decreasing loading until the fatigue threshold is reached. Due to the limited number of samples available for fatigue testing, this threshold is not determined. Since the amplitude of the cyclic loading has a major effect on the fatigue performance, the S-N relationship is determined for one specific loading amplitude. The amplitude is expressed as an R ratio value, which is the minimum applied load of 5 kN divided by the maximum applied load of 32 KN ($R = \sigma_{min}/\sigma_{max}$), for this experiment, $R=0.16$. The test setup is shown in Figure 4.63. All plates were loaded at a rate of 10 Hz. The overall cross sectional area of the lap joint was 95 mm x 3.76 mm (357.20 mm²) but for the calculation of the stress on the fatigue specimen, only the skin panels thickness was used since it was assumed that the stringer cross section did not contribute to any load carry capacity, Jung (2007). Therefore, the stress range applied to the skin panel cross sectional area (209.95 mm²) was 128.59 MPa (37% of AA 2024-T3 yield strength). A summary of the loading parameters for the fatigue testing is found in Table 4.4.

Specimen	Cross Sectional Area (mm ²)	Max Applied Load (KN)	Load Ratio (R)	$\Delta\sigma$ (MPa)	Frequency (Hz)
First as-welded	209.95	32	0.16	128.59	10
Second as-welded	209.95	32	0.16	128.59	10
First hammer peened	209.95	32	0.16	128.59	10
Second hammer peened	209.95	32	0.16	128.59	10

Table 4.4: Fatigue Test Specimen and loading parameters

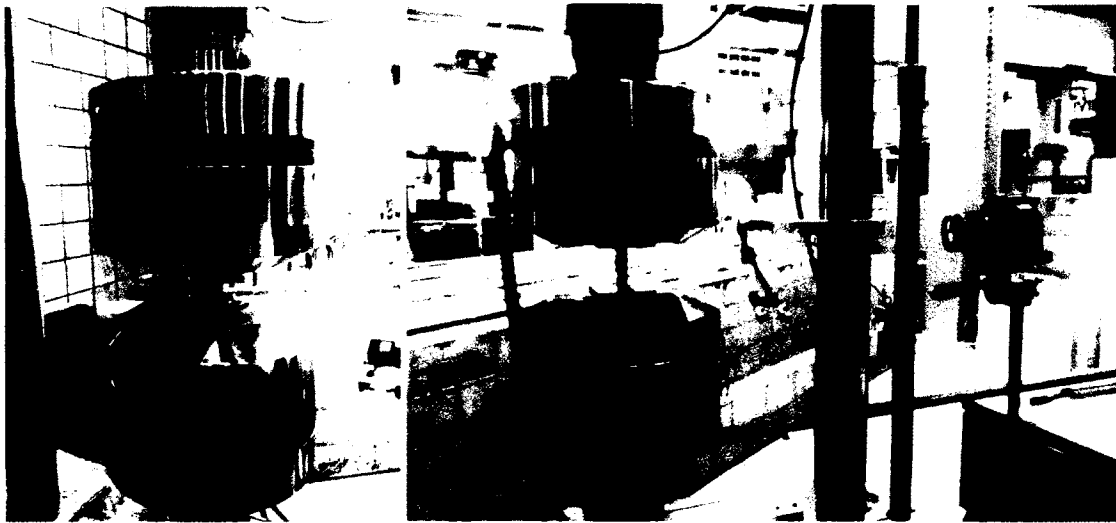


Figure 4.63: Fatigue test setup

Chapter 5

RESULTS AND DISCUSSION

The previous chapter outlined the experimental setup to study the residual stress profiles in the as-welded and hammer peened test specimens using the compliance method and neutron diffraction as well as fatigue testing. Firstly, this chapter presents the results of the residual stress profiles calculated using the crack compliance method in the through thickness (y), transverse (x) and longitudinal (z) direction for the as-welded test specimen and the through thickness (y) direction for the hammer peened test specimen. Neutron residual stress results in the three principal directions are presented next. The results of both methods are compared against one another to check the validity of the compliance method in measuring stress in these non-symmetrical lap joints in the various directions described above. Some qualitative discussion is made on the effects of the triaxial residual stresses on the distortion behaviour of the test specimens before and after hammer peening. The results of the fatigue tests are then presented which looks at fatigue lives of the specimen and a close examination of fracture surface using SEM. Finally, an examination of the failure location of the FSW lap joint is carried out.

5.1 Residual Stress Results Using Crack Compliance Method

5.1.1 Variation in Transverse Residual Stress (σ_x) Through The Thickness of The Weld (y-direction)

Variation in Transverse Residual Stress (σ_x) in As-welded Plate

The first set of residual stress results for the friction stir welded lap joint was the variation in transverse stress (σ_x) through the weld (through thickness direction) of the 3.76 mm plate shown in Figure 5.1. Similar to section 4.1.1.3, the fitted strain was calculated using all 10 Legendre polynomials from orders 2 to 11 of the bottom strain gauge compliance matrix in Figure 4.31. Figure 5.2 shows a comparison between the measured strains and the fitted strains, and Table 5.1 shows the average RMS errors (microstrain) associated

with using various number of compliance functions to fit the strain data given by Eq. 2.20.

$$\bar{u}_\varepsilon = \sqrt{\frac{1}{m-n} \sum_{i=1}^m (\varepsilon_i - \varepsilon_{f,i})^2} \quad (2.20)$$

Table 5.1 demonstrates that increasing the number of polynomials reduced the RMS error between fitted and measured strain values. Using just one polynomial to fit the strain results in an average RMS error of 408 microstrain, this error reduced to 17 microstrains when using more than 8 polynomials. The average RMS error levels off around the 9th and 10th order polynomial, which means that using more polynomials to fit the strain will not improve the accuracy of the fitted strain values. The user of this method has to decide whether it is worth spending the extra time to calculate a compliance function using higher order polynomials of the RMS between the fitted strain and measured strain is only improved by 0.43 microstrains. Using the fitted strain data for the bottom strain gauge and the calculated compliance functions, the values of the unknown coefficients, A_i , were determined using Eq. 2.12, and shown in Table 5.2.

$$\sigma_x(y) = \sum_{i=1}^n A_i P_i(y) = [P]\{A\} \quad (2.12)$$

The residual stress profile was then calculated by multiplying these coefficients with the corresponding Legendre polynomials in the series expansion of Eq. 2.1.

$$\sigma_x(y) = \sum_{i=1}^n A_i P_i(y) = [P]\{A\} \quad (2.1)$$

Figure 5.3 shows the total errors calculated using Eq.2.24 when using 9 orders of polynomial to calculate the stress profile.

$$S_{total,i} = \sqrt{S_{\varepsilon,i}^2 - S_{model,i}^2} \quad (2.24)$$

The errors are greatest at the beginning of the slitting, which corresponds to the distance furthest from the strain gauge location. The error becomes smaller as the slit approaches the strain gauge indicating that the residual stresses are most accurately calculated near

the strain gauge position. The total error associated with the calculated stress is only able to be calculated up to the 9th order polynomial because the calculated total error has two components; the stress variance due to variance in strain which can be calculated for all 10 polynomials and the stress variance from model error which can only be determined for $N-1$, where N is the total number of polynomials used. The residual stress in the through thickness residual stress profile of the as-welded test specimen using 10 polynomials is plotted in Figure 5.4.

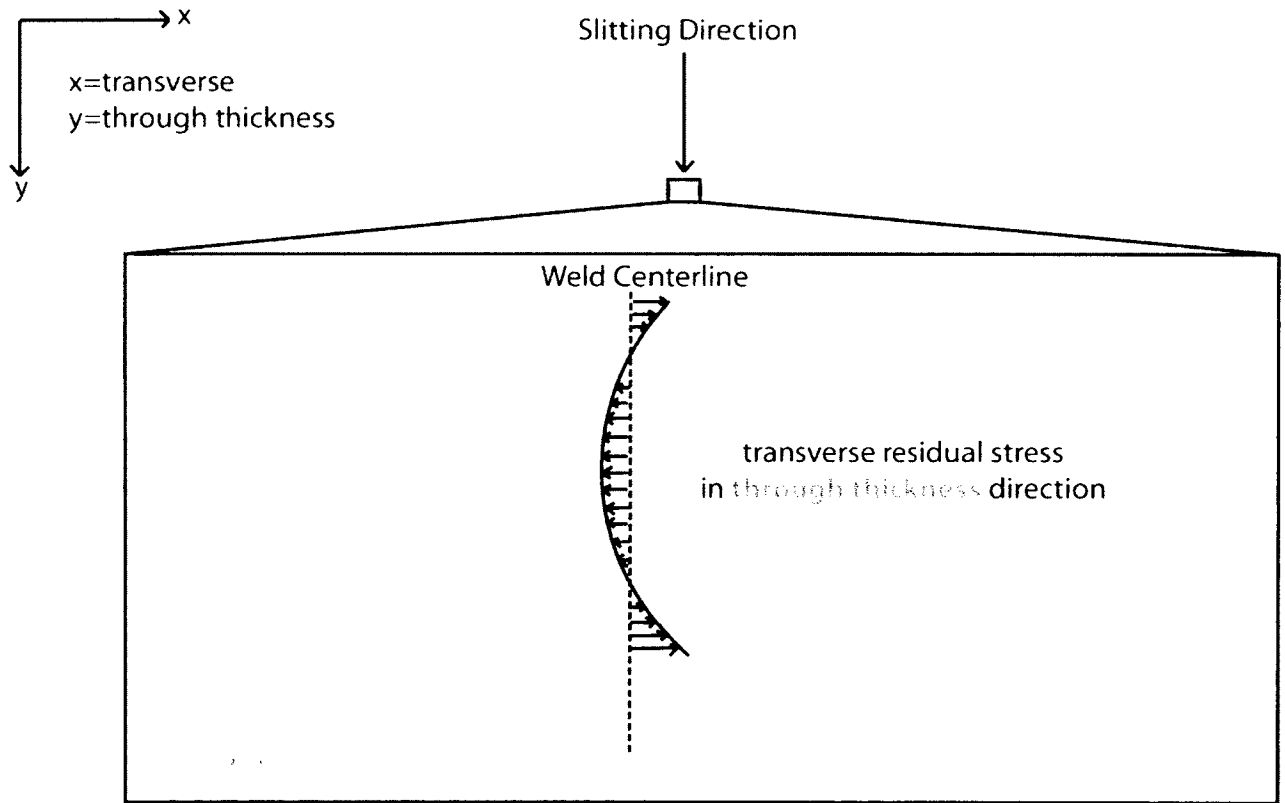


Figure 5.1: Variation in transverse residual stress (σ_x) in the through thickness direction of plate

Number of Polynomials	RMS error (microstrain)
1	408.80
2	313.89
3	139.11
4	72.96
5	35.34
6	30.71
7	17.92
8	17.80
9	18.32
10	17.89

Table 5.1: RMS error for strain fitting of bottom gauge using different number of polynomials

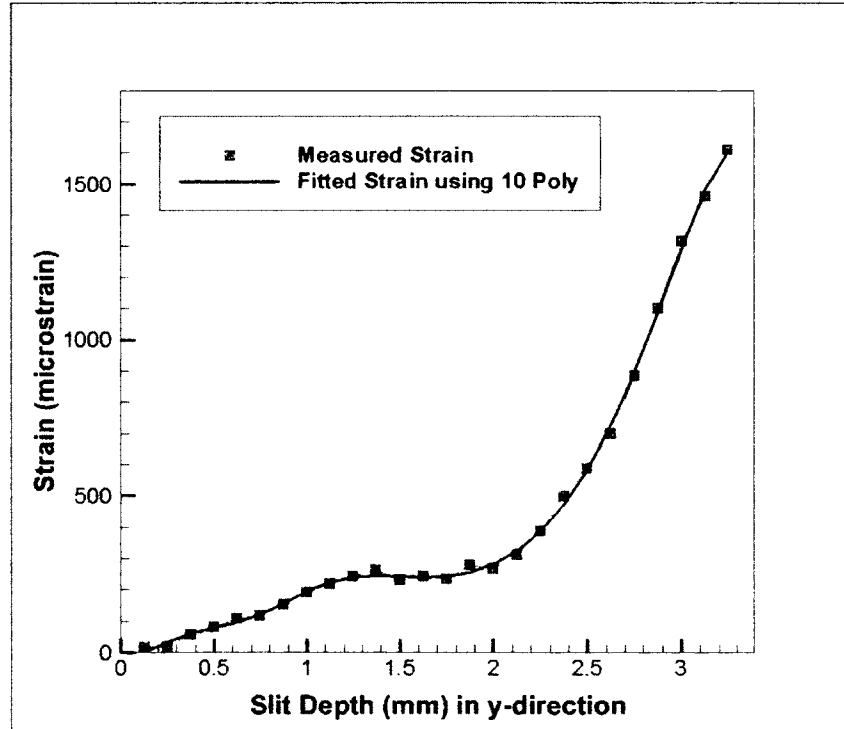


Figure 5.2: Fitted strain (FE model) vs. measured strain (strain gauge) values for as-welded test specimen

Polynomial Order	Coefficient, A
2	-5.10E+13
3	-3.07E+13
4	-9.51E+13
5	-1.26E+14
6	-9.04E+13
7	-8.93E+13
8	-8.03E+13
9	-1.28E+14
10	3.84E+13
11	-5.33E+13

Table 5.2: Calculated A_i values using different orders of polynomials

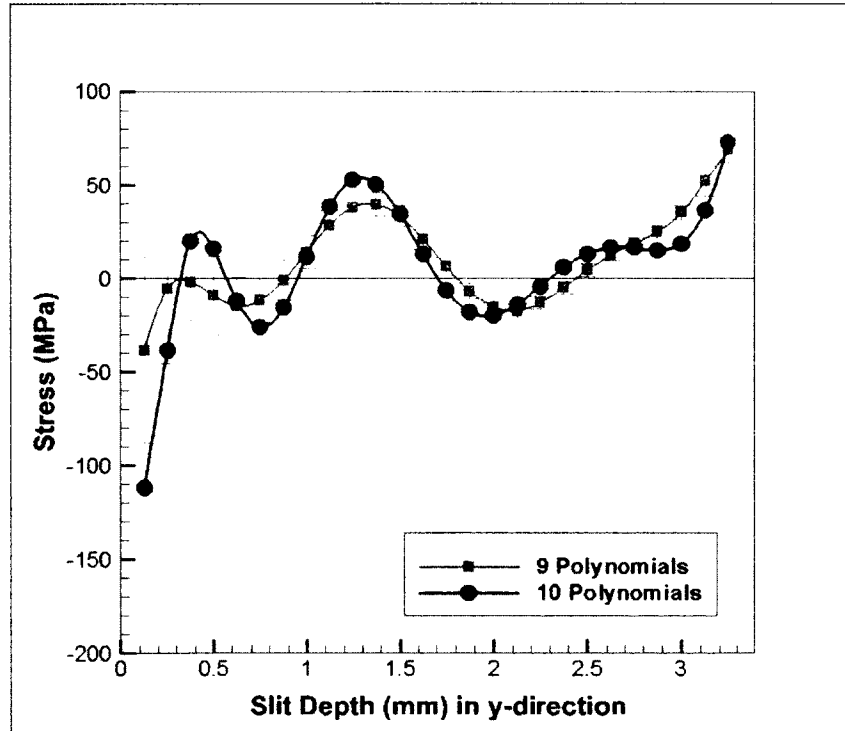


Figure 5.3: Total error of stress profile (σ_x) using Lp9 compared with using Lp10

The plot of Figure 5.4 shows that the as-welded test specimen had a compressive stress of 111 MPa at $y = 0.125$ mm, which then becomes tensile approximately 0.5 mm into the plate. The stress changes between modest levels of compression and tension for the remainder of the slit depth with stresses ranging from 52 MPa in tension to 19 MPa in compression. The maximum tensile stress was calculated 3.25 mm into the plate at 72.8 MPa (21% of AA 2024-T3 yield strength). The fluctuating residual stress profile of the as-welded specimen could be explained by the complex mixing of the two alloys in the through thickness direction as a result of the rotation and downward force of the welding tool. The weld pin acts to rotate and mix the two materials together while the wider shoulder presses downward on the material to contain the soften material from escaping. The downward pressure applied by the weld shoulder as the tool is moved along the weldment caused some of the soften material to push up under the tool tip and into the stringer layer. Upon cooling, different areas in the through thickness direction will cool and contract at different rates causing a variance in residual stresses.

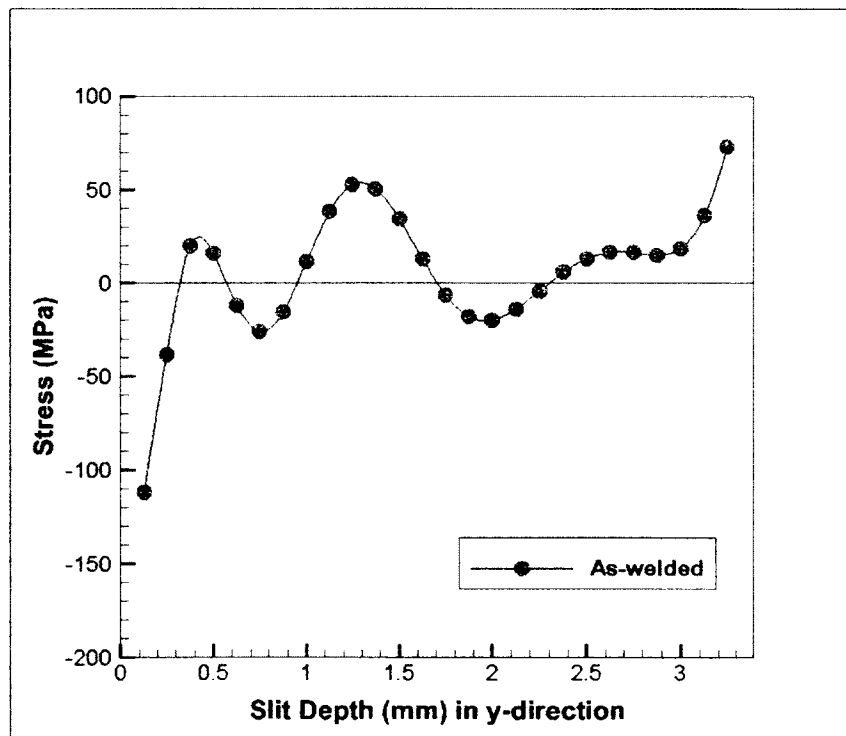


Figure 5.4: Variation in transverse residual stress (σ_x) in the through thickness direction of as-welded test specimen

The weld nugget is dominated by equiaxed grains which have been recrystallized after severe plastic deformation and has a compressive tensile stress. The recrystallization of grains in the weld nuggets also had the low hardness values and was measured at 136 HV. The HAZ has grains which are similar to that of the parent material since this region was not mechanically affected by the welding tool. As the name suggests, this regions is only affected by the heat generated from friction of the weld tool. The hardness value in the HAZ was 129 HV in the skin section which is similar to the hardness of the parent AA 2024-T3 material. The residual stress in this region was very low but there was a peak in tensile stress at approximately 3.25 mm into the plate. This region represents the transition between the HAZ and the parent AA 2024-T3 parent material. The tensile stress could be caused by the heat gradient that is present between the HAZ and the unwelded AA 2024-T3 material. In summary, the weld nugget contained low residual stresses while the edge of the weld zone contained the highest levels of residual stress.

Previous literature on the crack compliance method has examined the residual stress profile in the transverse and longitudinal direction of thin plates with profiles ranging from 30 mm to 70 mm in length with increments of slits ranging from 1-2 mm. Few literatures have examined the residual stress variation through the thickness of plates (less than 5 mm) and in most cases they are assumed to be negligible. The preliminary results of the through thickness, α_x , residual stress in the as-welded lap joint demonstrates that there is in fact a variation in the stress in the through thickness direction and that stress reached a maximum tensile stress of 72.8 MPa which is 21% of the skins yield strength of 345 MPa. More importantly these through thickness residual stresses proves that the crack compliance method can calculate changes in stress across a very thin cross section with slit increments of approximately 0.125 mm. Verification of these residual stresses will be demonstrated in later sections of this chapter.

Variation in Transverse Residual Stress (σ_x) in Hammer Peened Plate

The fitted strain for the hammer peened test specimen was calculated using the measured hammer peened strains from the slitting experiment and the compliance functions used in the as-welded plate since the FE model was identical for both cases. Figure 5.5 shows the fitted and measured strain values for the hammer peened test specimen using all 10 compliance functions. Table 5.3 is the RMS error of the fitted strain values using different number of polynomials, which levels off at 13 microstrains when using 8 or more polynomials to fit the strain data. Even with an average error of 13 microstrains, the fitted strains are almost identical to the measured strains. Figure 5.6 shows the total error calculated when using 9 polynomials compared to using all 10 polynomials which show the total error in the calculation of the residual stresses are greatest at the beginning of the slitting. Table 5.4 is the calculated values of the unknown coefficients, A_i .

Number of Polynomials	RMS error (microstrain)
1	629.37
2	413.69
3	222.74
4	147.87
5	38.91
6	22.03
7	15.79
8	13.04
9	13.39
10	13.38

Table 5.3: RSM error for strain fitting of bottom gauge using different number of polynomials

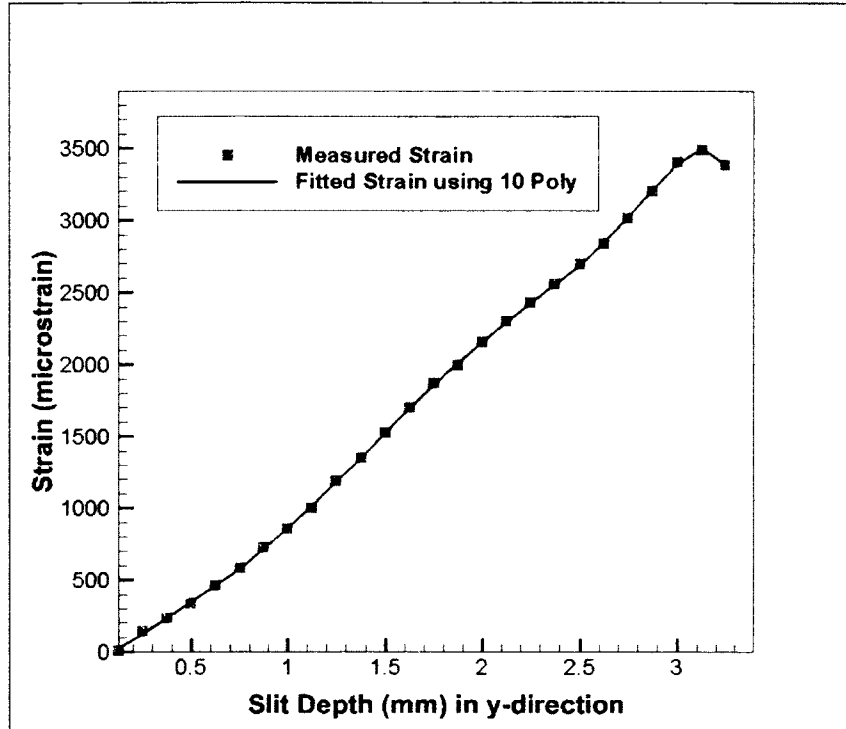


Figure 5.5: Fitted strain compared with measured strain values for hammer peened test specimen

Polynomial Order	Coefficient, A
2	-2.53E+14
3	-1.01E+14
4	-1.25E+14
5	-1.28E+14
6	-1.39E+14
7	-1.80E+14
8	-3.79E+13
9	-1.30E+14
10	2.56E+13
11	-2.99E+13

Table 5.4: Calculated A_i values using different number of polynomials

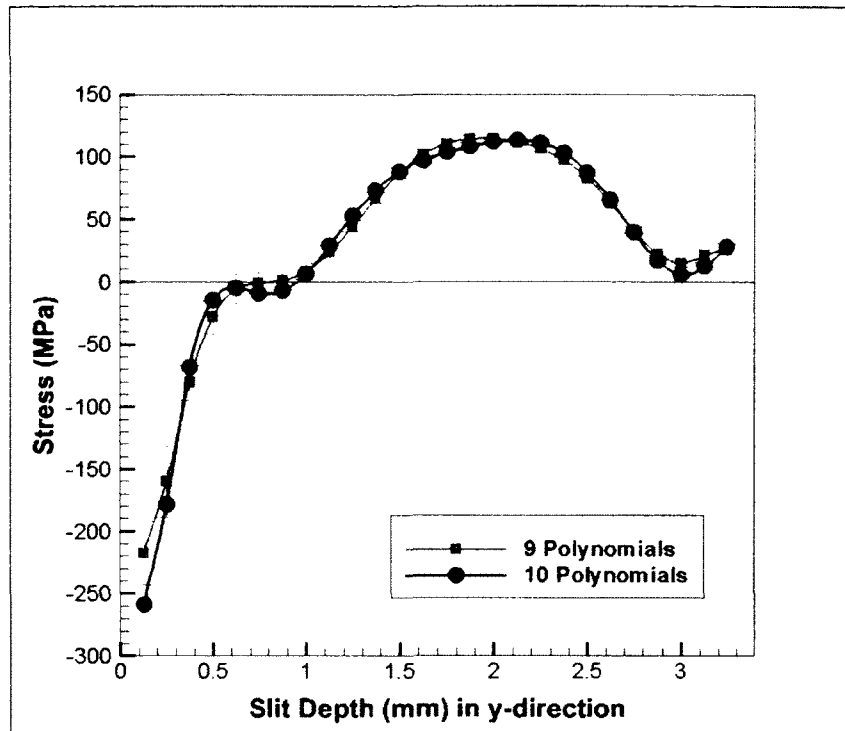


Figure 5.6: Total error for stress using Lp9 compared with using Lp10 for hammer peened specimen

In the hammer peened specimen, the effects of peening the surface is clearly visible. Figure 5.7 is the plot of the hammer peened residual stress profile (σ_x) in the through thickness (y) direction. The stresses at the top surface were compressive; but the magnitude of the stress was greater than that of the as-welded specimen. The compressive stress at the surface was measured at 259 MPa, which is more than half of the AA 7075-T6 stringer's yield strength (503 MPa). This demonstrates that applying the cold working process of hammer peening increases the compressive stress at the surface of the plate which may help delay surface cracks from nucleating and growing, resulting in an improvement in the life of the component. Since the as-welded plate already contained compressive stress in this region, the hammer peening caused those compressive stresses to increase in compression as demonstrated by the increase of stress from 111 MPa in the as-welded plate to 259 MPa in the hammer peened plate. The increase in compressive stress at the surface is only observed for the first 0.5 mm of the plate which suggest that the effects of the hammer peening only affects the top surface of

the material. However, there is also an increase in the tensile stress to 113 MPa approximately 2.125 mm into the plate, which was not present in the as-welded plate. The 113 MPa stress in the middle of the plate is 33% of the skin's yield strength and 22% of the stringer's yield strength. Since residual stresses remain in equilibrium, the tensile stress is a reactionary stress to the compressive stress induced at the surface. If any subsurface cracks were to form, this area would likely be the first site where crack nucleation would begin. The bottom of the plate contains a tensile stress of 28 MPa. Hammer peening caused the hardness of the material to increase in the stringer section and remained the same in the skin section of the lap joint. The peening process caused work hardening on the top surface of the welded plate which caused the hardness values to also increase. The hardness value measured at the weld centerline in the stringer and skin section after hammer peening was 154 HV and 123 HV respectively. The effects of hammer peening restored the hardness value of the welded region close to that found in the un-welded parent material.

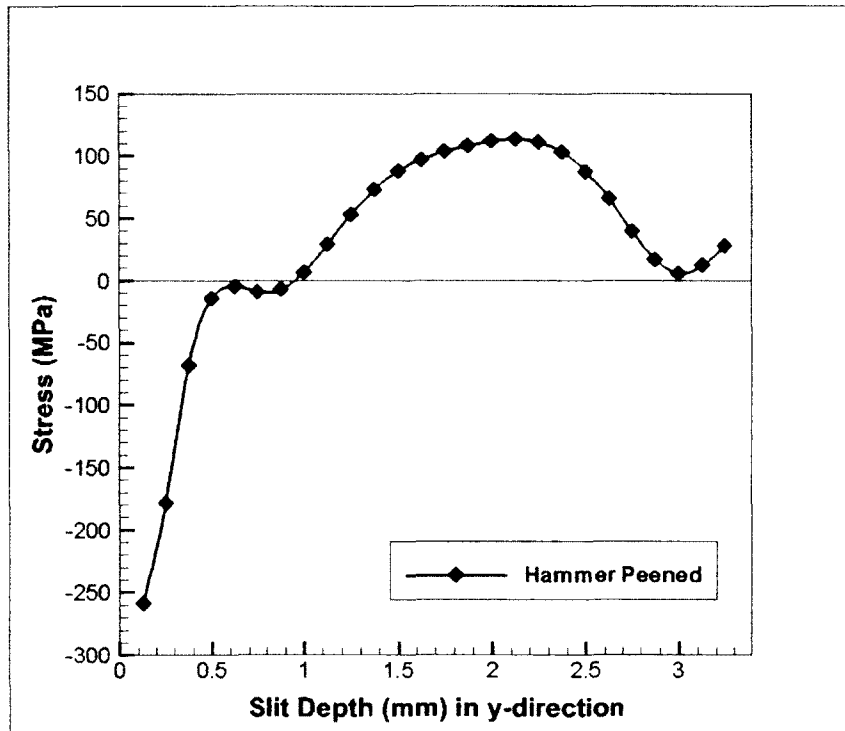


Figure 5.7: Transverse residual stress (σ_x) profile in the through thickness (y) direction of hammer peened test specimen

Figure 5.8 is the comparison of the as-welded and hammer peened through thickness residual stress profiles. The increase in compressive stress at the top surface of the hammer peened specimen had a dominating effect on the majority of the plate's thickness and therefore no trace of the original stress profile can be observed except for the bottom of the plate. At the bottom of lap joint, both specimens show similar tensile residual stresses. This suggests that the effects of hammer peening was not able to penetrate to this depth and so the residual stresses measured at the bottom surfaces of the lap joints are similar before and after hammer peening. If a crack growth is governed by only σ_x in the through thickness direction, these results suggest that surface cracks are not likely to form on the top surface of both test specimens since they both contain compressive stresses right below the surface which would assist in the delay of crack nucleation and growth. The hammer peened specimen would have an improved chance of preventing surface cracks since more stress is necessary to overcome the large compressive stresses from the peening process.

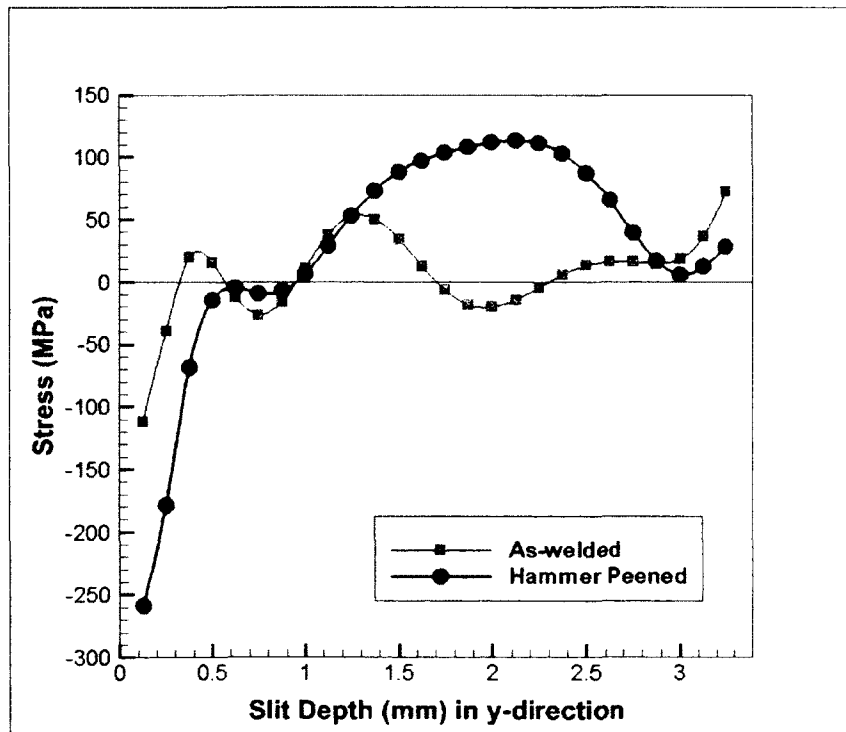


Figure 5.8: Comparison of the transverse stresses (σ_x) in through thickness (y) direction of both specimens

Figure 5.9 shows the process of calculating the fitted strain values, which are used to determine the residual stress profile using a combination of the measured strain from the slitting experiment and the FE compliances. As part of a consistency check to verify that the FE model and compliance functions used to calculate the residual stress were correct, the calculated residual stresses were applied to the original FE model used to create the compliance functions and the resulting back-calculated strains were determined at the bottom strain gauge position as shown in Figure 5.10.

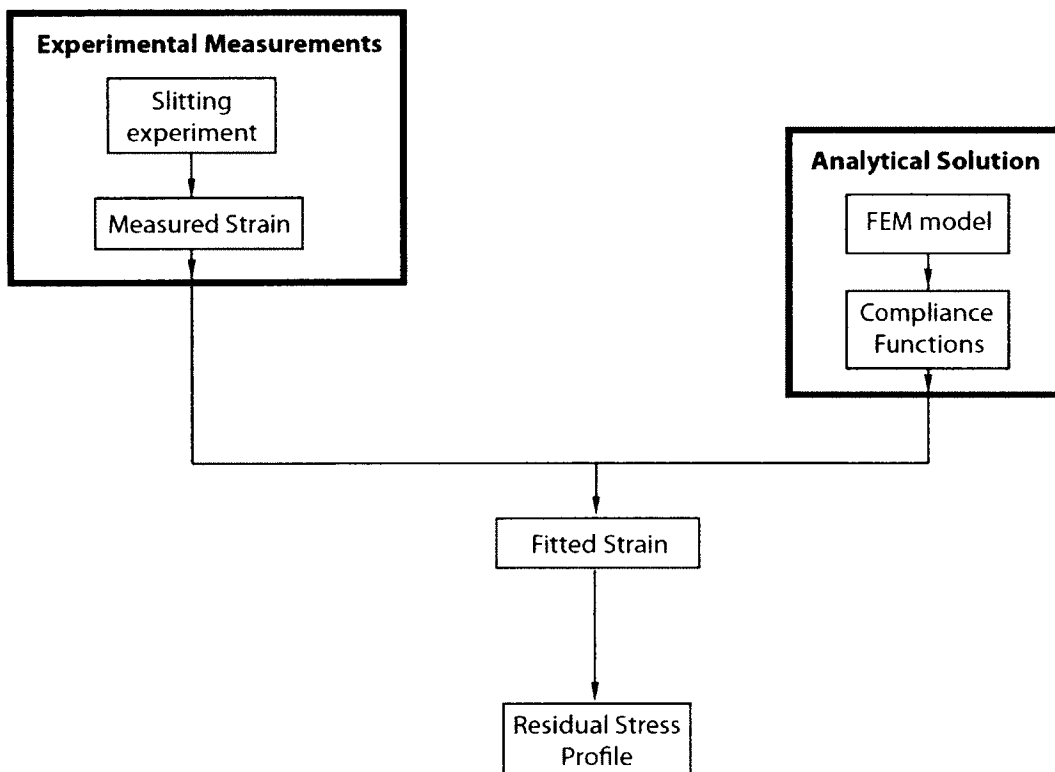


Figure 5.9: Calculation of residual stress from measured strain and FE compliances

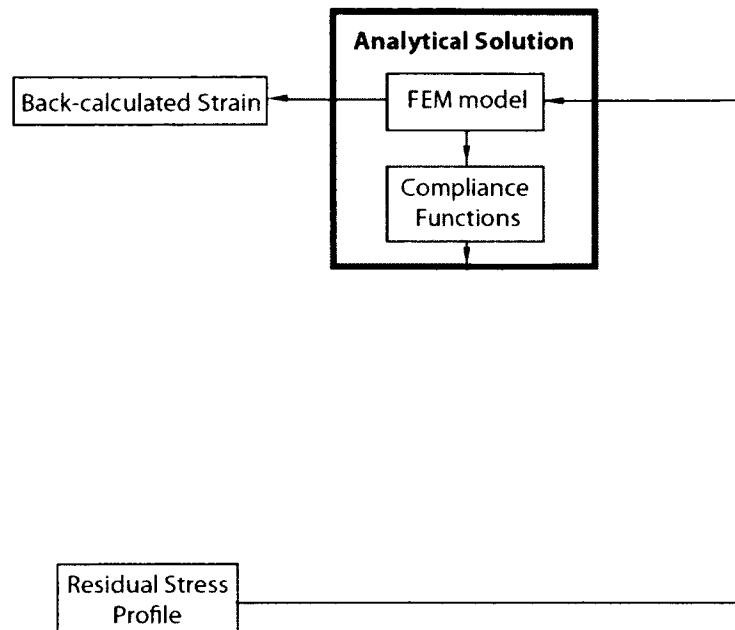


Figure 5.10: Back-calculated strains from back substitution of stress into FE model

These back-calculated strains were compared with the original measured strains from the slitting experiment represented in Figure 5.11 and plotted in Figure 5.12. From the plot, it can be seen that the FE model was able to calculate the correct value of strains from calculated stress and therefore the FE model was verified to be correct. Increase in the difference between the two strain values could be due to accumulative errors with increasing slit depths.



Figure 5.11: Comparison of measured and back-calculated strains

This process of back calculating the strains from calculated residual stress demonstrates the consistency of the FE model to produce the stress from strain and vice versa which is analytical component of the compliance method. The FE model is only used to calculate the residual stress from measured strains and therefore the resulting residual stress depends greatly on the actual values of strains measured by incremental slitting (experimental component of the compliance method). Factors affecting strain measurements include, material, gauge length and position, slit increment, and slitting method. These are independent factors from the FE model that will affect the resulting residual stress calculations using the FE model.

An independent verification of the residual stress profiles for the as-welded and hammer peened specimens will be examined in later sections of this chapter but the results of the residual stresses using the crack compliance method concludes that there is a significant

variation in residual stress both in the as-welded and hammer peened configuration. Notably, after the hammer peening was completed, the transverse residual stress (σ_x) in the through thickness (y) direction rearranged itself resulting in an increased compressive stress below the top surface of the weld and an increase in tensile stress further in the plate.

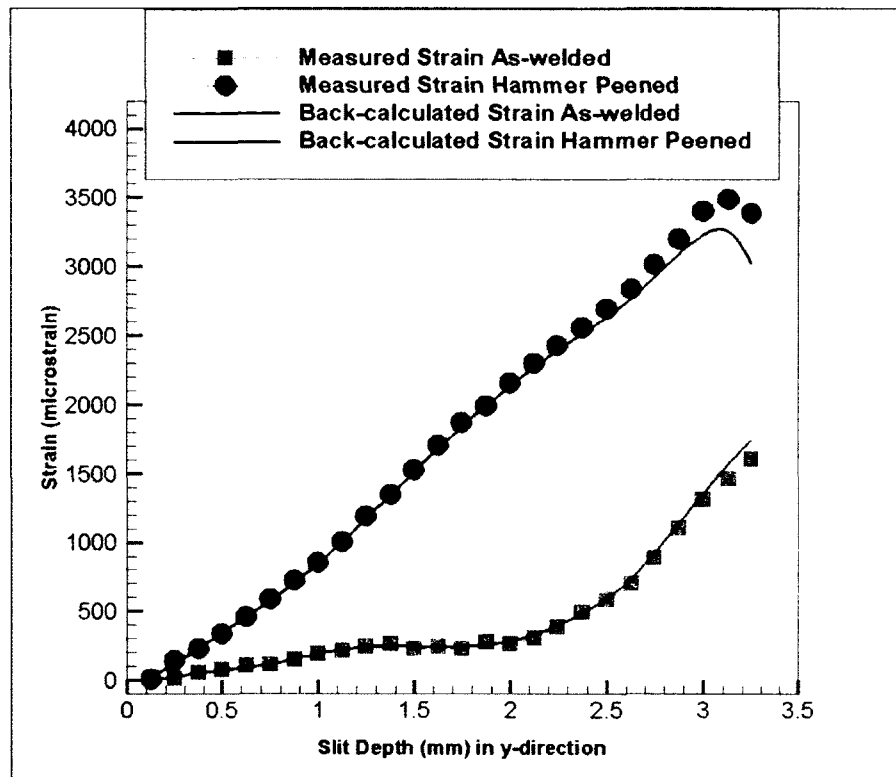


Figure 5.12: Verification of stress by putting back into FE model to determine corresponding strain

5.1.2 Variation in Longitudinal Residual Stress (σ_z) Across the Weld (x-direction)

The second set of residual stress results is the variation of the longitudinal stress, σ_z along the transverse plane of the weld in the x-direction, which is shown in Figure 5.13. This variation in stress was determined for the as-welded test specimen. A total of three strain gauges were used in this experiment and so the following is the results of the residual stress calculated using various combinations of the three strain gauges. Firstly, a single

strain gauge at location 3 (53.5 mm from edge of plate) was used to calculate the variation in stress, σ_z . Figure 5.14 is the fitted and measured strain from gauge 3 position, using all 10 polynomials; the lowest RMS error was calculated at 7.03 microstrains. Table 5.5 is the average RMS error associated with using different number of polynomials and Table 5.6 is the calculated A_i values.

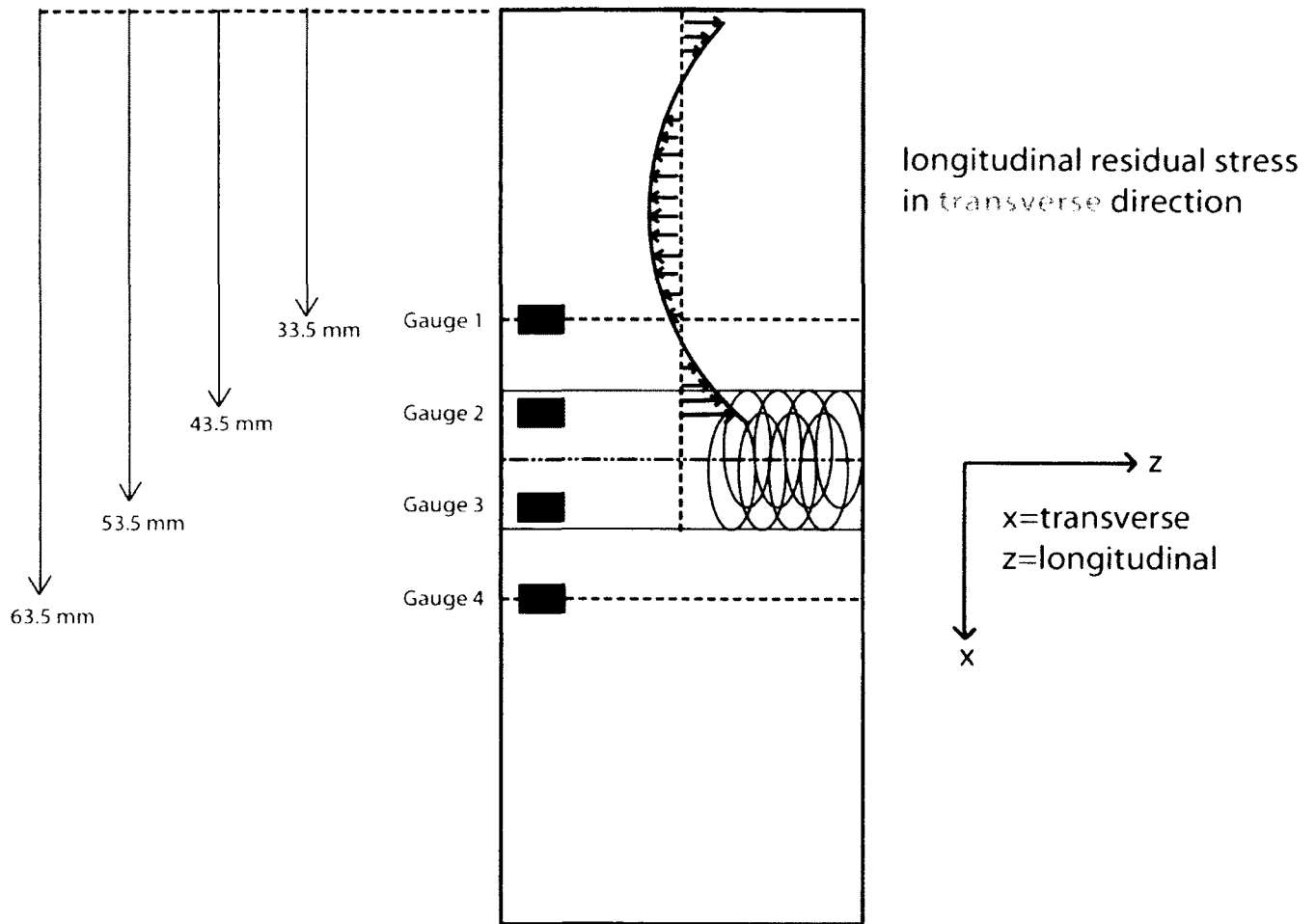


Figure 5.13: Variation in longitudinal residual stresses (σ_z) calculated in transverse direction

Number of Polynomials	RMS error (microstrain)
1	51.93
2	47.72
3	27.79
4	17.28
5	17.24
6	17.13
7	12.49
8	8.12
9	8.16
10	7.03

Table 5.5: RMS error for strain fitting at gauge 3 position

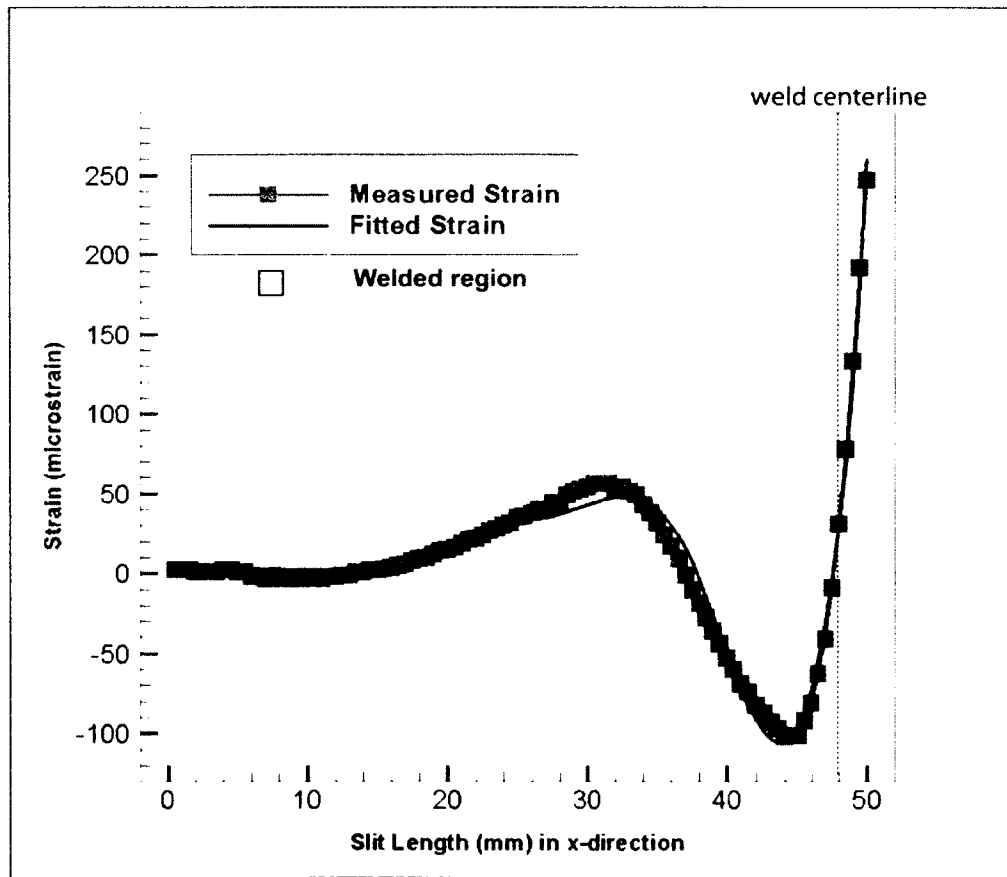


Figure 5.14: Fitted strain vs. measured strain values at gauge 3 position

Polynomial Order	Unknown coefficients, A_i
2	-8.79E+13
3	-2.73E+14
4	-3.86E+14
5	-2.92E+14
6	-2.21E+14
7	-7.28E+13
8	-2.32E+14
9	-2.32E+14
10	-3.21E+13
11	3.22E+14

Table 5.6: Calculated A_i values using different number of polynomials from gauge 3 position

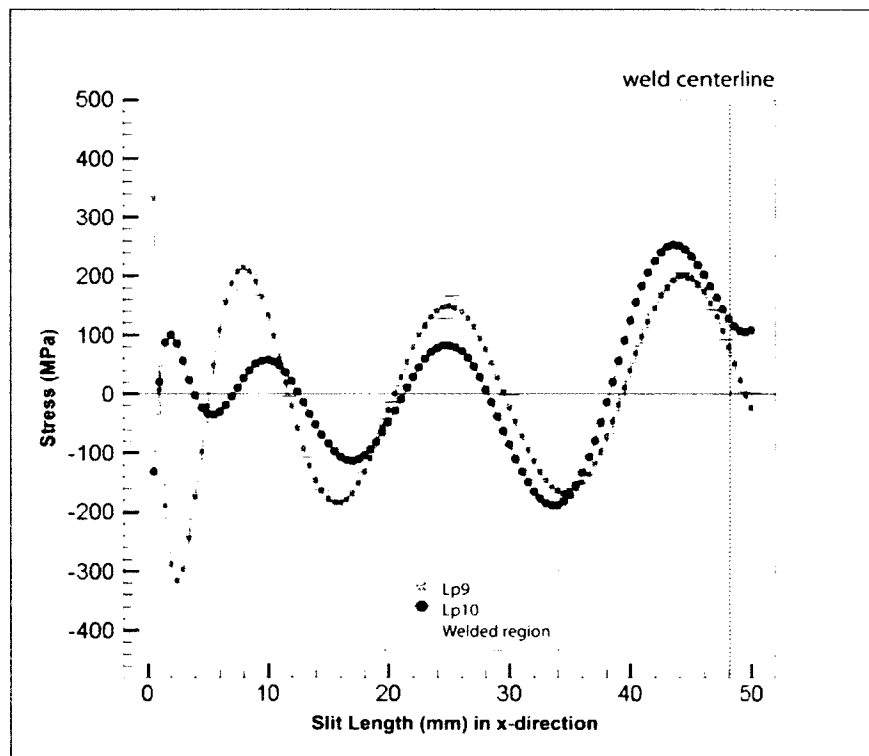


Figure 5.15: Variation in longitudinal residual stress (σ_2) calculated using 9 and 10 orders of polynomials with error bars

Figure 5.15 shows the total error comparing the stress profiles calculated using 9 polynomials as oppose to 10 polynomials and Figure 5.16 is the variation of residual stress (σ_z) in the transverse plane calculated from gauge 3 position alone.

The residual stress profile using gauge 3 alone shows that there is a maximum compressive stress (190 MPa) at $x = 33.5$ mm which corresponds to the region containing only the skin panel. There is a peak tensile stress at $x = 43.5$ mm of 252 MPa (50% of the stringer's yield strength and 73% of the skin's yield strength) which is the region that is between the weld nugget and TMAZ. The hardness profile recorded in this region was 143 HV in the stringer section and 122 HV in the skin section. The stress drops to 128 MPa at the weld centerline in the region that is called the weld nugget. The hardness value in the weld nugget was 143 HV in the stringer section and 116 HV in the skin section. The transverse residual stress profile shows that the highest stresses are located just at the edge of the welding tool between the weld nugget and the TMAZ and has the characteristics of an "M" shaped profile. High levels of residual stresses are expected in the weld region with compressive stresses in the un-welded material from the cooling and contraction of the weld region after welding is complete. To verify the FE model using the strain from just the gauge 3 position, the calculated stress was applied back into the FE model as a pressure load and the corresponding strain values at the gauge 3 position was determined and plotted in Figure 5.17. The plot show both measured and reported strains agree well with one another with a maximum difference of 105 microstrains at $x = 42.5$ mm from the edge of the plate. This region roughly corresponds to the distance where the thickness of the lap joint changes from single thickness of the skin panel to double thickness of the stringer/skin panel. The discrepancy in the two strain values can be attributed to the discontinuity of the specimen geometry changing from a section with single thickness to a section of double thickness. The FE model was simplified as a 2D model and did not take this material step into consideration in order to be able to use the crack compliance method in the transverse direction of the plate. Again, this back substitution of calculated residual stress to get original strain values demonstrates that the FE model is consistent in producing the residual stress results.

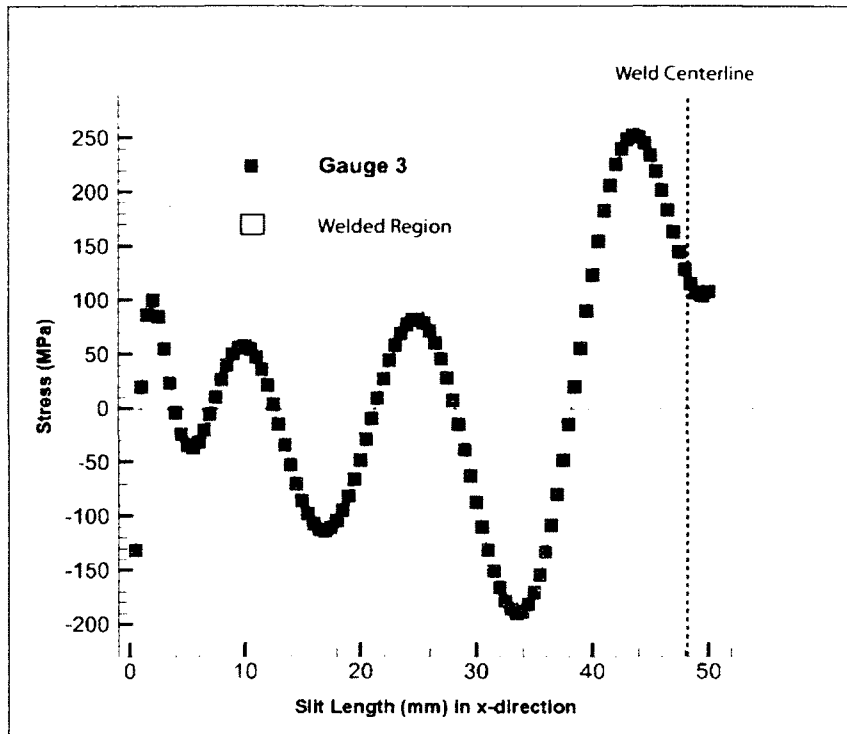


Figure 5.16: Variation in longitudinal residual stress (σ_z) across the weld for as-welded test specimen using gauge 3 alone

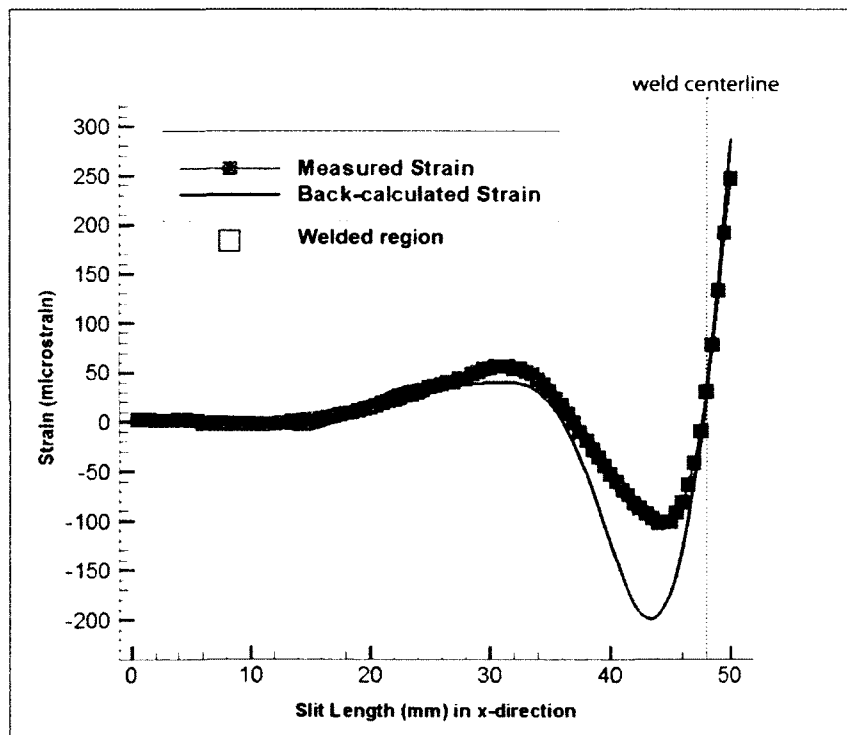


Figure 5.17: Back-calculated strain vs. original measured strain values in transverse direction

Figures 5.18 and 5.19 are the longitudinal residual stress variation (σ_z) plotted using gauges 1 (33.5 mm from edge of plate) and 2 (43.5 mm from edge of plate) respectively. The residual stress trend can be easily seen in Figure 5.20 where all three stresses are plotted together for the three different strain gauges. Using gauge 1 alone shows that the residual stresses away from the weld are low and mostly compressive. These values of stress agree with that found in butt welded joints at distances far from the weld region, Prime (2002). To compared the effects of calculating residual stresses from the three different gauge position, a slit length of $x= 0.5$ mm is chosen as a reference point to compare these three different residual stress values at this position. The residual stress using gauge 1 alone was 79 MPa in tension. At the same position gauge 2 and gauge 3 gave a stress value of 173 MPa and 131 MPa in compression respectively. Three gauges measuring three different values of strain for the first slit depth produced three different residual stress values. Since gauge 1 is closest to the first slit, it can only be assumed that it has the highest sensitivity to strain release from the slit produced from the WEDM and therefore produce the residual stress closest to the original residual stress present.

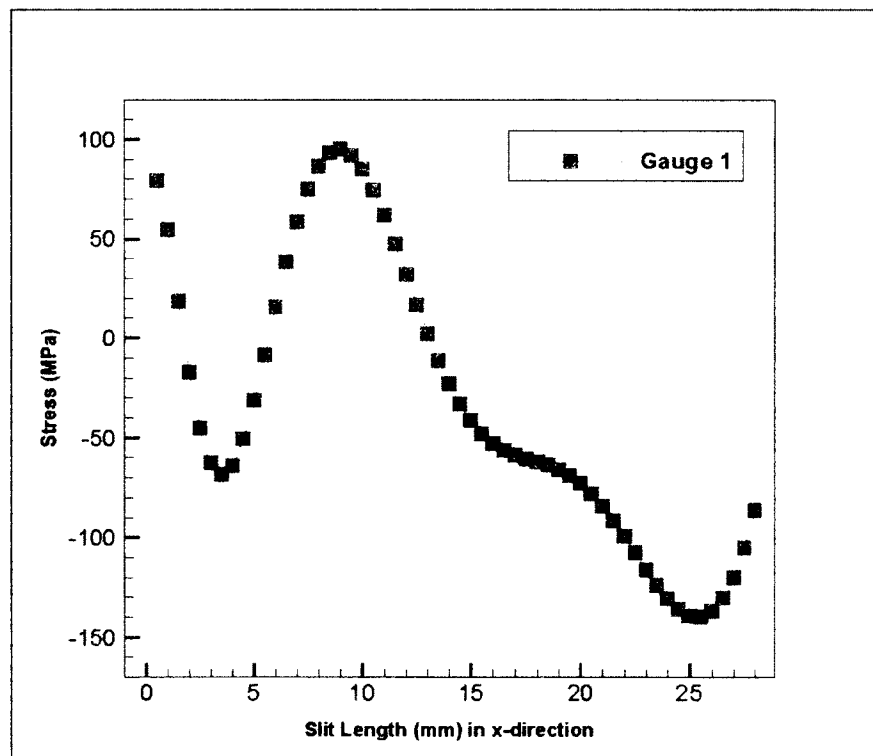


Figure 5.18: Variation in longitudinal residual stress (σ_z) across weld from gauge 1 position alone

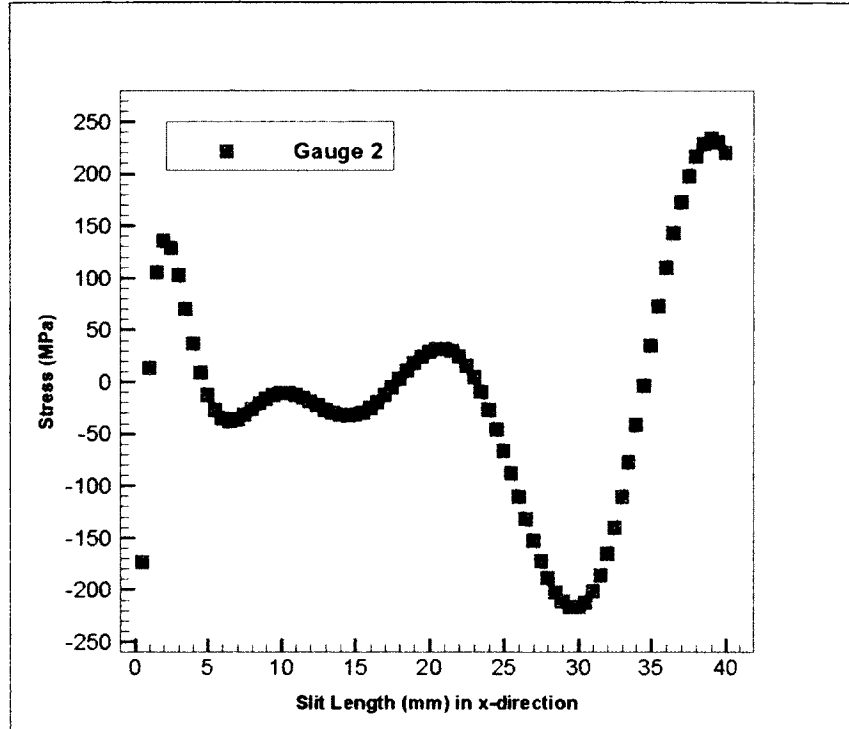


Figure 5.19: Variation in longitudinal residual stress (σ_z) across the weld from gauge 2 position alone

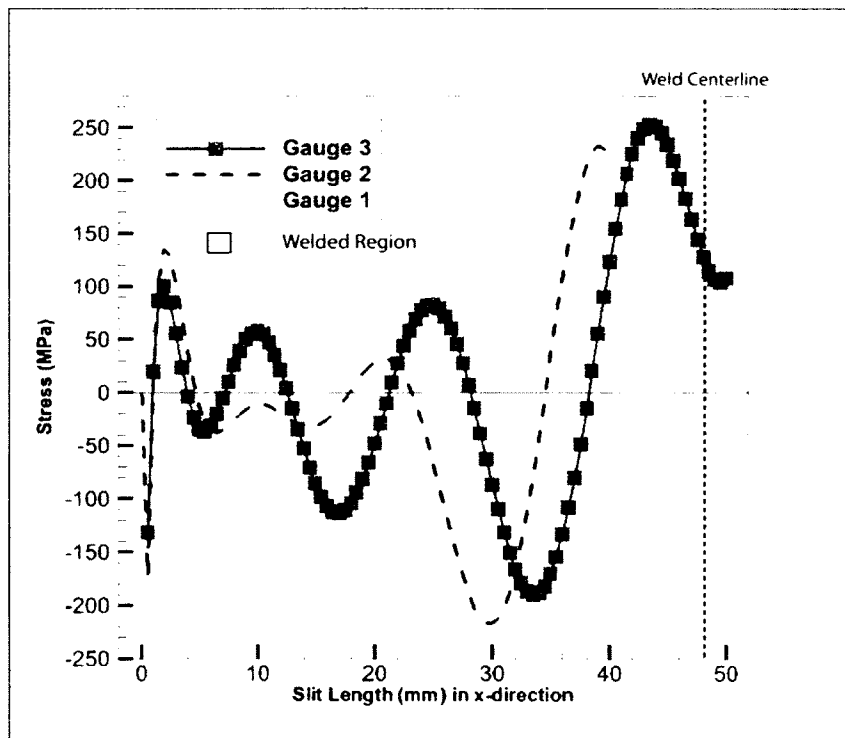


Figure 5.20: Comparison of longitudinal residual stresses (σ_z) in transverse direction from gauges 1,2 and 3

The next set of residual stress results examines the effect of using two gauges to determine the variation in longitudinal residual stress (σ_z) in the transverse (x) direction, which is a hybrid of the crack compliance method. Previously, only one gauge is used in the residual stress calculations. There has been literature on using a combination of two strain gauges, Rankin et al. (2003). These sets of results further investigate the effects of using a combination of two strain gauges by determining the residual stress from several combinations of two strain gauges along the surface of the specimen. Figure 5.21 shows the first 10 mm of the variation in longitudinal residual stress (σ_z) across the weld using various numbers of strain values from gauge 1 and then switching back to the strain values from gauge 3. It appears that using 5-15 strain values from gauge 1 to calculate the residual stress caused the stress to decrease in magnitude and converge to a single profile. When more than 15 strain values were taken from gauge 1, the stress profile diverges again and the magnitude of the stress increased. Therefore, it was determined that using 15 strain values from gauge 1 and the rest from gauge 3 gave the best residual stress profile. Using a combination of gauges 1 and 3 reduced the stress at the first slit depth of $x = 0.5$ mm from 131 MPa in compression to 19 MPa in tension. At a slit depth of 2 mm, using gauge 3 alone produced a stress of 100 MPa in tension compared to a stress of 21 MPa when using two gauges.

Figure 5.22 clearly shows the change in residual stress profile using gauge 3 strain values alone and using the first 15 strain values from gauge 1. Since the first 15 slits are closer to gauge 1 than gauge 3, the first 15 strain measurements measured at gauge 1 would be more sensitive to strain changes than taking the same 15 strain values from gauge 3 which is farther away from the slit. The high compressive stress at the beginning of the stress profile is reduced when using two gauges. Next, the residual stress profile using a combination of gauges 2 and 3 are plotted in Figure 5.23. The stress profile converges when using up to 20 strain values from gauge 2 and then switching to gauge 3. Figure 5.24 shows the residual stress profile using strain gauge 3 alone and that using a combination of gauges 2 and 3. Figure 5.24 shows that using gauges 2 and 3 had less of an effect on the residual stress profile than using gauges 1 and 3 because gauge 2 is closer

to gauge 3 than gauge 1. Gauge 1 position is able to measure changes in strains from the first few slits better than either gauges 2 or 3. Since the rest of the strains are taken from the gauge 3 position the stress profile for the remainder of the slit is the same when using two gauges and using just one gauge from gauge 3 position.

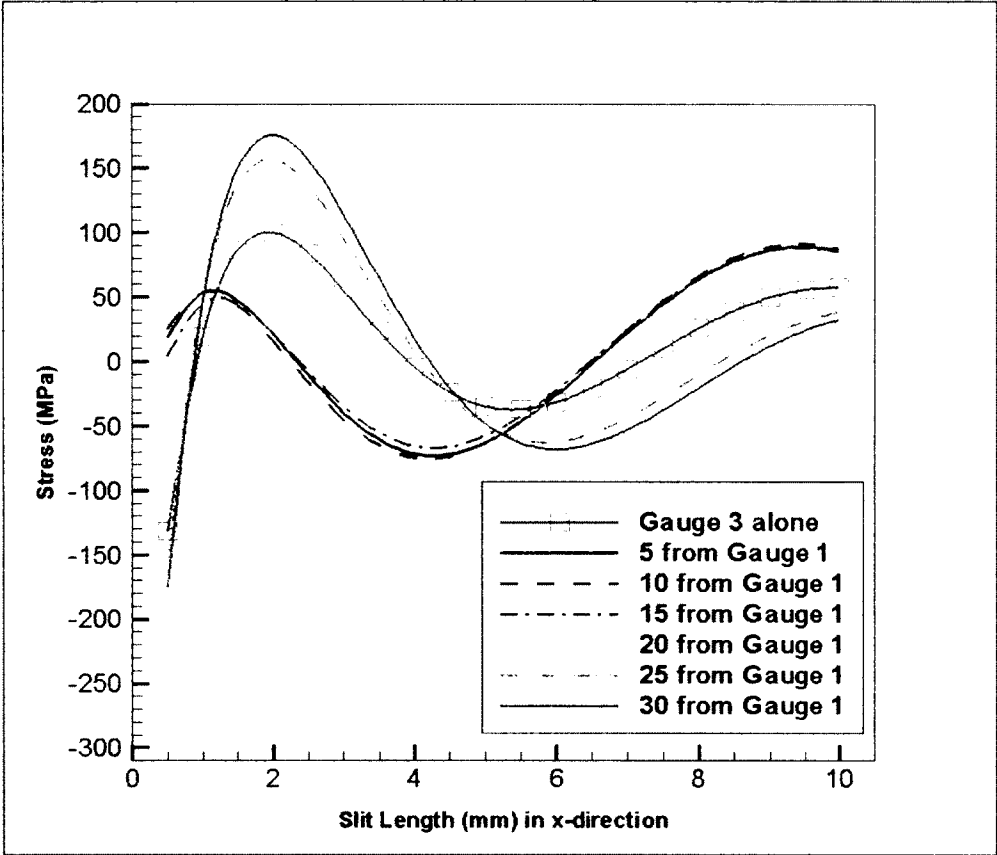


Figure 5.21: Variation in longitudinal residual stress (σ_z) using different combinations of gauges 1 and 3

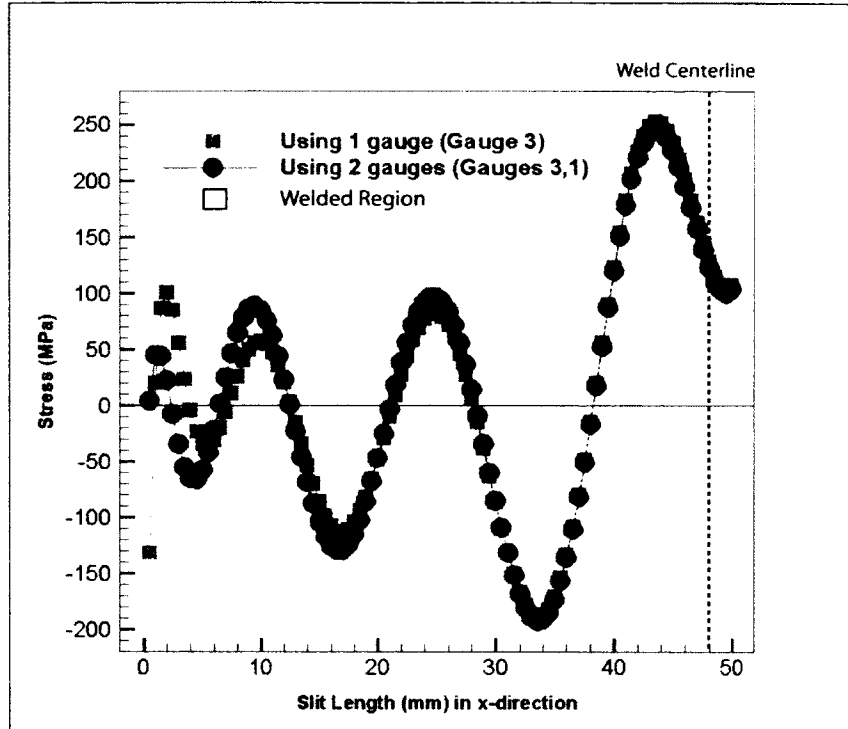


Figure 5.22: Variation in longitudinal residual stress (σ_2) in transverse (x) direction using a combination of gauges 1 and 3

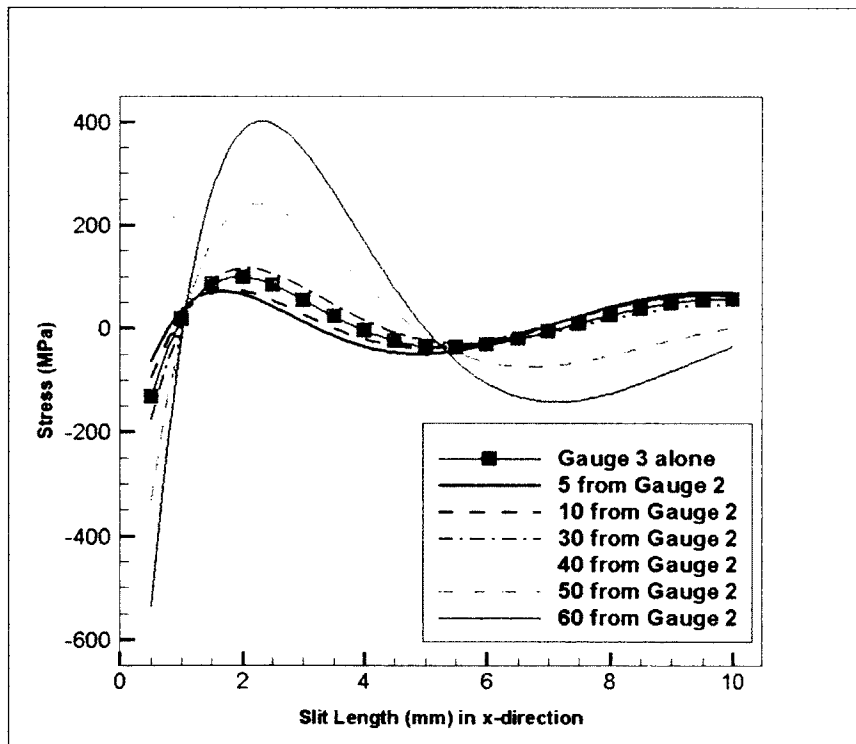


Figure 5.23: Variation in longitudinal residual stress (σ_2) using different combinations of gauges 2 and 3

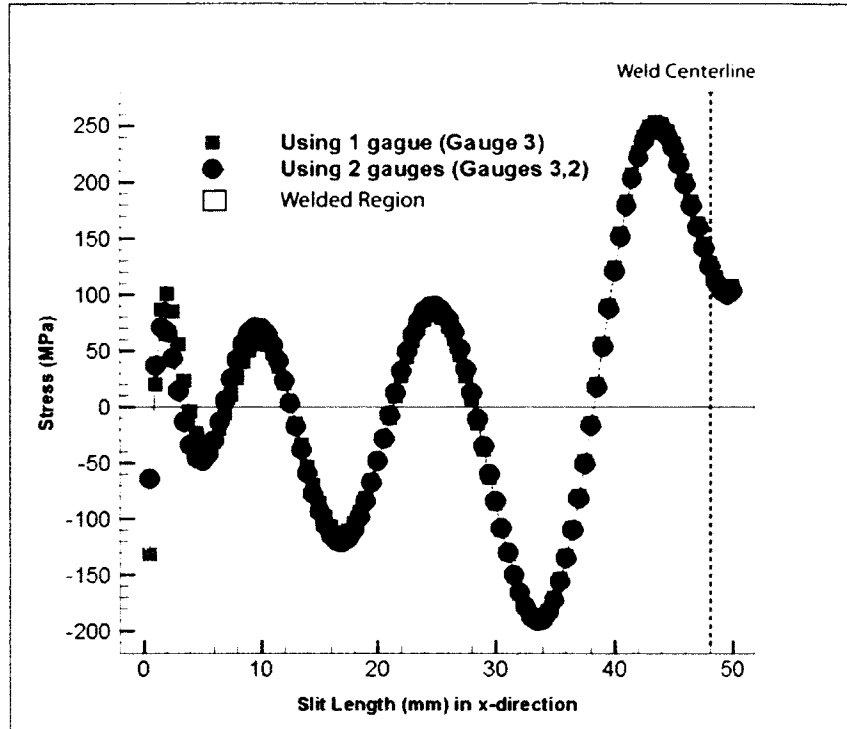


Figure 5.24: Variation in longitudinal residual stress (σ_z) in transverse direction using gauges 2 and 3

After determining the residual stress profile (σ_z) in the transverse direction of the as-welded specimen using different combinations of strain gauges and orders of polynomials, it was concluded that using a combination of gauges 1 and 3 gave the best profile of the residual stress in the transverse direction, which shows a peak in tensile residual stress in the weld region and reduced residual stresses further from the weld in the un-welded parent material. As stated before in section 4.1.1.3, there is no set criteria that is used to determine how many strain values from the second strain gauge is taken to calculate the residual stress profile. For this particular case two strain gauges (gauge 1 and 3) were used to help improve sensitivity of strains measured near the edge of the plate since gauge 1 was more sensitive to changes in strains than gauge 2 for the first few slit increments.

5.1.3 Variation in Transverse Residual Stress (σ_x) Along Weld Centerline in z-direction

The previous two sections examined the residual stress variation through the thickness (y) and in the transverse (x) direction of the plate. Since one of the objectives of the thesis was to study the triaxial residual stresses in these FSW lap joints, the residual stress profile in the third direction was required which was the variation in transverse residual stress (σ_x) along the weld. In this section, the final set of results is the variation in transverse residual stress (σ_x) along the weld centerline (z-direction) for the as-welded test specimen will be presented (Figure 5.25). Similar to the transverse residual stress measurement, a total of three strain gauges were used in this experiment as a hybrid of the crack compliance method. The residual stress profile from the first strain gauge position alone is examined first. At gauge 1 position (18.14 mm from edge of plate), strains were recorded for the first 12 mm of slitting. 10 polynomials were used to fit the strains, which gave an average RMS error of 5 microstrains shown in Table 5.7. The residual stress profile is calculated and plotted in Figure 5.26. The strain gauge 1 position located 18.14 mm from edge of the plate was able to record strains for the first 12 mm of the slitting experiment. The first two slit depths shows a difference in stress of over 1500 MPa. These large values of residual stresses, which are more than three times the yield strength of both parent materials, are not correct. Possible explanations for this large value of residual stress is the inability for gauge 1 position to measure sensitive strain values at the beginning of the slit, this will translate to an error in the residual stress values at the beginning of the slit. After the first 4 mm, the stresses are in the range of 103 MPa in tension to 120 MPa in compression which suggest strains measured closer to the strain gauge position were more accurate than the strains measured further away from the gauge. Another possible explanation for the large residual stresses could be a result of over simplification of the 2D FE model used to calculate the compliances for the slitting in the longitudinal (z) direction, which geometry was non-uniform in the out of plane direction. This resulted in an inadequate representation of the compliances for the transverse residual stresses (σ_x) in the longitudinal (z) direction.

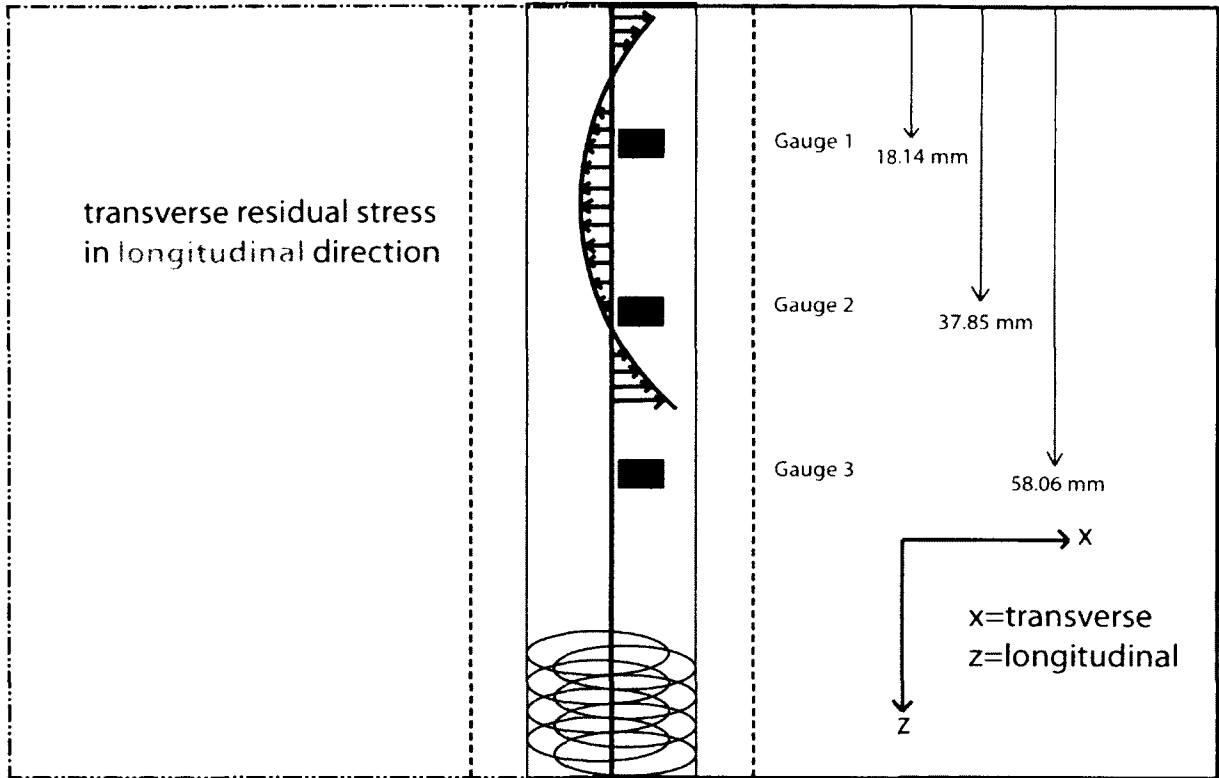


Figure 5.25: Variation in transverse residual stress (σ_x) along the weld centerline

Number of Polynomials	RMS error (microstrain)
1	21.14
2	17.07
3	12.53
4	11.09
5	7.49
6	6.38
7	5.34
8	4.59
9	4.58
10	4.78

Table 5.7: RMS error of fitted strains at gauge 1 position

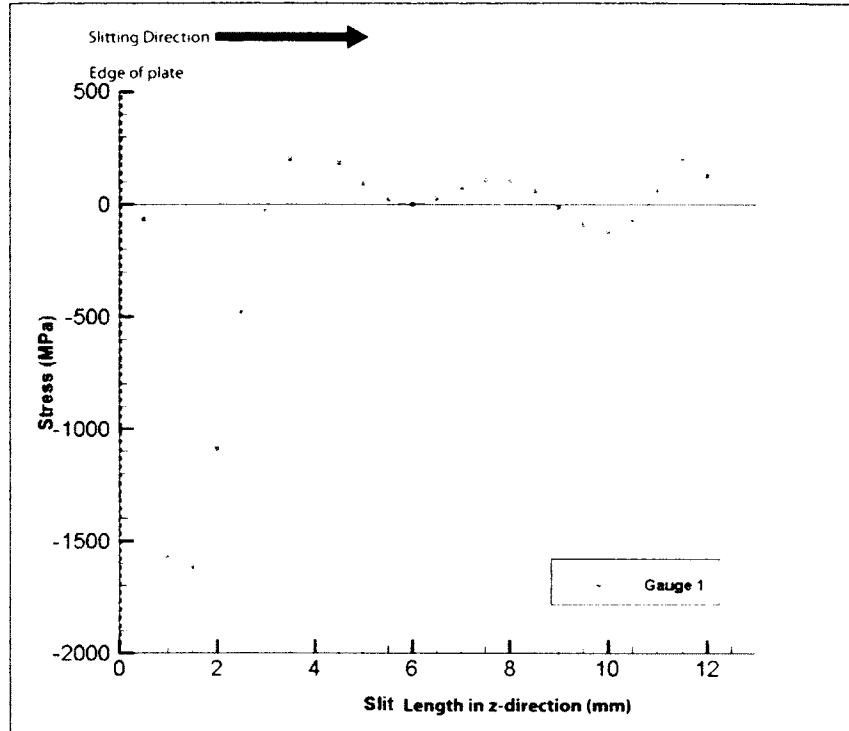


Figure 5.26: Variation in transverse residual stress (σ_x) in longitudinal direction from gauge 1 position

The same procedure was carried out for gauge 2 (37.85 mm from edge of plate) and gauge 3 (58.06 mm from edge of plate). At gauge 2 position, strain data was recorded up to $z = 30$ mm and at gauge 3 position, $z = 46$ mm. The RMS error between the fitted and measured strains for gauge 2 was 2.36 microstrain and 2.37 microstrain for gauge 3 position. The RMS error data for gauge 2 and 3 are summarized in Table 5.8 and 5.9 respectively. The longitudinal residual stress from gauge 2 and gauge 3 positions are plotted in Figures 5.27 and 5.28 respectively.

As a self-consistency check explained in section 5.1.1, the calculated residual stress was applied to the FE model and the resulting strains were recorded. These were called the back-calculated strains that were compared with the original measured strains using the strain gauges. Figure 5.29 is the back-calculated and original measured strain values at gauge 3 position, which verify the FE model used to calculate the residual stress is

correct. The two values of strains agree with one another quite well up to the last slit depth of $z = 46$ mm. The agreement between measured strain values and back-calculated strain values show that the error in residual stress may not be due to the model but due to the strain readings themselves. If the geometry was symmetrical about the slit line, any strain released should theoretically be the uniform about the slit line. If there is a protrusion on one side of the slit line, when the strain is released by slitting, one side of the component will have a different strain value than the other side. This non-uniform strain reading will cause errors in residual stress calculations.

Polynomial Order	RMS error (microstrain)
1	96.96
2	26.46
3	15.48
4	12.01
5	6.32
6	3.02
7	2.67
8	2.64
9	2.60
10	2.36

Table 5.8: RMS error of fitted strains at gauge 2 position

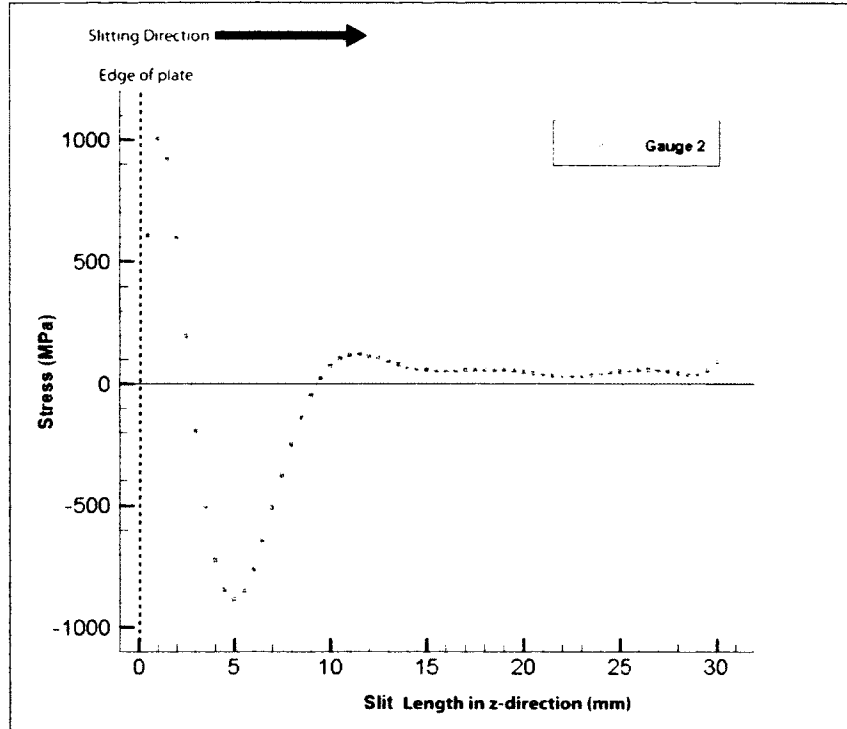


Figure 5.27: Variation in transverse residual stress (σ_x) in longitudinal direction from gauge 2 position

Polynomial Order	RMS error (microstrain)
1	15.92
2	15.86
3	11.74
4	7.91
5	7.89
6	5.40
7	5.19
8	5.21
9	2.46
10	2.37

Table 5.9: RMS error of fitted strains at gauge 3 position

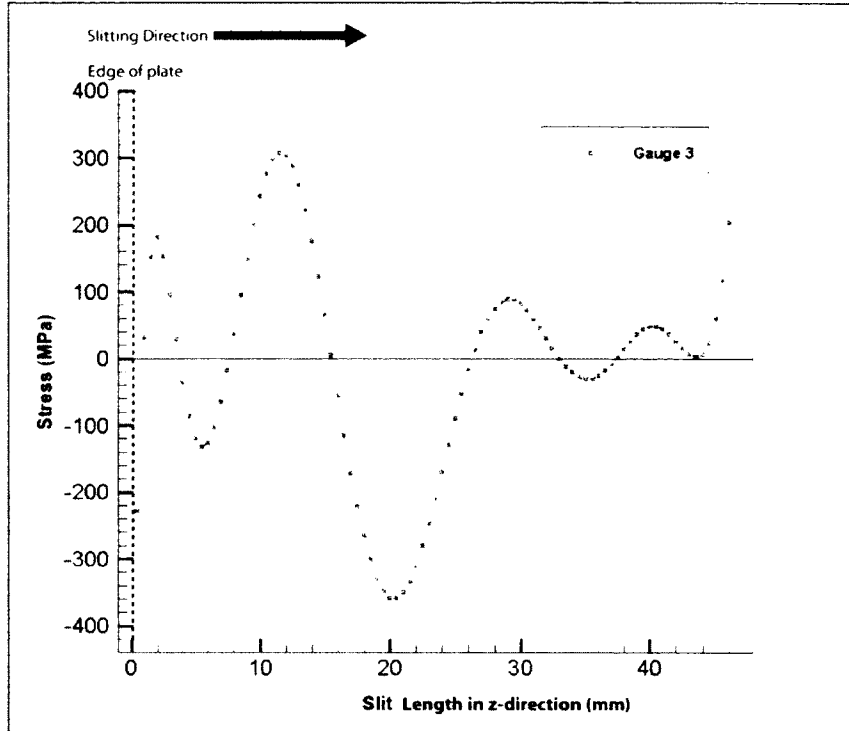


Figure 5.28: Variation in transverse residual stress (σ_x) along weld centerline from gauge 3 position

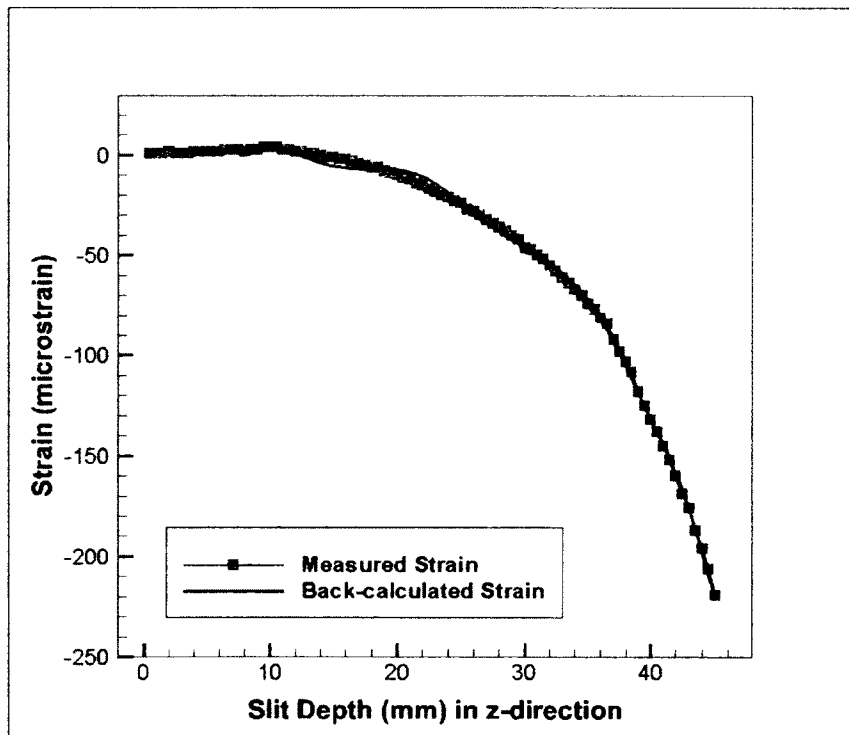


Figure 5.29: Gauge 3 back-calculated strains

The large increase and decrease in stress at the beginning of Figure 5.27 show that gauge 2 position had a similar problem with detecting accurate strain values for the first 10 mm of the slitting ranging from 1001 to -884 MPa. After a slit length of $z = 9.5$ mm, the remaining residual stress is in tension with a maximum stress of 120 MPa. For the gauge 3 position, the magnitudes of the stress at the beginning of the slit is lower than that recorded for the first two gauge positions and range from 306 to -358 MPa for the first 22 mm of slitting.

When examining the residual stresses from the three strain gauge positions, there is no clear pattern as to what the residual stress profile should be. Using different strain measurements from the three strain gauges produced residual stress profiles that were not comparable to one another with varying magnitudes of stress. It is concluded that the crack compliance is unable to capture the accurate change in residual stress in the longitudinal direction of the FSW lap joints due to over-simplification of the uniform, 2D FE model, which did not take into account the varying change in geometry of the stringer in the out-of-plane direction.

5.2 Independent Verification Using Neutron Diffraction

The variation in residual stresses in the three principal directions of the FSW lap joint in the as-welded configurations were calculated using the compliance functions and the FE model used to calculate the residual stress was verified for consistency of solution. Although the calculated stresses were checked for consistency, there was no independent verification method to determine the accuracy of these compliance method residual stresses. Therefore, the non-destructive method of neutron diffraction was chosen as the method of using neutrons to measure the strains in the FSW lap joints in both as-welded and hammer peened configurations. The following are the results of the residual stress variation in the as-welded and hammer peened specimens in the through thickness (y), transverse (x) and longitudinal (z) direction of the weld.

5.2.1 Neutron Diffraction Results of Residual Stress Components in Through Thickness (y) Direction

Transverse Residual Stress Component (σ_x)

The variations of the transverse residual stress component (σ_x) in the through thickness direction for the two specimens are plotted in Figure 5.30. The residual stresses at the top surface of both plates are compressive but the hammer peened plate had a compressive stress of 187 MPa compared to the 95 MPa stress in the as-welded plate. This compressive residual stress agrees with the fact that the post-welding surface finishing technique of hammer peening introduced a compressive stress at the top surface of the plate. Since the stresses at the top surface of the as-welded plate were already in compression, hammer peening caused the residual stresses to increase in compression. The residual stress in the as-welded plate had the highest tensile stress of 92 MPa, $y=1.62$ mm from the top surface. This stress is 18% of the stringer's yield strength. The residual stress becomes compressive (172 MPa) again at the bottom surface of the plate ($y=3.58$ mm). The bottom surface of the hammer peened plate was in compression but less than that of the as-welded plate. The stress at a depth of $y=3.58$ mm was 81 MPa in compression.

Table 5.10 is a comparison of the residual stresses plotted in Figure 5.30 of the transverse residual stress in the through thickness direction and at the weld centerline for both as-welded and hammer peened specimens. When comparing the change in residual stresses through the thickness of the plates at the 6 various depths, the average change in stress was 67.01 MPa. The greatest change in the two residual stresses was at a depth of 0.33 mm (y-direction) from the top surface of the plate of 92.11 MPa. The 92.11 MPa increase in compressive residual stress just below the surface of the FSW lap joint corresponds to the region, which has been plastically work by the peening process to induce compressive residual stresses below the top surface of the weld. Interestingly, there is an equal but opposite change of residual stress at the bottom surface of the plate at a depth of $y=3.58$ mm. Here is there a reduction of compressive stress with a magnitude of 90.41 MPa. This

reduction in compressive stress can be explained by the balancing of internal stresses caused by the peening process.

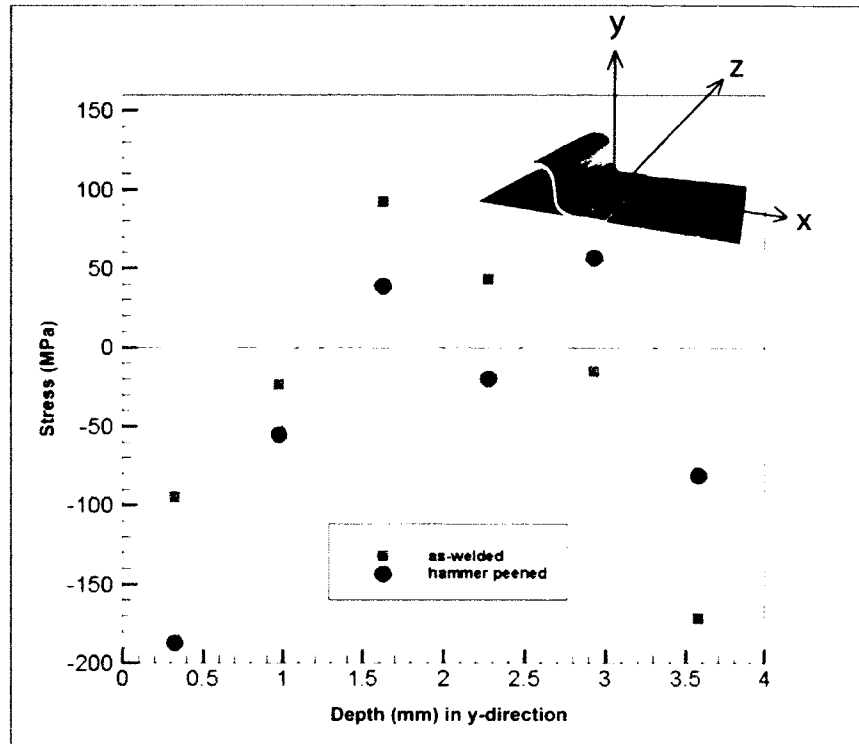


Figure 5.30: Transverse stress component (σ_y) in through thickness (y) direction at weld centerline

Position from top surface in y-direction (mm)	As-welded Stress (MPa)	Hammer Peened Stress (MPa)	Difference (MPa)
0.33	-95.11	-187.22	92.11
0.98	-23.70	-55.49	31.79
1.63	91.91	38.97	52.94
2.28	42.81	-20.01	62.82
2.93	-15.18	56.81	71.99
3.58	-171.83	-81.42	90.41

Table 5.10: Comparison of transverse residual stress (σ_y) in as-welded and hammer peened specimen in through thickness (y) direction at weld centerline

Normal Residual Stress Component (σ_y)

The variation of the normal stress component (σ_y) in the through thickness (y) direction for the two specimens were calculated and plotted in Figure 5.31. Both specimens had compressive stresses of approximately 95 and 84 MPa at the surface of the plate. At $y=1.63$ mm into the plate, the as-welded specimen was tensile at 68 MPa (20% of the skin's yield strength and 14% of stringer's yield strength) while the hammer peened specimen remained close to zero at 6 MPa in tension. At the bottom surface, the as-welded plate has the highest compressive stress of 120 MPa while the hammer peened plate had the highest tensile stress of 84 MPa (24% of skin's yield strength). Stress free boundary conditions states that normal stresses (σ_y) on surfaces of the plate have to be zero therefore, although the normal stresses measured in the through thickness (y) direction were not measured exactly at the two surfaces of the material, the residual stress profile should return to zero at the two surfaces of the FSW plate.

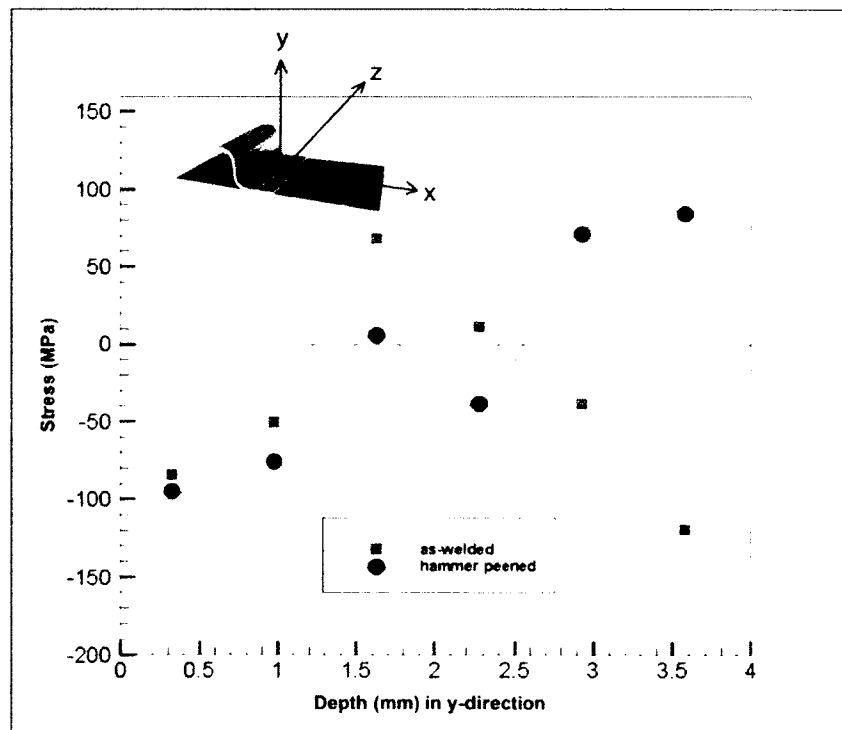


Figure 5.31: Normal stresses component (σ_y) in through thickness (y) direction at weld centerline

Longitudinal Residual Stress Component (σ_z)

The variation of longitudinal stress component (σ_z) in the through thickness (y) direction for the two specimens were plotted in Figure 5.32. The as-welded specimen has a tensile stress of 34 MPa right below the surface of the plate at a depth of $y = 0.33$ mm, which changed to a maximum tensile stress of 152 MPa (30% of the stringer's yield strength) in the middle of the plate at $y = 1.63$ mm, then to a compressive stress of 60 MPa at the bottom of the plate. The hammer peened specimen stress profile was similar to the as-welded profile but was mostly in compression. When comparing all three residual stresses in the though thickness direction, a pattern reveals that the as-welded specimen typically had a higher stress value than that of the hammer peened plate. This trend suggests that the process of hammer peening redistributes and in most cases reduces the residual stress in all three principal directions.

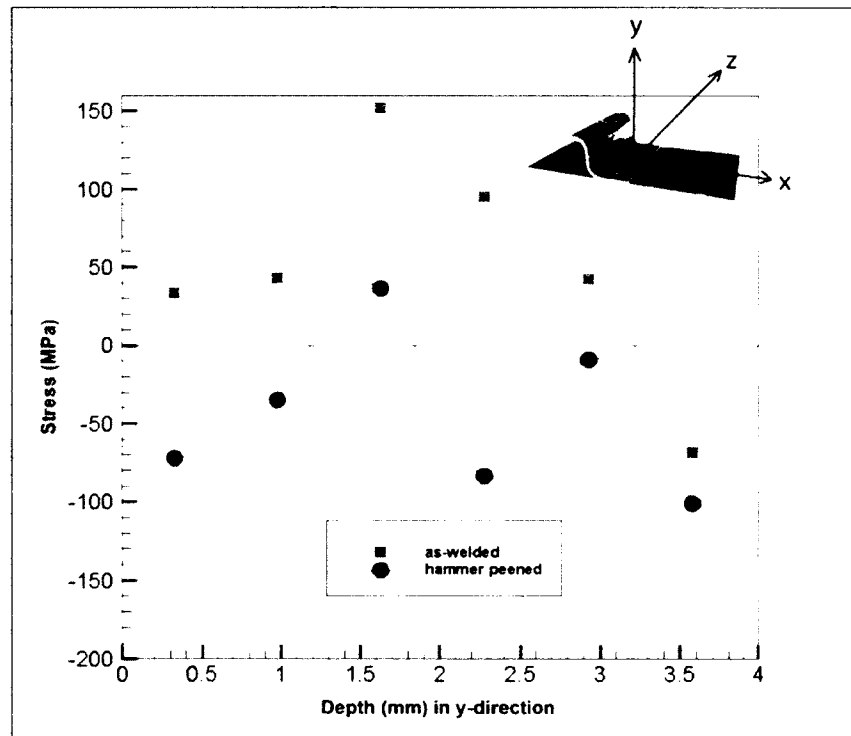


Figure 5.32: Longitudinal stress component (σ_z) in through thickness (y) direction

5.2.2 Neutron Diffraction Results of Residual Stress Component in Transverse (x) Direction

Longitudinal Stress Component (σ_z)

The longitudinal stress component (σ_z) on the transverse (x) plane for the as-welded plate were calculated at the top surface and bottom surface at $y = 0.375$ mm and $y = 2.925$ mm respectively by neutron diffraction. The residual stress at the center of the plate had to be interpolated to compare with the results of the compliance method, which was taken at the center of the plate. Since the stress at the top and bottom surface was known, a gradient or slope of the two points was calculated. Taking the gradient and multiplying it with the mid-distance of the plate's thickness gives the value of residual stress at the center of the plate. Similar calculations were performed for the hammer peened plate. Figure 5.33 shows the plot of σ_z on the transverse plane of the as-welded and hammer peened plate for the double pass weld configuration. It is important to mention the double pass configuration here because of the unique shape of the residual stress produced by the double passing of the weld tool. For a single pass FSW plate, the longitudinal stress typically exhibits an "M" shape profile with the highest measured tensile stresses at the edge of the weld tool and a decrease in the stress at the weld centerline. In Figure 5.33 it can be seen that the as-welded specimen exhibits a "double M" shape profile produced by the two passes of the FSW tool. The residual stress profiles show that there is two tensile stress peaks approximately 6 mm on either side of the weld centerline. This region represents the edge of the rotating tool. The residual stress in this region was 197 MPa, which is 57% of the skin's yield strength and 39% of the stringer's yield strength. At the weld centerline, the stress reduced to 113 MPa in tension. This decrease in stress at the weld centerline may be explained by the change in microstructure and hardness of the weld nugget due to recrystallization of the grains. The heavily worked grains of the weld nugget cause stresses to be relieved as the material cools down after welding. The corresponding hardness value at the weld centerline was recorded at 116 HV. Away from the weld centerline where the material is not affected by the stirring action of the tool, the stresses level off to around zero and the hardness value increased to that of the parent un-welded material (133 HV).

When comparing σ_z on the transverse plane before and after hammer peening, it can be seen that the hammer peened longitudinal stress has a similar profile to that of the as-welded stress but with much lower stresses and mostly in compression. The low stress suggest that the induced compressive stresses on the surface of the material cause the tensile stresses in the as-welded plates to also be reduced in the longitudinal (z) direction. The highest tensile stress measured in the peened plate was only 25 MPa at the weld centerline; otherwise, the stress distribution was entirely compressive.

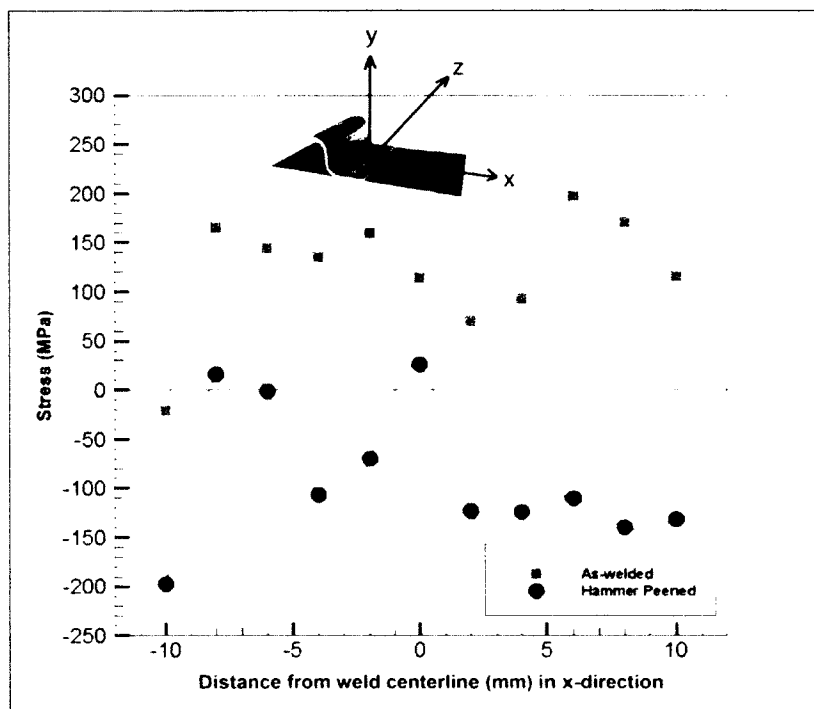


Figure 5.33: Longitudinal stress component (σ_z) on transverse plane of as-welded and hammer peened plate

Normal Residual Stress Component (σ_y)

The variation of the normal residual stress component (σ_y) in transverse (x) direction for both test specimens are plotted in Figure 5.34. It is interesting to note that both stress profile remain in tension across the weld except for the first slit position of the hammer peened specimen which was 47 MPa in compression. Both stress profiles were similar to

one another but the hammer peen stresses had lower magnitudes than the as-welded specimen. For an example, at a distance of $x=6$ mm on the right of weld centreline, the as-welded specimen had a stress of 284 MPa while the hammer peened specimen had a stress of only 89 MPa. The maximum tensile stress in the as-welded specimen was 284 MPa at a distance of $x=6$ mm on the right of the weld centreline. In the hammer peened specimen, the maximum tensile stress was 120 MPa at $x=-8$ mm on the left of the weld centerline

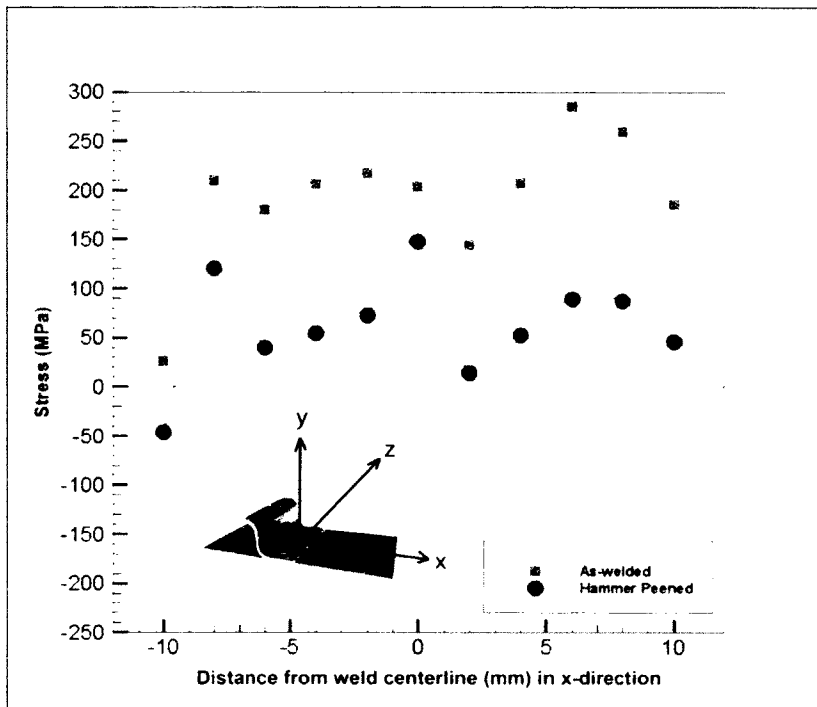


Figure 5.34: Normal residual stress component (σ_y) in transverse (x) direction for both specimens

Transverse Residual Stress Component (σ_x)

The variation of the transverse residual stress component (σ_x) in the transverse (x) direction of both specimens is shown in Figure 5.35. The as-welded stresses are higher than the hammer peened specimen at every slit depth. The maximum tensile stress in the as-welded plate was 239 MPa at a distance of $x = 6$ mm to right of weld centerline. This stress is 69% of the skin's yield strength and 48% of the stringer's yield strength. In the

hammer peened specimen, the maximum tensile residual stress was 122 MPa at $x = -8$ mm to the left of the weld centerline.

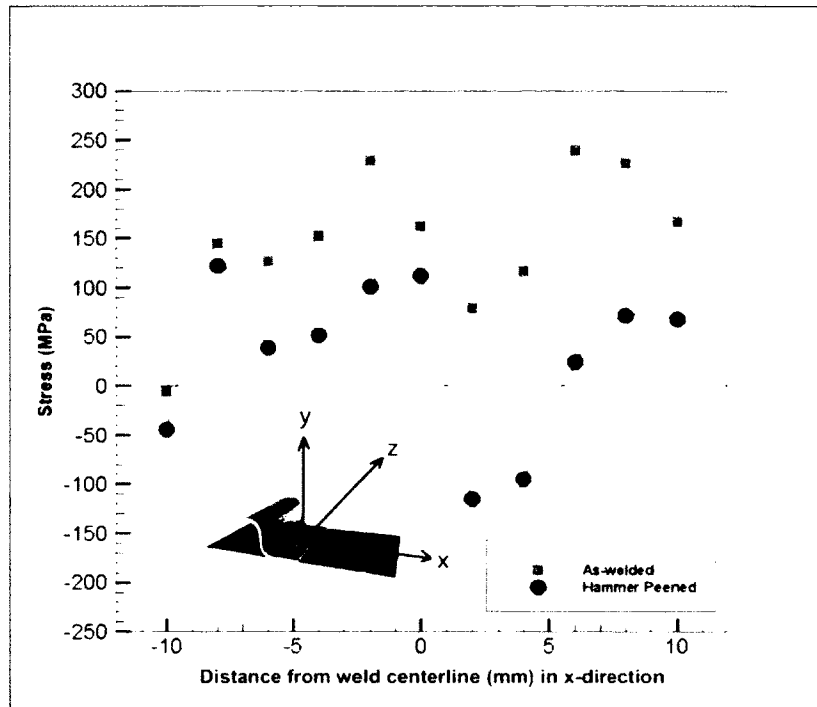


Figure 5.35: Transverse residual stress component (σ_x) in transverse (x) direction for both specimens

Table 5.11 is the comparison of residual stress between the as-welded and peened specimen of Figure 5.33, which is the longitudinal residual stress component (σ_z) on the transverse plane. The average change in residual stress across the weld was 209.86 MPa. The greatest change in residual stress from tension to compression was found at a distance of $x = 8$ mm from weld centerline at 310.87 MPa. These changes in the longitudinal component of residual stresses demonstrate that hammer peening had the greatest influence on the longitudinal residual stress components of these lap joints. Comparing point by point across the weld in the transverse direction, the effects of hammer peening reduced the tensile residual stresses at every single point and in most cases caused the stress to change from tension to compression.

Distance weld centerline (mm)	As-welded Stress (MPa)	Hammer Peened Stress (MPa)	Difference (MPa)
-10	-20.99	-198.01	177.02
-8	165.35	15.83	149.52
-6	144.19	-2.10	146.29
-4	134.50	-107.14	241.64
-2	159.29	-70.76	230.05
0	113.44	25.37	88.07
2	69.60	-123.40	193.00
4	92.47	-124.36	216.83
6	197.18	-110.51	307.69
8	170.85	-140.02	310.87
10	115.52	-131.91	247.43

Table 5.11: Comparison of longitudinal residual stress (σ_z) in as-welded and hammer peened specimen in transverse (x) direction

5.2.3 Neutron Results of Residual Stress Components in Longitudinal (z) Direction

Transverse Residual Stress Component (σ_x)

The last set of neutron diffraction results were the residual stress components along the weld of both specimens (z-direction). Figure 5.36 is the variation of the transverse residual stress (σ_x) in the longitudinal (z) direction for both test specimens. From the plot, the as-welded case shows a compressive stress of 26 MPa at the edge of the plate ($z= 5$ mm) moving to a tensile stress of 113 MPa and back down to a compressive stress of 35 MPa at $z = 90$ mm. This residual stress profile is typical of that in the longitudinal direction for welded components, Wanchuck et al. (2006). The residual stresses along the longitudinal direction are normally low in magnitudes with a drop in stress at both ends of the plate to a compressive stress due to the plate's end effect. Another possible explanation for the decrease in residual stress could be due to stresses introduced when the test specimens were cut from the original FSW plate. In contrast to the as-welded specimen, the hammer peened specimen shows a reversal in residual stress profile. At the

edge of the plate, the stress is tensile at 101 MPa (29% of skin's yield strength and 20% of the stringer's yield strength). At the opposite edge, the stress remained in tension with a magnitude of 64 MPa. Besides the two end values of the hammer peened specimen, the magnitude of residual stress (σ_x) in the hammer peened specimen is dramatically reduced when compared to the residual stress (σ_x) in the as-welded specimen.

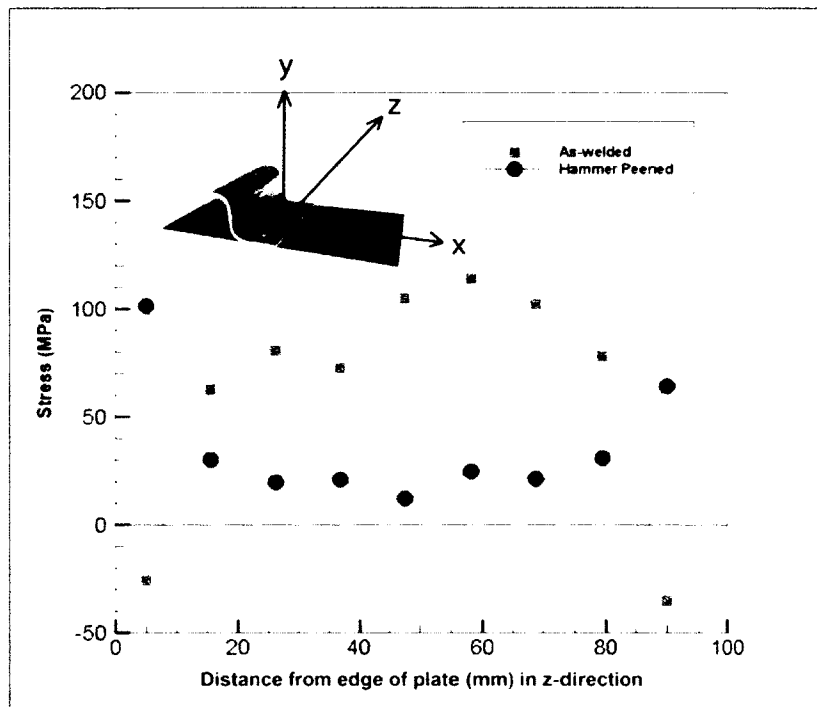


Figure 5.36: Transverse residual stress (σ_x) profile in the longitudinal (z) direction for both specimens

Table 5.12 is a tabulated comparison of the transverse residual stress (σ_x) profile in the longitudinal (z) direction for both specimens. Besides the two end of the plate, the hammer peened specimen shows a reduction in residual stresses moving along the weld in the z-direction. The average change in residual stress was 75.66 MPa, which is less than the average change in longitudinal residual stress (σ_z) in the transverse (x) direction. It is hard to say why hammer peening caused the two edges of the plate to change from compression to tension. The only explanation that can be given is again due to the redistribution of residual stresses after hammer peening. Since the middle section of the

plate experiences an increase in compressive stress, the two edges of the plate reacted by changing to tensile residual stresses.

Distance from edge of plate (mm)	As-welded Stress (MPa)	Hammer Peened Stress (MPa)	Difference (MPa)
5.00	-25.62	101.05	126.67
15.63	62.44	30.17	32.27
26.25	80.39	19.42	60.97
36.88	72.34	20.80	51.54
47.50	104.60	12.05	92.55
58.13	113.63	24.65	88.98
68.75	102.22	21.31	80.91
79.38	77.96	30.66	47.30
90.00	-35.46	64.31	99.77

Table 5.12: Comparison of transverse residual stress (σ_x) in as-welded and hammer peened specimen in longitudinal (z) direction

Normal Residual Stress Component (σ_y)

The variation in normal residual stresses (σ_y) for both specimens was plotted in Figure 5.37. Both specimens show very low residual stresses that were relatively flat along the weld line. The as-welded case shows stresses that were typically higher than the hammer peened specimen.

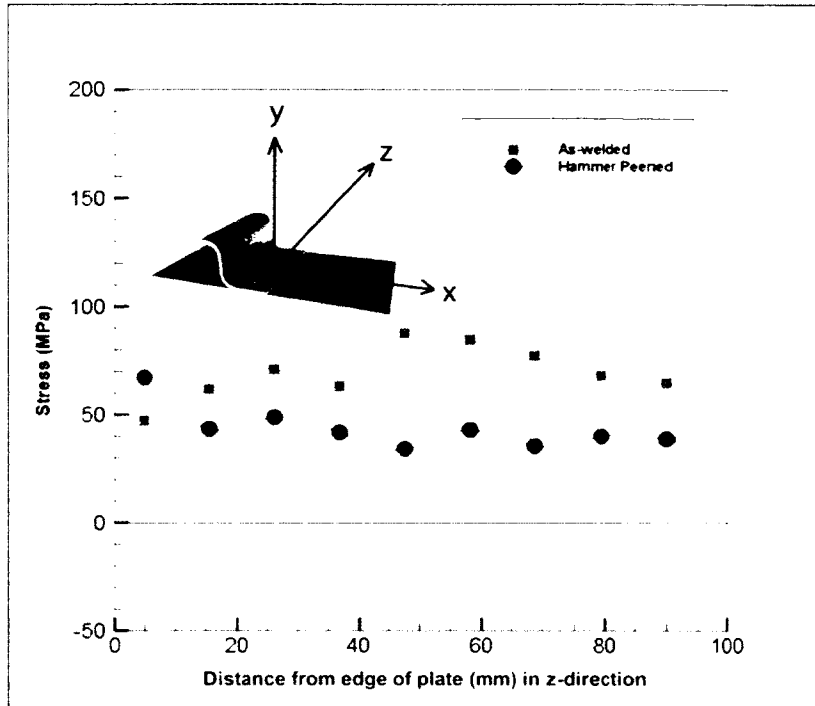


Figure 5.37: Normal residual stress component (σ_y) in the longitudinal (z) direction for both specimens

Longitudinal Residual Stress (σ_z)

The variation of the longitudinal residual stress component (σ_z) along the weld centerline is shown in Figure 5.38. Perhaps the stresses in this direction show the most significant change between the two test specimens. The residual stress in the as-welded specimen begins with a tensile stress of 65 MPa ($z = 5$ mm), this stress increased to 190 MPa in the middle of the weld ($z = 47.5$ mm) and drops down to 57 MPa at the other edge of the plate with a triangular shape profile. The residual stresses were dramatically reduced in the hammer peened specimen and the hammer peening has appeared to flatten out the triangular shape profile of the as-welded stresses. It is important to note that all longitudinal residual stresses in the longitudinal direction were in tension.

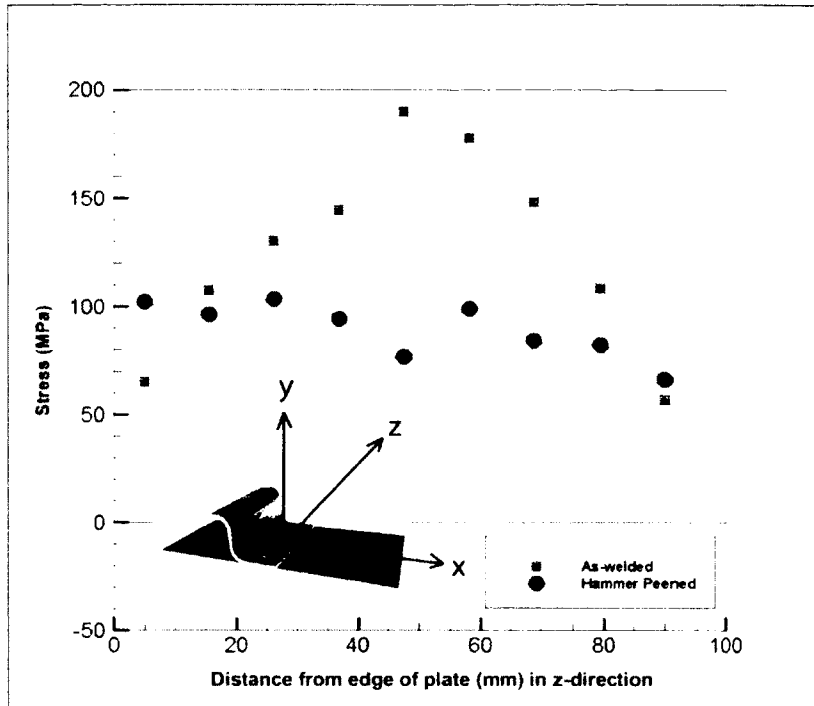


Figure 5.38: Longitudinal residual stress component (σ_z) in the longitudinal (z) direction for both specimens

Most literature studying residual stress examines the residual stress variations in one direction and one component of residual stress. In this thesis, the residual stress variation in three directions are looked at as well as the three components of those residual stress profiles so it can become very complex to conceptualize. The following is a triaxial vector representation of the residual stresses in the FSW lap joints in the transverse (x) direction to help visualize the change in direction and magnitudes of the stresses before and after hammer peening.

The highest tensile residual stress was calculated in the transverse (x) direction going across the weld. In this direction, the variation in transverse residual stress (σ_x) revealed that there were two peak tensile stresses: one to the right of the weld centerline, and one to the left of the weld centerline. Figure 5.39 is the triaxial residual stress 6 mm to the right of the welded centerline in the as-welded plate in the transverse direction. This

tensile stress was the greatest value in the transverse direction calculated at 239 MPa (69% of AA 2024-T3's yield strength). This stress reduced to 23 MPa in tension after hammer peening (7% of AA 2024-T3's yield strength) as shown in Figure 5.40. The significance of the high tensile stress in the transverse (x) direction is that coupled with cyclic loading of the lap joint, the stresses may reach values that are greater than the yield strength of the skin/stringer section and cause cracks to nucleate and grow.

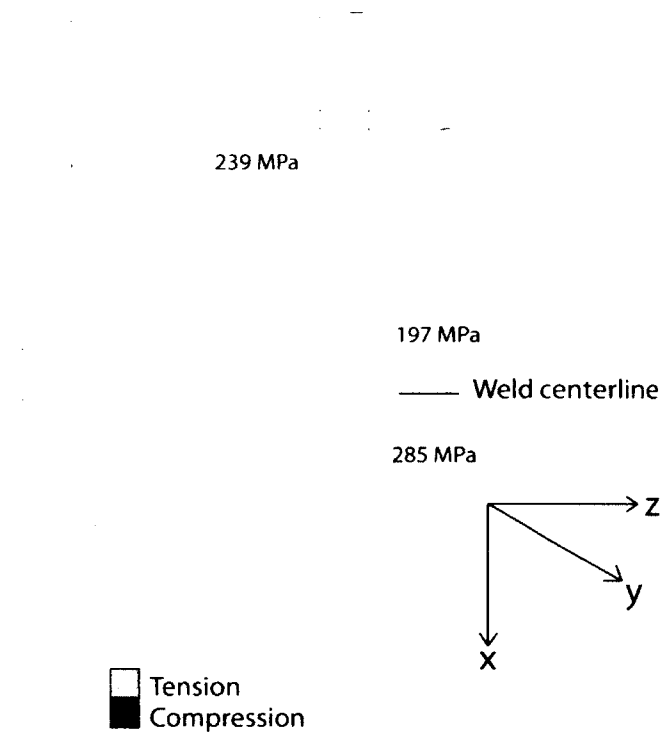


Figure 5.39: Triaxial residual stress 6 mm to the right of the welded centerline in the as-welded plate

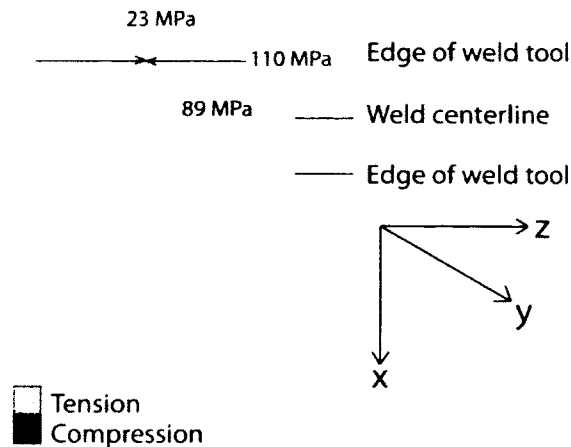


Figure 5.40: Triaxial residual stress 6 mm to the right of the welded centerline in the hammer peened plate

5.3 Comparison of the Residual Stress from the Crack Compliance Method and Neutron Diffraction

Once the residual stress profiles were calculated using two independent residual stress measurement techniques, the results of the two methods in each of the three principal directions were compared with one another to determine the validity of the hybrid crack compliance technique used to measure the residual stress profiles in these FSW lap joints. First, Figure 5.41 is the variation in transverse residual stress (σ_x) through the thickness of the plate (y-direction) from the compliance method and neutron method measured at three distances from the weld centerline. Since the neutron diffraction method was non-destructive, it was able to obtain strains at multiple locations on a single test specimen. The purpose of measuring the residual stress profile at different distances from the weld centerline was to observe how the residual stresses vary across the weld. In general, the three residual stress profiles calculated using neutron diffraction were similar in

magnitude at every slit depth except for a few points where they showed more disagreement with one another. This change in residual stress is possible because the rotation of the welding tool creates an asymmetric weld pattern and so the residual stresses measured on the right hand side may be different than that of the residual stresses on the left hand side of the weld centerline. For the as-welded test specimen, the stress profiles of both methods shows the same patterns and agree with one another.

Figure 5.42 shows the transverse residual stress (σ_x) calculated at the weld centerline using the compliance and neutron diffraction (with error bars). The six residual stress values determined from the neutron experiments show the same pattern as that of the compliance method. Unlike the error bars of the compliance method, which were calculated using equations, the error value of ± 30 MPa for the neutron diffraction stress result is the conventional average error associated with strain measurements by neutron diffraction.

Figure 5.43 is the transverse stress (σ_x) through the thickness of the plate from the compliance method and neutron method measured at three distances from the weld centerline for the hammer peened configuration and Figure 5.44 is the comparison of the two method's residual stress profiles measured at the weld centerline with error bars. Similar to the as-welded specimen, the neutron diffraction method residual stress profile agrees with the compliance method at every slit depth measured. Although there is some scatter of residual stresses between the two residual stress methods, the comparison of the residual stress profiles calculated in the through thickness (y) direction of the as-welded and hammer peened samples demonstrates that the crack compliance method was able to predict the trends of the transverse residual stress (σ_x) in the through thickness (y) direction with the same order of magnitudes as that of neutron diffraction.

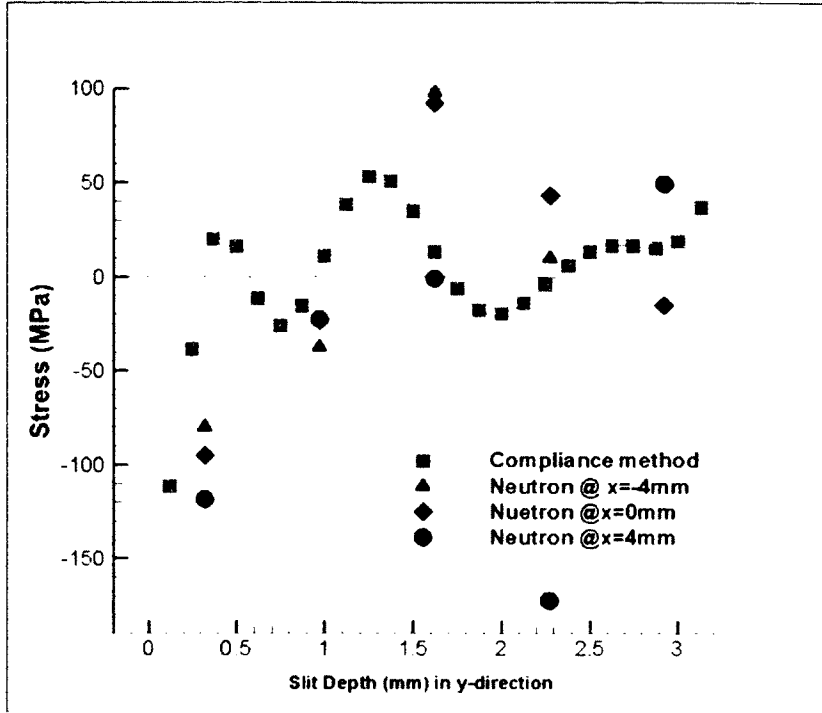


Figure 5.41: Comparison of transverse residual stresses (σ_x) in the through thickness (y) direction for as-welded plates using compliance and neutron methods

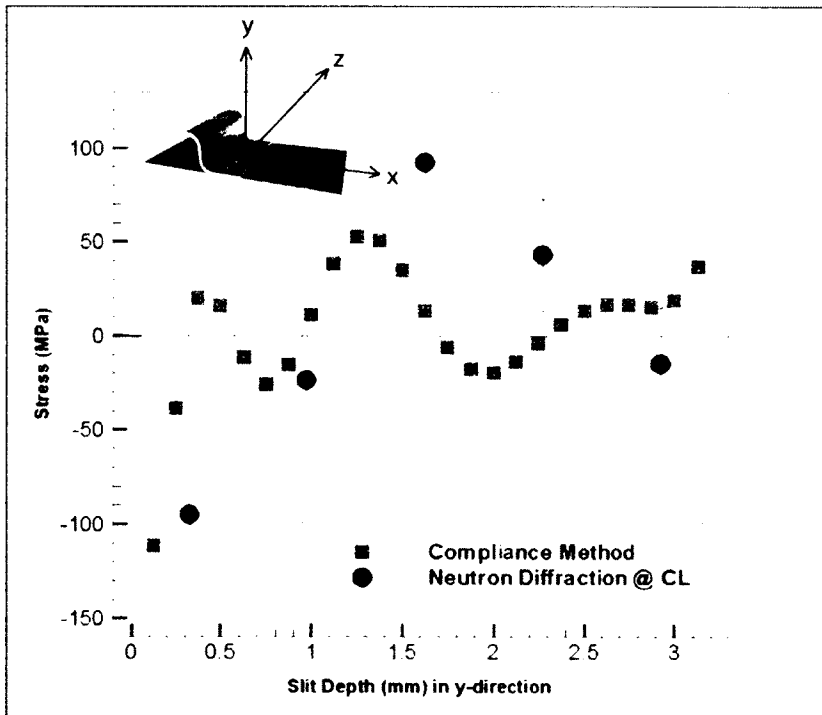


Figure 5.42: Comparison of transverse residual stresses (σ_x) in the through thickness (y) direction for as-welded plates using compliance and neutron methods at weld centerline with error bars

The tabulated comparison of the residual stresses calculated using the compliance method and neutron diffraction in the through thickness (y) direction of the as-welded specimen is shown in Table 5.13. It is important to note that since the slit depths and positions where the neutron diffraction are not measured using the same increments, the comparison of the compliance residual stress of Table 5.13 had to be interpolated to correspond to the same positions as the neutron diffraction. From Table 5.13, it can be seen that average difference in residual stresses through the thickness of the weld in the y-direction is 55.33 MPa. This average difference between the two residual stresses are acceptable when comparing residual stresses calculated using two different methods.

Depth from Top Surface of Plate (mm)	Compliance Residual Stress (MPa)	Neutron Residual Stress (MPa)	Difference (MPa)
0.33	-3.68	-95.11	91.43
0.98	5.84	-23.70	29.54
1.63	12.86	91.91	79.05
2.28	-2.35	42.81	45.16
2.93	16.30	-15.18	31.48

Table 5.13: Comparison of transverse (σ_x) residual stresses from compliance method and neutron diffraction for as-welded specimen in through thickness (y) direction

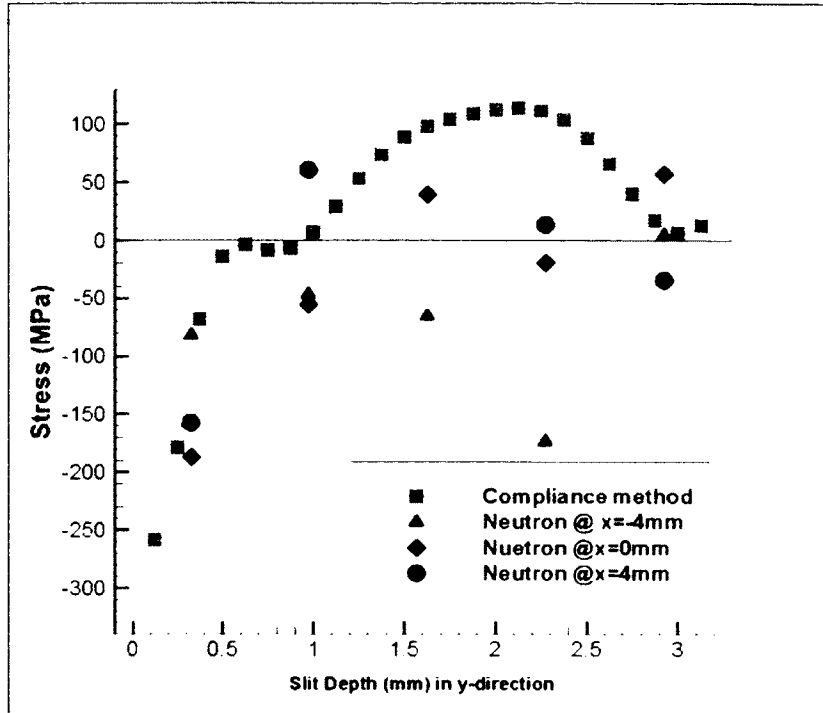


Figure 5.43: Comparison of transverse residual stresses (σ_x) in the through thickness (y) direction for hammer peened plates using compliance and neutron methods

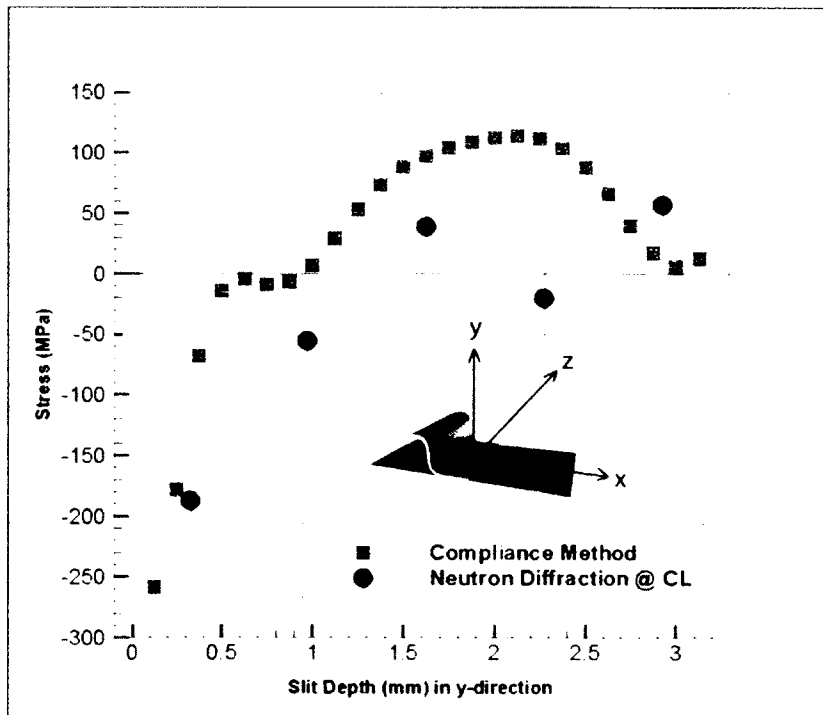


Figure 5.44: Comparison of transverse residual stresses (σ_x) in the through thickness direction for hammer peened plates using compliance and neutron methods at weld centerline with error bars

Similar to Table 5.13, Table 5.14 is the tabulated comparison of the transverse (σ_x) residual stresses measured using the two techniques for the hammer peened specimen. The average difference in stress through the thickness of the plate (y-direction) was 73.33 MPa. The greatest difference in residual stress between the two methods was found at a depth of $y = 2.28$ mm from the top surface of the plate. This area corresponds to the penetration depth of the FSW tool tip. It is possible that there is a complex mixing of material in this region, which is not uniform along the weld. This could therefore translate in difference of residual stresses taken at the same depth but at different locations along the weld.

Depth from Top Surface of Plate (mm)	Compliance Residual Stress (MPa)	Neutron Residual Stress (MPa)	Difference (MPa)
0.33	-112.48	-187.22	74.74
0.98	3.98	-55.49	59.47
1.63	97.52	38.97	58.55
2.28	109.62	-20.01	129.63
2.93	12.54	56.81	44.27

Table 5.14: Comparison of transverse (σ_x) residual stresses from compliance method and neutron diffraction for hammer peened specimen in through thickness (y) direction

The second comparison is the two longitudinal residual stress (σ_z) distributions in the transverse (x) direction. Figure 5.45 plots the residual stress profile from the neutron method of the as-welded and hammer peened specimens along with the as-welded stress profile measured using the hybrid compliance method. Since only the transverse residual stress (σ_x) was only measured for the as-welded specimen, discussion will look at the as-welded compliance and as-welded neutron results. From Figure 5.45, it can be seen that at the weld centerline, the neutron method is able to calculate the same trends in residual stress as the compliance stresses. The “M” shape profile can be seen using both methods

suggesting that the weld region contains high tensile residual stresses with decrease in residual stress around the weld centerline as a result of the recrystallization of the grains in the weld nugget. Also, the plot shows that hammer peening the surface of the welded specimens decreased the residual stress in the transverse (x) direction while still keeping the same residual stress profile. From the comparison, it is determined that both methods were able to calculate the same residual stress profile in the transverse (x) direction.

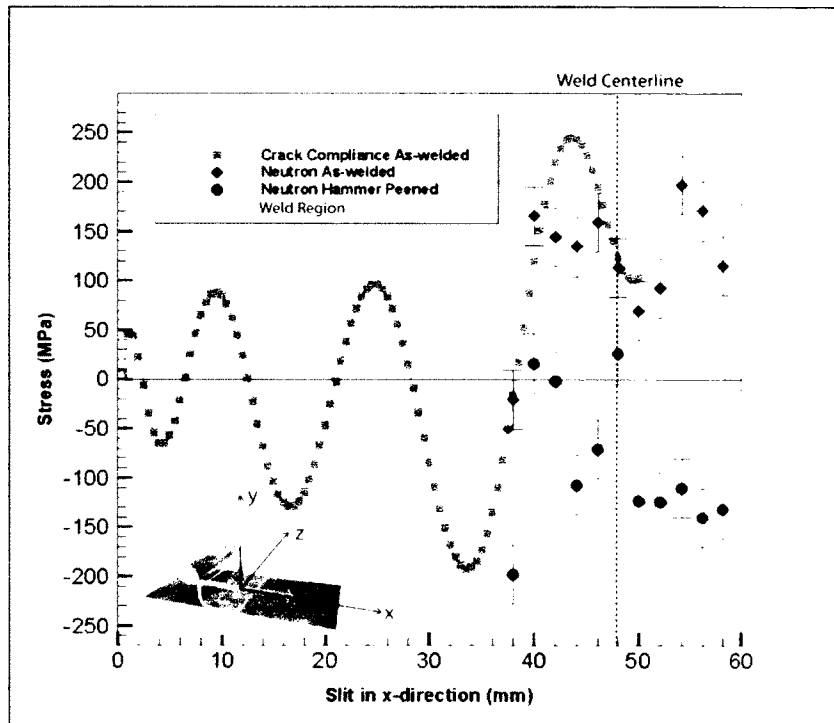


Figure 5.45: Comparison of longitudinal residual stress (σ_z) in transverse (x) direction from compliance and neutron methods

Table 5.15 is the tabulated comparison of the transverse (σ_x) residual stresses from compliance method and neutron diffraction for as-welded specimen in transverse (x) direction. Since the slit increment of the compliance method and increment of neutron diffraction were the same, interpolation was not required and a direct comparisons can be made at each point across the weld. The average difference in residual stress across the 12 mm length of weld was 48.63 MPa. The residual stresses from the compliance method

agree well with the residual stresses from neutron diffraction at every single position across the weld except of at a distance of $x = -4$ mm from the weld centerline where the difference in stress was 116.59 MPa.

Distance from weld centerline (mm)	Compliance Residual Stress (MPa)	Neutron Residual Stress (MPa)	Difference (MPa)
-10	-14.79	-20.99	6.20
-8	124.40	165.35	41.94
-6	225.40	144.19	81.20
-4	251.08	134.50	116.59
-2	201.65	159.29	42.36
0	127.88	113.44	14.44
2	107.27	69.60	37.67

Table 5.15: Comparison of transverse (σ_x) residual stresses from compliance method and neutron diffraction for as-welded specimen in transverse (x) direction

The final comparison is the transverse residual stress (σ_x) of both methods in the longitudinal (z) direction. The compliance method was only able to measure the residual stress profile halfway through the width of the plate while neutron diffraction was able to calculate the residual stress across the entire width of the plate. Figure 5.46 is the comparison in longitudinal residual stress profile for the two methods. The compliance method shows a residual stress profile with several peaks and valleys and the magnitudes of the stresses are much higher than that of the neutron method. There is no clear trend that demonstrates agreement in results between the two methods.

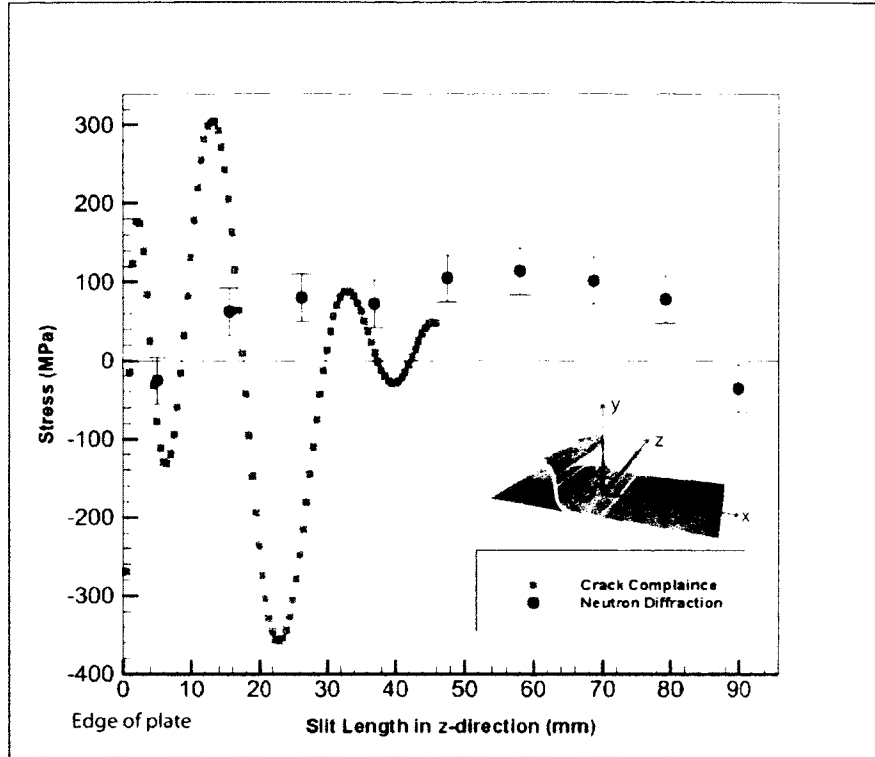


Figure 5.46: Comparison of transverse residual stress (σ_x) in the longitudinal (z) direction from compliance and neutron methods with error bars

Table 5.16 is the tabulated comparison of the residual stress from both methods. The compliance method residual stress did not agree with the neutron diffraction results and there seems to be no similarity between the two residual stress profiles. Also, the greatest difference in both residual stress values was at a distance of $z = 26.25$ mm of 312.92 MPa.

Distance from plate edge (mm)	Compliance Residual Stress (MPa)	Neutron Residual Stress (MPa)	Difference (MPa)
5.00	-78.45	-25.62	52.83
15.63	194.23	62.44	131.79
26.25	-232.53	80.39	312.92
36.88	13.06	72.34	59.28

Table 5.16: Comparison of transverse (σ_x) residual stresses from compliance method and neutron diffraction for as-welded specimen in longitudinal (z) direction

In conclusion, the independent measurement of the residual stress profile by neutron diffraction was successful in measuring the variation in residual stress profiles in the through thickness, transverse, and longitudinal direction for the as-welded and hammer peened configurations. The residual stresses obtained from neutron diffraction were compared with the residual stresses obtained from the crack compliance method and it was determined that two out of the three residual stress profiles for the as-welded specimen agreed with one another. The crack compliance method was unable to produce meaningful stress profiles in the longitudinal direction therefore the discussion of the variation in stress in the longitudinal (z) direction is based solely on the results from the neutron diffraction experiments. The following section will explain the success and shortcoming of the crack compliance method applied to a 3D test specimen based on the comparison of the residual stress in all three principal directions between the compliance method and neutron diffraction.

5.4 Validation of Using Crack Compliance Method on 3D and Asymmetrical Test Specimens

After comparing the residual stress profiles calculated using the crack compliance method and verifying them with the non-destructive method of neutron diffraction, some discussion is given on the validity of the application of the compliance method on complex, three dimensional, and asymmetric geometry of the FSW lap joint. The original objective was to measure the residual stresses in these friction stir welded lap joints in all three principal directions to have a better understanding of the role these complex residual stresses play in the distortion of the plates. The crack compliance method was chosen as the method of measuring the residual stress profiles. The basis of the compliance theory involved taking a 3D object and modeling it as a 2D FE model assuming that the geometry in the out-of-plane direction is uniform, therefore conventionally, the compliance method was applied to simple rectangular shaped components. The residual stress in any direction could be calculated since any orientation of the rectangular component could be modeled in 2D with the third direction consisting of a uniform geometry.

Relating to the FSW lap joints, one of the three directions of interest satisfied this criteria, which was the variation in transverse stress (σ_x) in the through thickness (y) direction since the out-of-plane geometry was uniform as shown in Figure 5.47. Verification of the through thickness residual stress profiles for both the as-welded and hammer peened test specimen by neutron diffraction concluded that the crack compliance method was successful in the calculation of the variation in transverse stress (σ_x) in the through thickness direction.

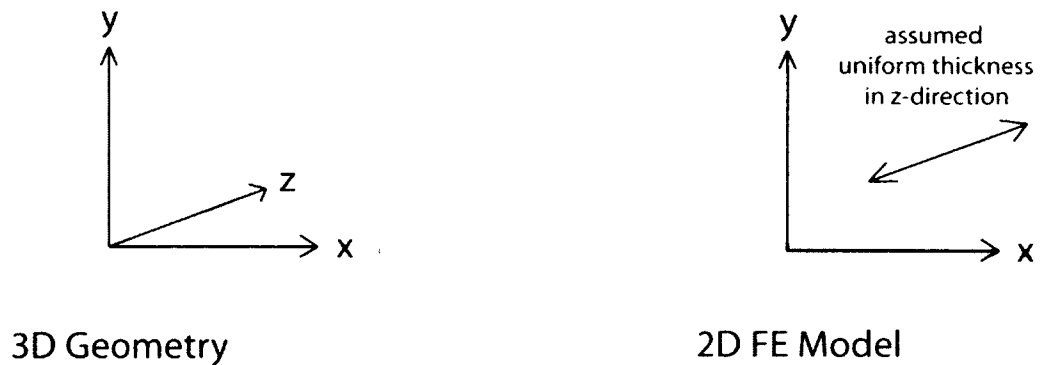


Figure 5.47: 3D stringer modeled in 2D FE model in x-y plane

An attempt was made to apply the 2D compliance method in the other two directions, which were the transverse (x) and longitudinal (z) directions. For the residual stress in the transverse direction, the FSW plate consisted of two different thicknesses; one thickness was where there was only the skin plate, the other thickness was the section with the stringer welded on top of the skin plate. At the beginning of the slitting, the plate was single thickness and further along the slitting, the plate was double thickness. To apply the 2D compliance method, the plate consisting of the two different thicknesses in the out-of-plane direction was simplified as a uniform thickness plate as shown in Figure 5.48. Verification of the variation in longitudinal stress (σ_z) in transverse (x) direction for the as-welded test specimen by neutron diffraction determined that the crack compliance method was successful in the calculation of the transverse residual stress profile near the weld centerline. These findings suggests that although the FSW specimens geometry was

non-uniform in the out-of-plane direction, the non-uniformity was small enough that the simplified 2D FE model was still able to calculate the compliances and the measured strains were able to calculate the longitudinal residual stresses (σ_z). The strain gauges were all placed above the protruding stringer shown in Figure 5.48.

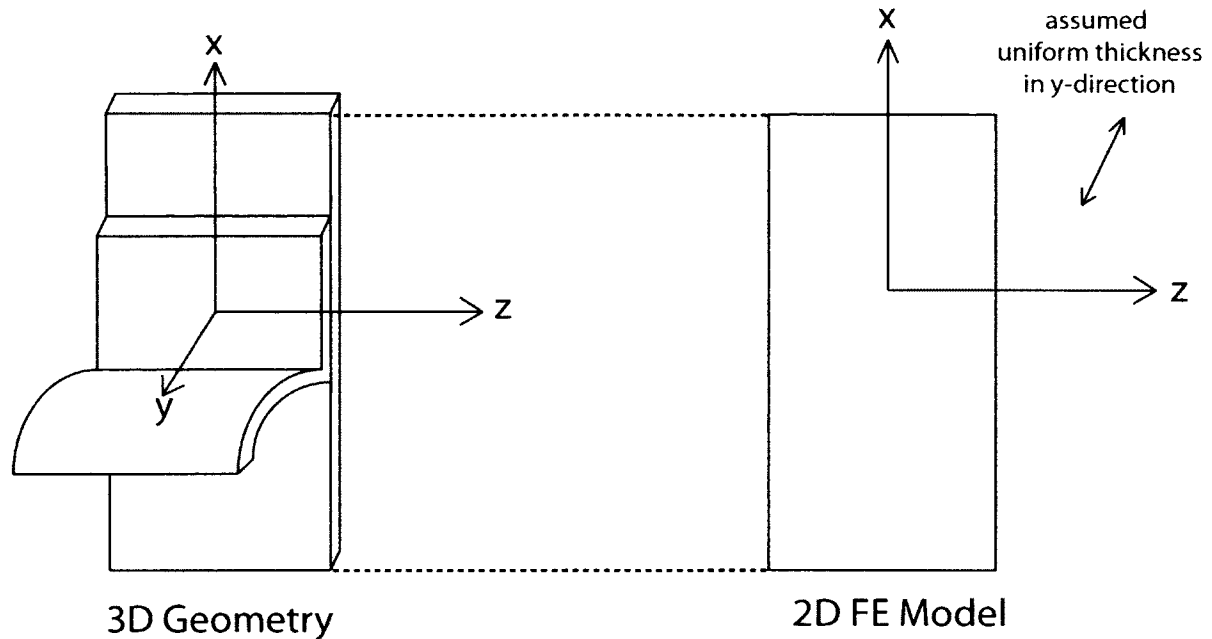


Figure 5.48: 3D stringer modeled in 2D FE model in x-z plane for transverse slitting experiment

For the third and final slitting direction, longitudinal (z-direction), a similar technique was used to simplify the 3D geometry as a 2D FE model. When looking at the residual stress (σ_x) in the longitudinal direction, at every slit depth, there is a stringer that protrudes out, in the out-of-plane direction. The protruding stringer was simplified as a 2D FE model and depicted in Figure 5.49. When comparing the longitudinal residual stress profile of both methods, the variation in transverse residual stress (σ_x) from the compliance method does not agree with the neutron method. Since neutron diffraction is a more reliable method, it is concluded that the over simplified 2D FE model of the FSW plate was unable to accurately calculate the residual stress profile in this longitudinal direction. The effects of the stringer cannot be ignored since it does affect the calculated compliances and strain measurements. Neglecting the stringer's influence on the

compliances will result in the residual stress profile calculated which does not agree with the neutron diffraction results.

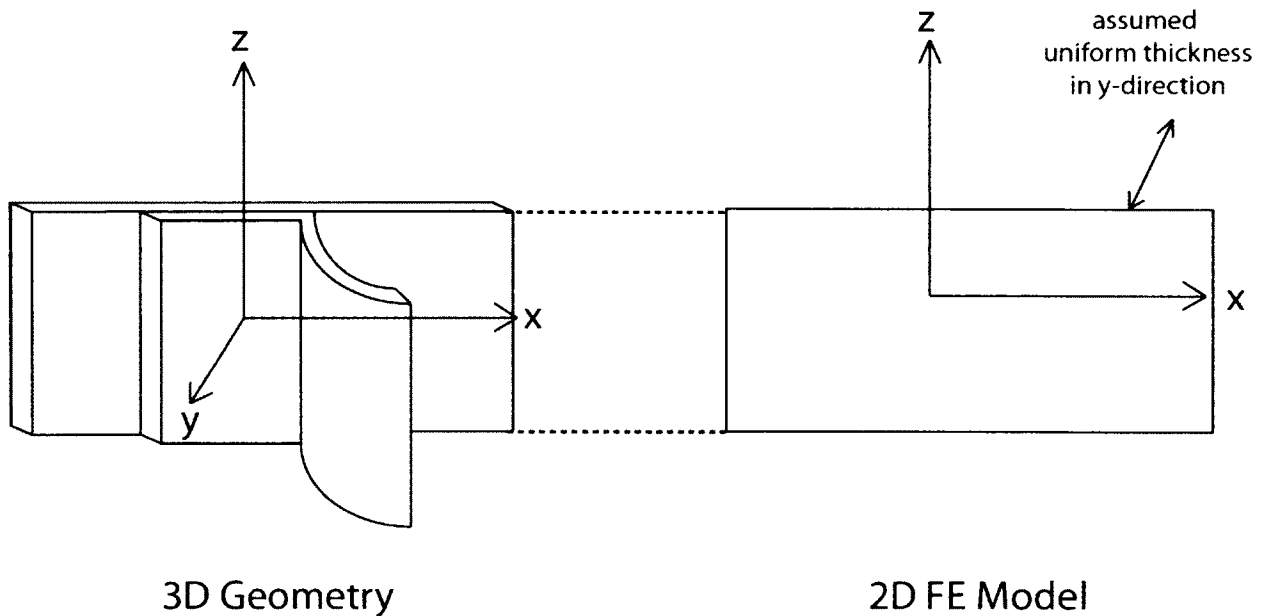


Figure 5.49: 3D stringer modeled in 2D FE model in x-z plane for longitudinal slitting experiment

The crack compliance method was able to successfully calculate the residual stress profiles in two of the three desired directions. This demonstrates that the compliance method has a promising future in more advanced geometries compared to the simple rectangular geometries that were being used conventionally with some limitations regarding geometry.

Neutron diffraction is a very well established method that has existed for over 50 years compared to the crack compliance method, which was developed in the past 15-20 years. However, neutron diffraction is not a readily available method for users who are interested in calculating the residual stress in a component. Neutron diffraction uses separated neutrons that are harnessed from a nuclear reactor source. There are only one or two nuclear reactors in each country that is set up with spectrometers for the purpose of neutron diffraction and beam time is very valuable. This is where the crack compliance

method is advantageous over neutron diffraction. A person or company interested in measuring the residual stress profile in a given component can use the demonstrated hybrid crack compliance method to calculate the stresses that are in that component economically. The only equipment that is required is a computer with an FEM software, some strain gauges and a wire EDM. This is compared with the millions of dollars required to maintain a nuclear reactor facility not to mention the hundreds of thousands of dollars for the different spectrometers required for diffraction experiments. If the same residual stress profiles can be predicted using the crack compliance method, this would be a more economical and practical method of measuring residual stresses. Calculating the residual stresses using FE models and measured strain gauges is not straightforward but with practice and experimentation, it can be used as a powerful tool to predict the stresses in unique and complex components, which were not be typically measured in the past.

5.5 Distortion in the Friction Stir Welded Lap Joint

The torsional distortion in the FSW lap joints suggests that it is caused by a combination of residual stresses in multiple directions. The following is a qualitative discussion on the residual stress profile in the through thickness (y), transverse (x), and longitudinal (z) directions and how they relate to the possible distortions of these FSW panels. First is a look at the angular rotation of the FSW lap joint caused by the transverse residual stresses (σ_x) through the thickness of the plate in the y-direction shown in Figure 5.50. The rotation occurs because the major part of the weld is on the top side of the neutral axis of the plates, thus inducing a greater compressive stress on the top surface. The transverse residual stress profile measured from the compliance method show a compressive stress at the top surface of the lap joint and a tensile stress at the bottom. These opposite stresses will cause a bending moment around the longitudinal axis, resulting in the angular distortion, Wanchuck et al. (2006). The protruding stringer on the left of the weld centerline obstructs the plate from rotating uniformly; therefore there may be a difference in deflection angle on either side of weld centerline.

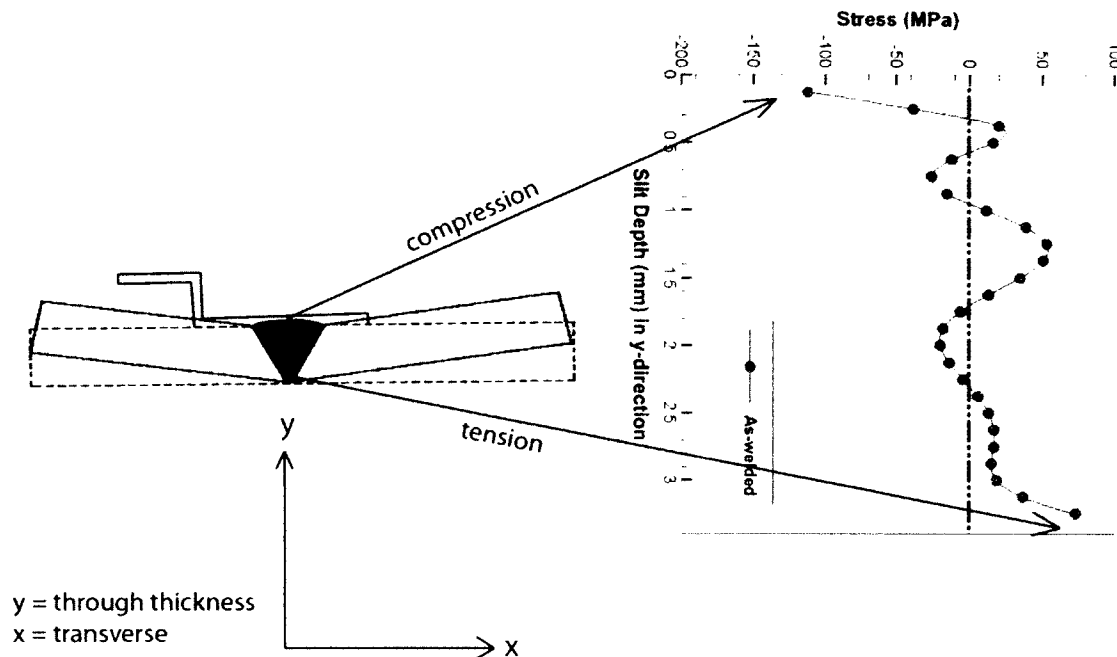


Figure 5.50: Angular rotation of FSW plate as-welded

Next is an examination of the effects longitudinal residual stresses in the transverse direction on distortion of the FSW plate. The frictional heat generated by the rotating tool caused the weld region to expand and upon cooling, the welded material contracted. This expansion and subsequent contraction of the weld is resisted by the surrounding cold material leading to the residual stress profile that is left in the vicinity of the weld as shown in Figure 5.51. The longitudinal residual stress in the transverse direction calculated by the compliance and neutron diffraction method has an “M” shape profile with tensile stresses predominately in the weld region balanced by compressive stresses in the surrounding un-welded parent material. The high tensile residual stresses in the weld region cause longitudinal shrinkage of the weld in the z-direction.

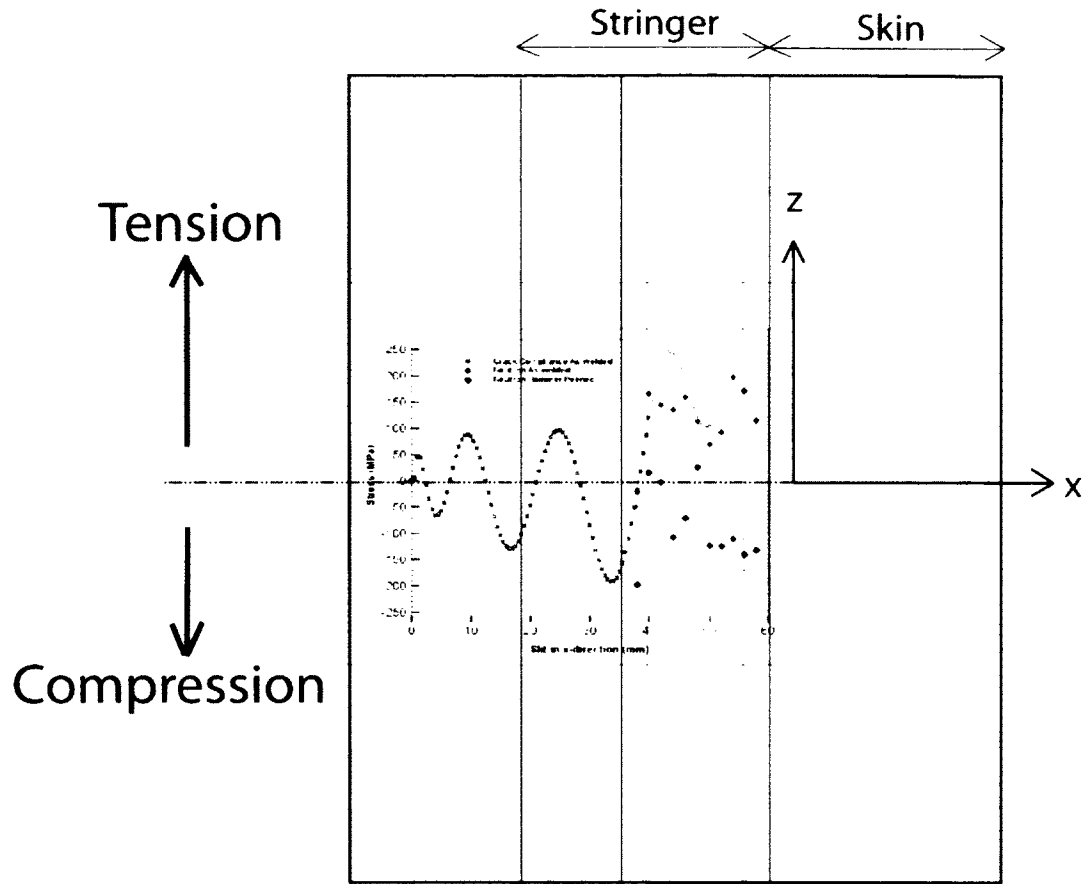


Figure 5.51: Longitudinal weld shrinkage due to longitudinal residual stress in transverse (x) direction of weld

When the weld cools down, it will cause shrinkage along the weld as well. Therefore, there will be a transverse shrinkage of the weld caused by the transverse residual stresses along the weld in the longitudinal direction shown in Figure 5.52.

The combination of the longitudinal and transverse shrinkage of the weld as well as angular rotation of the plate about the longitudinal axis caused the plate to become twisted after the weld has cooled down and the plate was removed from the clamps. The twisted FSW lap joint is shown on the left side of Figure 1.4.

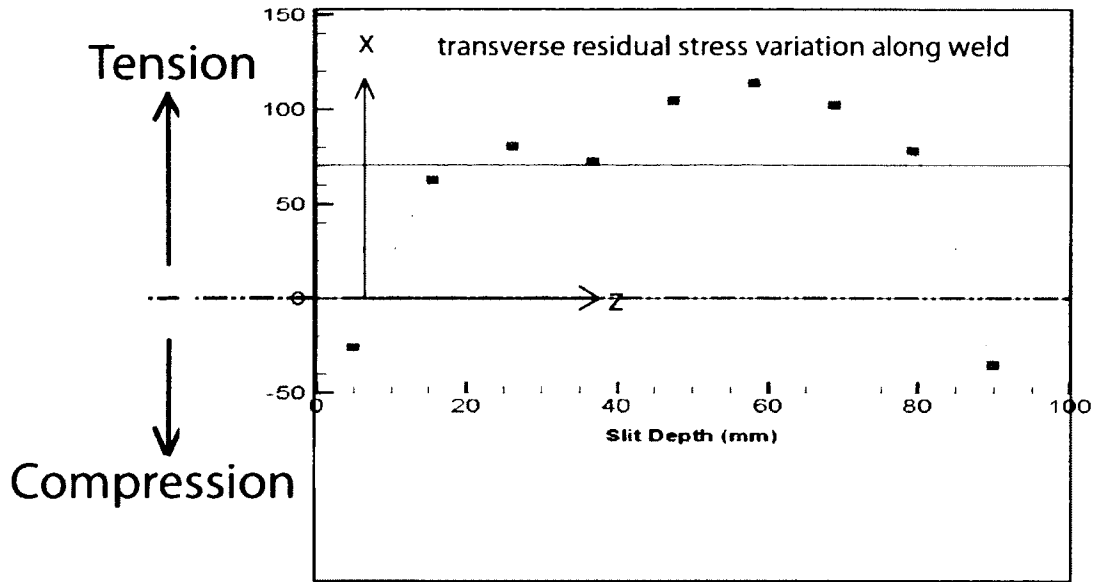


Figure 5.52: Transverse weld shrinkage due to transverse residual (σ_x) in longitudinal (y) direction of weld

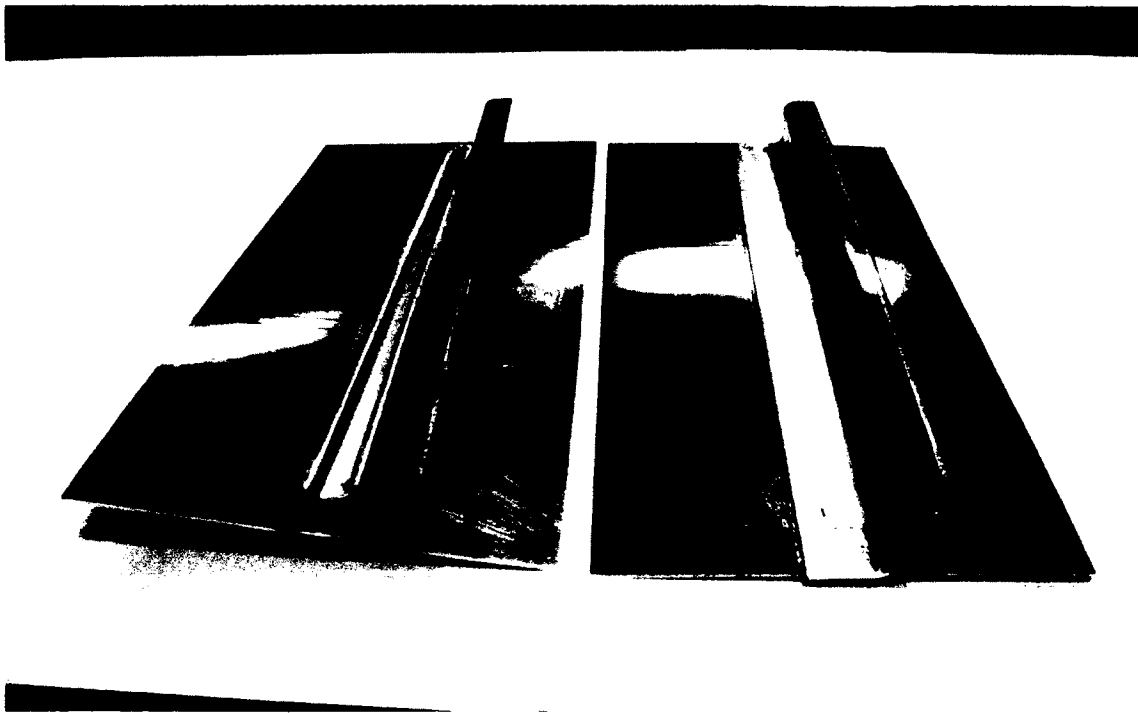


Figure 1.4: FSW plate before and after hammer peening [Merati, 2009]

When looking at the distortion, or lack thereof, in the hammer peened specimen, the results of the residual stress profiles calculated by neutron diffraction show that the residual stresses in the hammer peened plate is almost always lower than that in the as-welded plates in all three principal directions. The profile of the residual stresses in some cases was the same but the magnitudes of the stresses were reduced. The residual stresses in the hammer peened specimen may still be present but the magnitudes are low enough that any distortion in the plate is not visible and the plate appears straighter (Figure 1.4 right).

In conclusion, since this is a qualitative assessment of the effects of residual stresses on the distortion of the FSW lap joints, it can only be said that the cooling and contracting of the weld of the FSW lap joint set up tensile residual stresses in the vicinity of the weld. These residual stresses were the primary cause of the distortion in the as-welded lap joints. After hammer peening the surface of the weld region of the lap joint, the distortion appeared to have been removed. The examination of the residual stresses in the three principal direction show a reduction and/or redistribution in the residual stresses after hammer peening which translate to a reduction in the distortion of the FSW lap joint.

5.6 Results of Fatigue Performance

The first few sections of chapter 5 focused on the results of the residual stress profiles using the crack compliance method and independent verification using neutron diffraction. Two weld configurations were studied in the three principal directions. These residual stress results reveal the triaxial variation in residual stress in the FSW lap joints before and after hammer peening.

When engineers are designing a component, their design is primary driven by two factors: cost and safety. These two factors are related to residual stress since residual stresses has been related to premature cracking and failure of components under service

conditions. If these cracks reach a critical size, they will have to be repaired or replaced after a shorter amount of time and more money spent. Therefore, the main purpose of measuring residual stress in these FSW lap joints and in components in general is to relate these internal stresses to the life of the component. One method of determining the life of a component is to perform a fatigue test. The following section will present the results from several fatigue tests of the as-welded and hammer peened specimens under the same loading conditions. After failure, the fracture surfaces are examined to determine where the crack nucleated and how the complex residual stresses are related to the failure location.

5.6.1 Fatigue Life of Friction Stir Welded Specimens

The results are from the fatigue testing of the two sets of test specimens. All samples were cyclically loaded between 32 KN and 5 KN at 10 Hz, which is summarized in Table 5.17. For the given cross sectional area of the FSW lap joint, the maximum applied stress on the plate is 152.4 MPa. Figure 5.53 is the plot of the two sets of fatigue tests compared with fatigue test of continuous (DP_C) and discontinuous (DP) double pass FSW lap joints by Jung (2007). In Jung's experiments, Type I and Type II refers to double pass welding with outward hook and inward hook respectively. The fatigue results in this thesis will be compared with Jung's DP_C type II fatigue results since they have the same welding configurations as one another. Jung performed fatigue test at four different stress levels (10, 12, 15 and 20 ksi). Since Jung's maximum stress was 137.9 MPa and the stress for this fatigue experiment was 152.4 MPa. Extrapolation of the graph (dotted line) show that if the stress on Jung's continuous double pass lap joint was increased from 137.9 MPa to 152.4 MPa, the sample would fail at approximately the same number of cycles as the as-welded specimens in these fatigue experiments did. The first as-welded test piece (AW1) failed after 86,000 cycles and the second as-welded plate (AW2) lasted 10,000 cycles more and failed at 96,000 cycles. Failure of the two samples occurred very quickly and no visible cracks were noted before failure. A snap shot taken from a video recording of the failure shown in Figure 5.54a shows a 45 mm crack appearing on the bottom surface of the specimen. Within a fraction of a second, the crack

extended to the edge of the plate and caused total separation (Figure 5.54b). Figure 5.55 shows the location where the skin panel separated from the stringer for the first and second as-welded samples. The first sample failed 4 mm to the right of the weld centerline in the region between the weld nugget zone and TMAZ. The second sample failed at a similar location but on the opposite side 6 mm from weld centerline.

Specimen	Cross Sectional Area (mm ²)	Max Applied Load (KN)	Load Ratio (R)	$\Delta\sigma$ (MPa)	Frequency (Hz)	Cycles to failure
AW1	209.95	32	0.16	128.59	10	86,000
AW2	209.95	32	0.16	128.59	10	96,000
HP1	209.95	32	0.16	128.59	10	1,100,000
HP2	209.95	32	0.16	128.59	10	980,000

Table 5.17: Cycles to failure for FSW lap joints

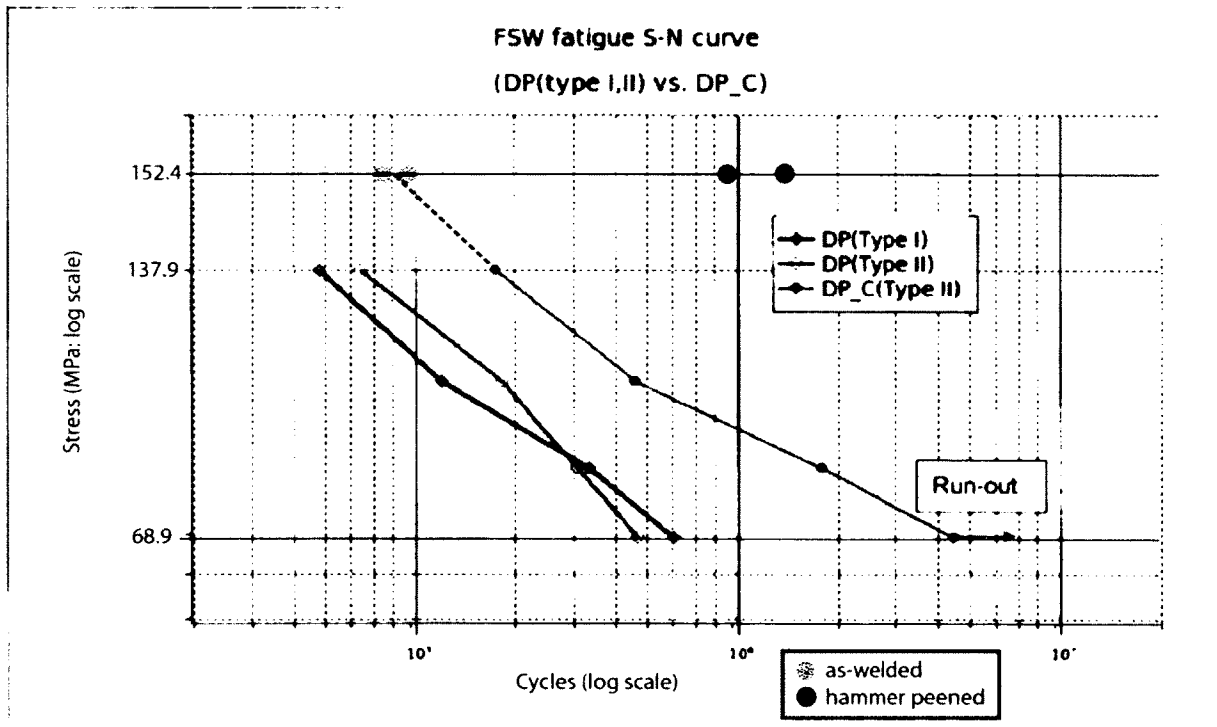


Figure 5.53: Cycles to failure of as-welded and hammer peened test specimens compared with previous fatigue testing of FSW lap joints, [Jung, 2007]

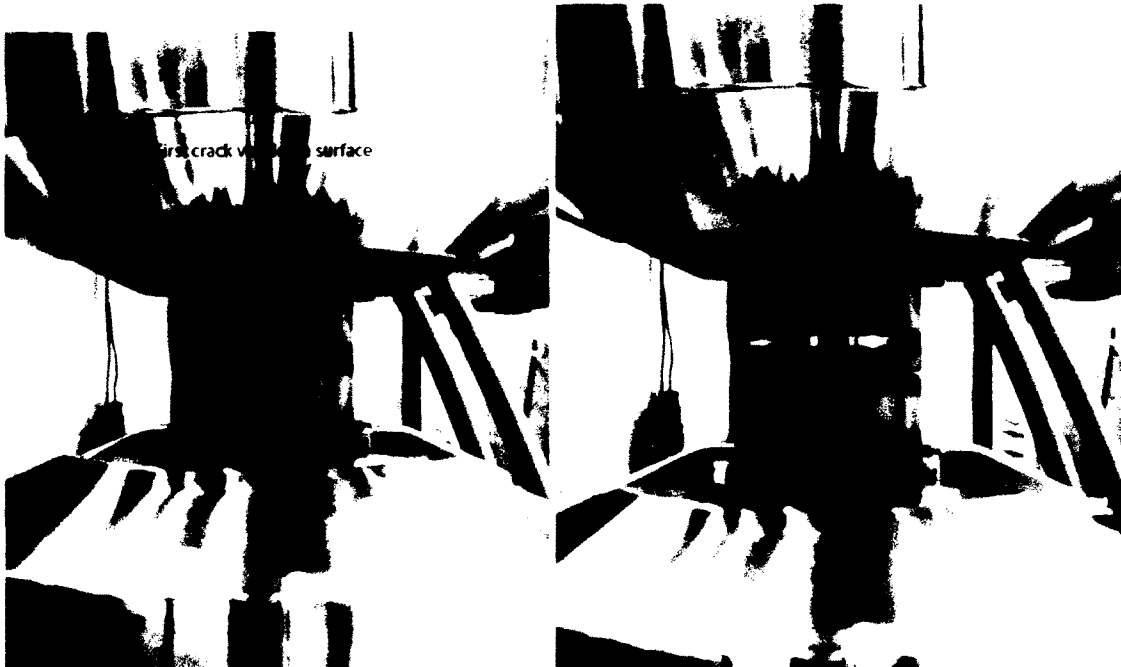


Figure 5.54: a) First visible crack in specimen, b) total separation of specimen

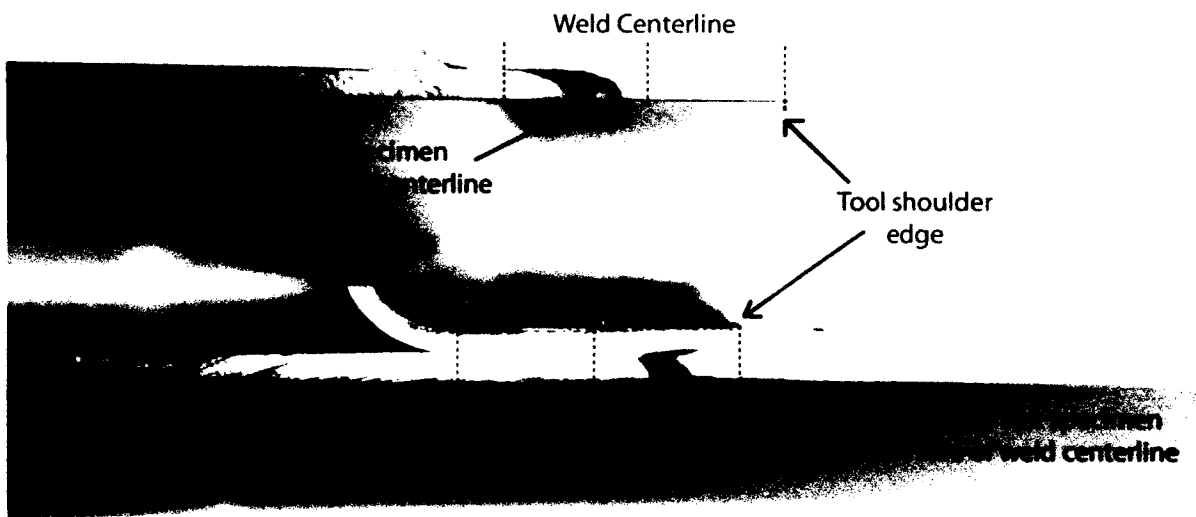


Figure 5.55: Location of as-welded plate separation from fatigue testing

Identical loading parameters were used on the fatigue tests of the hammer peened plates, which failed after a much longer period of cycles than the as-welded specimens. Figure 5.53 plots the results of the hammer peened specimen with the as-welded specimens to show the effects of peening the weld on fatigue life. At a maximum stress level of 152.4 MPa, the first hammer peened specimen (HP1) failed after 1,100,000 cycles. This specimen did not fail near the weld centerline but instead failed right at the edge of the hydraulic grips contact with the plate. The crack appeared to have started from the edge and grew through the thickness of the plate, causing failure and complete separation. It is important to note that fretting (rubbing or chafing fatigue) was a possible failure mechanism as opposed to cyclic fatigue in this test specimen, which is common in aluminum alloys. Since the failure occurred exactly at the edge of the grips and the test specimen, it is believed that the vibration from the grip on the test specimen caused fretting to occur in the plate, leading to a nucleation of an edge crack and finally failure of the specimen. If fretting did not occur, the hammer peened specimens could have failed a much longer number of cycles or even become a run-out. The second hammer peened plate (HP2) failed at 980,000 cycles. Similar to the as-welded specimens, the hammer peened plate separated 14 mm from the weld centerline placing it just beyond the weld region in the parent AA 2024-T3 skin section. Figure 5.56 shows the location of separation of the two hammer peened fatigue test specimens. Figure 5.56a shows failure of plate occurred at the grip in the un-welded skin section. Figure 5.56b show the crack initially approximately started 15 mm from the weld centerline but does move towards the weld but instead the crack grows away from the weld region towards the un-welded skin section.

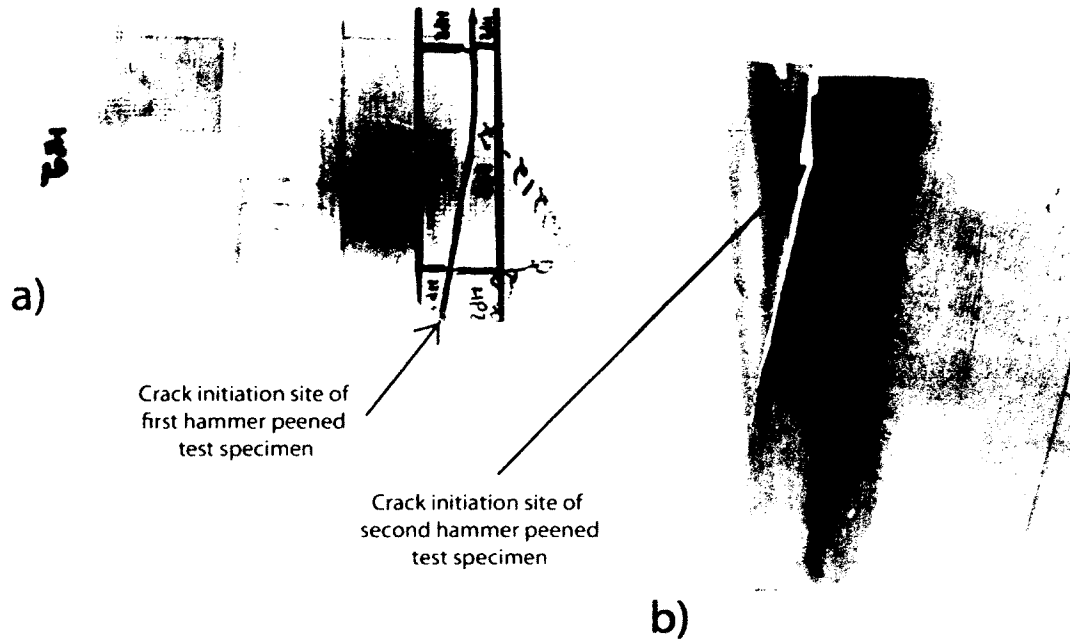


Figure 5.56: Location of both hammer peened plate separation from fatigue testing

5.6.2 Examination of Fracture Surfaces Using Fractography

To get a better understanding of the fatigue failure and possible crack nucleation sites of the FSW lap joints, all four failed specimens were cut into small samples for close examination of the fracture surface using a scanning electron microscope (SEM). Figure 5.57 shows the fracture surface of the first as-welded fracture surface (left) and second as-welded fracture surface (right). Although both specimens failed on either side of weld centerline, the fracture pattern of both surfaces are very similar to one another. Both specimens showed characteristic signs of fatigue growth patterns with multiple edge cracks at the interface between the stringer and the skin panel. The multiple cracks appear to originate from the interface and grew in a semi-elliptical pattern as marked by the dash lines. The SEM images of both fracture surfaces at low magnification reveal the dark region is the fatigue or slow fracture zone and the lighter regions is the overload zone or fast fracture zone. The fast fracture zone is the region where the final catastrophic failure occurs by ductile failure.

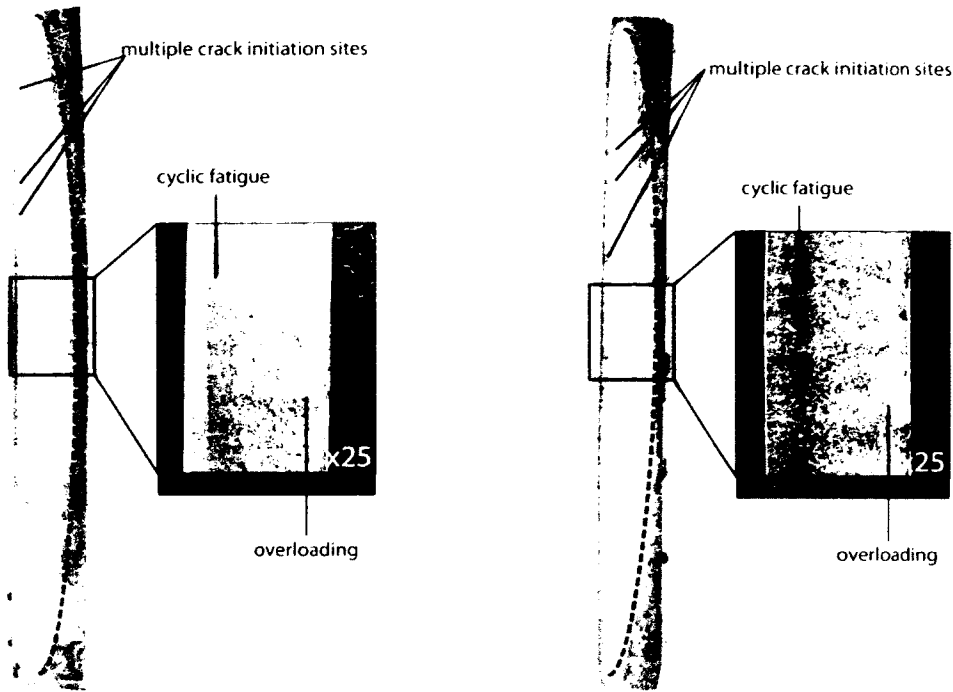


Figure 5.57: Fracture surface of both as-welded specimens showing similar crack growth patterns

For both as-welded specimens, multiple edge cracks 0.2 mm to 0.4 mm in length were found along the interface between the stringer and skin panel. Figure 5.58 is an SEM image at high magnification (x790) showing various ridges that outline the development of a micro edge crack growing into the skin plate and coalescing together to form larger cracks which then join to form a single elliptical crack. Figure 5.59 is a SEM image of the transition between the slow fracture (smooth surface) and overloading (rough surface) of the specimen showing a contrast in fracture surface of the two regions. It appears that the fatigue occurred for 40 % of the skin panels cross section before the remaining cross section was overloaded. Figure 5.60 and 5.61 show the typical fracture surfaces of the fatigue region and overload region of the first and second as-welded specimens respectively. Again, both specimens exhibit similar fracture surfaces in both regions. Typical surface of the cyclic fatigue crack growth was smooth with small uniform fractures of the grains. The small and uniform fracture surface of the fatigue region of Figure 5.60a and 5.61a could also be due to the recrystallization of the parent material. After FSW, the high plasticize grains of the parent material, which are normally much larger and elongated, becomes recrystallized and equiaxed. In contract, the fracture surface of the overloaded region in Figure 5.60b and 5.61b appears to be rough and the

tear in the grains is random and much larger than that of the fatigue region. Dimples or dark spots represent microvoids, which coalesce together to form internal microcracks (highlighted areas). These structures are typical of those found on the fracture surface of aluminum alloys due to ductile failure mode.

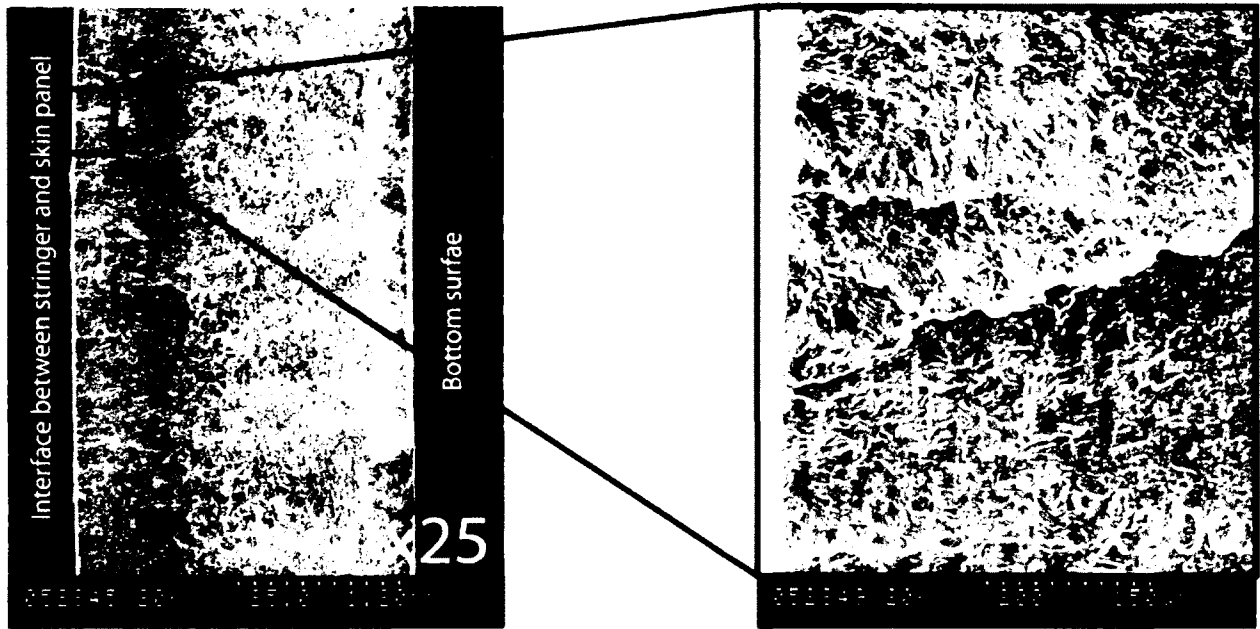


Figure 5.58: Multiple crack nucleation sites originating from an edge crack at x790 magnification

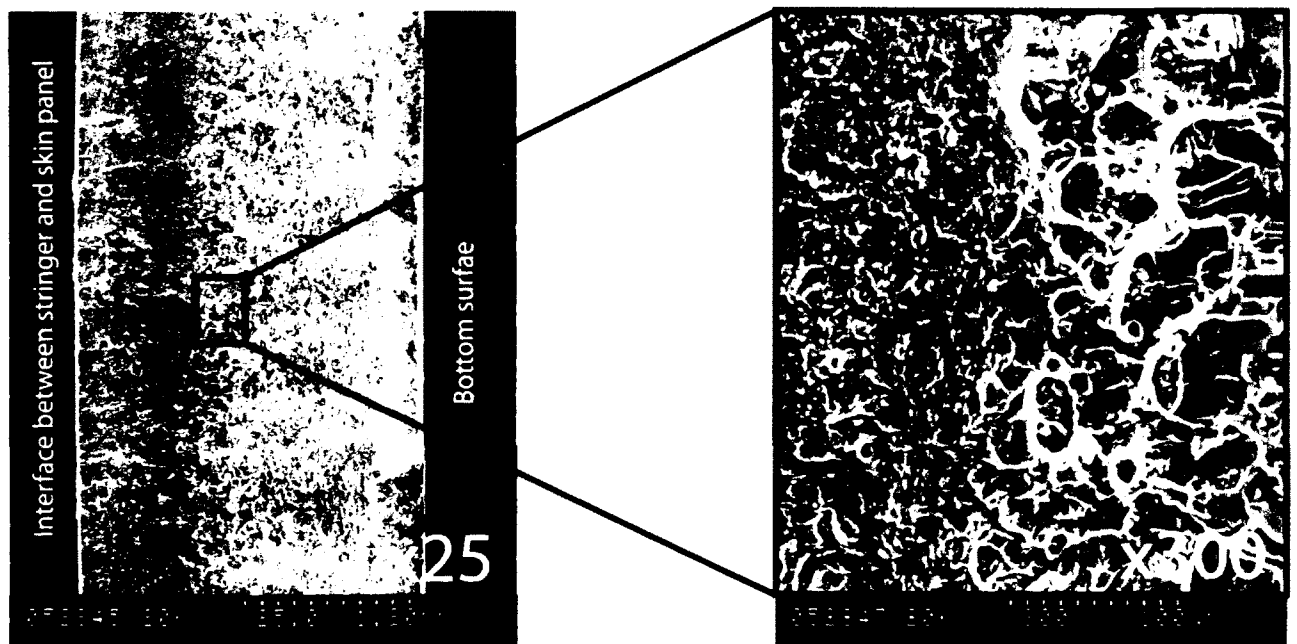


Figure 5.59: Transition between fatigue crack growth and fatigue overload at x300 magnification

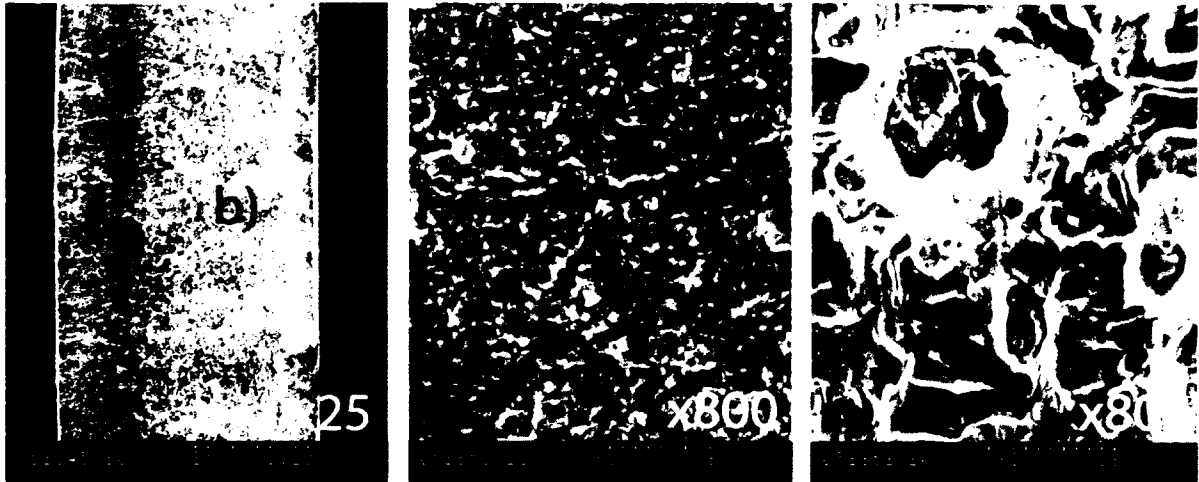


Figure 5.60: Fracture surface of a) slow fatigue region, b) overload region of first as-welded specimen at x800 magnification

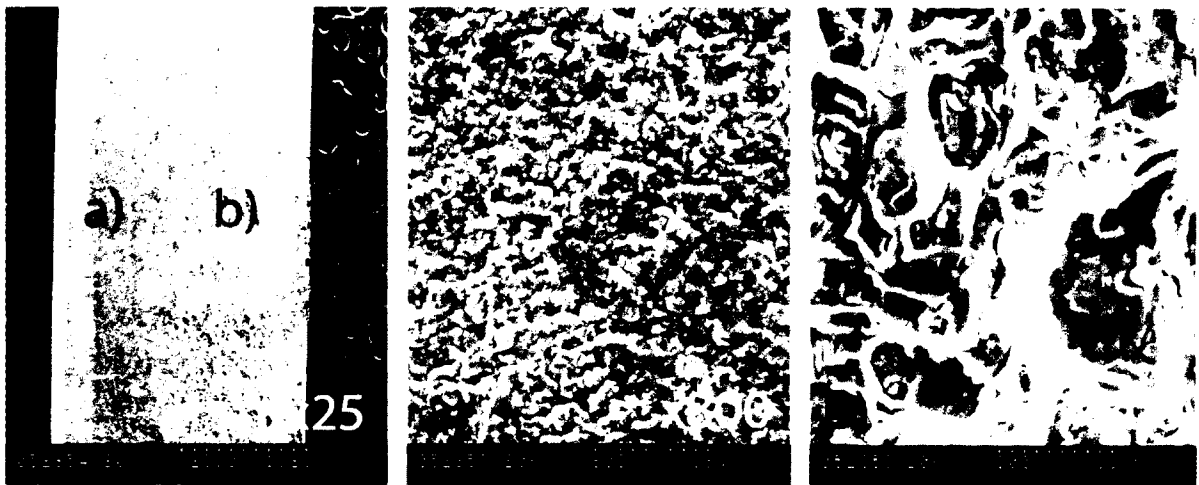


Figure 5.61: Fracture surface of a) slow fatigue region, b) overload region of second as-welded specimen at x800 magnification

Final failure occurred when the shear stress caused the remaining cross section to tear and since the shear stress is greatest at 45 degrees to the applied load, the resulting profile of the fracture resembles a distinctive cup and cone profile seen in Figure 5.55. In conclusion, comparing the fracture surfaces of the two as-welded specimen show that the failure characteristics of both specimens were very similar to one another. This is a testament to the uniformity of the weld at different area of the FSW plate because under constant cyclic loading, both specimens failed at the same locations, similar number of cycles and both fracture surface exhibit common fracture characteristics. Figure 5.62 is

the fracture surface of the first hammer peened specimen, which failed after 1,100,000 cycles. The cause of failure of this specimen was due to fretting and it was determined that the crack originated from a dimple made from the indentation teeth of the hydraulic grip. Figure 5.63 shows a larger image of the dimple and a 490x magnification of crack growth emanating from the dimple. Once the crack extended to a length equal to the thickness of the skin panel (2.21 mm), the remaining section separated due to overloading of the specimen; this fast fracture region exhibited signs of a rough fracture surface.

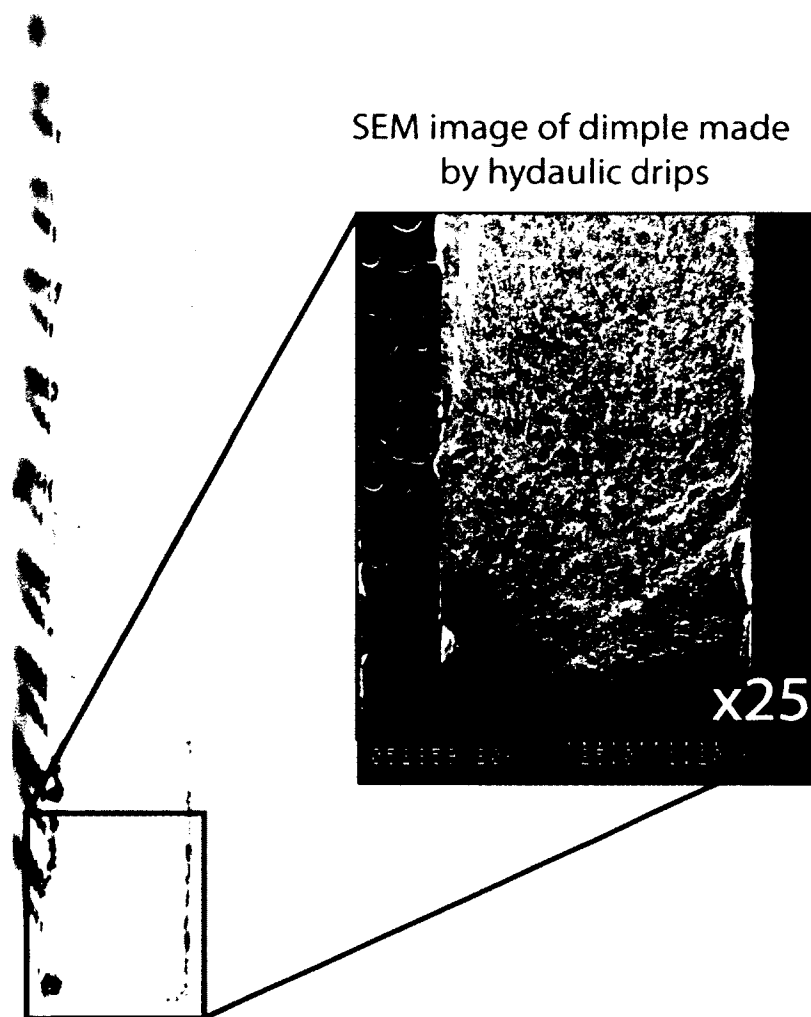


Figure 5.62: Fracture surface of first hammer peened specimen showing failure originating from edge of plate due to fretting at x25 magnification

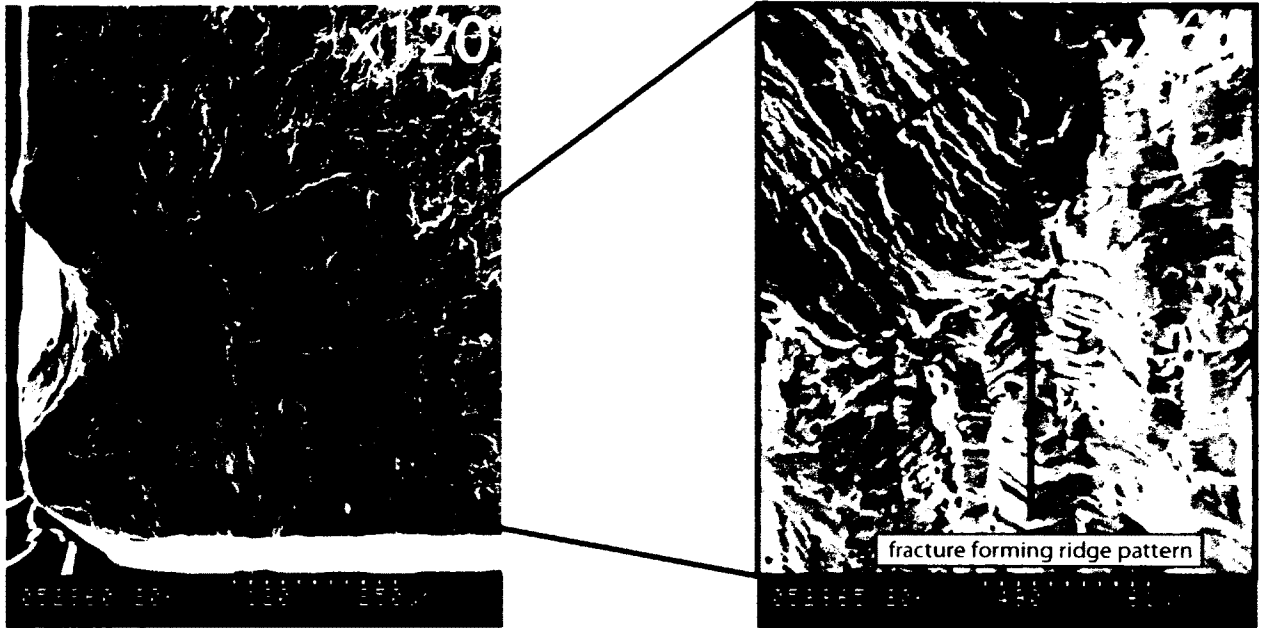


Figure 5.63: 490x magnification of crack growth emanating from dimple of the hydraulic grip at x490 magnification

Figure 5.64 shows the two fracture surfaces of the crack growth region and the overloaded region. Similar to the as-welded specimens, the fracture surface of the fretting region (Figure 5.64a) was smooth and the fracture all occur in one direction. Figure 5.64b is the rough fracture surface in the overload region with larger fractures that were random.

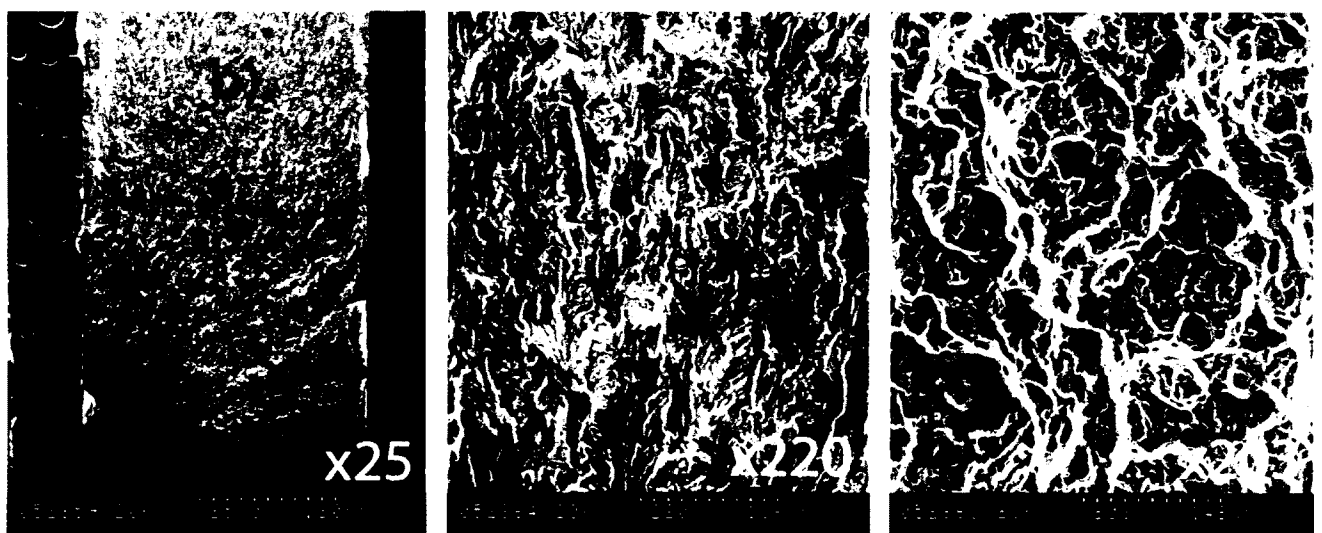


Figure 5.64: Fracture surface of a) typical fretting region x220 b) overload region x203

Figure 5.65 is the fracture surface of the second hammer peened specimen where the crack is assumed to have originated from. Unlike the as-welded specimen, there was no clear sign of striation patterns or slow fracture, which represents fatigue under cyclic loading. The only noticeable marking on the hammer peened fracture surface was a black residue seen in Figure 5.65 which was not found anywhere on the as-welded fracture surfaces. This black residue could have been left behind as a FSW defect. From the rough surface of the second hammer peened specimen it is possible that the specimen was able to withstand the cyclic loading and unloading for 980,000 cycles before failing by instantaneous ductile fracture in the un-welded region of the lap joint.

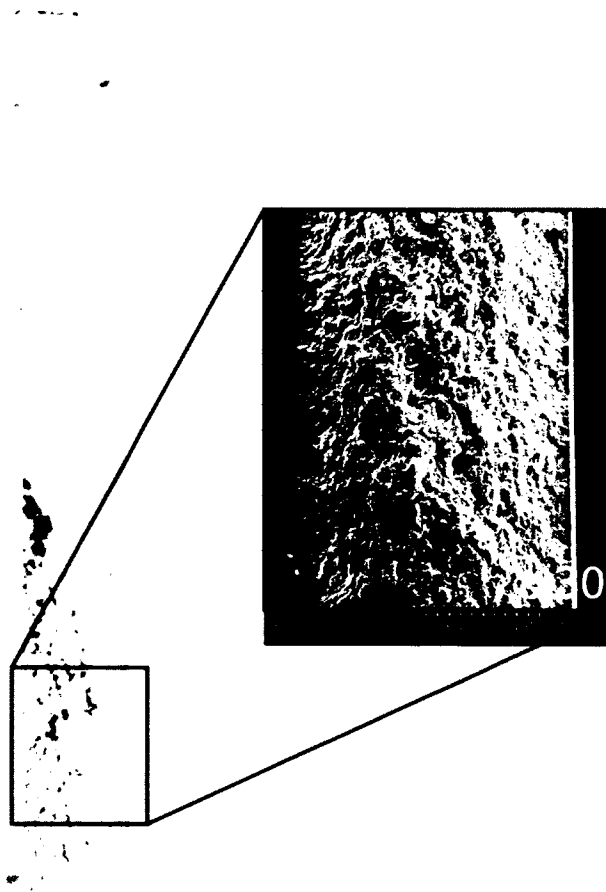


Figure 5.65: Fracture surface of second hammer peened specimen with no clear indication of crack growth pattern

5.7 Examination of Failure Location in the FSW Stringer-to-skin Lap Joints

The first part of the thesis examined the methods of calculating the residual stresses in the FSW stringer-to-skin plates as-welded and after hammer peening. The second part of the thesis examined the material properties of the FSW plates, which included hardness profile. The third part of the thesis studied the fatigue performance of the FSW lap joints as well as fractographic examination of fracture surface to determine where the crack originated.

One of the primary goals of measuring these residual stresses is to have a better understanding of how these residual stresses affect the performance of these aerospace structures. This entails studying the causes of failure of the stringer-to-skin lap joint under service conditions due to the residual stresses present. Therefore, this section will combine all the quantitative measurements listed above to explain how the internal residual stresses in these FSW lap joints effects their performance and more importantly where the failure will occur which very few literatures have attempted to do.

In the as-welded test specimen, two peak transverse residual stresses (σ_x) were located on either side of the weld centerline in the region roughly between the weld nugget and the TMAZ. Figure 5.66 shows the highest value of transverse residual stress (σ_x) found at $x=6$ mm to the right of the weld centerline. This tensile residual stress was 70% of the AA 2024-T3's yield strength.

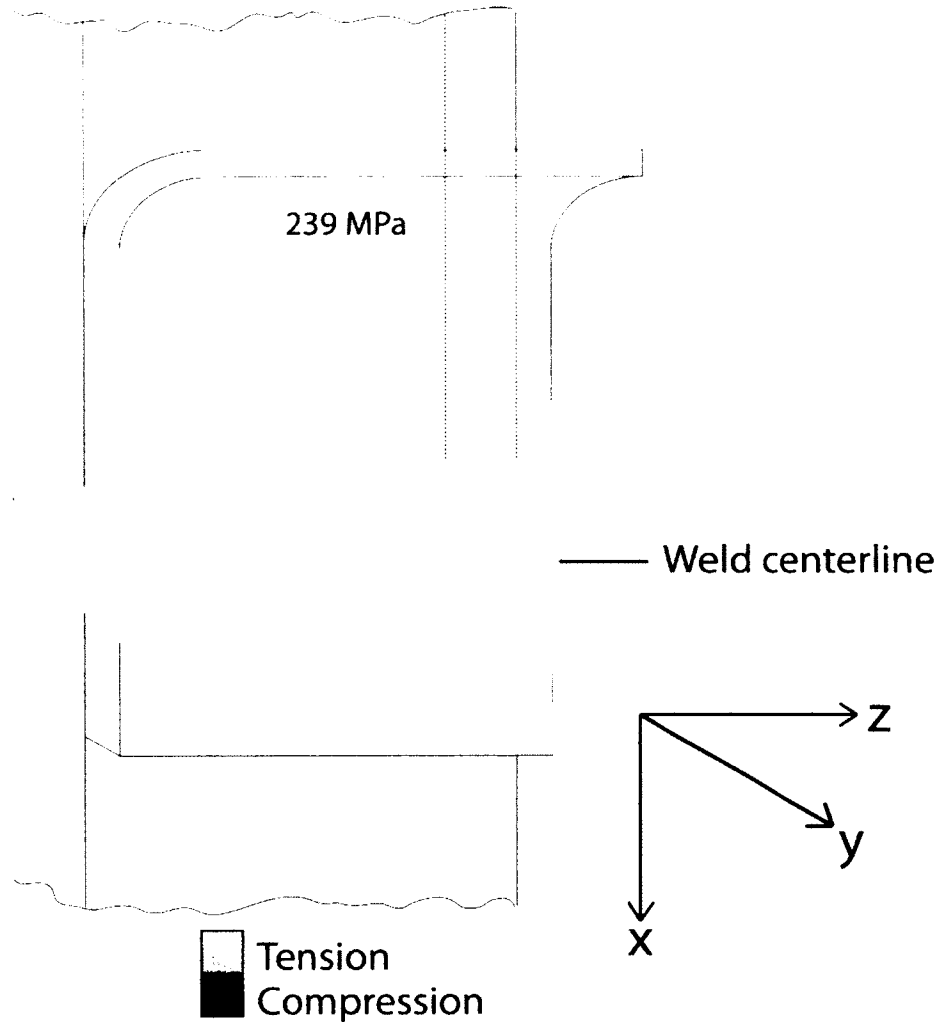


Figure 5.66: Highest transverse residual stress across the weld in first as-welded test specimen

The hardness value measured in the skin section at a distance of $x = 6$ mm to the right of the weld centerline was 129 HV. This hardness value is low compared to the stringer and skins nominal hardness values of 175 HV and 137 HV respectively. The interface between the weld nugget and the TMAZ corresponds to low hardness regions because the original structure in this region is over aged and there is not enough solute left in the material. This area of the weld will be relatively ineffective in inhibiting dislocation motion and the strain localization in the softened area of the weld will result in degradation in the mechanical properties, Hatamleh (2007).

The low hardness value and high tensile residual stress coupled with the cyclic loading of 86 MPa caused the residual stress in this region to the left of the weld centerline to be greater than the yield strength of the skin section causing crack to nucleate and eventual separation of the lap joint in the skin panel, 6 mm to the right of the weld centerline as shown in Figure 5.67.

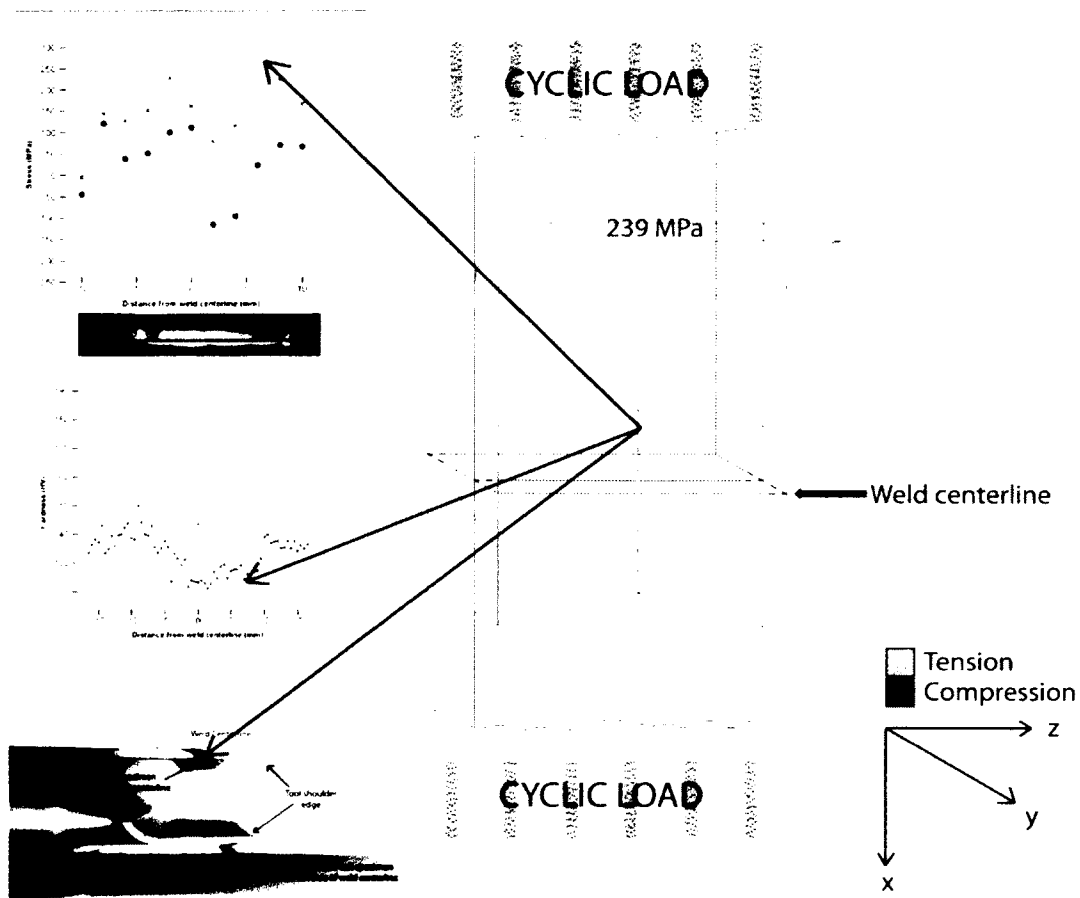


Figure 5.67: Failure of first as-welded sample due to combination of high tensile residual stress and low hardness value to the right of weld centerline ($x = 6\text{mm}$) in region between weld nugget and TMAZ

On the left hand side of the weld centerline at a distance of $x = -2\text{ mm}$, there was a second peak tensile stress measured at 224 MPa, which is 65% of the AA 2024-T3's yield strength as shown in Figure 5.68. The hardness value measured at this location was

118 HV. Again, the combination of the high tensile stress and low hardness value caused the plate to fail 2 mm to the left of the weld centerline in the skin section as shown in Figure 5.69.

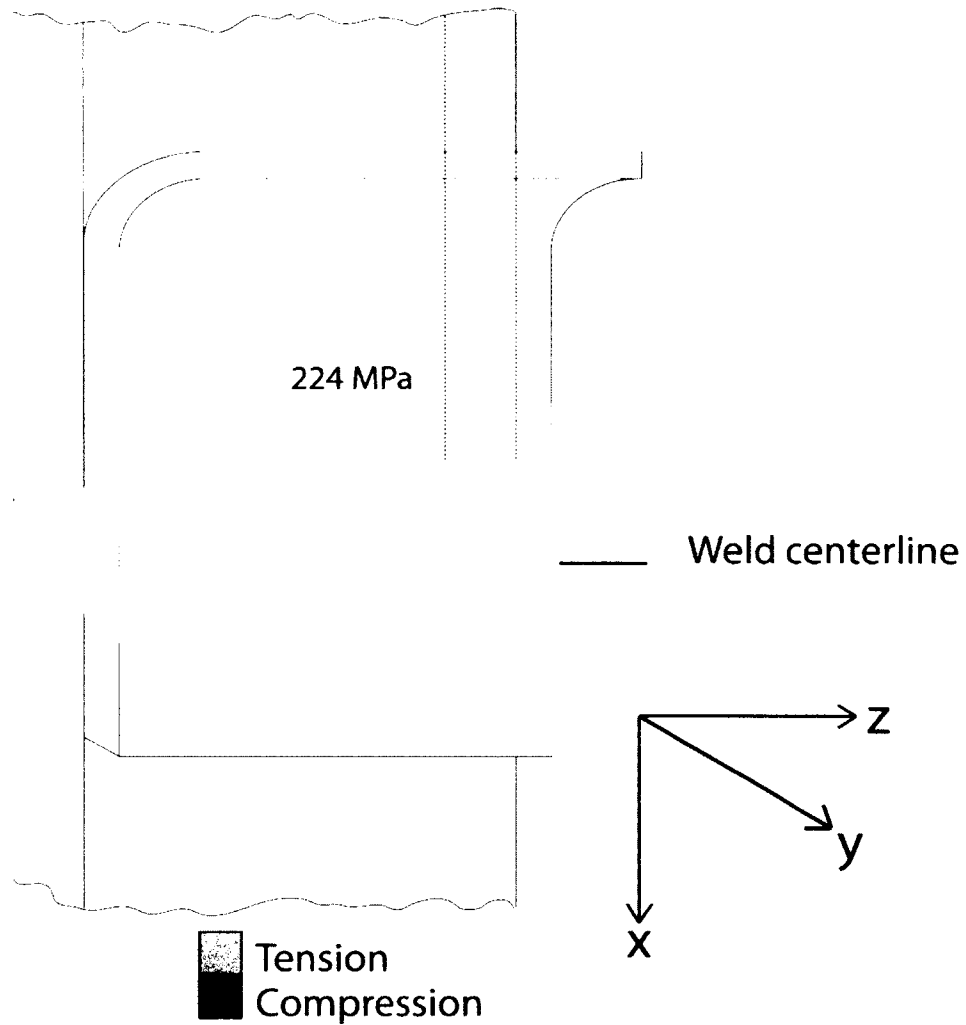


Figure 5.68: Highest transverse residual stress across the weld in second as-welded test specimen at $x = -2$ mm from left of the weld centerline

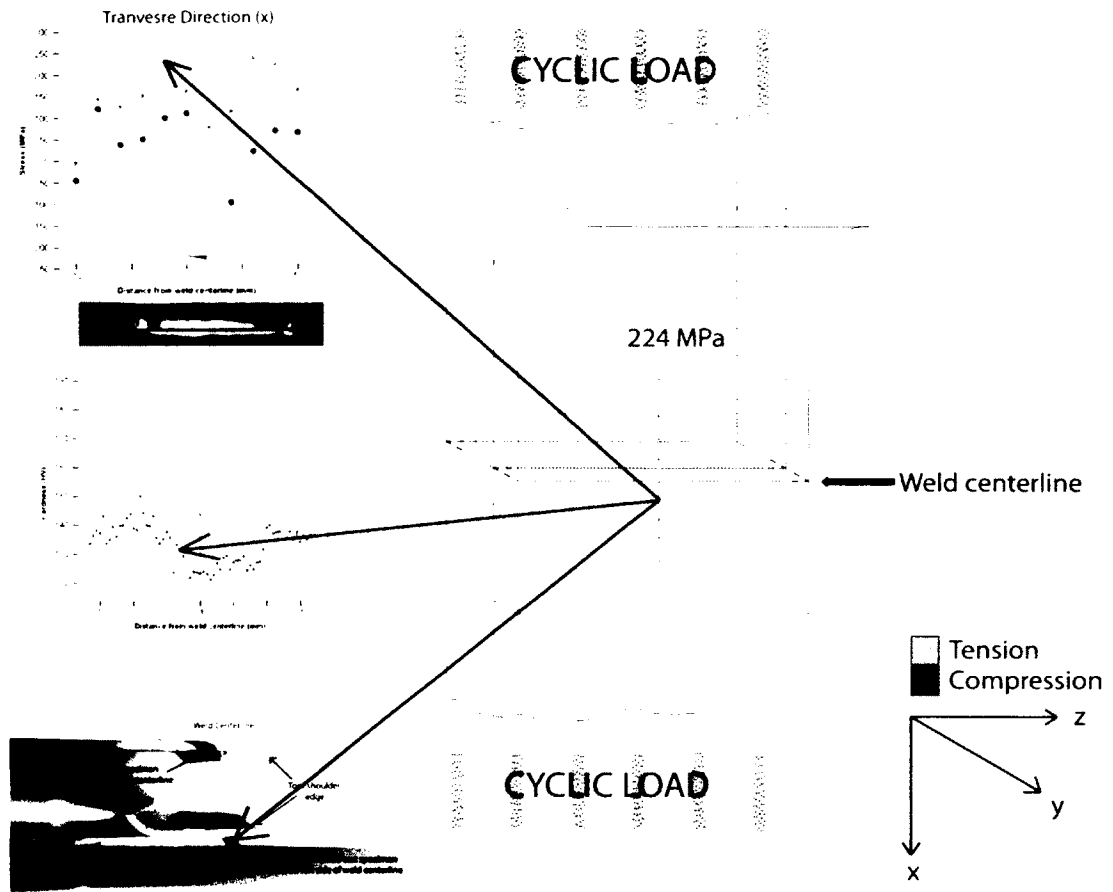


Figure 5.69: Failure of second as-welded sample due to combination of high tensile residual stress and low hardness value $x = -2\text{mm}$ to left of weld centerline

Defects Found In FSW Lap Joints

This section relates the failure locations in the FSW lap joints to residual stress and hardness of material but it is important to note that defects found in the weld region of these FSW lap joints are also a major factor affecting the crack nucleation site. As shown in Figure 3.12, large voids were found in the weld region between the weld nugget and TMAZ. These voids are left behind during the mixing process due to inadequate mixing of the softened material. A combination of tool tip, rotation and translation speed could have caused these voids to form. The average length of these voids is 0.2 mm long perpendicular to the weld direction. High tensile residual stresses in the weld region and

cyclic loading could cause cracks to nucleate from these defect locations. From the examination of failure locations of these FSW lap joints, it is concluded that the voids found in Figure 3.12 corresponds to the location near the failure location of the fatigue specimen. Therefore it is believed that the as-welded FSW lap joints failed at these voids due to a combination of high tensile residual stress, reduced hardness and cyclic loading.

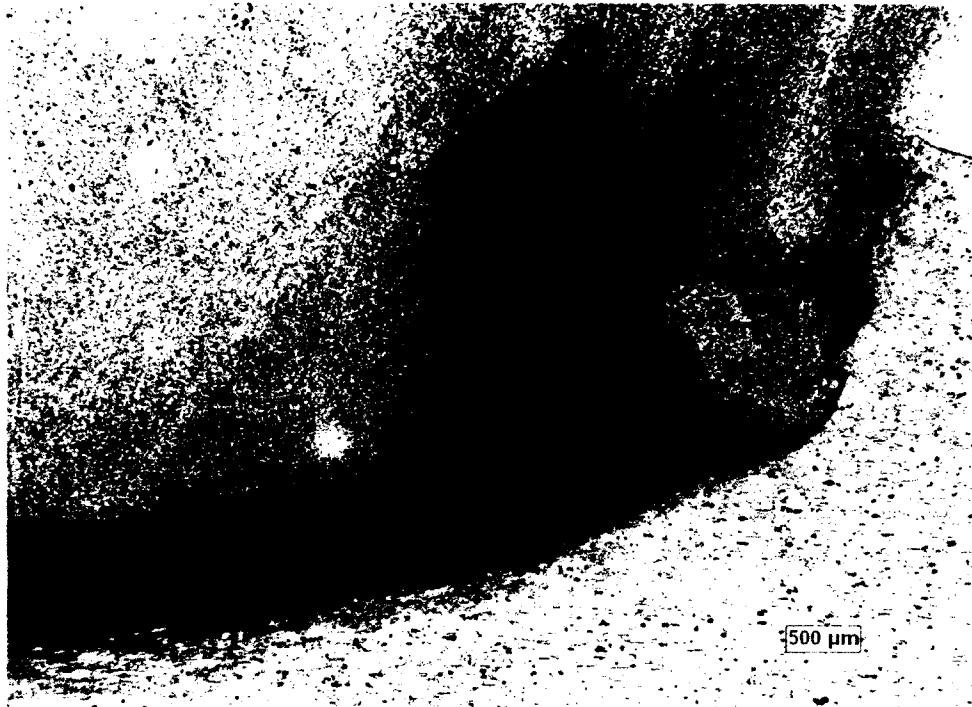


Figure 3.12: Large voids found at edge of weld tool between weld nugget and TMAZ

It has been shown through fatigue testing that the hammer peened specimens outlived the as-welded specimens under the same loading conditions. However, the crack nucleation site is unclear since the two hammer peened specimens failed at approximately the same number of cycles but at different locations and also due to different modes of failure. The following is an explanation as to why the hammer peened specimens were able to outperform the as-welded specimens.

There were two main effects of peening the surface of the FSW lap joint. The first effect was to reduce the distortion in the plate. This reduction in distortion is due to the reduction or redistribution of residual stress in the lap joint. The residual stress results from neutron diffraction of both welding conditions demonstrated that the hammer peened specimen had a lower magnitude of residual stress compared to the as-welded specimen in all three principal directions. This reduction in residual stress can explain the reduction in distortion present in the plate.

The second effect of hammer peening is an increase in the hardness of the material near the top surface of the lap joint. From the hardness testing, it was demonstrated that hammer peening the surface of the FSW lap joint help increase the hardness of both material (skin and stringer) to the same level of hardness as the parent, un-welded materials. This increase in hardness, which translates to an increase in the material's yield strength, could help increase the fatigue lives of these lap joints. Other than increasing the fatigue life, the failure location moved outside of the weld region, which typically is the weakest region of a welded component.

In terms of defects, hammer peening the surface of the material would not likely remove the voids and defects found at the weld toe and interface between the two materials in the lap joint configuration.

The main conclusion taken from the examination of failure locations of the FSW lap joints before and after hammer peening is that the effects of hammer peening reduced the residual stresses in all three principal directions of the plate. The redistribution of residual stresses moved the fatigue failure location of these lap joints outside of the weld region. It is shown from previous literature, Straon et al. (2002) that the weld region of a welded component is the weakest region where crack typically nucleate from. Especially the overlap weld toe on the advancing side of the weld has a detrimental effect on fatigue life

Dalle et al. (2000). Therefore, the benefit of hammer peening is to extend the life of the component as well as move the failure location outside of the weld region.

In terms of the effects of the residual stresses present in these lap joints, the following conclusions can be made: The residual stresses are the primary cause of the distortion in plates, when talking about fatigue performance of these FSW lap joints, the effect of residual stresses help rise (tensile stresses) or lower (compressive stresses) the mean stress or load ratio, R , of the applied loading but the location of crack nucleation and failure location is caused by a combination of defects found in weld toe and the reduced hardness due to FSW and the increase in residual stress.

The knowledge of the residual stresses produced from the FSW process can be used by aircraft designers as a guide when designing aircraft components such as these stringer-to-skin lap joints based on the damage tolerance approach. The designer has two choices; they can keep the residual stresses which are present in the as-welded configuration and design the aircraft to be serviced within the time period which is safe for that level of residual stress, or they can alter the residual stresses so that the fatigue life is improved and the aircraft is able to be in service for a longer period of time. The decision will be based on how much improvement on the lives of the component is achieved by the post welding process and how much money will that cost the manufacturers. Maintenance workers would be interested in the failure locations of these lap joints because it will allow them to focus on the weld region where failure is most likely to occur when detecting cracks and other defects in the lap joints.

Chapter 6

CONCLUSIONS AND RECOMMENDATIONS

6.1 Conclusions

The primary objective of this thesis was to develop a method of predicting the residual stresses resulting from the FSW process in the stringer-to-skin lap joint based on the crack compliance method. Prior to the work presented in this thesis, there was very little literature on the residual stresses and their effects on these FSW stringer-to-skin lap joints. The following are some conclusions regarding the results of the residual stress profiles of the FSW lap joints calculated using the crack compliance method:

- The feasibility of the crack compliance method (conventionally used on simple rectangular geometries) on determination of residual stress profiles in FSW aluminum lap joint was demonstrated by successfully re-calculating the residual stresses in three previous experiments using the crack compliance method (Chapter 4, section 4.1.1.1-3).
- The transverse residual stress (σ_x) through the thickness of the 3.76 mm as-welded and hammer peened test specimens were determined using the crack compliance method. Verification of FE model was successful by applying the calculated stress profile back into FE model and calculating the corresponding strain values (Chapter 5, section 5.1.1).
- The variation of transverse residual stress (σ_x) in the through thickness (y) direction of the as-welded plate was a result of the complex mixing of the materials by welding tool (Figure 5.4).
- Transverse residual stress (σ_x) at the top surface of hammer peened plate were highly compressive, 57% higher than in as-welded plate. Such an increase in the compressive stress at the material surface by hammer peening can help prevent surface crack growth (Figure 5.8).
- A maximum tensile stress of 113 MPa was present in the mid-section of the hammer peened plate as a reaction to the compressive stresses at the top surface; this stress could affect sub-surface crack nucleation and growth (Figure 5.7).

- The longitudinal residual stress (σ_z) in the transverse (x) direction of the as-welded plate was calculated using a hybrid version of the crack compliance method in which multiple strain gauges were placed along the plate and used in the calculation of the residual stress.
- Longitudinal residual stress (σ_z) across the weld resemble a “double M” shaped profile with a peak tensile stress at $x = 43.5$ mm of 252 MPa (50% of the stringer’s yield strength and 73% of the skin’s yield strength) which is the region between the weld nugget and TMAZ (Figure 5.22). This unique profile is a result of the second pass of the welding tool.
- The transverse residual stress (σ_x) in the longitudinal (z) direction in the as-welded specimen using the crack compliance method was not successful because FSW geometry in the out-of-plane direction was too complex to be simplified in 2D FE model (Figure 5.49).

An independent, non-destructive method of neutron diffraction was conducted on the two FSW lap joint configurations. The three components (σ_x , σ_y , σ_z) of residual stresses in all the three principal directions were determined. The following are some concluding remarks of the results of neutron diffraction:

- Neutron diffraction was successful in calculating the residual stress profiles in the three principal directions for both as-welded and hammer peened configurations.
- Neutron diffraction results were compared with crack compliance method and the residual stresses in two out of the three principal directions agreed with one another. Those two directions were the through thickness (y) and transverse (x) directions (Figures 5.42, Figure 5.44, Figure 5.45).
- Results of neutron diffraction tests show a reduction in tensile residual stresses in the three principal directions after hammer peening. (Chapter 5, section 5.2).
- Neutron diffraction is a well-established and reliable method of obtaining residual stresses in metallic components. However, since neutron diffraction is not readily

available and economical for most users; the crack compliance method is a very practical alternative solution to predicting the residual stress profiles.

- Furthermore, the calculation and verification of the transverse residual stress in the through thickness (y) direction of the weld and the longitudinal residual stress across the weld (x -direction) of the FSW lap joint demonstrated that the crack compliance method conventionally applied to simple uniform and rectangular geometries were successfully applied to more complex and non-uniform geometries with some limitations. Therefore, the application of the crack compliance method now has a potential to be used on a much wider range of components and geometries that were not able to be examined prior to the work presented in this thesis.
- For the determination of residual stress profile in the through thickness direction of the 3.76 mm lap joint, it was concluded that using the compliance method is advantageous over neutron diffraction since the gauge volume of neutron diffraction only allowed for the measurement of stress at 6 positions (0.5 mm intervals) compared to 28 positions using the crack compliance method because of the ability of the wire EDM to make small increments (0.125 mm intervals).

A secondary objective was to qualitatively relate the effects of these residual stresses on the distortion present in the lap joints after the FSW process. The following are several conclusions on the distortion of the FSW lap joints due to residual stresses:

- Distortion and twist in as-welded FSW lap joint are caused by the presence of residual stresses in the transverse, longitudinal, and through thickness direction.
- Angular rotation of the FSW lap joint caused by the transverse residual stresses (σ_x) through the thickness of the plate in the y -direction (Figure 5.50).
- Longitudinal and transverse residual stresses are caused by longitudinal and transverse shrinkage of the weld (Figure 5.51 and Figure 5.52 respectively) upon cooling.
- Neutron diffraction stress results of the hammer peened specimen show a reduction in tensile residual stresses in all three principal directions. This

reduction in residual stress subsequently relieved the distortion in the 3.76 mm FSW plate.

The final objective of the thesis was to carry out a fatigue performance test on these FSW lap joints in the as-welded and hammer peened configurations to examine the effects of residual stresses on failure location and fatigue lives. The fatigue experiments, though limited, concluded that:

- Under the same loading parameters and maximum applied stress of 152 MPa, fatigue lives of hammer peened specimens were ten times greater than that of as-welded specimens. The hammer peened specimen failed after $10e^6$ cycles (Table 5.17).
- Failure of as-welded test specimens ($10e^5$ cycles) occurred in the skin section of the weld in the region between weld nugget and TMAZ.
- Failure of hammer peened test specimens occurred at different locations away from weld region, one being caused by fretting.
- Fracture surface of crack initiation site was examined using SEM and it was concluded that failure occurred in skin section of weld and growing to bottom surface of plate by ductile failure.
- Hardness profiles for both weld configurations were measured at several locations from weld centerline, which showed the hardness values were lowest in the weld region of as-welded test specimens (Chapter 3, section 3.3).
- Hardness values increased in stringer section after hammer peening due to work hardening effects of peening the top surface of the weld (Figure 3.19).
- Relating the fatigue failure locations with the hardness profiles and calculated residual stresses in the as-welded FSW plate reveal that the most likely regions for fatigue crack nucleation is located in the skin section in the region between the weld nugget and TMAZ where a peak tensile stress and lowest hardness value was measured (Figure 5.67 and Figure 5.69).
- Failure occurred due to a combination of weld defects, reduced hardness of material due to friction stir welding process and tensile residual stresses.

Damage tolerant design is used extensively in aircraft construction and is mandatory for large civil aircraft. Hence, the distribution of residual stress arising from the friction stir weld process and fatigue failure under aircraft service loading will be a major role in these damage tolerant design processes. Although the heat associated with friction stir welding is lower than conventional arc welding methods, the shrinkage of the weld caused residual stresses to be present throughout the 3.76 mm stringer-to-skin lap joint. Since the calculated residual stresses in the hammer peened specimen were almost always lower than that in the as-welded specimen in all three principal directions and because the as-welded specimens failed at the weld region at a much shorter number of cycles than hammer peened specimen, it is concluded that the tensile residual stresses and welding defects play a critical role in the performance and failure of these as-welded FSW lap joints. The nature of these residual stresses and its distribution within the welded component is a complex and not easily understood phenomenon, but with the hybrid residual stress calculation technique demonstrated in this thesis, it is possible to determine the residual stresses in the FSW as-welded lap joints. Furthermore, with a post-welding technique of hammer peening, the residual stresses and distortion was reduced and fatigue life was dramatically enhanced.

6.2 Contributions

The following is a summary of the main contributions this thesis presents to the research and scientific community. The topics of friction stir welding and the residual stress measurement using the crack compliance method are both relatively new areas of research. Both topics are of high interest and there has been a lot of literature written on both subject matters. There has been no literature measuring the residual stress variations through thin cross section of materials. Most of the literature using both destructive and non-destructive methods of measuring residual stresses measures variation in stresses for samples with thicknesses greater than 10 mm thick. The high spatial resolution of the crack compliance method has successfully resolved the variation in stress through the thickness of such a thin cross-section less than 4 mm thick. These results have never been demonstrated prior to the work of this thesis. Secondly, most literature dealing with

residual stress variation look at stress profiles in one or two directions (transverse and longitudinal). When one is studying the properties of a weld and how that relates to crack growth and fatigue failure of these welded components, knowing the stress profile in one direction is insufficient. This thesis measures the residual stress profile in all three principal directions for the FSW stringer-to-skin lap joint. The final and probably most interesting contribution that resulted from this thesis is the application of the 2D crack compliance method on more asymmetrical geometries. When the author was doing a literature review of the crack compliance method, the author wanted to find literature on the crack compliance method being applied to geometries that were not symmetrical and was not able to find any such experiments. The compliance method used to measure stress variation through plates and blocks of square material have been examined extensively. The first residual stress measurement was through the thickness of the stringer-to-skin lap joint which satisfied the compliance methods requirement which that the geometry in the through thickness direction was constant. Modelling the stringer, as an entire 2D cross section was successful in producing residual stress results that were later verified with neutron diffraction. The success of applying the compliance method to asymmetrical geometry means that other geometries similar to the stringer-to-skin lap joints can be studied. The material and dimensions may be different but the proposed crack compliance technique in this thesis remains the same.

6.3 Recommendations

Originally neutron diffraction was not available in the thesis and the destructive method of crack compliance was chosen as the method of residual stress measurement. All compliance calculations were performed prior to neutron diffraction and so the residual stress profiles are measured at different sections of the same FSW plates. Ideally if neutron diffraction were available at the beginning of the thesis, the order of residual stress measurements would begin with non-destructive evaluation followed by destructive evaluation of each test specimen. Also, neutron diffraction measurements in the through thickness direction was taken at 6 points which help show the basic trends in the through thickness profile. To obtain a more complete profile in the through thickness direction,

more points can be taken in the through thickness direction which involves using a smaller gauge volume and decreasing the distance between strain data points. Fatigue testing can be improved by having more samples for testing. The FSW panels that were available for the experiments in this thesis were manufactured in a limited quantity prior to the start of this project. Therefore, the number of test specimens that could be cut and used for the various experiments in this thesis was also limited. For the fatigue testing, only two sets of samples were tests at a single cyclic load level and the fatigue threshold for both specimens was not able to be determined. If more specimens were available for testing, different loads could be applied to the specimen to determine the fatigue threshold of these lap joints.

6.4 Future Work

To develop potentially new topics of study based on the current research in this thesis, the basic understanding of the original objectives has to first be achieved. Only after spending a significant amount of time on the calculations of the residual stresses in the FSW lap joints using the crack compliance method were these future work able to be proposed. Hammer peening is a post-welding process that was able to increase compressive stresses at the surface of weld zone, reduce overall residual stresses in all three principal directions of FSW lap joints. However, this post-welding process might not always be available for FSW lap joints in large structures which are manufactured and assembled on site, therefore it is worth examining if the welding parameters themselves can be changed so that these residual stresses resulting from the welding process can be used in a way to benefit the mechanical properties of the structures. All friction stir welding in this thesis was performed using a single rotation and translation speed. To further study the effects of weld parameters on residual stress profiles in these stringer to skin lap joints, several lap joints could be welded with different welding parameters and the residual stresses calculated based on the proposed methods in this thesis could be applied to see if increasing the weld speed or rotation speed will increase or decrease the residual stresses originally measured in this work. Previous studies have already demonstrated the effects of tool rotation and translation speed on simple butt-

welded geometries. Other residual stress relief methods such as stretching and heat treatments can be conducted on these FSW lap joints. The crack compliance method can be used to measure the residual stresses in these different stress relieved lap joints and compared with the hammer peened lap joints.

In this thesis, only two welding configurations were examined and in particular, the post welding process of hammer peening was studied. There are several other post welding techniques that can be used to alter or relieve the residual stresses from the FSW process such as other peening methods, tensioning and heat treatment. Future designer and engineers can examine the effects of these post-welding processes on the residual stress and failure lives of these components based on the residual stress measurement techniques demonstrated in this thesis. The residual stress in the hammer-peened specimen was determined by the crack compliance method and neutron diffraction. A potential future work involves studying the effects of other peening methods on the FSW stringer to skin lap joints such as shot peening and laser peening. The advantages and disadvantages of both methods could be weighted against that of the hammer peening method.

Currently the crack compliance method is applied to 3D components that have a simple, rectangular geometry that can be simplified in a 2D FE model. If the crack compliance method could be further developed based on the research of this thesis to be used on more complex asymmetrical geometries, it would find a very valuable niche in the field of residual stress measurements of complex components. The improvement involves developing a way to model the object as a 3D FE model to obtain the compliance functions, which are used to calculate the residual stress profiles.

Finally, the objectives of this thesis did not include examination of thermal distributions in the FSW lap joints and how these distributions affect the residual stresses. A possible

future work would include measuring the residual stresses in the FSW process as the weld is being formed. Neutron diffraction is able to perform in-situ experiments, which will determine the strains in the component during the welding process. The heat distribution during welding can also be measured and related to any residual stresses present at the time of welding before the component is released from the clamps.

6.5 Publication and Presentations

The following is a list of publications and presentations that was based on the work of this thesis.

1. Poster Presentation at the Residual Stress Summit, Tahoe City, California, USA. "*The Application of the Crack Compliance Method on a Friction Stir Welded Lap Joint: Preliminary Calculations*". September 26-29, 2010.
2. Oral Presentation at CASI AERO11, Montréal, Canada. "*Residual Stress Measurement of a Friction Stir Welded Stringer-to-skin Lap Joint Based on the Crack Compliance Method*". April 26-28, 2011.
3. Publication in AERO11 Proceedings. "*Residual Stress Measurement of a Friction Stir Welded Stringer-to-skin Lap Joint Based on the Crack Compliance Method*". April 2011.
4. Publication in CASI Journal, in press. "*Measurement of Through Thickness Residual Stress in FSW Plate Using Crack Compliance Method*". 2012.
5. 1st place winner of the ASM poster competition. "*The Application of the Crack Compliance Method on a Friction Stir Welded Lap Joint*". March 27, 2012.
6. Oral Presentation at 15th International Conference on Experimental Mechanics, Porto, Portugal. "*The Investigation of the Tri-axial Residual Stresses in a Friction Stir Welded Lap Joint*". July 21-28, 2012.

7. Publication in ICEM15 Proceedings. "*The Investigation of the Tri-axial Residual Stresses in a Friction Stir Welded Lap Joint*". July 2012.

8. Oral Presentation at the 9th International Conference on Residual Stress, Garmisch, Germany. "*Residual Stress Measurement of a Friction Stir Welded Lap Joint by Neutron Diffraction*". October 7-9, 2012.

9. Publication in ICRS9 proceedings. "*Residual Stress Measurement of a Friction Stir Welded Lap Joint by Neutron Diffraction*". October 2012.

10. Publication in Journal of Material Science B, in review. "*Comparison Between Destructive and Non-destructive Residual Stresses in a Friction Stir Welded Lap Joint*". December 2012.

REFERENCES

1. ABAQUS User Manual, 2004, Version 6.7.3, Hibbit, Karlsson & Sorensen, Inc.
2. A. Ali, M.W. Brown, C.A. Rodopoulos, S. Gardiner, 2006, "Characterization of 2024-T351 Friction Stir Welding Joints", *ASM International*, Vol. 4, pp. 83-96.
3. J. Altenkirch, A. Steuwer, M. Peel, D.G. Richards, P.J. Withers, 2008, "The effect of tensioning and sectioning on residual stresses in aluminum AA7749 friction stir welds", *Materials Science & Engineering*, Vol. 448, pp. 16-24.
4. M. Beghini, L. Bertin, P. Raffaelli, 1995, "An Account of Plasticity in the Hole Drilling Method of Residual Stress Measurement", *Journal of Strain Analysis for Engineering Design*, Vol. 30, pp. 227-233.
5. P.R. Bevington, D.K. Robinson, 1992, "Data Reduction and Error Analysis for the Physical Sciences", *McGraw-Hill*, Inc, Boston, MA.
6. G. Bussu, P.E. Irvin, 2002, "The role of residual stress and heat affected zone properties on fatigue propagation in friction stir welded 2024-T351 aluminum joints", *International Journal of Fatigue*, Vol. 25, pp. 77-88.
7. Cheng, and I. Finnie, 1985, "A method for measurement of axisymmetric residual stresses in circumferentially welded thin-walled cylinders", *Journal of Engineering Material and Technology*, Vol. 107, pp. 181-185.
8. W. Cheng, I. Finnie, 1990, "The Crack Compliance Method for Residual Stresses Measurement", *Welding in the World*, Vol. 28, pp. 103-110.
9. W. Cheng, I. Finnie, 1991, "An Experimental Method for Determining Residual Stresses in Welds, in Modeling of Casting, Welding, and Advanced Solidification Processes", *The Mineral, Metals, and Materials Society*, pp. 245-252.

10. W. Cheng, I. Finnie, O. Vardar, 1991, "Measurement of Residual Stresses Near the Surface Using the Crack Compliance Method", *Journal of Engineering Materials and Technology*, Vol. 113 pp. 199-204.
11. W. Cheng, I. Finnie, M.B. Prime, 1992, "Measurement of Residual Stresses Through the Thickness of a Strip Using the Crack Compliance Method", *Residual stresses III- Science and Tech, Proc Thrid International Conference Residual Stresses*, Vol. 2, pp. 1127-1132.
12. C.D. Dalle, 2000, "Effect of Weld Imperfections and Residual Stresses on the Fatigue Crack Propagation in Friction Stir Welded Joints", *Second International Conference on Friction Stir Welding Proceedings*, pp. 2-10.
13. C.D. Dalle, E. Lima, J. Wegener, T. Buslaps, 2001, "Investigations on Residual Stresses in Friction Stir Welds", *The Welding Institute*. pp.556.
14. D. Deng, H. Murakawa, 2008, "Prediction of welding distortion and residual stress in thin butt-welded joint", *Computational Materials Science*, Vol. 43, pp. 353-365.
15. A.T. Dewald, J.E. Rankin, M.R. Hill, M.J. Lee, H. Chen, 2004, "Assessment of Tensile Residual Stress Mitigation in Alloy 22 Welds Due to Laser Peening", *Journal of Engineering Materials and Technology*, Vol. 126, pp. 465-473.
16. L. Dubourg, P. Doran, and S. Larose, 2007, "Prediction and Measurements of Thermal Residual Stresses in AA2024-T3 Friction Stir Welds as a Function of Welding Parameters", *Aerospace Manufacturing Technology Center*.
17. K. Elangovan, 2008, "Influence of tool pin profile and welding speed on the formation of friction stir processing zone in AA2219 aluminum alloy", *Journal of Materials Processing Technology*, Vol. 200, pp. 163-175.
18. M. Ericsson, L.Z. Jin, R. Sandtrom, 2005, "Fatigue properties of friction stir overlap welds", *International Journal of Fatigue*, Vol. 68, pp. 456-468.

19. Fett, 1996, "Determination of residual stresses in components using the fracture mechanics weight function", *Engineering Fracture Mechanics*, Vol. 55, pp. 571-576.
20. Gharghoury, 2009, "Absolute measurement of strain", Personal word document, cited 2011.
21. J. Goldak, M. Asadi, J. Nielsen, 2009, "Comparison and Analysis of Prediction of Residual Stress in a Constrained Weld with Experimental Data", *Department of Mechanical and Aerospace Engineering*, Carleton University.
22. O. Hatamleh, 2007, The Effects of Laser Peening and Shot Peening on Mechanical Properties in Friction Stir Welded 7075-T7351 Aluminum, ASM International, Vol.17, pp. 688-694.
23. M.R. Hill, W.Y. Lin, 2002, "Residual Stress Measurement in a Ceramic Material", *Journal of Engineering Materials and Technology*, Vol. 124, pp. 185-191.
24. T. Holden, J.H. Root, R.A. Holt, M. Hayashi, 1995, "Neutron-diffraction measurements of stress" *PhysicaB*, Vol. 213, pp. 793-796.
25. M.T. Hutchings, 1992, "Measurement of Residual and Applied Stress Using Neutron Diffraction", *Nato ASI Series*, Vol. 216, pp. 3.
26. I. Finnie, 1996, "Computer Aided Assessment and Control of Localized Damage", *Proceeding of The International Conference*, pp. 37-51.
27. M. James, M. Mahoney, D. Waldron, 1999, "Residual Stress Measurement in Friction Stir Welded Aluminum Alloys", *Proceedings of the 1st International Symposium on Friction Stir Welding*, California.
28. K.V. Jata, K.K. Sankaran, J.J. Ruschau, 2000, "Friction-Stir Welding Effects in Microstructure and Fatigue of Aluminum Alloy 7075-T7451", *Metall. Mater. Trans*, Vol. 31, pp. 2181-2192.

29. M. Jung, The Fatigue Characteristics of Friction Stir Welded Stiffened Panel Structure, Masters Thesis, 2007.
30. M.H. Khandakar, J. Khan, A.P. Reynolds, 2006, Journal of Materials Processing Technology, Vol. 174, pp. 195-203.
31. W. Lee, 2005, "Effects of the Local Microstructures on the Mechanical Properties in FSWed Joints of 7075-T6 Al alloy", *Zeitschrift fuer Metallkunde/Mater. Res. Adv. Tech*, Vol. 96, pp. 940-947.
32. A.J. Leonard, S.A. Lockyer, 2003, "Flaws in Friction Stir Welds", 4th *International Symposium on Friction Stir Welding*.
33. A. Merati, 2009, "Overlap Friction Stir Welding of Stringer to Skin Joint".
34. A. Merati, M. Gallant, "Friction stir lap welding of AA7075-T6 stringers on AA2024-T3 skin", 2009.
35. M.T. Milan, W.W. Bose, J.R. Tarpani, and A.M.S. Malafaia, 2007, "Residual Stress Evaluation of AA2024-T3 Friction Stir Welded Joints", *Journal of Materials Engineering and Performance*, Vol. 16, pp. 86-92.
36. G. Montay, O. Sicot, A. Maras, E. Rouhau, M. Francois, 2009, "Two Dimensions Residual Stresses Analysis Through Incremental Groove Machining Combined with Electronic Speckle Pattern Interferometry", *Experimental Mechanics*, Vol. 49, pp. 459-469.
37. K.K. Mustafa, S. Aydin, K. Erdimc, 2006, "Effects of tool rotation and pin diameter on fatigue properties of friction stir welded lap joints", *International Journal Advance Manufacturing Technology*, Vol. 36, pp. 877-882.
38. R. Nandan, 2008, "Residual Stress in Friction Stir Welded Butt Joints", *Process in Material Science*, Vol. 53, pp. 980-1023.

39. S. Nervi, B.A. Szabo, 2006, "On the estimation of residual stresses by the crack compliance method", *Computer Methods in Applied Mechanics and Engineering*, Vol. 196, pp. 3577-3584.
40. A.C. Nunes, E.L. Bernstein, J.C. McClure, 2004, "A Rotating Plug Model for Friction Stir Welding", *Welding Journal Research Supplement*, Vol. 32, pp. 345-351.
41. M. Peel, A. Steuwer, and M. Preuss, 2003, "Microstructure, mechanical properties and residual stresses as a function of welding speed in aluminum AA5083 friction stir welds", *Acta Materialia*, Vol. 51, pp. 4791-4801.
42. M.B. Prime, Experimental Procedure for Crack Compliance (Slitting) Measurements of Residual Stresses, pp. 1-6.
43. M.B. Prime, 1998, "Measuring residual stress and the resulting stress intensity factor in compact tension specimens", *Fatigue Fracture Engineering Material Structure*, Vol. 22, pp. 195-204.
44. M.B. Prime, 1999, "Residual stress measurement by successive extension of a slot: The crack compliance method", *Applied Mechanics Reviews*, Vol. 52, No. 2, pp. 75-96.
45. M.B. Prime, 2004, "Sample Files and Calculations for Slitting (Crack Compliance) Method For Measuring Residual Stress", *Los Alamos National Laboratory*, The Regents of the University of California.
46. M.B. Prime, 2006, "Uncertainty Analysis, model error, and order selection for series-expanded, residual stress inversion solutions", *Journal of Engineering Materials and Technology*, Vol. 128, pp. 175-185.
47. M.B. Prime, 2010, "Plasticity Effects in Incremental Slitting Measurement of Residual Stresses", *Engineering Fracture Mechanics*, Vol. 77, pp. 1552-1566.
48. M.B. Prime, T. Gnaupel-Herold, J.A. Baumann, 2006, "Residual stress measurements in a thick, dissimilar aluminum alloy friction stir weld", *Acta Materialia*, Vol.54, pp. 4013-4021.

49. M.B. Prime, and M.R. Hill, 2002, "Residual stress, stress relief, and inhomogeneity in aluminum plate", *Scripta Materialia*, Vol. 46, pp. 77-82.
50. M.B. Prime, R.J. Sebring, J.M. Edwards, D.J. Huges, 2004, "Laser surface-contouring and spline data-smoothing for residual stress measurements", *Society for Experimental Mechanics*, Vol. 44, pp. 176-184.
51. M.B. Prime, R.J. Sebring, J. Edwards, J. Baumann, R. Lederich, 2004, "Contour method determination of parent part residual stresses using a partially relaxed FSW test specimen", *Proceedings of the 2004 SEM X International Congress & Exposition on Experimental and Applied Mechanics*, California.
52. W. Qiu-cheng, K.E. Ying, 2003, "Evaluation of residual stress relief of aluminum alloy 7050 by using crack compliance method", *Transcript of Nonferrous Metal Society China*, Vol. 13, pp. 5-13.
53. X.Q. Qian, Z.H. Yao, Y.P. Cao, 2004, "An Inverse Approach for Constructing Residual Stress Using BEM", *Engineering Analysis with Boundary Elements*, Vol. 28, pp. 205-211.
54. S.R. Rajesh, H.S. Bang, H.J. Kim, 2007, "Analysis of complex heat flow phenomenon with friction stir welding using 3D analytical model", *Advanced Materials Research*, Vol. 15, pp. 339-344.
55. S.R. Rajesh, H. Bang, W. Seong, H. Kim, 2007, "Numerical determination of residual stress in friction stir weld using 3D-analytical model of stir zone", *Journal of Materials Processing Technology*, Vol. 187, pp. 224-226.
56. J. E. Rankin, M.R. Hill, 2003, "Measurement of thickness-average residual stress near the edge of a thin laser peened strip", *Journal of Engineering Materials and Technology*, Vol. 125, pp. 283-293.

57. A.P. Reynolds, W. Tang, T. Gnaupel-Heral, H. Prask, 2003, "Structure, properties, and residual stress of 304L stainless steel friction stir welds", *Scripta Materialia*, Vol. 48, pp. 1289-1294.
58. J. Root, K.V. Jata, K. Sadananda, 2003, "Residual stress effects on near-threshold fatigue crack growth in friction stir welds in aerospace alloys", *International Journal of Fatigue*, Vol. 25, pp. 939-948.
59. G.S. Schajer, E. Altus, 1996, "Stress Calculation Error Analysis for Incremental Hole Drilling Residual Stress Measurements", *Journal of Engineering Materials and Technology*, Vol. 118, pp. 120-126.
60. I. Sjoerd, A. Murphy, R. Benedictus, 2006, "Post-buckling failure of welded aluminum panels", *Structural Dynamic, and Materials Conference*, pp.1-17.
61. P. Staron, M. Kocak, S. Williams, 2002, "Residual stresses in friction stir welded Al sheets", *Applied Physics A Materials Science & Processing*, Vol.74, pp.1161-1165.
62. M.A. Sutton, A.P. Reynolds, 2002, "A Study of Residual Stresses and Microstructure in 2024-T3 Aluminum Friction Stir Butt Welds", *Journal of Engineering Materials and Technology*, Vol. 124, pp. 215-221.
63. R. Talwar, D. Bolser, R. Lederich, 2001, "Friction Stir Welding of Airframe Structures".
64. R.K. Uyyuru, S.V. Kailas, 2005, "Numerical Analysis of Friction Stir Welding Process", *Journal of Materials Engineering and Performance*, Vol., 15, pp.505-518.
65. S. Tochilin, D. Nowell, D.A. Hills, 1998, "Residual Stress Measurement by the Crack Compliance Technique", *Experimental Mechanics*, Vol. 45, pp. 1313-1318.
66. S. Vaidyanathan, and I. Finnie, 1971, "Determination of residual stresses from stress intensity factor measurements", *Journal of Basic Engineering*, Vol. 93, pp. 242-246.

67. W. Wanchuck, C. Hahn, W.B. Donald, 2006, “Angular distortion and through-thickness residual stress distribution in welded 6061-T6 aluminum alloy”, *Material Science & Engineering*, Vol. 437, pp. 64-69.
68. X.L. Wang, Z. Feng, S.A. David, 2000, 6th International Conference on Residual Stresses, IOM Communications, p. 1408.
69. Website, “Dave’s RV-7A Building Logs”,
<http://www.dualrudder.com/rv7/category/fuselage/center-fuselage/page/2/>, cited 2011.
70. Website, “Definition: fuselage” www.websters-dictionary-online.org/definitions/fuselage, cited 2012.
71. Website, “Don’s Bush Caddy R-120”, www.donsbusheady.com, cited 2012.
72. Website, “Fatigue Life Evaluation S-N Curve”, www.doestoc.com/docs/38722869, cited, 2012.
73. Website, “First Flight: Williams EJ22 ‘Eclipse’ Engine, <http://www.aero-news.net/index.cfm?do=main.textpost&id=e0c5c572-35a9-403e-8278-95f67e836ed5>, cited 2011.
74. Website, “Friction Stir Welding (FSW)”, Dr. Ing, Ulise, German Aerospace Center, Institute of Materials Research, www.dlr.de/wf/en/desktopdefault.aspx/tabid-2132/2294_read-3738/, cited 2011.
75. Website, “FSW Application”, <http://www.fswelding.com/application-of-friction-stir-welding-in-aircraft-structures/fsw-application>, cited 2012.
76. Website, “Friction Stir Welding at TWI”, Stephan Kallee, www.materialteknologi.hig.no, cited 2011.
77. Website, “Introducing our new full sized B-24J/PB4Y-1 fuselage hull section”, Gary Velasco, www.fightingcolors.com, cited 2011.

78. Website, "Least Squares Fitting"
<http://mathworld.wolfram.com/LeastSquaresFitting.html>, cited 28/04/2009.
79. Website, "Lockheed Martin friction stir welds Orion test article", Rob Coppinger,
www.flightglobal.com/blogs/hyperbola/2009, cited 2011.
80. Website, "Nuclear Fission: Basics", www.atomicarchive.com/Fission/Fission1.shtml,
cited 2012.
81. Website, "Real time feedback control for materials testing",
<http://www.mstarlabs.com/apeng/uwaterloo.html>, cited 2012.
82. Website, "Semi-monocoque fuselage", <http://airspot.ru/articls/how-its-made-sukhoy-superjet-100-photos>, cited 2012.
83. Website, "Structural Failures, Part 1", Nanette South Clark, 2009,
www.anengineersaspect.blogspot.ca, cited 2011.
84. S.W. Williams, 2001, "Welding of Airframes using Friction Stir", *Air and Space Europe*, Vol. 3. Pp. 34-42.
85. W. Woo, Z. Feng, X. L. Wang, D.W. Brown, 2007, "In situ neutron diffraction measurements of temperature and stresses during friction stir welding of 6061-T6 aluminum alloy", *Science and Technology of Welding and Joining*, Vol. 12, pp. 298-303.
86. W. Woo, Z. Feng, X. L. Wang, C.R. Hubbard, 2009, "Neutron diffraction measurements of time-dependent residual stresses generated by severe thermomechanical deformation", *Scripta Materialia*, Vol. 61, pp. 624-627.
87. W. Woo, T. Ungar, Z. Feng, E. Kenik, B. Clausen, 2009, "X-Ray and Neutron Diffraction Measurements of Dislocation Density and Subgrain Size in a Friction-Stir Welded Aluminum Alloy", *Metals & Materials Society and ASM International*, Vol. 41, pp. 1210-1216.

88. Y. Zhang, S. Ganguly, L. Edwards, M.E. Fitzpatrick, 2004, "Cross-sectional mapping of residual stresses in a VPPA weld using the contour method", *Acta Materialia*, Vol. 52, pp. 5225-5232.
89. X.K. Zhu, Y.J. Chao, 2003, "Numerical simulation of transient temperature and residual stresses in friction stir welding of 304L stainless steel", *Journal of Materials Processing Technology*, Vol. 146, pp. 263-272.

Appendix

APPENDIX A

MATLAB algorithm based on code provided by Michael Prime to solve for residual stress using the crack compliance method. This algorithm is the main code, which calls upon several smaller functions to complete the calculations of the residual stress. In the main code, all the material properties and parameters are set. Parameters such as using one gauge or two gauges, Poisson's ratio, Young's modulus, and number or orders used in the fitting of the strains are set in this main algorithm.

```
% solve.m:
% Initalize
clear;format compact
global Xbig1 Xbig2 Fbig1 Fbig2 dbig dbig2 color dmax header
A=0;rmserror=0;leg2(1,:)='data    ';
% Set parameters, <***** indicates parameters to set
%E=73 %73,0.33
E= 81.92122; %Aluminum E'=73 Gpa/(1-..33^2)
%E=78.55459544; %Aluminum E=70 Gpa/(1-.33^2)
%E=76.923407692; %Aluminum E'=72 Gpa/(1-.28^2)
%E=76.923407692; %Aluminum E'=86 Gpa/(1-.28^2)
igages=1;      % number of gages in least squares fit           <*****
run='txt';     % Name on data files                             <*****
ifig=1;        % figure to start plotting on                   <*****
dmax=3.25% (need to set for Legendre series only) <*****
ichoic=2;     % 1 = 1 plot per order, 2 = plot per # points <*****
ordermin=1;   % Run fits from ordermin to ordermax            <*****
ordermax=6;   %                                               <*****
```

```

iSeries = 4;    % 1 = Power series, 2 = Fourier      ,          <*****
                % 3 = Piecewise bottom half, 4=Legendre    <*****
readAll(run,iSeries,igages); % call function to read in data files
if igages==1
    ncuts=length(dbig);
else % only need to set for two gage problems
    nc11=1;nc12=59; % use cuts nc11 to nc12 from gage 1      <*****
    nc21=1;nc22=20; % use cuts nc21 to nc22 from gage 2    <*****
    leg2(2,:)= 'data    ';
end
head(iSeries,run,E) % write some info to screen
if iSeries ~= 4
    dmax=max(dbig) % Except for Legendre, assume comps normalized by max depth
end
%----- one plot per fit order -----
if icoice==1
    index=1;
    for iorder=ordermin:ordermax      %
        leg3(index,:)=sprintf('terms %2.0f,iorder);
        fprintf('\n----- iorder = %g \n' ,iorder)
        h2=setUpPlot(dbig,dbig2,Fbig1,Fbig2,ifig,igages); % plot raw data and label axes
        title([header(iSeries,') ' Terms = ' num2str(iorder)])
        jindex=0;
        for j=1:2:5 %Loop: Number of points less than max to use (1=all points) <*****
            jindex=jindex+1;
% select correct portions of compliance, strain matrices
        if igages==1

```

```

nc=ncuts+1-j;
fprintf('\nnumber of cuts = %g \n',nc)
X=-Xbig1(1:nc,1:iorder)/E;F=Fbig1(1:nc);d=[0 dbig(1:nc)']';
leg1(jindex,:)=sprintf('%2.0f points',nc);
else

nc1b=nc12+1-j;
fprintf('\nnumber of cuts used = %g-%g gage1 & %g-%g gage2
\n',nc11,nc1b,nc21,nc22)
X=-[Xbig1(nc11:nc1b,1:iorder);Xbig2(nc21:nc22,1:iorder)]/E;
F=[Fbig1(nc11:nc1b);Fbig2(nc21:nc22)];d=[0 dbig(1:max(nc1b,nc22))']';
leg1(jindex,:)=sprintf('%2.0f points',nc1b);
end
% Do least squares fit
[Fguess,A,s_var,rmserror(iorder),stress]=LSQfit(A,X,F,d,iorder,iSeries);
% plot fits to strain data
if igages==1
[h2(jindex+1)]=StrainPlot([0 Fguess'],d,ifig,jindex);% 0 added plot strain to origin
else
Fguess1=Fguess(1:nc1b-nc11+1);
Fguess2=Fguess(nc1b-nc11+2:size(Fguess));
[h2(jindex+2)]=StrainPlot(Fguess1,dbig(nc11:nc1b),ifig,jindex);
StrainPlot(Fguess2,dbig2(nc21:nc22),ifig,jindex);
end
% plot stresses
[h(jindex)]=Splot(A,s_var,d,iorder,jindex,iSeries,stress);
leg2(jindex+igages,:)=sprintf('rms = %6.2f',rmserror(iorder));
% write info to screen

```

```

    fprintf('Coefficients = ');fprintf('%8.1f ',A(:,iorder))
    fprintf('\nrmserror = %.3g \n' ,rmserror(iorder))
end % end j loop

% Add legends
    legend(h,leg1);subplot(2,1,1);legend(h2,leg2)
    ifig=ifig+1; index=index+1;
end % end iorder loop

%----- one plot per # of data points-----
else
jindex=0;
for j=1:1:1 % Number of points less than max to use (1 = all points)
    <*****
    stress=[];s_var=[];total_error=[];
    jindex=jindex+1;
    if igages==1
        nc=ncuts+1-j;
        fprintf('\nnumber of cuts = %g \n',nc)
    else
        nc1b=nc12+1-j;nc=nc1b;
        fprintf('\nnumber of cuts used = %g-%g gage1 & %g-%g gage2
\n',nc11,nc1b,nc21,nc22)
    end
    leg3(jindex,:)=sprintf('%2.0f cuts',nc);
[h2]=setUpPlot(dbig,dbig2,Fbig1,Fbig2,ifig,igages); % plot raw data and label axes
title([header(iSeries,:) ' , Number of Cuts = ' num2str(nc)])
    index=0;
for iorder=ordermin:ordermax

```

```

index=index+1;

% select correct portions of compliance, strain matrices
if igages==1
    X=-Xbig1(1:nc,1:iorder)/E;F=Fbig1(1:nc);d=[0 dbig(1:nc)'];
else
    nc1b=nc12+1-j;
    X=-[Xbig1(nc11:nc1b,1:iorder);Xbig2(nc21:nc22,1:iorder)]/E;
    F=[Fbig1(nc11:nc1b);Fbig2(nc21:nc22)];d=[0 dbig(1:max(nc1b,nc22))'];
end

% Perform least squares fit
[Fguess,A,s_var(:,iorder),rmserror(iorder,jindex),stress(:,iorder)]=LSQfit(A,X,F,d,iorder,i
Series);

% plot fits to strain data
if igages==1
    [h2(index+1)]=StrainPlot([0 Fguess'],d,ifig,index);% 0 added plot strain to origin
else
    Fguess1=Fguess(1:nc1b-nc11+1);
    Fguess2=Fguess(nc1b-nc11+2:size(Fguess));
    [h2(index+2)]=StrainPlot(Fguess1,dbig(nc11:nc1b),ifig,index);
    StrainPlot(Fguess2,dbig2(nc21:nc22),ifig,index);
end

% plot stresses
%[h(index)]=Splot(A,s_var(:,iorder),d,iorder,index,iSeries,stress(:,iorder));
leg1(index,:)=sprintf('%2.0f terms',iorder);
leg2(index+igages,:)=sprintf('rms = %6.2f',rmserror(iorder,jindex));
end % end iorder loop

order_error=[];

```

```

for io=ordermin:ordermax-1
    order_error(:,io)=std(stress(:,io:io+1))';
    total_error(:,io)=sqrt(order_error(:,io).^2+s_var(:,io).^2);
    [h(io+1-ordermin)]=Splot(A,total_error(:,io),d,io,io+1-ordermin,iSeries,stress(:,io))
end
h(ordermax+1-ordermin)=plot(d,stress(:,ordermax),color(ordermax+1-ordermin));
% add legends
legend(h,leg1);subplot(2,1,1);legend(h2,leg2)
ifig=ifig+1;
if 1 % plot error stuff ("if 1" runs this, "if 0" skips it)
    % calculate global error estimators from pointwise errors
    for iii=ordermin:ordermax-1
        rms_s_var(iii,jndex)=norm(s_var(:,iii))/sqrt(length(s_var));
        rms_total_error(iii,jndex)=norm(total_error(:,iii))/sqrt(length(s_var));
        rms_order_error(iii,jndex)=norm(order_error(:,iii))/sqrt(length(s_var));
    end
    % s_var goes to one order higher than others:
    rms_s_var(ordermax,jndex)=norm(s_var(:,ordermax))/sqrt(length(s_var));
    max_s_var(:,jndex)=max(s_var(2:length(s_var),:));
    % if we take max s_var starting from scond term, we skip bad 1st point
    % plot global error estimators
    figure(ifig);clf
    title(sprintf('strain error, number of cuts = %g',nc))
    % change "semilogy" to "plot" to get linear scale
    semilogy(ordermin:ordermax,rms_s_var(ordermin:ordermax,jndex),'c+-')

hold on;

```

```

semilogy(ordermin:ordermax,max_s_var(ordermin:ordermax,jindex),'mo-')
semilogy(ordermin:ordermax-1,rms_order_error(ordermin:ordermax-1,jindex),'r-x')
semilogy(ordermin:ordermax,rmserror(ordermin:ordermax,jindex),'g*-')
semilogy(ordermin:ordermax-1,rms_total_error(ordermin:ordermax-1,jindex),'b*-')

legend('rms stress variance','max stress variance','model error','unbiased error in strain
fit','total error')

xlabel('# of terms in expansion');

title('Choosing order')

ifig=ifig+1;

end

end % end for

end % end if

%-----

```

Appendix B

The following is the user defined subroutine used to apply the load to slit face of FE model based on Legendre polynomials. For each slit depth, 10 different loads are applied to the slit face based on the Legendre polynomials orders 2 to 11.

```

subroutine dload(f,kstep,kinc,time,noel,npt,layer,kpst,
& coords,jltyp,sname)

```

```
include 'ABA_PARAM.INC'
```

```
dimension time(2), coords(3)
```

```
character*80 sname
```

c Older abaqus versions (pre 6.1?) do not have "sname" in argument list

```
y=1-coords(2)/30.0
```

```
f=6.0*y**2-6.0*y+1.0
```

```
c f=(2.0*y-1.0)*(10.0*y**2-10.0*y+1.0)
```

```
c3 f=70.0*y**4-140.0*y**3+90.0*y**2
```

```
c & -20.0*y+1.0
```

```
c4 f=(2.0*y-1.0)*(126.0*y**4-252.0*y**3
```

```
c & +154.0*y**2-28.0*y+1.0)
```

```
c5 f=924.0*y**6-2772.0*y**5+3150.0*y**4
```

```
c & -1680.0*y**3+420.0*y**2-42.0*y+1.0
```

```
c6 f=(2.0*y-1.0)*(1716.0*y**6-5148.0*y**5
```

```
c & +5742.0*y**4-2904.0*y**3+648.0*y**2
```

```
c & -54.0*y+1.0)
```

```
c7 f=12870.0*y**8-51480.0*y**7+84084.0*y**6
```

```
c & -72072.0*y**5+34650.0*y**4-9240.0*y**3
```

```
c & +1260.0*y**2-72.0*y+1.0
```

```
c8 f=(2.0*y-1.0)*(24310.0*y**8-97240.0*y**7
```

```
c & +157300.0*y**6-131560.0*y**5+60346.0*y**4
```

```
c & -14872.0*y**3 +1804.0*y*y-88.0*y+1)
```

```
c9 f= 184756.0*y**10.0-923780.0*y**9.0+1969110.0*y**8.0
```

```
c & -2333760.0*y**7.0
```

```
c & +1681680.0*y**6.0-756756.0*y**5.0+210210.0*y**4.0-34320.0
```

```
c & *y**3.0+2970.0*y**2.0-110.*y+1.0
```

```
c10 f=(2*y-1)*(352716*y**10-1763580*y**9+3737110*y**8-4366960*y**7+306
```

```
c  &7480*y**6-1325116*y**5+346450*y**4-52000*y**3+4030*y**2-130*y+1)
c    write(7,99) y,f
c    write(6,99) y,f
67  format(a13,1f8.4,a18,1f8.4)
99  format(2f10.2)
    return
    end
```